

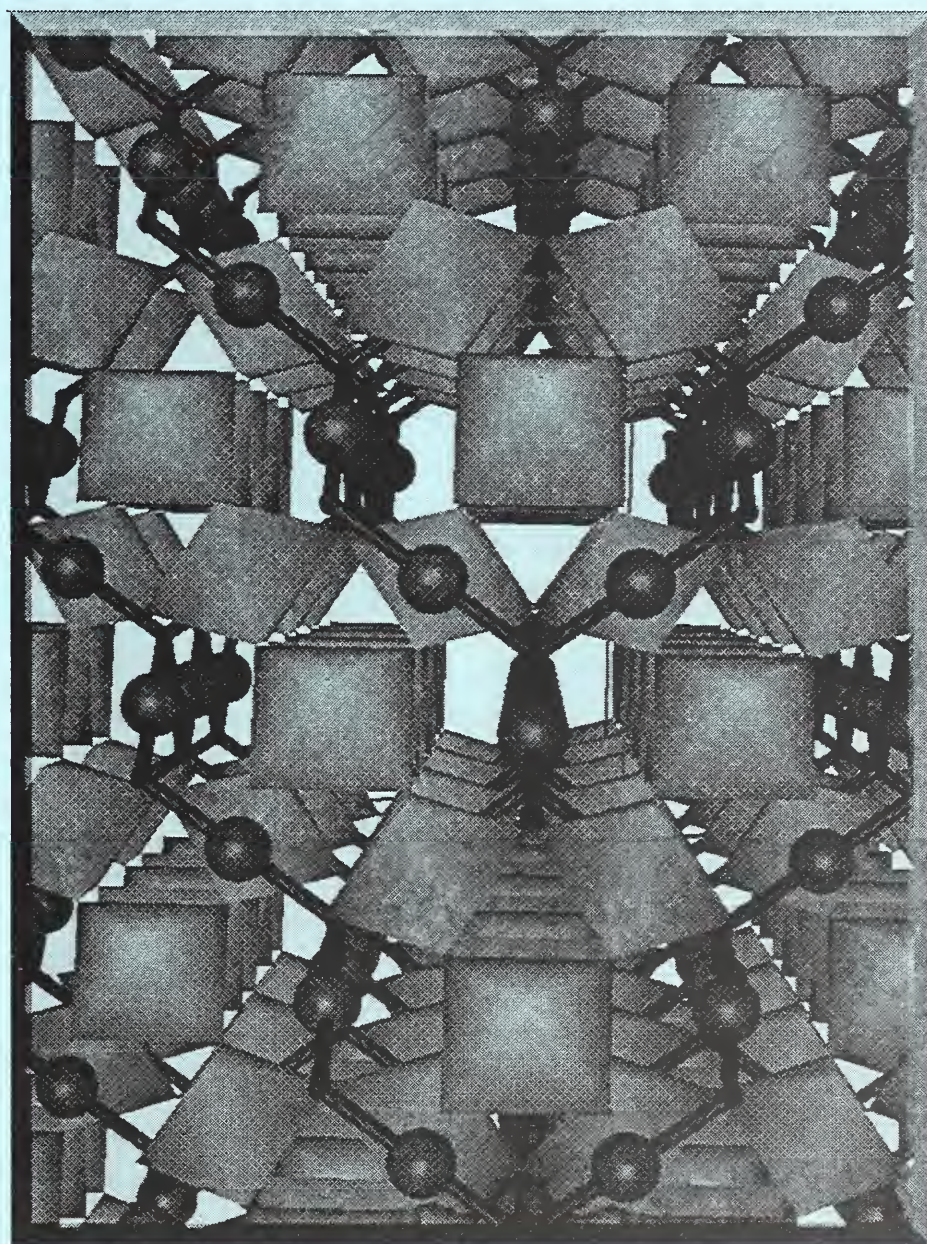
NAT'L INST. OF STAND & TECH R.I.C.
A11105 156513

NIST
PUBLICATIONS

MSEL

Materials Science and Engineering Laboratory

REACTOR RADIATION



NISTIR 5966
U.S. Department of Commerce
Technology Administration
National Institute of Standards
and Technology

QC
100
U56
NO.5966
1996

Technical Activities 1996

Reactor Radiation

Structural analysis of $\text{Ti}_2\text{Mn}_2\text{O}_7$ pyrochlore, an exhibitor of colossal magnetoresistance, has been completed using powder neutron diffraction and single-crystal x-ray diffraction. As shown schematically in the figure, the structure features MnO_6 octahedra connected by corner-shared oxygens. Nearly 100% suppression of resistance has been observed in thin films of manganite, increasing interest in these materials for use as magnetic storage media. The fact that the origin of CMR in these materials appears to be fundamentally different from that of the perovskites may lead to a new route to the use of CMR in this class of application.



Materials Science and Engineering Laboratory

REACTOR RADIATION

J.M. Rowe, Chief
T.M. Raby, Deputy

NISTIR 5966
U.S. Department of Commerce
Technology Administration
National Institute of Standards
and Technology

Technical Activities 1996



U.S. DEPARTMENT OF COMMERCE
Michael Kantor, Secretary
TECHNOLOGY ADMINISTRATION
Mary L. Good, Under Secretary for Technology
NATIONAL INSTITUTE OF STANDARDS
AND TECHNOLOGY
Arati Prabhakar, Director

Abstract

This report summarizes all the programs that use the NIST reactor. It covers the period for October 1995 through September 1996. The programs range from the use of neutron beams to study the structure and dynamics of materials through nuclear physics and neutron standards to sample irradiations for activation analysis, isotope production, neutron radiography, and nondestructive evaluation.

KEY WORDS: activation analysis; cold neutrons; crystal structure; diffraction; isotopes; molecular dynamics; neutron; neutron radiography; nondestructive evaluation; nuclear reactor; radiation.

DISCLAIMER

Certain trade names and company products are identified in order to adequately specify the experimental procedure. In no case does such identification imply recommendation or endorsement by the National Institute of Standards and Technology, nor does it imply that the products are necessarily the best for the purpose.

FOREWORD

This has been an outstanding year for the NIST Research Reactor and associated facilities from any perspective. During 1996, the reactor operated 249 20 MW days, the second best year on record. The new cold source went into routine operation, providing all of the instruments in the Cold Neutron Research Facility with substantial intensity gains. The science and engineering results produced were exciting, and many researchers were welcomed here - both old and new friends. And last, but far from least, the political situation at the end of the year was far more settled than last year, and we were able to concentrate on our jobs.

The reactor modifications and upgrades that were completed during the long shutdown proved their worth during this first complete year of operation, in which the reactor returned to 20 MW. All of the systems are working well, and virtually all of the unexpected shutdowns were the result of interruptions to commercial power. As mentioned above, in spite of the problems at the beginning of the year (furloughs, government shutdowns), the reactor operated for 249 days at 20 MW during calendar year 1996, a record exceeded only once in prior years. We adopted a more predictable schedule for reactor startup and shutdown, and posted this schedule on the home page. There were no problems worthy of mention during the entire year of operation.

Another component which was installed during the long shutdown, the liquid hydrogen cold source, operated almost as well as the reactor. There were only two instances in which the source prevented immediate restart of the reactor after commercial power interruption, leading to a source availability of over 99% (defined as fraction of time source was ready to operate when the reactor was ready to operate). The combined reactor and cold source operated 100 % of the scheduled hours during the year, with more than 95 % of that operated at the time originally scheduled. Equally if not more importantly, the source neutronic performance equaled or exceeded expectation, providing gains of 3-7 over the wavelengths of interest for all cold neutron instruments.

The reactor and cold source performance was fully matched by the staff and users, who produced a steady stream of stimulating and important results. Many of the instruments were substantially improved or replaced during the shutdown, including the powder diffractometer, the residual stress instrument, and the horizontal scattering path reflectometer. Combining the increased power level of operation, the improved cold source and the improved instruments, it is fair to say that there has been a revolutionary increase in the capabilities of the facility. The highlights of the impact which this has had are stressed in this report.

Finally, the future outlook for the facility is excellent. NIST management is committed to the upgrade and relicensing of the facility to extend the operation for two decades beyond 2004. We have begun to upgrade the thermal neutron instruments, and will expand that effort in the next few years. We are committed to continual improvement of our facilities, performance, and scientific programs and look forward with anticipation to the coming challenges.

J. M. Rowe
Chief
Reactor Radiation Division

CONTENTS

Abstract	iv
Foreword	v
Chemical Physics of Materials	1
Yttrium and Lanthanum Hydrides	1
Interstitial Hydrogen in C ₆₀	5
The Hydration Reaction During Cement Curing	7
Neutron Scattering Studies of Disordered Carbon Anode Materials	9
Electrides	12
Research Topics	14
Affiliations	16
Magnetism and Superconductivity	17
Magnetizing a Quantum Spin Chain	17
Pr Magnetism in Cuprates	18
Magnetoresistive Oxides	20
Exchange-Biased Superlattices	22
Coupled Charge and Spin Ordering	17
Research Topics	25
Affiliations	27
Crystallography	29
Instrumentation and Software	29
Phase Analysis	29
Crystal Structures	31
Zeolite SRM Characterization	33
Database Activities	34
Research Topics	35
Affiliations	37
Surface and Interfacial Studies	39
The New Reflectometer at NG-1	39
Molecular Beam Epitaxy Chamber for In-Situ Neutron Scattering	40
Hydrogen Induced Changes in the Magnetic Ordering of Fe-V (001) Superlattices	42
Location of Peptides in Alkanethiol/Phospholipid Biomimetic Bilayer Membranes	44
Interlayer Coupling in Annealed Ni-Fe/Cu Multilayers	46
The Magnetic Structure of Cr in Fe/Cr(001) Superlattices	48
Block Copolymer Films on Brushes: Controlling Lamellar Wetting	49
Surface-Induced Phase Segregation in Disordered Diblock Copolymers	51
Influence of Diblock Copolymer on Polymer Blend Phase Behavior	53
Relaxation of Polymeric Bilayers below the Bulk Glass Transition Temperatures	54
Research Topics	55
Affiliations	57

Macromolecular and Microstructure Studies	58
Complex Fluids	58
Polymers	62
Research Topics	65
Affiliations	68
Neutron Beam Applications	70
Neutron Diffraction Measurement of Residual Stress	70
Neutron Diffraction Measurement of Texture	75
Neutron Autoradiography Program	75
Research Topics	77
Affiliations	78
Analytical Chemistry	79
Nuclear Methods Group	79
Smithsonian Institution	84
Food and Drug Administration	85
University of Maryland	86
Research Topics	87
Affiliations	89
Neutron Interactions and Dosimetry	90
Fundamental Neutron Physics	90
Neutron Fields and Standards	92
Research Topics	93
Affiliations	94
Polymers Division Programs	95
Interfaces and Thin Films	95
Blends	96
Melts and Solutions	97
Pressure Studies	100
Research Topics	100
Affiliations	101
Exxon Research at the CNRF	102
Pure Component Properties and Mixing Behavior in Polyolefine Blends	102
Blends of Block Copolymers with Homopolymers	102
Microstructure and Rheology of Polymeric Micellar Solutions	102
Simultaneous Measurements of Viscosity and Structure for Rod-like Micelles	103
Structure and Flow Properties of Rod-like Micelles with Associating Polymers	103
High Resolution SANS Characterization of Asphaltene Particles	103
Research Topics	104
Affiliations	105
University of Minnesota Programs	106
Research Projects	106

Research Topics	108
Affiliations	108
Instrumentation Development	109
High-Flux Backscattering Spectrometer	109
Neutron Spin Echo Spectrometer	111
Disk Chopper Time-of-flight Spectrometer	111
New Filter Analyzer Neutron Spectrometer (FANS)	114
Monochromator Development	116
Perfect Crystal SANS Diffractometer	118
Implementation of Polarized Neutron SANS	118
Research Topics	118
Affiliations	119
MSEL Programs	120
Biotechnology	120
Ceramic Coatings	120
Evaluated Materials Data	121
High Temperature Superconductivity	122
Reactor Operations and Engineering	123
Guest Researchers and Collaborations	124
Organizational Charts	127
Personnel Roster	129
NBSR and CNRF Resident Staff	130
Research and Engineering Staff	133
Technical Staff	137
Technical and Professional Committee Participation and Leadership	138
Publications	142

Chemical Physics of Materials

Research at the NBSR which falls into this category typically involves inelastic neutron scattering measurements of the dynamics of molecular solids, various inclusion compounds, and structurally disordered materials. These studies yield detailed information on the atomic and molecular interactions responsible for many properties of these systems. For cases involving either rotational excitations or hydrogen motions or both, this information is difficult, if not impossible, to obtain by other means. Furthermore, since thermal neutron wavelengths are comparable to interatomic spacings, one is able to ascertain the geometry of the various motions in a way unmatched by other spectroscopic probes. Each of these attributes is featured in one or more of the examples that are highlighted here.

Yttrium and Lanthanum Hydrides

The interaction of hydrogen with the rare-earth metals has been the subject of numerous investigations due to the interesting temperature- and concentration-dependent structures and properties observed in the α -phase solid solutions as well as the various ordered metallic and semiconducting hydride phases. This interest has intensified recently due to the discovery of the novel switchable optical properties of rare-earth hydride films [1]. Neutron scattering methods have been crucial for gaining a better understanding of the hydrogen binding potentials and ordering in these systems. Over the past year, we have directed our studies [2] toward obtaining a more comprehensive understanding of the structure, phases, and dynamics for two representative systems, YH_x and LaH_x , up to $x=3$. We present here an extensive summary of these results.

The neutron vibrational spectra of the different phases of YH_x shown in Fig. 1, illustrate the marked differences in the H density of states (DOS). At low H concentrations below

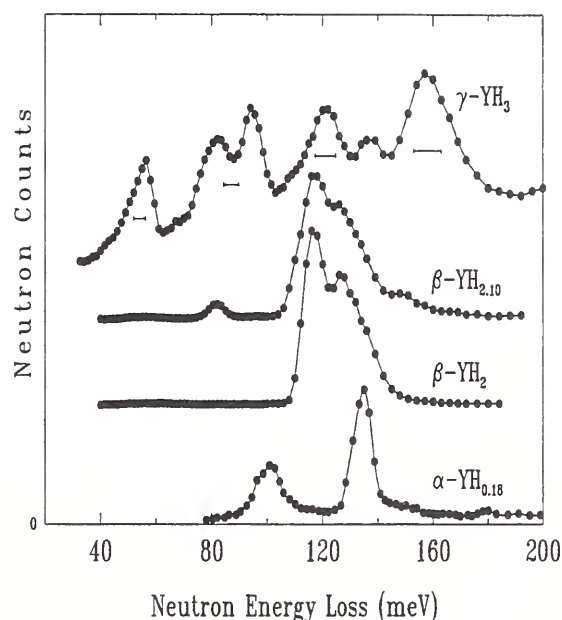


Figure 1. Comparison of the low-resolution vibrational spectra for $\alpha\text{-YH}_{0.18}$, $\beta\text{-YH}_2$, $\beta\text{-YH}_{2.10}$ and $\gamma\text{-YH}_3$ at low temperature. The horizontal bars correspond to the calculated instrumental resolution.

$x \approx 0.2$, an α -phase solid solution exists with H residing in the tetrahedral (t) interstices of the hexagonal-close-packed (hcp) metal lattice, which is stable down to near absolute zero. Below 150-170 K, a short-range ordering occurs involving the alignment of pairs of H atoms (in second-nearest-neighbor t sites separated by a metal atom) into zigzag-shaped, c -axis-directed chains. This novel pairing potential and the associated rapid proton hopping have been reviewed extensively in previous reports.

Above $x \approx 0.2$, YH_x precipitates out into the β -phase dihydride $\beta\text{-YH}_2$, forming a face-centered-cubic (fcc) Y lattice with H fully occupying the t interstices. For $2 < x < 2.10$, the excess H atoms partially occupy the octahedral (o) interstices. This can be seen clearly in

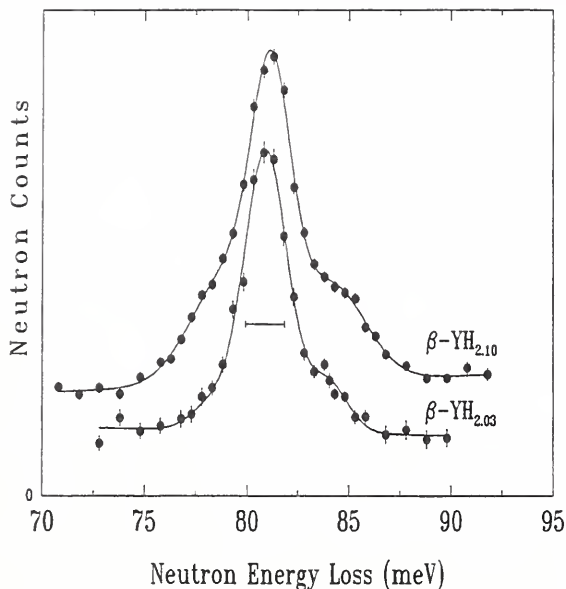


Figure 2. High-resolution H_o vibrational spectra for β - $YH_{2.03}$ and β - $YH_{2.10}$ at 10 K.

the H DOS spectra for β - YH_2 and β - $YH_{2.10}$ in Fig. 1. The pure dihydride spectrum yields a broad complex doublet centered at ~ 123 meV due to the vibrations of the t -site H (H_t) atoms. Isotope-dilution experiments show that the complex vibrational DOS for the H_t atoms is a manifestation of H-H dynamic interactions, similar to that observed in α - YH_x . In particular, diluting the H atoms with heavier D atoms in the β -phase dihydride causes a collapse of the broad band due to optical phonon dispersion into a much sharper singlet feature representative of an isotopically-isolated H_t atom situated in a cubic potential.

The superstoichiometric dihydride β - $YH_{2.10}$ (Fig.1) possesses a similar doublet, as well as a small lower-energy feature at 81.2 meV due to the vibrations of the o -site H (H_o) atoms. Near this upper β -phase boundary, there are indications that the H_o atoms develop a short-range-ordered arrangement akin to the long-range ($I4/mmm$) order expected for the hypothetical cubic $YH_{2.25}$ stoichiometry, in

which only every fourth (042) o -site plane is occupied by hydrogen. This behavior is consistent with the low-temperature vibrational spectra of the H_o atoms in β - $YH_{2.03}$ and β - $YH_{2.10}$ in Fig. 2. The H_o spectra display a concentration dependence similar to those for the superstoichiometric dihydrides of Tb and La. In all these systems, the H_o DOS is found to be sensitive to the temperature- and concentration-dependent arrangement of the H_o atoms in the o -site sublattice. For $x = 2.03$, the low-concentration H_o atoms are predominantly isolated in a local cubic environment and possess a sharp DOS. Minor sideband contributions are attributed to the small fraction of H_o atoms that participate in small clusters of short-range order at this H_o concentration. As x increases to 2.10, the extent of the short-range order increases, as evidenced by the growth of the sidebands with respect to the central feature.

In actuality, for H concentrations above $x = 2.10$, γ -phase YH_3 precipitates out, reverting to an hcp metal lattice, which is typical of the other heavier rare-earth trihydride systems. Neutron powder diffraction (NPD) results for YD_3 indicate a $P3\bar{c}1$ structure in which the D atoms occupy unusual interstitial positions of a c -axis-elongated hcp metal lattice, instead of the more conventional o and t sites (see Fig. 3). The D_o atoms are displaced vertically toward the metal planes from their ideal o -site positions, with one-third and two-thirds of the atoms located at in-plane ($m1$) and near-plane ($m2$) three-fold positions, respectively. The D_t atoms are displaced horizontally also in a correlated fashion to accommodate the presence of the D_m atoms. The γ - YH_3 spectrum in Fig. 1 shows the complexity of the H vibrational DOS. A complete mode assignment of the spectrum is in progress. Considering the sizes and geometries of the m and t sites, it is believed that the c -axis-polarized vibrations of the H_m atoms account for the lowest-energy asymmetric feature at 57 meV.

Unlike YH_x , the light rare-earth hydride LaH_x maintains its fcc metal sublattice over the entire concentration range $2 \leq x \leq 3$. This leads

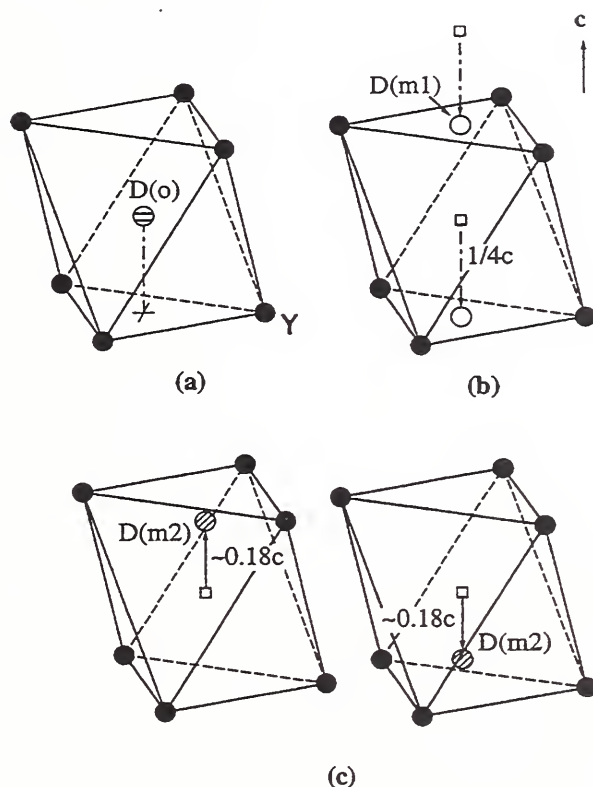


Figure 3. The displacement of the D atoms from (a) the hypothetical ideal *o* sites defined by the hcp metal sublattice to (b) the in-metal-plane and (c) the near-metal-plane *m* sites in the actual γ -YD₃ structure.

to a more complicated phase diagram and more significant and variegated H-H interactions over this H-concentration range. This is mirrored by the low-temperature H vibrational spectra for the *x*-dependent series of La hydrides in Fig. 4. Upon increasing the H concentration from $x = 2$ (where the spectrum reflects only H_t vibrations) to $x = 3$, the H_t DOS (i.e., the features above ~ 80 meV) transforms into a complex distribution of peaks due to *x*-dependent H_t - H_o and H_t - H_t interactions. Concomitantly, the contributions from the H_o DOS emerge and grow in a way dictated by *x*-dependent H_o - H_o interactions. In particular, as discussed earlier for the β -YH_{*x*} spectra in Fig. 2, the relatively sharp DOS at 70.7 meV for the predominantly isolated H_o atoms in LaH_{2.03} transforms into a broadened bimodal distribution peaked at 68.3

meV and 74.0 meV for LaH_{2.25}. The latter H_o DOS is a reflection of the $I4/mmm$ order which is stabilized at low temperature. The long-range order in the H_o sublattice of LaH_{2.25} is accompanied by a cubic-to-tetragonal lattice distortion. In this structure, all nearest-neighbor *o* sites surrounding the H_o atoms are vacant, suggesting that a repulsive H_o - H_o interaction drives the H_o ordering. Due to the presence of significant *x*-dependent H-H interactions in these systems, the local site symmetry of the H_o atoms may no longer be considered to be cubic, since the positions of the surrounding H_o neighbors must also be included. Consideration of the noncubic symmetry of the $I4/mmm$ -ordered H_o sublattice in LaH_{2.25} and the relative intensities of the bimodal peaks leads to the assignment of the stronger, higher-energy component to degenerate H_o vibrational modes polarized in the *ab* plane and the weaker, lower-energy component to the orthogonal singlet H_o vibrational mode along the *c* direction. This suggests similar assignments for the spectral sidebands found for the H_o DOS in β -YH_{2.10} in Fig. 2, except for that in that case the H_o ordering is shorter-ranged.

As the H concentration increases to LaH_{2.50}, the relative intensities of the bimodal components of the H_o DOS become reversed and further broadened. In this instance, the ideal, low-temperature, long-range-ordered structure as determined for LaD_{2.50} by NPD has $I41/amd$ symmetry. The H_o ordering can be described as a repeating sequence of four (042) *o*-site planes comprised of two adjacent filled planes followed by two adjacent empty planes. Again, based on symmetry and relative intensity arguments, the stronger, lower-energy component of the H_o DOS would be assigned to the degenerate H_o vibrational modes polarized in the *ab* plane and the weaker, higher-energy component to the orthogonal H_o vibrational mode polarized along the *c* direction. This is in contrast to the assignment in LaH_{2.25}, where the *c*-axis mode is the softer mode.

Figure 5 illustrates the effects of D-D inter-

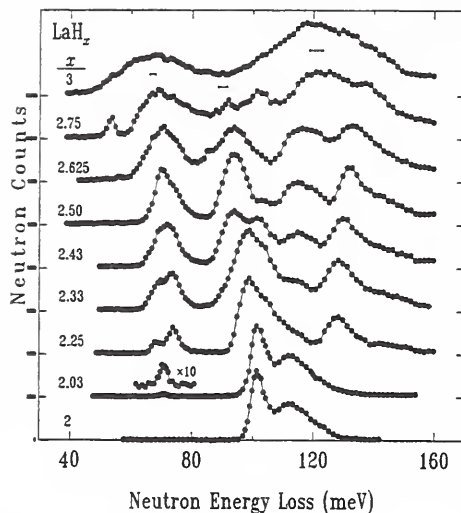


Figure 4. High-resolution vibrational spectra for LaH_x ($2 \leq x \leq 3$) near 10 K.

actions on the D_o DOS for $\text{LaD}_{2.50}$ by a comparison with the D_o DOS for $\text{La}(\text{H}_{0.9}\text{D}_{0.1})_{2.50}$. Similar to the isotope dilution results for α - $\text{YH}_{0.18}$ and β - YH_2 , dilution of the D atoms with the lighter H atoms causes a collapse of the D_o DOS into a much sharper feature. Again, this demonstrates the presence of significant dynamic coupling interactions within the D_o sublattice of $\text{LaD}_{2.50}$ as the origin of the vibrational line broadening.

The H DOS for $\text{LaH}_{2.75}$ in Fig. 4 is worthy of mention due to the emergence of unusual features at 53.4, 92, and 102 meV. These features appear to smear out or disappear as the temperature is increased above the tetragonal-to-cubic phase transition near 240 K. Low-temperature NPD measurements of $\text{LaD}_{2.75}$ are suggestive of the presence of a minor second phase of unknown structure besides a main tetragonal phase possessing long-range D_o ordering. Further experiments are underway to determine whether these DOS features may indeed be related to the presence of some secondary phase.

At the highest H concentration, LaH_3 , the two extremely broad H_o and H_t components of the H DOS in Fig. 4 reflect considerable

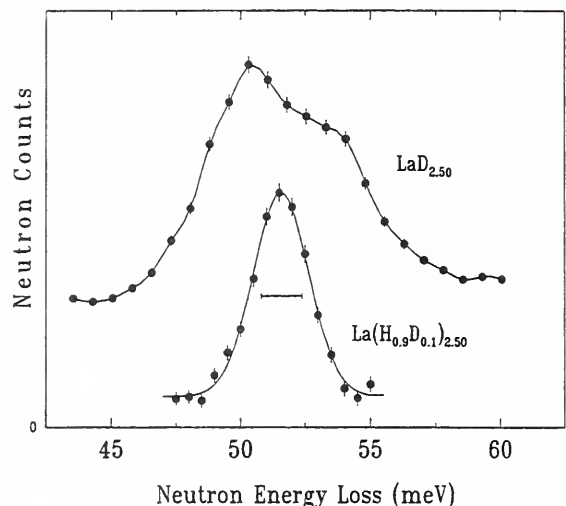


Figure 5. Comparison of the high-resolution D_o vibrational spectra for $\text{LaD}_{2.50}$ and $\text{La}(\text{H}_{0.9}\text{D}_{0.1})_{2.50}$ at 10 K.

optic-phonon dispersion due to H-H interactions. Recent high-resolution NPD measurements of LaD_3 indicate a complex phase change involving a probable displacement and/or ordering of the D_o atoms below 260 K. Quasielastic scattering measurements on LaH_3 at room temperature and below suggest rapid localized H motions in the α -site interstices, probably amongst off-center positions along the $[111]$ directions.

Finally, investigations have been undertaken in order to characterize more carefully the H and D site distributions in mixed-isotope rare-earth hydrides. In particular, both NPD and spectroscopic measurements of $\text{La}(\text{H}_{1-y}\text{D}_y)_{2.50}$ ($0 \leq y \leq 1$) confirm that an isotopic enrichment of H with respect to D occurs in the α -sites and is maximized at low temperature. For example, for $\text{La}(\text{H}_{0.2}\text{D}_{0.8})_{2.50}$, Rietveld refinements have indicated that the H/D isotopic ratio in the α -site sublattice varies from 41/59 at 15 K to 30/70 at 300 K and 26/74 at 400 K. The range of values is significantly different from the overall H/D stoichiometric ratio of 20/80. The physics behind this phenomenon is currently being explored.

Interstitial Hydrogen in C₆₀

The C₆₀ lattice has large interstitial sites which can accommodate various molecular species. Analyzing the behavior of impurity molecules placed in these sites provides information about both the intermolecular potential of C₆₀ and the dynamics of molecules trapped in confined spaces. For neutron scattering experiments molecular hydrogen is the ideal interstitial species to study. Besides having the highest incoherent neutron scattering cross section free hydrogen acts as an ideal quantum mechanical rigid rotor with the largest energy spacing between rotational levels of any molecular system. The isotopic shift on substituting D₂ for H₂ is also the largest of any species.

The high symmetry of the hydrogen molecule places additional quantum mechanical constraints on the spin statistics governing its rotational behavior. Molecular hydrogen comes in two forms, ortho-hydrogen which has a total nuclear spin of 1 and para-hydrogen which has a spin of 0. Due to the principle of indistinguishability the overall wavefunction must be anti-symmetric. This constrains ortho-hydrogen to stay in a state for which the rotational quantum number J is odd while para-hydrogen must have J even. Due to the extremely slow conversion rate, a system cooled to low temperatures maintains its room temperature ortho to para ratio. At 4.2 K $\sim 75\%$ of the molecules are in the $J = 1$ state and 25% in the $J = 0$ state. That the system is far from thermal equilibrium proves very advantageous in performing low temperature neutron energy gain measurements.

Experimentally the sample consists of 10 g of commercially obtained (MER Corporation) pure C₆₀ powder, sealed inside a high pressure aluminum cell. The system is evacuated and hydrogen gas is directly introduced from a standard cylinder at ~ 2000 psi. This pressure is maintained for 5 hours while the sample is heated to a temperature of 330 K. The sample is then cooled below 150 K. The interstitial H₂ is now "frozen" inside the C₆₀ lattice and any free gas

is pumped away.

Diffraction data are obtained on a sample loaded with D₂ using the 32-detector high-resolution powder diffractometer on BT-1. Scans are taken over a period of 24 hours with the sample temperature maintained at 10 K and the diffractometer operating at a wavelength at 1.54 Å. The low temperature $Pa\bar{3}$ phase of C₆₀ has two tetrahedral and one octahedral interstitial sites per molecule. Previous experiments have shown that He, Ne, H₂, N₂, H₂O, and O₂ all enter into the C₆₀ lattice interstitially [3-5]. NMR work has confirmed that at least in the case of interstitial O₂ the octahedral site is occupied exclusively [3]. In our case the locations of the D₂ molecules are determined by neutron diffraction. A Rietveld refinement of the diffraction pattern taken at 10 K shows that 42 % of the octahedral sites are filled with randomly oriented D₂ molecules. This is in good agreement with outgassing results which show that for every C₆₀ molecule there are 0.4 molecules of D₂. There is no evidence for any occupancy of the tetrahedral sites.

Incoherent inelastic neutron scattering data are obtained using the Fermi-chopper time-of-flight (TOF) spectrometer operating with a wavelength of 4.8 Å. The data are taken for the same sample in the same cell, and prepared under the same conditions as those of the diffraction study. Figure 6 shows the TOF data taken in energy gain and integrated over all detectors covering a Q range from 2 to 4 Å⁻¹. The sample temperature, 30 K, is such that at 15 meV the energy gain side of the spectrum should be suppressed by a factor of more than 10⁵ relative to the energy loss side. Practically this is very useful since there is essentially no scattering from the C₆₀ and the sample cell whereas the lack of ortho to para conversion for H₂ molecules means that scattering associated with the $J=1$ to $J=0$ transition is not suppressed at all. The peak in the spectrum shown in Fig. 6 is fitted to a resolution limited Gaussian profile of width 1.4 meV centered at 14.2 meV. This peak position corresponds to a shift of 3.4% from that of free

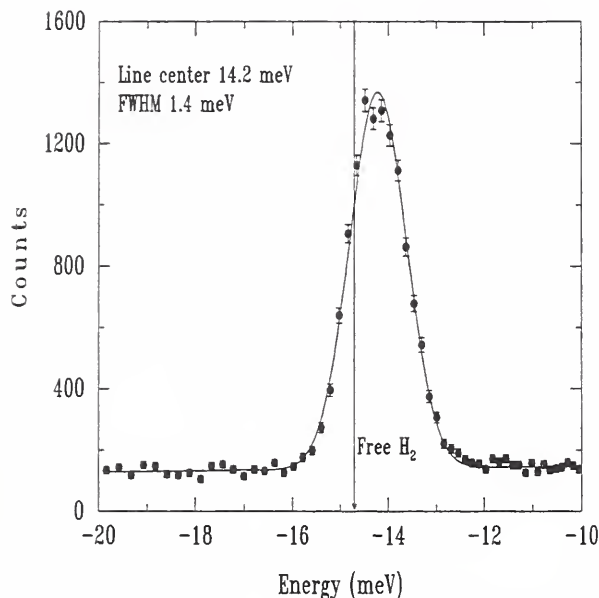


Figure 6. Time-of-flight energy gain spectrum of interstitial H_2 in C_{60} . The data are taken at 30 K.

hydrogen which is centered at 14.7 meV [6]. The relatively small shift in energy from that of the idealized rigid rotor implies that the interstitial hydrogen is rotationally quite free. However the sharpness of the peak and the fact that there is no shift in the peak position with Q confirm that the H_2 molecule is translationally bound to the lattice.

Figure 7 shows the temperature dependence of the energy gain spectrum. Each curve is obtained by subtracting the results for a pure C_{60} sample at the same temperature. The main peak shows no apparent shift in position with temperature while broadening from a FWHM of 1.4 meV at 30 K to 4.2 meV at 200 K. In addition to the main peak all the higher temperature spectra show a secondary peak centered at 28.0 meV. This corresponds to the $J=2$ to $J=1$ rotational transition which occurs at 29.4 meV in free hydrogen. Since the $J=2$ state is neither the ground state for ortho or para-hydrogen, it is not thermally populated at 30 K and the transition is not observed in the lowest temperature spectrum.

D_2 having twice the mass of H_2 but the same

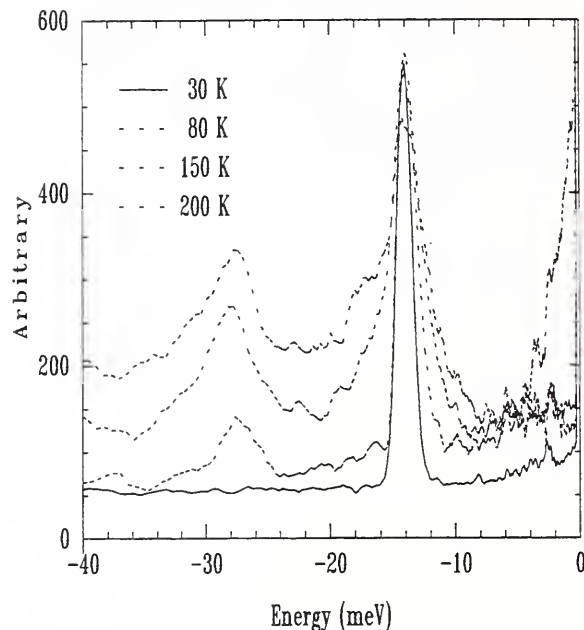


Figure 7. The temperature dependence of the energy gain spectrum for interstitial H_2 in C_{60} .

internuclear separation has a rotational constant which is half that of H_2 , and therefore its $J=1$ to $J=0$ transition occurs at 7.35 meV. The intensity of the D_2 transition is predicted to be reduced by a factor of 27 relative to that of H_2 . Figure 8 shows TOF data for a $\text{C}_{60}(\text{D}_2)_{0.4}$ sample taken at 10 K. The transition is now split into a doublet with peaks centered at 7.4 and 6.7 meV. Both peaks are resolution limited, having widths of 0.6 and 0.5 meV respectively. Their relative intensities are identical to within 3%.

The fact that the D_2 sample shows a splitting in its peak while the H_2 does not is somewhat surprising. Symmetry arguments show that an octahedral potential is not sufficient to cause a splitting in the m_J levels of the $J=1$ rotational level. However, since the C_{60} molecules are not truly spherical, the interstitial molecules experience a potential which is of a slightly lower symmetry than octahedral and in fact corresponds to the full $Pa\bar{3}$ symmetry of the lattice. This could in principle cause a splitting in the m_J levels. However numerical calculations show that

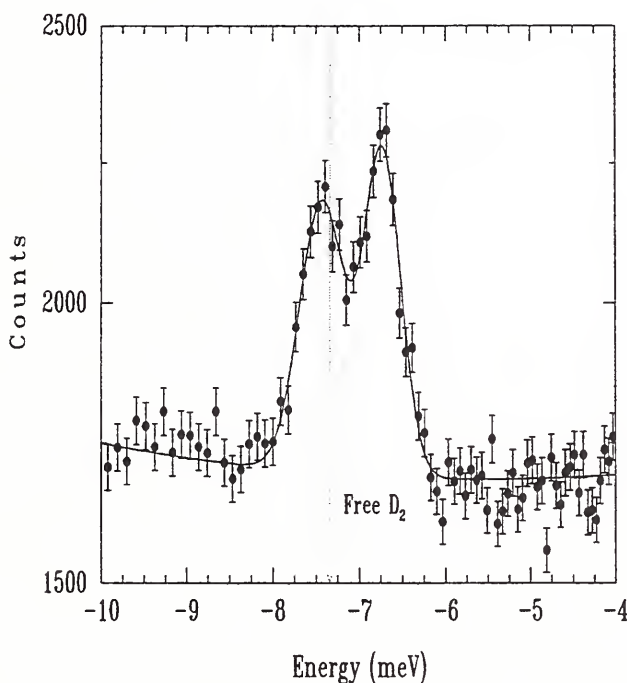


Figure 8. Time-of-flight energy gain spectrum of interstitial D_2 in C_{60} . The data are taken at 10K.

the splitting for H_2 should be comparable to that of D_2 . An alternate explanation is that the splitting in the D_2 case occurs through the accidental degeneracy of the rotational level with the T_{1u} phonon mode of the C_{60} lattice which is centered at 6.8 meV.

Future work will focus on testing these hypotheses by examining the excited state rotational transitions of $C_{60}(D_2)_{0.4}$ and the effects of hydrostatic pressure on the ground state transition of $C_{60}(H_2)_{0.4}$. Knowledge of the precise transition energies should contribute to a detailed model of the carbon-hydrogen interactions in this material.

The Hydration Reaction During Cement Curing

The reaction mechanism between tricalcium silicate (C_3S) and water is the principal factor in the setting and hardening of Portland cement. Given its importance, this reaction has been studied by a number of investigators in order to predict accurately the development of strength

in concrete. However the kinetics of the reaction and even the specific mechanisms are not completely understood. The chemical reaction is represented using cement terminology by



where X , Y , Z are all unknown and CSH is the final amorphous product of calcium silicate hydrate which has a variable composition and stoichiometry.

Neutron scattering provides a direct method for quantifying the conversion of free water to bound water during the above reaction. For a given value of the scattering vector, Q , the quasi-elastic energy transfer spectrum can be described, in the simplest model, by the sum of a Gaussian function, representing elastic scattering from fixed hydrogen, and a single Lorentzian function representing the scattering from translationally "free" water molecules. The incoherent scattering function then has the form:

$$S_{inc}(Q, \omega) = A \left[\frac{1}{\sigma\sqrt{2\pi}} e^{-\frac{\omega^2}{2\sigma^2}} \right] + B \left[\frac{\Gamma}{\pi(\Gamma^2 + \omega^2)} \right] \quad (2)$$

where A is the number density of bound hydrogen atoms, B is the number density of translationally free hydrogen atoms (all of which are assumed to be in the form of water), Γ is the Lorentzian full width at half maximum, and the Gaussian standard deviation σ is determined by the resolution of the spectrometer.

The experimental data are fitted to the function in Eq. 2 and the free parameters A , B , and Γ are extracted. We then define a free water index (FWI); $FWI = B/(A + B)$. The FWI represents the fraction of water molecules which are still liquid-like free water on a neutron time scale of $\sim 10^{-10}$ s. The FWI initially starts off at unity as the water and cement are mixed and then decreases with time as the cement cures. The free water is principally consumed either through the molecules binding into the final gel-like structure of the CSH cement or through the

water chemically reacting to form calcium hydroxide.

The quasi-elastic measurements are performed using the Fermi chopper time-of-flight spectrometer operating with an incident wavelength of 4.8 Å. The C3S powder obtained from CTL laboratories is mixed with distilled water to produce a paste with a 0.4 water/cement ratio by weight. This is spread into a 0.5 mm thick layer on an aluminum cell which is then sealed. The sample is maintained at a constant temperature throughout the experiment. The results are averaged into 30 minute slices with data being taken continuously for the first 36 hours and thereafter at selected times for up to 60 days. The hydration results for samples cured at 20, 30 and 40 °C are shown in Fig. 9. As expected all three curves start with an initial FWI of unity. In each case the FWI decreases slowly at first but is followed by a sudden sharp drop in the amount of free water. The rapid decrease occurs after ~15 % of the free water has been consumed. The duration of the delay period depends on temperature varying from 5 hours at 40 °C, to 19 hours at 30 °C, and extending to as long as 33 hours at 20 °C.

The rapid decrease in the FWI could occur either through the sudden incorporation of water into the CSH gel structure or through a sharp increase in the formation of calcium hydroxide. The presence of calcium hydroxide can be determined through neutron inelastic spectroscopy since it has a distinctive excitation centered at ~41 meV. Neither our initial C3S powder nor the final CSH product has a peak in this energy region. Thus by continually taking inelastic spectra for the curing cement sample and mapping out the growth in the 41 meV peak we can monitor the formation of calcium hydroxide. Figure 10 shows the results of such an analysis. With the sample maintained at 20 °C inelastic spectra are taken every hour using the BT4 filter analyzer spectrometer. The data clearly show that the sudden drop in the FWI is caused by the onset of calcium hydroxide formation.

Theoretical arguments suggest that the on-

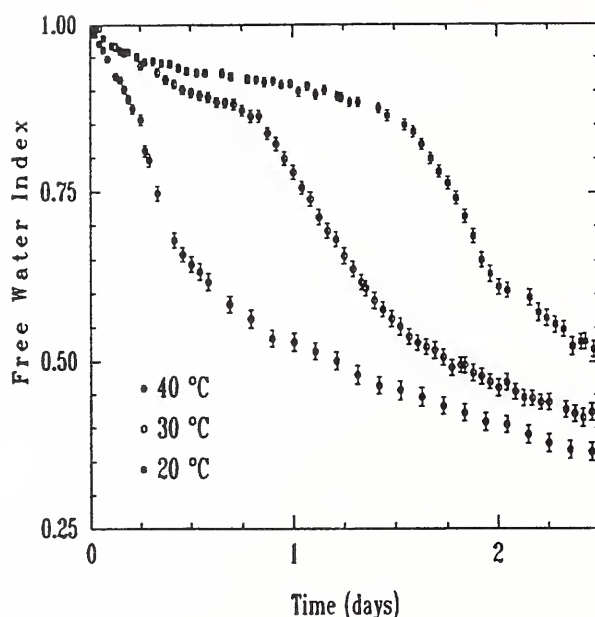


Figure 9. The hydration of C3S as measured by the fraction of free water.

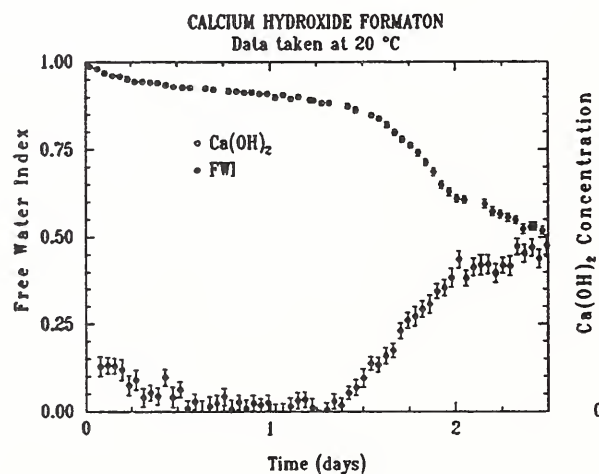


Figure 10. A comparison of calcium hydroxide formation as measured by inelastic neutron spectroscopy with the changes in the free water index during the hydration of C3S.

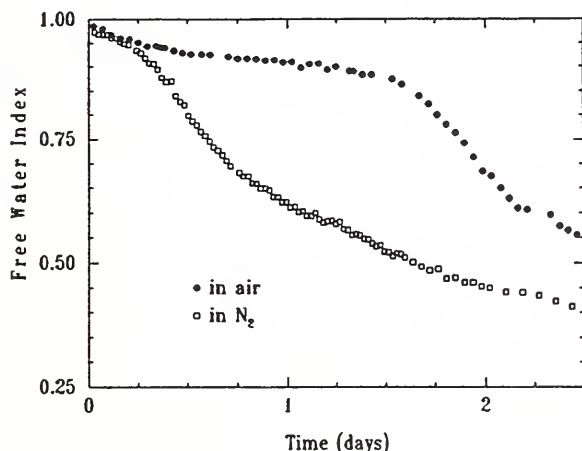


Figure 11. The effect of environmental conditions on the hydration of C3S.

set of calcium hydroxide formation may be controlled by the changing pH of the cement paste [7]. It has been speculated that the presence of CO_2 in air increases the number of carbonate ions in the cement paste, which in turn act as a buffer preventing the pH from rising to a point where calcium hydroxide is formed. To investigate this possibility we mixed and sealed the samples in a pure N_2 atmosphere. Figure 11 shows the dramatic difference between samples mixed in N_2 as opposed to air. The N_2 -mixed sample has its FWI decreasing much earlier than air mixed samples, however the two do converge to a similar FWI after several weeks.

From these results the following picture of C3S hydration emerges. Hydration commences almost immediately after mixing. The initial rate is quite temperature dependent, suggesting that it is controlled by a diffusion process. After a delay period which varies from several hours to a few days depending on temperature the consumption of free water suddenly increases. This occurs due to the onset of calcium hydroxide formation. The delayed formation of calcium hydroxide is a somewhat surprising result which is not apparent in more traditional techniques such as isothermal calorimetry [8]. The large

difference in results between N_2 and air mixed samples strengthens the case for a strong dependence on carbonate concentration. This will be pursued in future experiments in which we plan to systematically vary the CO_2 concentration of the mixing environment, while measuring directly the pH of the curing sample.

Neutron Scattering Studies of Disordered Carbon Anode Materials

In recent years, considerable progress has been made in the development of rechargeable lithium batteries. Early problems with safety and limited cycle life were solved by replacing the lithium metal anode with lithium intercalation compounds such as LiWO_2 or LiC_6 (lithium-graphite), for which the chemical potential of the intercalated Li is close to that of Li metal. Layered materials like LiNiO_2 and LiCoO_2 , which have potentials of about 4 V against Li, are used as cathodes. Lithium ions then shuttle back and forth through an electrolyte to intercalate either the cathode or the anode host, respectively as the battery is discharged or charged.

Carbon-based anodes show the most promising properties in lithium-ion batteries. In order to maximize the stored energy per unit mass, it is important to determine which types of carbon react reversibly with the largest amount of lithium. Carbons prepared by heating soft-carbon precursors to temperatures above 2400°C are well graphitized and show Li uptake capacity corresponding to $\sim 350 \text{ mAh/g}$ of carbon (for comparison, crystalline LiC_6 corresponds to 372 mAh/g). On the other hand, materials obtained by pyrolyzing organic solids in inert gas at $T \leq 700^\circ\text{C}$ exhibit surprisingly large capacities reaching almost 900 mAh/g [9]. It was realized that carbons prepared at these temperatures contain substantial residual hydrogen, and an empirical correlation between Li capacity and H concentration was found, suggesting a limiting value of one "excess" Li per H [9].

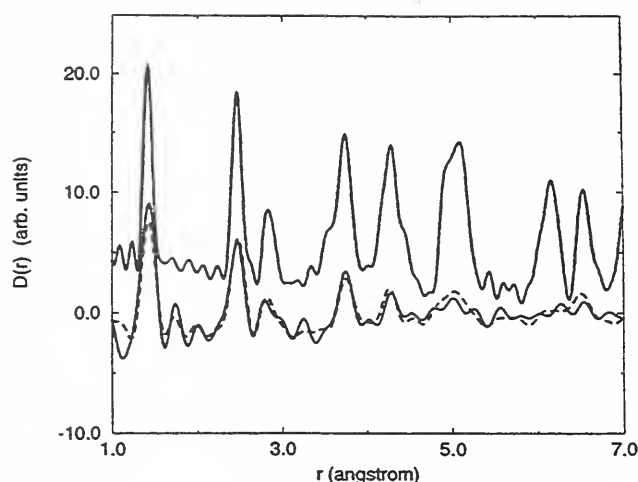


Figure 12. Differential correlation functions $D(r)$ of disordered carbons DC650 (solid curve) and DC1000 (dashed curve). The upper solid curve represents graphite $D(r)$, origin shifted vertically for clarity.

The high capacity materials display only weak and broad peaks in x-ray diffraction. It is believed that carbon atoms form planar aromatic structures (called graphene sheets) that are terminated with H atoms at their edges. The x-ray data suggest that there are regions where 3 to 10 of these sheets are stacked in a more or less parallel fashion, separated by regions that may consist of buckled single layers of tetrahedrally bonded carbon.

We have employed a variety of neutron scattering techniques to study the composition, local structure and vibrational dynamics of several disordered carbon anode materials [10]. Samples were synthesized by pyrolyzing epoxy Novolac resin poly[(phenyl glycidyl ether)-co-formaldehyde] at 650 °C (denoted DC650) and at 1000 °C (DC1000), and a commercial byproduct of coal tar pitch processing (denoted NT10) was also studied. Standard analytical methods (e.g. combustion) as well as prompt gamma activation analysis (PGAA) were used to determine the hydrogen content. The atomic ratios H/C in DC650, DC1000 and NT10 were found to be 0.24 ± 0.01 , 0.04 ± 0.01 , and 0.38 ± 0.01 , respectively.

The local structure of these materials was

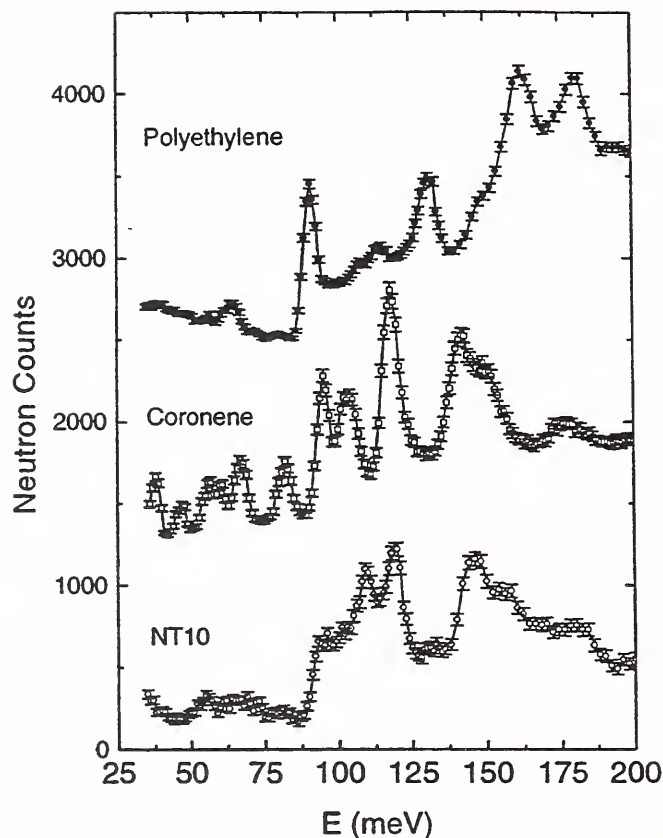


Figure 13. Inelastic neutron scattering spectra of the disordered carbon NT10 (hydrogen content 28 at.%), coronene, and polyethylene, measured at 16K using the Be filter spectrometer. The spectra are offset vertically for clarity.

studied by radial distribution function (RDF) analysis of pulsed time-of-flight neutron diffraction data. This part of the work was carried out at IPNS (Argonne National Laboratory) using the Glass-Liquid-Amorphous Material Diffractometer (GLAD). The experimental pair correlation functions of the disordered carbons are quite similar, most peaks occurring at the same position as in graphite (Fig. 12), thus confirming the hexagonal planar local motif and sp^2 -hybridized carbon network [10]. The peak intensities are weaker than in graphite and vanish with increasing interatomic distances ($> 6 \text{ \AA}$) due to the finite size of graphene fragments.

Based on results of semiempirical and ab initio quantum mechanical calculations, a second mechanism for Li uptake was proposed [11].

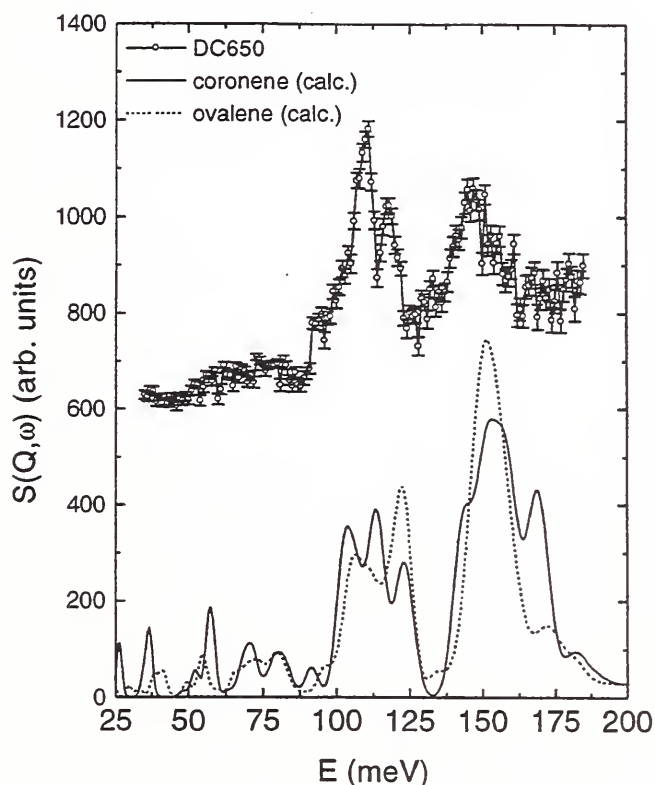


Figure 14. The comparison of calculated $S(Q, \omega)$ of coronene and ovalene with the inelastic scattering spectrum of the DC650 carbon (19 at.% hydrogen), measured with the Be/graphite filter.

The calculations predict that in parallel with the usual lithium intercalation (interstitial Li centered over a carbon ring) Li also binds covalently to H-terminated carbon atoms on the edge of a graphene fragment. However, the bonding mechanism will only be operative if the edge carbons are saturated with one proton; two edge protons would result in a chemically inert methylene moiety $>\text{CH}_2$.

In order to probe the local hydrogen environment at the edges of graphene fragments, inelastic neutron scattering experiments were performed using the filter-analyzer neutron spectrometer installed on the beam tube BT-4 of the NIST reactor. Since the vibrational modes involving H motions depend on the molecular geometry, in addition to the anode materials we also measured the molecular solid coronene (a hexagonal shaped aromatic molecule $\text{C}_{24}\text{H}_{12}$)

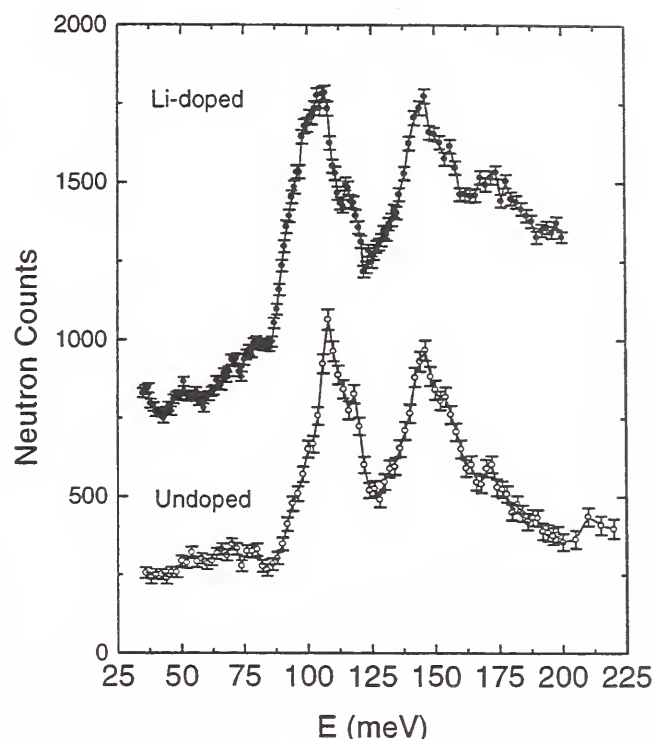


Figure 15. Inelastic neutron scattering spectra of DC650 before and after lithium doping, measured at 16K using the Be filter. The latter is shifted vertically for clarity.

which is a typical representative of polycyclic aromatic hydrocarbons with a single proton per edge carbon, and polyethylene $(-\text{CH}_2-)_n$ provided the information on the methylene group modes.

Figure 13 shows the inelastic scattering spectra of the highly hydrogenated carbon NT10, coronene and polyethylene, measured at 16 K (the data were renormalized to approximately the same hydrogen content). There is clearly a very good correspondence between the spectra for NT10 and coronene, and both are quite dissimilar to polyethylene. The scattering spectrum of coronene was calculated using ab initio and semiempirical methods, and the vibrational modes were identified. The intense peaks between 90 and 125 meV correspond to modes that involve C-H bending out of the molecular plane, the adjacent hydrogens moving in different relative phases. The broader maximum near

140 meV originates from C–H in-plane bending vibrations. Similar assignments can be made for the features observed in NT10. There are also several smaller but well defined peaks in coronene below 90 meV. These represent the molecular skeleton deformations (mainly C–C–C bond angle bending). In contrast, the methylene groups produce peaks in the spectrum of polyethylene which correspond to the well-known CH_2 rocking, twisting and wagging vibrations. These experiments have convincingly confirmed that the amount of CH_2 groups in our carbon samples is small.

In Fig. 14, we compare the scattering spectrum of DC650 with a calculated $S(Q, \omega)$ for coronene and a larger aromatic hydrocarbon, ovalene ($\text{C}_{32}\text{H}_{14}$). Due to their different edge topologies, the theory predicts small changes mainly in the relative intensities of peaks in the 90–125 meV region. Such differences are indeed observed between NT10 and DC650, although the peaks are at almost identical frequencies. The scattering from the DC1000 carbon was very similar to DC650, albeit with much smaller intensity due to the lower H content. We conclude that the low- T pyrolyzed disordered carbons can be reasonably well modeled as a distribution of large polyaromatic hydrocarbons.

Experiments to investigate the effects of Li-doping have been initiated. The samples were doped electrochemically, using Li metal electrode and nonaqueous electrolytes. The best doping was achieved in the DC650 material, to a final C/Li ratio slightly more than 3 (the presence of Li was confirmed by PGAA). The inelastic neutron scattering spectra for both undoped and Li-doped DC650 are shown in Fig. 15. The first strong maximum in the doped sample appears downshifted by 2–3 meV and broadened relative to the undoped carbon. A very similar effect is observed in polyacetylene, and can be explained by charge transfer from the dopant to the host. Theoretical calculations show that more pronounced changes can be expected in the frequency range below 40 meV. Together with the ongoing structural analysis, further inelas-

tic scattering measurements on the fermi chopper spectrometer are planned to explore the low-frequency dynamics of these materials.

Electrides

Electrides and alkalides are crystalline ionic salts in which the anion is either a bare electron or a negatively charged alkali metal. A non-reducible macrocyclic organic complexant encapsulates the cationic alkali metal and prevents recombination of the anionic electron with the alkali metal. Complexants used so far have been crown ethers (formula: $((\text{CH}_2)_2\text{O})_6$), which pair to form a cation sandwich, and cryptands (formula: $\text{N}((\text{CH}_2)_2\text{O}(\text{CH}_2)_2\text{O}(\text{CH}_2)_2)_3\text{N}$), which hide the cation within their own cage [12].

Crystallographic studies of several forms of electride indicate that in nearly all cases the cationic complexes order in such a way that systems of interconnected cavities are formed, in which the anionic electrons have been shown to be confined [13]. These void spaces are continuous throughout the crystal and are largely responsible for the interesting properties of the electrides. Although electrides sometimes behave as ordinary salts, there is evidence that the electrons trapped in the interstitial cavities can interact (and in some cases become delocalized) by means of the pores connecting the cavities, resulting in enhanced transport and unusual optical and magnetic properties. Electrides thus provide a unique laboratory in which the interactions of electrons in solids can be studied.

Recent IR and Raman spectroscopic measurements suggest that the trapped electrons may interact with vibrational motions in the crystal. We have therefore undertaken neutron vibrational spectroscopic measurements of alkalide and electride potassium cryptand complexes in order to examine the interaction of the trapped electrons with phonons in the crystal and internal modes of the complexant. If the trapped electrons did indeed couple to the crystal vibrations, some or all of the observed modes should exhibit shorter lifetimes, manifested as broader inelastic peaks measured in the

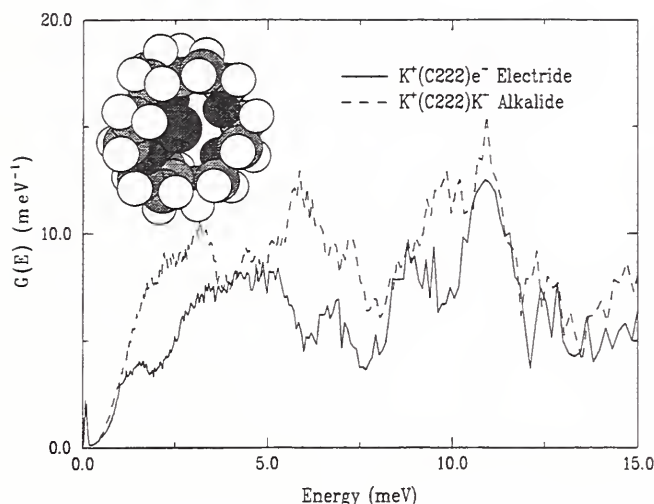


Figure 16. Low frequency vibrational density of states of the alkalide $K^+(C222)K^-$ and electride $K^+(C222)e^-$. Above ~ 15 meV, the vibrational spectra are virtually identical for both compounds. Inset: Structure of the $K^+(C222)$ cryptand cation. The potassium ion is encapsulated within a cage formed by the three $(CH_2)_2O(CH_2)_2O(CH_2)_2$ legs of the cryptand which are joined at the poles by nitrogen atoms.

electride compared with those in the alkalide. Filter analyzer measurements of the vibrational density of states (VDOS) of both materials at 15 K revealed that, above 15 meV, the spectra are virtually identical and no such broadening is observed. Neutron time of flight spectroscopic measurements (Fig. 16), measured under nearly the same conditions, show that below 15 meV the VDOS exhibit, marked differences which could in fact be attributed to electronic coupling with low-frequency motions.

Efforts are currently underway to understand the high and low frequency vibrational spectroscopy of these systems. Ab-initio molecular dynamics calculations on an isolated potassium cryptand complex using the Gaussian94 software package qualitatively reproduce the features of the measured VDOS above 15 meV and demonstrate considerable promise for the assignment of the observed internal modes. In the low frequency region, the differences between the electride and alkalide spectra could

be attributed to electronic coupling with lattice modes, internal modes, or combinations of the two. As the structures of the two specimens are very similar, one would expect that differences in the spectra are due more to contributions from the internal modes than from the lattice modes. In any case, more theoretical work is needed to separate these contributions.

References

- [1] J. N. Huiberts, R. Griessen, J. H. Rector, R. J. Wijngaarden, J. P. Dekker, D. G. de Groot, and N. J. Koeman, *Nature* **380**, 231 (1996).
- [2] T. J. Udovic, J. J. Rush, Q. Huang, and I. S. Anderson, *J. Alloys Compounds* (1997) in press.
- [3] R. A. Assink, et al., *J. Mater. Res.* **7**, 2136 (1992).
- [4] S. A. FitzGerald and A. J. Sievers, *J. Chem. Phys.* **101**, 7283 (1994).
- [5] J. E. Schirber, et al., *Phys. Rev. B* **51**, 12014 (1995).
- [6] I. F. Silvera, *Rev. Mod. Phys.* **52**, 393 (1980).
- [7] R. A. Livingston, et al., in 5th International Conference on Neutrons in Research and Industry (Heraklion, Crete, 1996).
- [8] M. Kaminski and W. Zielenkiewicz, *Cement and Concrete Res.* **12**, 549 (1982).
- [9] J. R. Dahn, T. Zheng, Y. Liu, and J. S. Zue, *Science* **270**, 590 (1995).
- [10] P. Zhou, P. Papanek, R. Lee, J. E. Fischer, and W. A. Kamitakahara, *J. Electrochem. Soc.*, submitted (1996).
- [11] P. Papanek, M. Radosavljevic, and J. E. Fischer, *Chem. Mater.* **8**, 1519 (1996).
- [12] M. J. Wagner, and J. L. Dye, *Ann. Rev. Mater. Sci.* **23**, 223 (1993).
- [13] R. H. Huang, M. K. Faber, K. J. Moeggenborg, D. L. Ward, and J. L. Dye, *Nature* **331**, 6157 (1988).

Research Topics

Inelastic Neutron Scattering Study of YH_3 , YD_3 , and TbH_3

T. J. Udovic²⁷ and J. J. Rush²⁷

Inelastic Neutron Scattering Study of the Nb-H(D) Phase Diagram

B. Hauer³², R. Hempelmann³², D. Richter¹³, T. J. Udovic²⁷, and J. J. Rush²⁷

Dynamics of μ in $\alpha - \text{ScH}_x$ Solid Solutions

F. N. Gygas⁹, A. Amato⁹, I. S. Anderson¹⁵, A. Schenck⁹, G. Solt²⁶, and T. J. Udovic²⁷

Dynamics and Spectroscopy of Hydrogen and Deuterium in Crystalline Pd_9Si_2

T. J. Udovic²⁷, J. J. Rush²⁷, T. B. Flanagan⁴⁴, H. Noh⁴⁴, and Y. Andersson⁴⁵

Inelastic Neutron Scattering Study of $\text{La}(\text{H}_y\text{D}_{1-y})_x$ ($2 \leq x \leq 3$)

T. J. Udovic²⁷, Q. Huang²⁷, J. J. Rush²⁷, and I. S. Anderson¹⁵

Dynamics of Octahedral-site Protons in LaH_x

T. J. Udovic²⁷, J. J. Rush²⁷, and I. S. Anderson¹⁵

Hydrogen Dynamics in $\text{ZrBeH}_{1.5}$

F. Altorfer^{27,38}, T. J. Udovic²⁷, and B. Hauback¹⁶

OH Dynamics in $\text{Sr}(\text{OH})\text{Br}$

F. Altorfer^{27,38}, W. Buehrer¹⁹, and H. D. Lutz⁴³

Hydrogen Dynamics in NaNH_2

F. Altorfer^{27,38}, J. Senker³⁶, and H. Jacobs³⁶

NH_3 Dynamics in $\text{Co}(\text{NH}_3)_2\text{Cl}_2$

F. Altorfer^{27,38} and R. Essmann⁴³

Ammonia Dynamics in $\text{Zn}(\text{NH}_3)_4\text{I}_2$ and $\text{Zn}(\text{NH}_3)_2\text{I}_2$ and Their Deuterated Analogs

F. Altorfer^{27,38} and R. Essmann⁴³

Ammonia Dynamics in $\text{Zn}(\text{NH}_3)_4\text{Br}_2$ and $\text{Zn}(\text{NH}_3)_2\text{Br}_2$ and Their Deuterated Analogs

F. Altorfer^{27,38} and R. Essmann⁴³

Hydrogen Dynamics in the Trioxane Silica Sodalite

F. Altorfer^{27,38}, W. Buehrer¹⁹, and C. Braunbarth^{35a}

Dynamics and Spectroscopy of Hydrofluorocarbons Encaged in NaX and NaY Zeolites

N. C. Maliszewskyj²⁷, T. J. Udovic²⁷, R. R. Cavanagh^{28a}, J. J. Rush²⁷, M. K. Crawford⁸, and D. R. Corbin⁸

Dynamics and Spectroscopy of Templating Molecules in CIT 1 Zeolite

B. H. Toby²⁷, N. C. Maliszewskyj²⁷, D. A. Neumann²⁷, and M. Davis⁵

Dynamics of Benzene in Si-Y Zeolite

L. Bull³⁴, R. Morris³⁴, A. K. Cheetham³⁴, D. A. Neumann²⁷, and J. M. Nicol²³

The Hydration of Cementitious Materials

S. A. FitzGerald²⁷, D. A. Neumann²⁷, J. J. Rush²⁷, and R. A. Livingston^{24a}

Inelastic Neutron Scattering Study of H_5O_2^+ Ions and their Partially Deuterated Analogs in $(\text{H}_5\text{O}_2)_3\text{PW}_{12}\text{O}_{40}$

N. C. Maliszewskyj²⁷ and T. J. Udovic²⁷

Electron-Phonon Coupling in Potassium Cryptand Electrides

N. C. Maliszewskyj²⁷, D. A. Neumann²⁷, D. J. Gilbert²², and J. L. Dye²²

Orientational Dynamics of P_4 Molecules in White Phosphorus

W. A. Kamitakahara²⁷, D. A. Neumann²⁷, F. Gompf¹⁷, and Q. Huang²⁷

X-ray Diffraction Study of the Orientational Phase Transition in Solid Cubane C_8H_8

T. Yildirim^{38,27}, P. M. Gehring²⁷, D. A. Neumann²⁷, P. E. Eaton³⁵, and T. Emrick³⁵

Neutron Scattering Study of the Dynamics of Solid Cubane C_8H_8

P. M. Gehring²⁷, T. Yildirim^{38,27}, D. A. Neumann²⁷, P. E. Eaton³⁵, and T. Emrick³⁵

Calculation of Bragg and Diffuse Scattering in C_{60}

J. R. D. Copley²⁷ and K. H. Michel³³

Orientational Coordinates and Mode Coupling in C_{60}

K. H. Michel³³ and J. R. D. Copley²⁷

Multiple Order Parameter Description of the First Order Phase Transition in C_{60}

K. H. Michel³³ and J. R. D. Copley²⁷

Towards a Microscopic Approach to the Intermolecular Interaction in Solid C_{60}

S. Savin⁴², A. B. Harris⁴², and T. Yildirim^{27,38}

Lattice Dynamics and Diffraction of K_1C_{60} in the Orthorhombic Phase: A Neutron Scattering Study

- R. L. Cappelletti²⁵, H. M. Guerrero²⁵, T. Yildirim^{27,38}, and D. A. Neumann²⁷
- Neutron Scattering Study of Na_2C_{60} in the (P,T)-Plane**
T. Yildirim^{27,38}, D. A. Neumann²⁷, S. F. Trevino²⁷, and J. E. Fischer⁴²
- Synthesis and Properties of Mixed Alkali-Metal-Alkaline-Earth Fullerides**
T. Yildirim^{27,38}, J. E. Fischer⁴², P. W. Stephens²⁸, and P. Petit¹⁴
- Fulleride Superconductors and Orientational Order: T_c vs. Lattice Constant in $\text{Na}_2\text{Rb}_x\text{Cs}_{(1-x)}\text{C}_{60}$**
T. Yildirim^{38,27}, J. E. Fischer⁴², R. Dinnebier⁴, P. W. Stephens²⁸, and C. L. Lin³⁰
- Fulleride Superconductors: Dependence of T_c on Average Molecular Valence**
T. Yildirim^{27,38}, L. Barbedette⁴², J. E. Fischer^{42,27}, C. L. Lin³⁰, J. Robert¹⁴, and P. Petit¹⁴
- Intramolecular Dynamics of C_{60} -piperazine**
A. K. Qasba²⁴, D. A. Neumann²⁷, J. E. Fischer⁴², A. Smith⁷, and P. Klosowski^{38,27}
- Rotational Dynamics of C_{61}H_2 and C_{61}D_2**
J. E. Fischer⁴², D. A. Neumann²⁷, J. R. D. Copley²⁷, P. A. Heiney⁴², J. J. Rush²⁷, R. M. Strongin⁴², L. Brard⁴², and A. B. Smith III⁷
- ESR Evidence for Phonon-Mediated Resistivity in Alkali Fullerides**
P. Petit¹⁴, J. Robert¹⁴, T. Yildirim^{27,38}, and J. E. Fischer⁴²
- Interstitial Hydrogen in C_{60}**
S. A. FitzGerald²⁷, D. A. Neumann²⁷, L. J. Santodonato²⁷, J. R. D. Copley²⁷, T. Yildirim^{27,28}, and J. J. Rush²⁷
- Quasielastic Neutron Scattering of the Dynamics of NH_3 in $(\text{NH}_3)_2\text{Na}_3\text{C}_{60}$**
M. Green⁴¹, D. A. Neumann²⁷, T. Yildirim^{38,27}, and M. J. Rosseinsky⁴¹
- Dynamics of Layered Silicates-Influence of Intercalated Water and Cation Substitution**
N. Wada^{31a} and W. A. Kamitakahara²⁷
- Layer Shearing Modes in Li-Graphite Compounds**
W. A. Kamitakahara²⁷, C. Bindra⁴², and J. E. Fischer⁴²
- Structure and Dynamics of Amorphous Carbons**
P. Zhou⁴², W. A. Kamitakahara²⁷, P. Papanek^{27,42}, and J. E. Fischer⁴²
- Dynamics of Oxygen-Deficient Silica Glass**
S. Das² and W. A. Kamitakahara²⁷
- Vibrational Densities of States for Cubic and Hexagonal Boron Nitride**
W. A. Kamitakahara²⁷, D. A. Neumann²⁷, G. Doll¹⁰, B. Sweeting¹⁰, and A. W. Moore¹
- Low Energy Dynamics of Doped Poly(p-phenylene vinylene)**
P. Papanek^{27,42}, J. E. Fischer⁴², J. L. Sauvajol⁴⁰, A. J. Dianoux¹⁵, G. Mao^{44a}, M. J. Winokur^{44a}, and F. A. Karasz³⁹
- Intramolecular Dynamics of Doped Poly(p-phenylene vinylene)**
P. Papanek^{27,42}, J. E. Fischer⁴², J. L. Sauvajol⁴⁰, A. J. Dianoux¹⁵, G. Mao^{44a}, M. J. Winokur^{44a}, and F. A. Karasz³⁹
- Polarized Vibrational Density of States of Alkali-Doped Polyacetylene**
P. Papanek^{27,42}, J. E. Fischer⁴², J. L. Sauvajol⁴⁰, P. MacNellis¹⁴, and C. Mathis¹⁴
- Measurement of the Phonon Density of States in Various Energetic Materials**
S. F. Trevino⁴⁶ and L. Fried²⁰
- Intramolecular Dynamics of Kevlar**
N. C. Maliszewskyj²⁷, T. J. Udovic²⁷, M. K. Crawford⁸
- Low Energy Dynamics of Isotopically Substituted Nylon 6.6**
N. C. Maliszewskyj²⁷, T. J. Udovic²⁷, M. K. Crawford⁸
- Molecular Dynamics Studies of the Structure and Dynamics of Lipid Bilayers**
D. J. Tobias^{42,27}, K. Tu⁴², and M. L. Klein⁴²
- Molecular Dynamics Simulations of a SAM/DPPC Bilayer**
D. J. Tobias^{42,27}, K. Tu⁴², M. L. Klein⁴², and A. Plant^{3,6}
- Inelastic Neutron Scattering Study of Ribonuclease-A**
G. Gilliland^{3,6}, A. Hernandez^{38,6}, J. J. Rush²⁷, S. Krueger²⁷, T. J. Udovic²⁷, and J. R. D. Copley²⁷

Molecular Dynamics Simulations of the Temperature Dependence of Protein Dynamics

D. J. Tobias^{42,27} and M. L. Klein⁴²

High-Frequency Phonon Dispersion in $\text{La}_{1.85}\text{Sr}_{0.15}\text{CuO}_4$

A. H. Moudden¹⁸, P. M. Gehring²⁷, L. Vasiliu-Doloc^{27,38}, B. Hennion¹⁸, M. Matsuda⁴, G. Shirane⁴, Y. Endoh³¹, I. Tanaka⁴⁷, and H. Kojima⁴⁷

Affiliations

¹Advanced Ceramics Corp.

²American University

³Biotechnology Div., NIST

⁴Brookhaven National Laboratory

⁵California Institute of Technology

⁶CARB

⁷Drexel University

⁸E. I. DuPont

⁹Eidg. Technische Hochschule, Zurich, Switzerland

¹⁰General Electric Corp. Res. and Dev.

¹³Institut für Festkörperforschung, Germany

¹⁴Institute Charles Sadron, France

¹⁵Institute Laue-Langevin, France

¹⁶Institutt for Energiteknikk, Norway

¹⁷Karlsruhe Nuclear Research Center, Germany

¹⁸Laboratoire Léon Brillouin, France

¹⁹Laboratory for Neutron Scattering, Switzerland

²⁰Lawrence Livermore National Laboratory

²²Michigan State University

²³Moltech Corp.

²⁴Montgomery Blair High School

^{24a}Office of Advanced Research, FHWA

²⁵Ohio University

²⁶Paul Scherrer Institut, Switzerland

²⁷Reactor Radiation Division, NIST

²⁸SUNY Stony Brook

^{28a}Surface & Microanalysis Div., NIST

³⁰Temple University

³¹Tohoku University, Japan

^{31a}Toyo University, Japan

³²Universität des Saarlandes, Germany

³³University of Antwerp, Belgium

³⁴University of California, Santa Barbara

³⁵University of Chicago

^{35a}University of Constance, Germany

³⁶University of Dortmund, Germany

³⁸University of Maryland

³⁹University of Massachusetts

⁴⁰Université Montpellier II, France

⁴¹University of Oxford, UK

⁴²University of Pennsylvania

⁴³University of Siegen, Germany

⁴⁴University of Vermont

^{44a}University of Wisconsin

⁴⁵Uppsala University, Sweden

⁴⁶U. S. Army Research Laboratory

⁴⁷Yamanashi University, Japan

Magnetism and Superconductivity

This year has been a particularly exciting one with the restart of the NBSR at the beginning of the fiscal year, giving us a full year of neutron scattering experimentation. All the instruments saw an increase in flux over previous reactor cycles because of the return to full 20MW operations, as well as an increase in thermal neutron instrument capabilities due to various improvements installed during the long shutdown. The cold neutron instruments saw a dramatic improvement in intensity with the installation of the new liquid hydrogen cold source, as detailed elsewhere in this report. However, the most exciting news regards the inauguration of two new cold neutron instruments, the cold neutron triple axis instrument (SPINS) and the cold neutron reflectometer (NG-1). Both have polarized beam capabilities, and they are opening up new regimes to explore. We anticipate that our area of research will make extensive use of these new capabilities in the years to come. Several highlights of research during the past year are summarized below.

Magnetizing a Quantum Spin Chain

The cold neutron spectrometer SPINS has enabled new types of experiments in magnetism at NIST, in particular experiments that probe spin dynamics in high magnetic fields at energies equal to or less than the energy scale (Zeeman energy) set by the magnetic field. The first such experiment was carried out on a one-dimensional spin- $\frac{1}{2}$ antiferromagnet called Copper-Benzoate[1]. With an exchange constant $J=1.57$ meV, a laboratory field of $H=7$ T represents a large perturbation on magnetism in Copper Benzoate. Nonetheless, the magnetic bandwidth in this system is large enough that a cold neutron triple axis spectrometer such as SPINS can resolve details of the excitation spectrum. Thus the experiment was able to probe the dynamic spin correlation function of a quantum antiferromagnet in an unusual and interest-

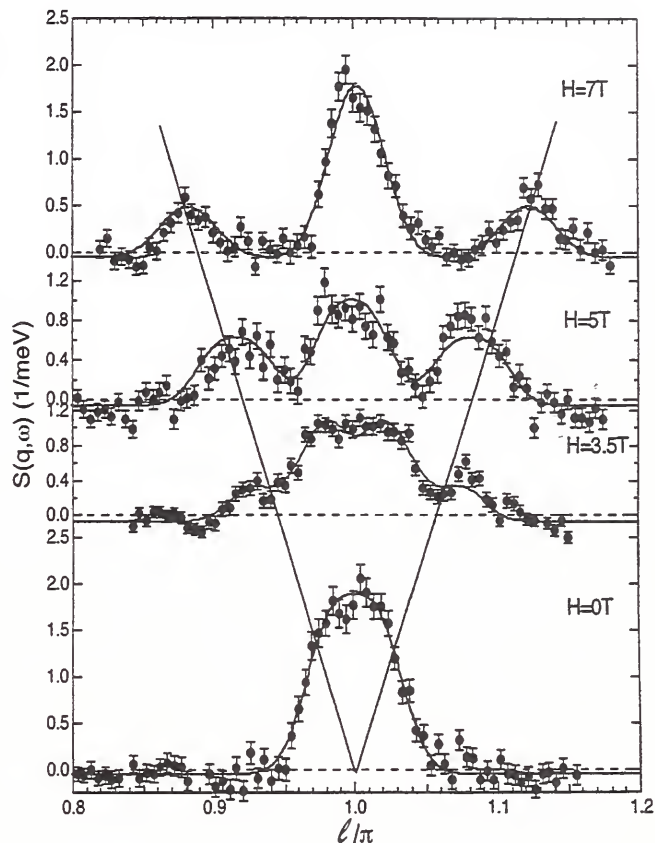


Figure 1. Constant energy scans at $\hbar\omega = 0.2$ meV for various values of applied magnetic field in the one dimensional spin $\frac{1}{2}$ antiferromagnet Copper Benzoate ($J = 1.47$ meV). The data come from the SPINS triple axis spectrometer operated with coarse collimation and fixed final energy 2.5 meV. The lines through the data were calculated for propagating resolution-limited modes with a gap of 0.2 meV and a velocity corresponding to the measured zero field spinon velocity.

ing regime of parameter space: $\hbar\omega \ll g\mu_B H \approx J$.

Figure 1 shows the main result of the experiment in the form of four constant-energy scans probing low energy excitations ($\hbar\omega = 0.21$ meV) for different values of applied magnetic field. At zero field there is a peak for $q = \pi$, which indicates a tendency towards antiferromagnetic correlations that double the unit cell. Application

of a magnetic field leads to additional low energy fluctuations at incommensurate wave vectors whose separation \tilde{q}_i from π increases in proportion to the applied field.

To understand the origin of this field-induced length scale it is necessary to know the nature of the low energy excitations in a $S=\frac{1}{2}$ one-dimensional antiferromagnet. Theories and experiment have established that these take the form of so-called unbound spinons, which are weakly interacting spin- $\frac{1}{2}$ defects in the resonating valence bond ground state of the spin chain. Application of a magnetic field lowers the energy of a magnetized state containing a finite density of such spin polarized defects. If each spinon is an $S=\frac{1}{2}$ object and their mean spacing is λ then the average magnetization per copper atom is $M=g\mu_B S/\lambda$. The characteristic wave vector, \tilde{q}_i , can thus be written in terms of the magnetization as $\tilde{q}_i = 2\pi/\lambda = 2\pi M/(g\mu_B S)$. The solid lines in Fig. 1 show this field-dependent wave vector, which is seen to track the position of the incommensurate side peak quite well. The presence of this incommensurate soft mode was in fact predicted almost 20 years ago using the Bethe ansatz. Numerical simulations and theories based on the fermion representation of the spin chain indicate that incommensurate soft modes may be a rather general non-classical feature of one-dimensional antiferromagnets. Even so, this experiment is the first to observe the effect in a real $S=1/2$ antiferromagnet, a fact which may be traced to the difficulty of accessing the relevant parameter regime.

In addition to inducing an incommensurate mode, the field also produces a gap in the excitation spectrum. The gap is approximately 0.2 meV for $H=7$ T both at the commensurate and at the incommensurate wave vector. This is at least an order-of-magnitude greater than the upper limit that experiments set for any gap in zero applied field. Thus there appears to be a field-induced crossover from gapless (and hence massless) commensurate excitations to massive incommensurate excitations in copper benzoate. Since no gap was predicted

by theories for isotropic Heisenberg chains, exchange anisotropies or perhaps interchain coupling may be important for explaining this part of the experiment.

Experiments are now underway to study the low-energy high-field properties of other systems to examine how general the phenomenon of incommensurate magnetized states is in quantum magnets without low-temperature Néel order.

Pr Magnetism in Cuprates

The magnetic order of the rare-earth ions in cuprate superconductors has been an area of active interest since shortly after the discovery of this class of materials. Typically the rare-earth moments order at very low temperature ($\sim 1K$), and this order readily coexists with superconductivity. A singular exception to this behavior is found for the class of cuprates that contain Pr, which generally are not even metallic let alone superconducting. Hence the physical properties of the Pr cuprates have been studied extensively in order to understand why only Pr suppresses the superconducting state while the other rare earths exhibit very little effect. The magnetic ordering of the Pr is also anomalous in that the ordering temperatures are more than an order-of-magnitude higher ($\sim 15K$) than for the other rare-earth systems, indicating much stronger exchange and hybridization effects for the $4f$ Pr electrons. In particular, all the rare-earths (R) that form the stable $RBa_2Cu_3O_7$ structure are 90^+ K superconductors, except for Pr which is an insulator. The first neutron diffraction experiments on powder $PrBa_2Cu_3O_7$ revealed a simple antiferromagnetic ordering of Pr ions, with an ordered moment of $0.74 \mu_B$ and Néel temperature of 17 K. These observations were in good agreement with magnetic susceptibility and specific heat measurements, and more recent measurements on single crystals have verified this general behavior. The magnetic ordering has been studied in detail in a variety of related Pr cuprate compounds as a function of oxygen concentration and as a function of Y (and other rare earth) substitution on the Pr site, and a

general understanding of the behavior of Pr in these cuprates has emerged in terms of strong hybridization of the $4f$ electrons near the Fermi level. However, a recent NMR study has challenged this conventional picture, and concluded that the Pr in the 1-2-3 system, and by extension in the other cuprates as well, has only a very small ordered magnetic moment ($0.017 \mu_B$). The observed low-T neutron diffraction peaks would then originate from a change in the order of Cu spins rather than from Pr order. Such a possibility cannot be immediately excluded by previous measurements because the Pr and Cu moments are comparable in size, and because the Pr material is especially sensitive to small concentrations of dopants which strongly affect the magnetism and may leave open to interpretation the results of various measurements. For example, in the growth of single crystals the magnetic properties were found to be drastically affected by inadvertent contamination from the crucible. We have therefore carried out new experiments[2] on a high-quality sample of polycrystalline $\text{PrBa}_2\text{Cu}_3\text{O}_7$, as well as on a single crystal grown in a crucible that does not contaminate the sample. Our results unambiguously demonstrate the development of the simple long-range antiferromagnetic order for the Pr moments in $\text{PrBa}_2\text{Cu}_3\text{O}_7$, as established in the original studies.

The general magnetic behavior in the $\text{RBa}_2\text{Cu}_3\text{O}_{6+x}$ system is very interesting as both Cu and rare earth ions can have magnetic moments. The crystal structure is essentially tetragonal ($a \approx b$) with $c \approx 3a$, and there are three sets of Cu layers. Two of these are equivalent Cu layers that have an oxygen between the Cu ions along the a and b directions, and are known as Cu planes. The other type of Cu layer, which is known as the Cu chain layer, has oxygen ions only along the b -axis. This oxygen can be readily removed, and in the oxygen deficient insulator $\text{RBa}_2\text{Cu}_3\text{O}_6$ the Cu spins in the planes order antiferromagnetically with Néel temperatures (T_N) as high as 525K. The spins lie in the a - b plane, and the observed magnetic Bragg

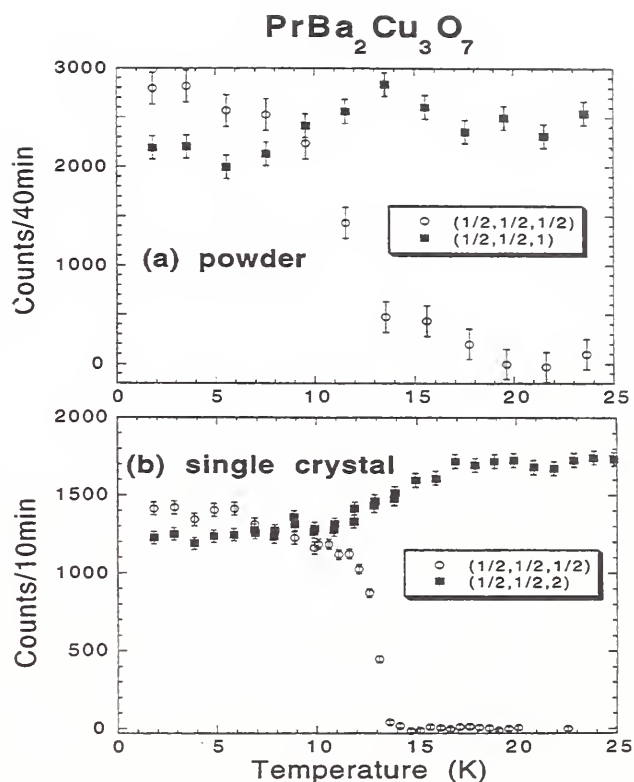


Figure 2. Temperature dependence of the Pr and Cu magnetic peaks (background is subtracted) for (a) powder and (b) single crystal samples. Both $(1/2, 1/2, 1)$ and $(1/2, 1/2, 2)$ magnetic peaks originate predominantly from Cu ordering while the Pr ordering is responsible for $(1/2, 1/2, 1/2)$ peak.

peaks can be indexed as $(h/2, k/2, l)$, which is referred to as “whole-integral” peaks since l is an integer. With appropriate doping either directly on the chain site, or on the Ba site, the chain spins can also develop an ordered moment at low temperatures, and the observed magnetic peaks can be indexed as $(h/2, k/2, l/2)$, which is referred to as “half-integral” peaks. If the Cu spins in the chains were to develop a moment, the half-integral magnetic peaks would increase in intensity while the whole-integral peaks decrease to zero. Finally, at low temperatures the rare-earth ions, which are located in the body-centered position between the two Cu planes, order antiferromagnetically.

The NMR study speculated that the new magnetic Bragg peaks that develop in

$\text{PrBa}_2\text{Cu}_3\text{O}_7$ at low temperatures originate from a change in the spin structure of the Cu planes rather than from Pr ordering. In the present $\text{PrBa}_2\text{Cu}_3\text{O}_7$ samples, new magnetic Bragg peaks are observed below 13.5 K, and the temperature dependence of the $(1/2, 1/2, 1/2)$ peak is shown in Fig. 2. The spins in the Cu-O planes order at high T, and they have their full saturated moments at low T. Thus to accommodate the development of new Bragg peaks the whole-integral peaks must decrease proportionately in intensity (and are in fact expected to vanish at low T). The temperature dependence of the $(1/2, 1/2, 1)$ and $(1/2, 1/2, 2)$ magnetic Bragg peaks associated with the Cu plane ordering is shown in Fig. 2. The Néel temperature is 281 K, with the intensity varying smoothly with temperature into the low-T regime. We then see only a very small anomaly in the intensity as the half-integral peaks develop. These data therefore rule out the possibility that the new half-integral peaks are due to a Cu spin reorientation. They also rule out the possibility that the new Bragg peaks originate from an ordering of the Cu spins in the chain layer, since when the Cu spins are observed to order (in doped samples) the intensities of the whole-integral peaks are observed to decrease to zero. Moreover, the relative intensities of the half-integral magnetic peaks we observe are qualitatively different than the intensities observed when the Cu chain spins order.

We conclude that the magnetic diffraction data are only consistent with the assumption that it is the Pr spins that are ordering at 13 K. The small drop in the $(1/2, 1/2, 1)$ and $(1/2, 1/2, 2)$ intensities at low temperature (Fig. 2) is then the result of weak coupling between the Cu and Pr spins as the Pr orders. In addition, detailed analysis of these data as a function of Q strongly suggests on the basis of the magnetic form factor that these new peaks arise predominantly from the Pr magnetic moments, and further work on larger single crystals is underway. These results directly contradict the NMR study, which claimed that the Pr ions

in $\text{PrBa}_2\text{Cu}_3\text{O}_7$ have a (non-magnetic) Γ_1 singlet as a crystal-field ground state and (essentially) no ordered magnetic moment. It thus appears that the conventional picture of strong hybridization of the 4f electrons is the correct explanation for both the high magnetic ordering temperature for the Pr and the absence of metallic conduction in the Pr-containing cuprates.

Magnetoresistive Oxides

The correlated dynamics of spins and charges near the Mott transition has been under very active investigation recently in doped lanthanum manganites $\text{La}_{1-x}\text{A}_x\text{MnO}_3$, both because they exhibit anomalously large magnetoresistance effects near the Curie temperature, and because the physics of this class of materials is directly related to the high- T_c superconducting copper oxides. Like the cuprates, these materials are in the vicinity of an insulator-metal transition, as well as magnetic and structural instabilities, while to date no superconductivity has been found. Rather, they exhibit exotic properties such as a dramatic increase in the conductivity when the system orders ferromagnetically, either by cooling in temperature or by applying a magnetic field. These dramatic changes in conductivity with field have attracted enormous technological interest because of their potential use in devices such as read/write heads and sensors.

The magnetic, electrical, and structural properties of these systems were studied during the '50s and '60s, and the evolution of the magnetic properties with band filling was well explained by the double exchange hopping mechanism. However, the newly discovered colossal magnetoresistive (CMR) effects as well as the observed field-induced structural transitions cannot be explained within this model. It has been suggested that an understanding of these materials must include, in addition to the double exchange mechanism, strong electron correlations and/or a strong electron-phonon interaction. The existence of strong electron correlations is expected to affect the magnetic ordering and the magnetic excitation spectrum, and thus

the spin dynamics can provide crucial information for determining the itinerancy of the system and the importance of the electron correlations. In particular, it is important to determine how the magnetic ordering and spin dynamics evolve with doping. We have performed a series of diffraction and inelastic scattering experiments on the $\text{La}_{1-x}\text{Sr}_x\text{MnO}_3$ materials for $x=0.15$ and 0.25 , for which sizeable single-crystals can be grown by the floating zone technique. The magnetic ordering evolves from an undoped antiferromagnetic insulating state to a metallic ferromagnetic state upon doping. Our $x=0.15$ crystal showed two transitions in the electrical conductivity, marking the onset of ferromagnetic long-range order at $T_C = 235\text{K}$, and a weak spin canting below $T_{CA} = 200\text{K}$. Because the spin canting is very weak, the system is a ferromagnet to a fairly good approximation throughout the entire magnetically ordered regime. The $x=0.25$ sample is a pure ferromagnet for all $T < T_C$.

We have investigated the spin dynamics in the $(0,1,0)$ and $(0,0,1)$ high-symmetry directions in the $x=0.15$ system[3]. In the long wavelength regime the magnetic excitations are conventional spin-waves, with a dispersion relation given by $E = E_0 + Dq^2$, where E_0 is the spin-wave energy gap and D is the spin stiffness constant. The spin-wave gap E_0 is too small ($< 0.05\text{ meV}$) to be measured directly in energy scans at $q = 0$ with the best resolution available (0.04 meV FWHM on SPINS). This indicates that this system is indeed a very "soft" ferromagnet, comparable to the amorphous metglas materials. However, the spin stiffness constant D estimated from low-energy magnetic excitations has slightly different values in the two directions, indicating a small anisotropy of exchange interactions.

The spin-wave excitations have been measured to the zone boundaries in both directions, and the results at 10K are plotted in Fig. 3. By fitting with an anisotropic Heisenberg model with nearest-neighbor interactions, we obtained in-plane and inter-plane ferromagnetic exchange interactions that differ by about 10%. This indicates that the $x=0.15$ system is not an ideal

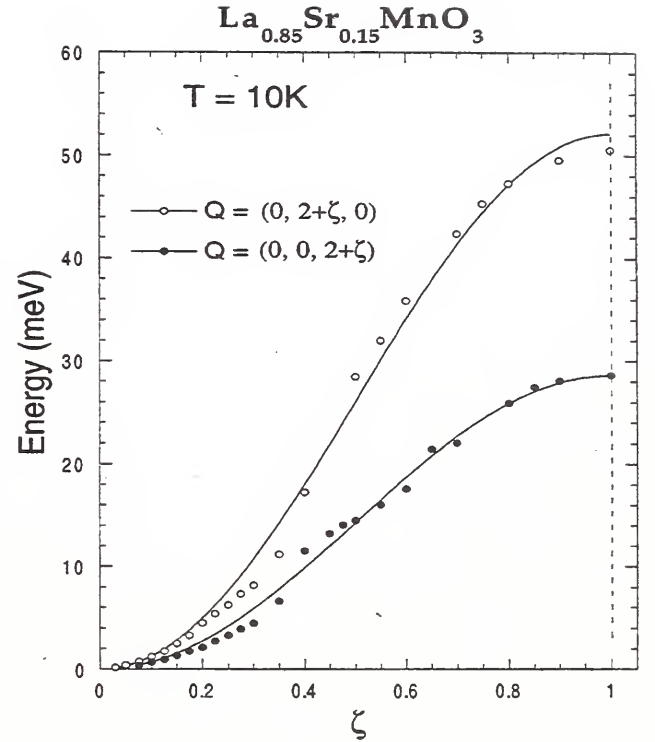


Figure 3. Spin-wave dispersion along $(0,1,0)$ (open circles) and along $(0,0,1)$ (closed circles) at 10K . Solid curves are fits to an anisotropic Heisenberg model with nearest-neighbor interactions.

isotropic ferromagnet, in contrast to the optimally doped $x=0.33$ materials (or the pyrochlore $\text{Ti}_2\text{Mn}_2\text{O}_7$ that we are currently investigating). More interesting, though, is that the magnetic excitations develop large intrinsic linewidths with increasing q , even at low temperatures. Figure 4(a) shows an energy scan at the zone boundary in the $(0,1,0)$ direction at 10K , well below T_C . The FWHM is approximately 22 meV , much larger than the instrumental resolution of 6.7 meV . This demonstrates that conventional magnons are not eigenstates of this system, with the most likely explanation being that there is a strong magnon-electron interaction that causes this large damping. Moreover, increasing the temperature has a dramatic effect on the spin-wave linewidths. At $T = 100\text{K}$, still well below T_C , the magnetic excitation appears to be completely overdamped, as can be seen in Figure 4(b). This behavior contrasts

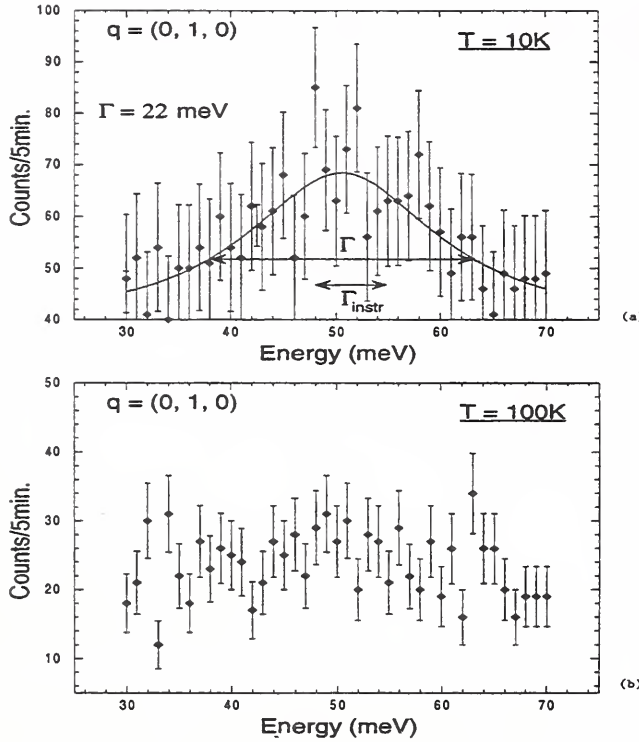


Figure 4. (a) Magnetic inelastic spectrum collected at 10K at the (0,1,0) zone boundary, showing a substantial intrinsic linewidth even at low temperatures. (b) Same spectrum as above, collected at $T = 100K$, showing that the magnetic excitation at the zone boundary is completely overdamped at $T = 100K$, well below $T_C = 235K$.

markedly with the expectations for a conventional localized-spin ferromagnet, and indicates that there are additional strongly temperature-dependent contributions to the spin-wave damping. Both of these anomalous damping effects may be due to the itinerant nature of the e_g electrons that are associated with the metallic conductivity and double-exchange mechanism. Finally, we also note that in the q -range around 0.4 there is an anomaly in both dispersion relations. In this region there is a possible crossing of modes that may be related to the existence of the spin canted phase, or to a magnon-phonon interaction. Identifying the nature of these excitations is challenging both theoretically and experimentally, and further work is in progress.

Exchange-biased Superlattices

In Fe_3O_4/CoO superlattices, the hysteresis loop of the ferrimagnetic Fe_3O_4 is shifted along the field axis after field cooling through the Néel temperature of the antiferromagnetic CoO layers[4]. This so-called exchange biasing effect has been observed for a variety of bilayer and multilayer systems, including Fe_3O_4/NiO , Fe/FeF_2 and $Ni_{80}Fe_{20}/FeMn$. Theories suggest that the effect originates from local exchange coupling at the interfaces between the ferromagnetic and antiferromagnetic components, which have competing anisotropies. While these multilayers show great promise for applications as magnetoresistive sensors, the strong dependence of the biasing field, H_B (i.e., field shift), on the layer thickness and growth morphology constrains the fabrication process.

In order to probe directly the magnetic structure of the antiferromagnetic layer, we performed neutron diffraction studies[5] of [001] Fe_3O_4/CoO superlattices grown at Philips Laboratory by molecular beam epitaxy techniques. We examined a series of 1" diameter samples on MgO substrates with bilayer thicknesses ranging from 50 to 200 Å. For these elastic diffraction experiments, the samples were mounted on either the BT-9 or BT-2 triple axis spectrometers with the [220] in-plane axis and [004] surface normal defining the scattering plane. In this geometry, we scanned the (222), (111) and (220) reflections along the Q , growth-axis and in-plane directions at various temperatures.

Due to the differences between the Fe_3O_4 and CoO crystalline symmetries, the separation of the scattering from the individual Fe_3O_4 and CoO layers is straightforward. Specifically, the registry of the Fe_3O_4 spinel lattice is not preserved across intervening CoO interlayers because the orientation of the Fe tetrahedral sites relative to the CoO rocksalt template is not unique. Growth-axis scans through the (220) reflection, which is extinct for the CoO lattice, reveal that the coherence of the Fe_3O_4 is limited to a single layer by these stacking faults. Fig. 5 shows growth-axis scans through

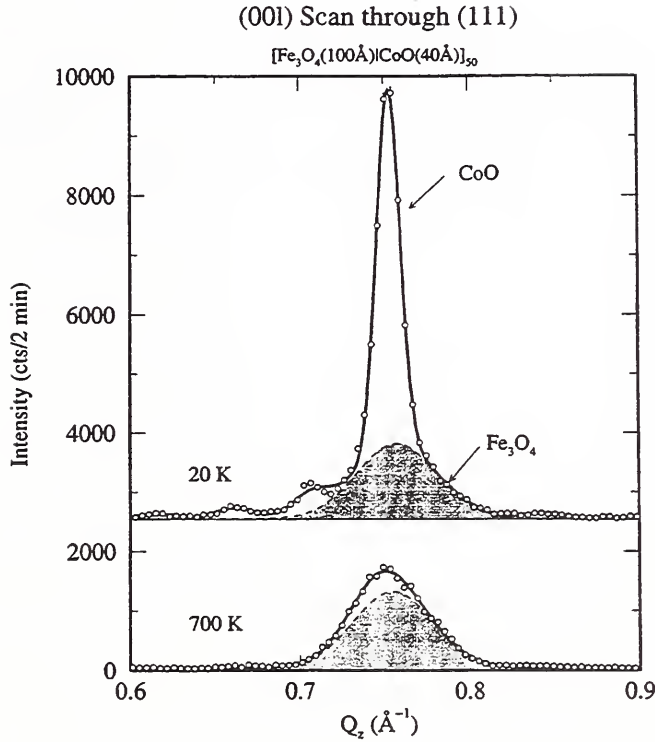


Figure 5. Neutron diffraction scans along the $[00l]$ direction through the (111) reflection for the superlattice $[\text{Fe}_3\text{O}_4(100\text{\AA})|\text{CoO}(40\text{\AA})]_{50}$ at 20 K and 700 K. The solid curves denote fits to Gaussians. The dashed line delineates the Fe_3O_4 scattering contribution (broad Gaussian) from that of the CoO (superlattice peaks).

the (111) magnetic reflection for the sample $[\text{Fe}_3\text{O}_4(100\text{\AA})|\text{CoO}(40\text{\AA})]_{50}$ at 20 K and 700 K. The data are comprised of a narrow peak with superlattice sidebands and a broad peak. Comparing these data with scans through the (220) reflection, we conclude that the latter arises from the ferrimagnetic ordering of Fe_3O_4 , and the former results from the antiferromagnetic ordering of the CoO layer. Thus the CoO structural and magnetic order is long range ($> 300 \text{\AA}$) and propagates coherently across several bilayers.

We note that in-plane scans through the (111) reflection also show a broad and narrow component, associated with the Fe_3O_4 and CoO ordering respectively. Surprisingly, the in-plane coherence length of the Fe_3O_4 is less than 100\AA . Since these scans are insensitive to the growth-axis stacking faults, we speculate that an island-

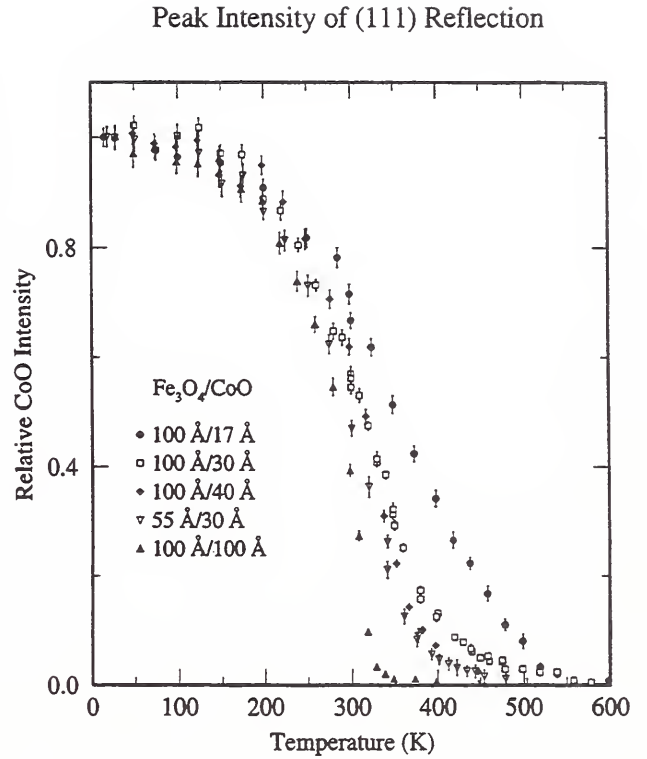


Figure 6. Peak intensity of the (111) reflection plotted as a function of temperature for all of the $\text{Fe}_3\text{O}_4/\text{CoO}$ superlattices, as labeled. The temperature-independent contribution from the Fe_3O_4 layers has been subtracted.

like growth process could lead to planar defects, assuming that each Fe_3O_4 cluster is randomly seeded relative to its neighbors across the CoO template. These defects may lead to magnetic frustration across the superlattice interfaces.

By monitoring the temperature-dependent intensity of the narrow and broad component of the (111) reflection, we have determined independently the magnetic order parameters of the bilayer components. The intensity of the latter (e.g., Fig. 5) is constant up to 700 K, consistent with the ordering temperature for bulk Fe_3O_4 ($T_{\text{Curie}} = 858 \text{ K}$). The intensity for the narrow CoO component is plotted as a function of temperature in Fig. 6 for all of the samples considered. It persists well above $T_{\text{Néel}} = 291 \text{ K}$ for bulk CoO. In fact, the ordering temperature of the CoO layer appears to systematically

approach that of the Fe_3O_4 layer as the relative thickness of the CoO layer is reduced. Mean-field calculations indicate that this is a direct consequence of local exchange coupling at the superlattice interfaces. Magnetization measurements reveal that the blocking temperature [i.e., $T_B = T(H_B = 0)$] does not track the ordering temperature as expected, but rather *decreases* with decreasing CoO layer thickness.

This contradictory behavior indicates that the CoO anisotropy is somehow weakened in superlattices with thin CoO layers. We hope to learn more about these competing anisotropies from upcoming diffraction measurements of the CoO antiferromagnetic order as a function of field. Judging by similar studies of $\text{Fe}_3\text{O}_4/\text{NiO}$ superlattices, we believe that these experiments will provide significant insight into the origin of the biasing behavior in these $\text{Fe}_3\text{O}_4/\text{CoO}$ superlattices.

Coupled Charge and Spin Ordering

Charge and spin orderings in real space have attracted much attention due to their role in the superconductivity of the cuprates. The real-space segregation of holes and spins was attributed to the anomalous suppression of superconductivity in $\text{La}_{2-x}\text{Ba}_x\text{CuO}_4$ with $x = \frac{1}{8}$, and was suggested to explain many of the novel properties of the layered copper oxides. Static charge and spin stripes were also found in $(\text{La},\text{Nd})_{1.875}\text{Sr}_{0.125}\text{CuO}_4$, which does not exhibit superconductivity. These findings led to an interpretation of the inelastic peaks explored earlier in superconducting cuprates as due to dynamic fluctuation of these stripes. The charge and spin stripes were first observed on $\text{La}_{2-x}\text{Sr}_x\text{NiO}_{4+\delta}$ by electron diffraction and neutron diffraction, respectively. For $\text{La}_{2-x}\text{Sr}_x\text{NiO}_{4+\delta}$ with excess hole concentration $\epsilon = x + 2\delta$, the charge order is characterized by the wave vector $(\epsilon, \epsilon, 0)$ and the spin order by $(\frac{1}{2} + \frac{\epsilon}{2}, \frac{1}{2} + \frac{\epsilon}{2}, 0)$ with respect to a reciprocal lattice point of the tetragonal structure. Such a relationship between the spin- and charge-ordering wave vectors is a characteristic signa-

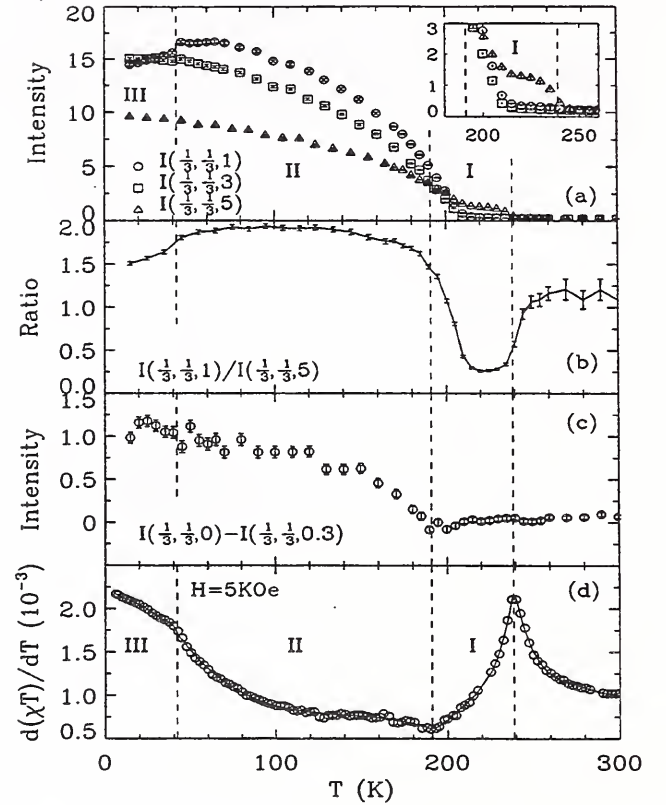


Figure 7. Elastic neutron scattering intensities of several superlattice peaks and bulk susceptibility data. (a) Temperature dependence of the superlattice peak intensities at $Q = (\frac{1}{3}, \frac{1}{3}, 1)$, $(\frac{1}{3}, \frac{1}{3}, 3)$, and $(\frac{1}{3}, \frac{1}{3}, 5)$. The data are in arbitrary units. (b) Ratio of the $(\frac{1}{3}, \frac{1}{3}, 1)$ to $(\frac{1}{3}, \frac{1}{3}, 5)$ peak intensity. (c) Temperature dependence of the spin-order superlattice peak intensity. Units are the same as those in (a). (d) $\frac{d}{dT}(\chi T)$ in emu/mole. The line is a guide to the eye.

ture of charge stripes that are magnetic antiphase domain walls.

Neutron scattering measurements on $\text{La}_{1/3}\text{Sr}_{2/3}\text{NiO}_4$ consistently yielded $\epsilon = 0.333(2)$. A new glassy state of the charge stripe in $\text{La}_{1/3}\text{Sr}_{2/3}\text{NiO}_4$ was discovered by detailed temperature measurements of the superlattice peak intensities and of the correlation length. Fig. 7 displays the order parameter measurements of the superlattice peaks (in (a), (b), and (c)) and the bulk susceptibility measurement, $d(\chi T)/dT$ (in (d)) [5]. The $(\frac{1}{3}, \frac{1}{3}, l)$ peak with even-integer l is purely magnetic. For odd-integer l , charge-

order scattering is dominant. As shown in Fig. 7(a), the charge peaks—especially the $(\frac{1}{3}, \frac{1}{3}, 5)$ reflection—start developing at 239K where $d(\chi T)/dT$ exhibits an anomaly. Upon cooling, however, the intensity develops at an unusually slow rate, followed by a rapid enhancement at ~ 190 K where $d(\chi T)/dT$ shows a weak feature. As T decreases to 10K, the peaks continue to grow in intensity. For T lower than 60K, the $(\frac{1}{3}, \frac{1}{3}, 1)$ peak decreases with a corresponding anomaly in $d(\chi T)/dT$. The existence of the three T regimes below 239K is clearer in the ratio of the $(\frac{1}{3}, \frac{1}{3}, 1)$ peak intensity to the $(\frac{1}{3}, \frac{1}{3}, 5)$ one, as depicted in Fig. 7(b). These three distinct phases are denoted as phase I, II, III with decreasing T order. Fig. 7(c) shows the T -dependence of the pure spin contribution to the $(\frac{1}{3}, \frac{1}{3}, 0)$ peak. The contribution of the long tail of the $(\frac{1}{3}, \frac{1}{3}, 1)$ charge peak to the $(\frac{1}{3}, \frac{1}{3}, 0)$ peak was assumed to be the same as that at $(\frac{1}{3}, \frac{1}{3}, 0.3)$ and subtracted. The non-zero intensity below ~ 190 K demonstrates that the spin ordering does not occur in phase I ($190\text{K} < T < 239\text{K}$), but only in phases II and III.

Some interesting aspects of the three phases were discovered in elastic Q-scans along the perpendicular direction to the stripes in the NiO_2 planes. The in-plane charge correlation length turns out to be quasi-long-range in phases II and III. However, in phase I, this correlation length drastically shortens to ~ 80 Å, which is about five times the characteristic wavelength of the charge modulation. The in-plane spin correlation length is about three times shorter than the structural correlation length. There seems to be only subtle differences between phases II and III, both of which exhibit quasi-long-range in-plane correlations. The transition is probably a structural transition in the hole lattice. Phase I, however, has short-range charge order in the absence of spin order, which is drastically different from the other two phases. We conclude that in $\text{La}_{1/3}\text{Sr}_{2/3}\text{NiO}_4$ the majority of holes are localized below 239K, with the stripe correlations poorly developed in the glassy phase I, and then becoming quasi-long-range ordered below 190K.

References

- [1] D. Dender, D. Davidović, D. Reich, C. Broholm, K. Lefmann, and G. Aeppli, *Phys. Rev. B* **53**, 2583 (1996); D. Dender, P. Hammar, D. Reich, C. Broholm, and G. Aeppli, preprint (1996).
- [2] S. Skanthakumar, J. W. Lynn, N. Rosov, G. Cao and J. E. Crow, *Phys. Rev. B* **55** (RC in press); S. Skanthakumar, J. W. Lynn, S. Uma and A. Erb (preprint); J. W. Lynn, *J. Alloys and Compounds* (in press).
- [3] L. Vasiliev-Doloc, J.W. Lynn, A.H. Moudden, A.M. de Leon-Guevara, A. Revcolevschi, *J. Appl. Phys.* (to be published).
- [4] P. J. van der Zaag, L. F. Feiner, R.M. Wolf, J.A. Borchers, Y. Ijiri and R.W. Erwin, (in preparation); P.J. van der Zaag, A.R. Ball, L.F. Feiner, R.M. Wolf and P.A.A. van der Heijden, *J. Appl. Phys.* **79**, 5103 (1996); J.A. Borchers, R.W. Erwin, S.D. Berry, D.M. Lind, J.F. Ankner, E. Lochner, K.A. Shaw and D. Hilton, *Phys. Rev. B* **51**, 8276 (1995).
- [5] S.-H. Lee and S-W. Cheong (preprint)

Research Topics

Anisotropic Spin Hamiltonians due to Spin-Orbit and Coulomb Exchange Interactions

T. Yildirim^{27,43}, A. B. Harris⁷¹, Amnon Aharony⁷², and O. Entin-Wohlman⁷²

Antiferromagnetic Order in TbBiPt and NdBiPt

C. Broholm¹³, R. Robinson¹⁷, and P. C. Canfield⁶²

Characterization of the Magnetic Structure and Interlayer Coupling in Nd/Y Superlattices

B. A. Everitt⁴², J. A. Borchers²⁷, R. W. Erwin²⁷, M. B. Salamon⁴², B. J. Park⁴², C. P. Flynn⁴², and J. J. Rhyne⁴⁵

Crystal and Magnetic Structures of NiF_3

L. Chacon³⁷, N. Rosov²⁷, and J. W. Lynn²⁷

Crystal Structure and Magnetic Ordering of the Rare Earth and Cu Moments in $(\text{R}_{1.5}\text{Ce}_{0.5})\text{Ba}_2\text{Cu}_2\text{NbO}_{10}$ ($\text{R}=\text{Nd}, \text{Pr}$)

N. Rosov²⁷, J. W. Lynn²⁷, H. B. Radousky¹⁵, M. Bennahmias³⁸, T. J. Goodwin³⁸, R. N. Shelton³⁸

Effect of Superconductivity on the Lattice Dynamics of $\text{Ba}_{0.6}\text{K}_{0.4}\text{BiO}_3$

S. Skanthakumar^{27,43}, J. W. Lynn^{27,43}, and S. N. Barilo⁶

Effects of Ga-Doping on the Magnetic Ordering of Pr in $\text{PrBa}_2\text{Cu}_3\text{O}_7$

W.-H. Li²⁰, C. J. Jou²⁰, S. T. Shyr²⁰, K. C. Lee²⁰, J. W. Lynn²⁷, H. L. Tsay²¹, and H. D. Yang²¹

Field Dependence of the Magnetic Structure in $\text{Fe}_3\text{O}_4/\text{NiO}$ Superlattices

R. W. Erwin²⁷, J. A. Borchers²⁷, D. M. Lind¹¹, K. A. Shaw¹¹, and P. Stoyanov¹¹

Field Induced Incommensurate Spin Correlations in the $S=1/2$ One-dimensional Antiferromagnet Copper Benzoate

D. C. Dender¹³, D. H. Reich¹³, C. Broholm¹³, and G. Aeppli⁸¹

Ground-State Selection in FCC and BCT Antiferromagnets due to Quantum Disorder

T. Yildirim^{27,43}, A. B. Harris⁷¹, and E. F. Shender³⁷

High-frequency Phonon Dispersion in $\text{La}_{1.85}\text{Sr}_{0.15}\text{CuO}_4$

A. H. Moudden^{56,63}, L. Vasiliu-Doloc^{27,43}, B. Hennion⁵⁶, P. M. Gehring²⁷, G. Shirane⁷, Y. Endoh⁵³, I. Tanaka⁵², H. Kojima⁵²

Incommensurate and Commensurate Magnetic Structures in the Magnetoresistive $\text{R}_2\text{Ni}_3\text{Si}_5$ Materials

S. Skanthakumar^{27,43}, J. W. Lynn^{27,43}, and L. C. Gupta³⁰

The Invar Effect in $\text{Fe}_{65}\text{Ni}_{35}$

N. Rosov²⁷, J. W. Lynn^{27,43}, M. Acet³³

Magnetic Order in the Superconductor $\text{RNi}_2\text{B}_2\text{C}$

J. W. Lynn²⁷, S. Skanthakumar^{27,43}, Z. Hossain³⁰, L. C. Gupta³⁰, R. Nagarajan³⁰, C. Godart⁶³, and S. K. Sinha¹⁰

Magnetic Order, Structure, and Spin Dynamics of $(\text{La}_{1-x}\text{Ca}_x)\text{MnO}_3$

R. W. Erwin²⁷, J. A. Borchers²⁷, J. W. Lynn²⁷, Q. Huang²⁷, A. Santoro²⁷, and J. L. Peng⁴³

Magnetic Ordering and Structure of $(\text{Pr}, \text{Nd})_{1-x}\text{Ce}_x\text{Sr}_2\text{Cu}_2(\text{Nb}, \text{Ta})\text{O}_{10}$

N. Rosov²⁷, J. W. Lynn^{27,43}, T. Goodwin³⁸, R. Shelton³⁸, and H. Radousky¹⁷

Magnetic Ordering and Structure of $\text{PrBa}_2\text{Fe}_3\text{O}_8$

N. Rosov²⁷, J. W. Lynn^{27,43}, M. Seyedahmadian⁸², T. Yeun⁸²

Magnetic Ordering in $\text{Co}_3(\text{BTCA})_2 \cdot 4\text{D}_2\text{O}$, A Low Dimensional Ferromagnet

N. Rosov²⁷, C. Landee⁸¹, C. Wynn⁸¹

Magnetic Ordering in $\text{Dy}_5\text{Os}_4\text{Ge}_{10}$

S. Skanthakumar^{27,43}, J. W. Lynn²⁷, L. C. Gupta³⁰, M. Lin¹⁰, and S. K. Sinha¹⁰

Magnetic Ordering of Pr and Cu in $\text{TlBa}_2\text{PrCu}_2\text{O}_{7-y}$

W.-H. Li²⁰, K. C. Lee²⁰, J. W. Lynn²⁷, C. C. Lai^{20a}, and H. C. Ku^{20a}

Magnetic Ordering of Pr in $\text{Pb}_2\text{Sr}_2\text{PrCu}_3\text{O}_8$

W. T. Hsieh²⁰, W.-H. Li²⁰, K. C. Lee²⁰, J. W. Lynn²⁷, J. H. Shieh^{20a}, and H. C. Ku^{20a}

Magnetic Properties of Ru in SrRuO_3 and $\text{Sr}_3\text{Ru}_2\text{O}_7$

S. Skanthakumar^{27,43}, J. W. Lynn^{27,43}, G. Cao¹¹, and J. E. Crow¹¹

Magnetic Structure Determination in Exchange-Biased $\text{Fe}_3\text{O}_4/\text{CoO}$ Superlattices

J. A. Borchers²⁷, R. W. Erwin²⁷, Y. Ijiri²⁷, P. van der Zaag⁸⁰, and R. M. Wolf⁸⁰

Magnetic Structure Determination for FeF_2 Thin Films

J. A. Borchers²⁷, R. W. Erwin²⁷, D. Lederman⁷⁹, J. Nogues⁷⁹, and I. K. Schuller³⁹

Modification of the Spin Density Wave in Cr Films

P. Bodeker²⁸, A. Schreyer²⁸, J. A. Borchers²⁷, and H. Zabel²⁸

Observation of Pr Magnetic Order in $\text{PrBa}_2\text{Cu}_3\text{O}_7$

S. Skanthakumar^{27,43}, J. W. Lynn^{27,43}, N. Rosov²⁷, G. Cao¹¹, J. E. Crow¹¹, S. Uma⁷⁶, and A. Erb⁷⁷

Order Parameter Measurements in CMR Perovskite Films

Y. Ijiri²⁷, J. A. Borchers²⁷, R. W. Erwin²⁷, J. W. Lynn²⁷, C. Kwon⁴³, M. Robson⁴³, and R. Ramesh⁴³

Orientation of the Moments in Exchange Biased NiO and CoO Films

J. A. Borchers²⁷, R. W. Erwin²⁷, K. Takano³⁹, A. E. Berkowitz³⁹, and R. Kodama³⁹

Polarization Analysis of the Magnetic Excitations in Invar

J. W. Lynn²⁷, N. Rosov²⁷, M. Acet³⁸, and H. Bach²⁸

Polarized Neutron Study of the Spin Glass State in $\text{SrCr}_{9p}\text{Ga}_{12-9p}\text{O}_{19}$ Single Crystals

S. H. Lee⁴³, S.-W. Cheong⁸², C. Broholm¹³, and G. Aeppli⁸¹

Pressure Dependence of Magnetic Fluctuations in the $S=1$ One-dimensional Antiferromagnet NENP

I. P. Zaliznyak¹³, D. C. Dender¹³, G. Xu¹³, C. Broholm¹³, and D. H. Reich¹³

Single-Ion Anisotropy and Crystal Field Effects in R_2CuO_4 ($\text{R}=\text{Nd}, \text{Sm}, \text{Pr}, \dots$)

T. Yildirim^{27,43}, R. Sachidanandam⁷², Amnon Aharony⁷², and A. B. Harris⁷¹

Single-Ion Anisotropy and Exchange Coupling in Y_2BaNiO_5

G. Xu, J. F. DiTusa, T. Ito, H. Takagi, K. Oka, C. Broholm¹³, and G. Aeppli⁸¹

Spin Correlations Close to Impurities in $\text{Y}_{2-x}\text{Ca}_x\text{BaNiO}_5$

Guangyong Xu, J. F. DiTusa, T. Ito, H. Takagi, K. Oka, C. Broholm¹³, and G. Aeppli⁸¹

Spin Correlations in the Spin Glass State of $\text{SrCr}_{9p}\text{Ga}_{12-9p}\text{O}_{19}$ Single Crystals

S. H. Lee⁴³, S.-W. Cheong⁸², C. Broholm¹³, and G. Aeppli⁸¹

Spin Dynamics of Er^{3+} in $\text{ErBa}_2\text{Cu}_3\text{O}_7$

S. Skanthakumar^{27,43}, J. W. Lynn^{27,43}, F. Dogan⁷⁸

Spin Dynamics of the Mn ions in $\text{La}_{1-x}\text{Ba}_x\text{MnO}_3$

S. Skanthakumar^{27,43}, J. W. Lynn^{27,43}, J. L. Peng⁴³, and R. L. Greene⁴³

Spin Wave Dispersion Relations in the Magnetoresistive Pyrochlore $\text{Ti}_2\text{Mn}_2\text{O}_7$

J. W. Lynn²⁷, L. Vasiliu-Doloc^{27,43}, and M. A. Subramanian⁷⁴

Structure and Dynamics of $(\text{La-Sr})\text{MnO}_3$

L. Vasiliu-Doloc^{27,43}, J. W. Lynn²⁷, A. H. Moudden^{56,63}, A. M. de Leon-Guevara, and A. Revolovschi⁷⁵

Suppression of T_N in CoO/MgO Superlattices

Y. Ijiri²⁷, J. A. Borchers²⁷, R. W. Erwin²⁷, P. van der Zaag⁸⁰, and R. M. Wolf⁸⁰

Temperature Dependence of Magnetic Fluctuations in the $S=1/2$ One-dimensional Antiferromagnet Copper Benzoate

D. C. Dender¹³, D. H. Reich¹³, C. Broholm¹³, and G. Aeppli⁸¹

Three-dimensional Spin Structure of $\text{Sr}_2\text{CuO}_2\text{Cl}_2$; Field Dependent Neutron Scattering Study

T. Yildirim^{27,43}, S. Skanthakumar^{27,43}, and J. W. Lynn^{27,43}

Two-dimensional Magnetic Order in $\text{Pb}_2\text{Sr}_2\text{TbCu}_3\text{O}_8$

S. Y. Wu²⁰, W. T. Hsieh²⁰, W.-H. Li²⁰, K. C. Lee²⁰, J. W. Lynn²⁷, and H. D. Yang²¹

Vortex Lattice and Melting in Nb

J. W. Lynn²⁷, N. Rosov²⁷, and T. E. Grigereit⁴³

Vortex Lattice Structure and Melting in $\text{Ba}_{0.6}\text{K}_{0.4}\text{BiO}_3$

J. W. Lynn²⁷ and S. N. Barilo⁶

Affiliations

¹Allied Signal Corp.

²Army Armament RD&E Center

³Argonne National Lab

⁴Arizona State University

⁵AT&T Bell Laboratories

⁶Belarus Academy of Sciences

⁷Brookhaven National Lab

⁸Charles University, Prague

⁹Columbia University

¹⁰Exxon Research & Engineering

¹¹Florida State University

¹²Institut Laue-Langevin

¹³Johns Hopkins University

¹⁴KFA Jülich

¹⁵Lawrence Livermore Laboratory

¹⁶Lehigh University

¹⁷Los Alamos National Laboratory

¹⁸McMaster University

¹⁹Morris Research, Berkeley

²⁰National Central U., Taiwan

^{20a}National Tsing Hua U. (Taiwan)

²¹Nat'l Sun Yat-Sen U, Taiwan

²²Nippon Electric Co.

²³Oak Ridge National Lab

²⁴Philips Research Labs

²⁵Princeton University

- ²⁶Purdue University
- ²⁷Reactor Radiation Division
- ²⁸Ruhr Universitte
- ²⁹SUNY at Binghamton
- ³⁰Tata Inst. of Fundamental Res., Bombay
- ³¹Universita di Brescia, Italy
- ³²Universitt Bochum, Germany
- ³³Universitt Duisberg, Germany
- ³⁴Universitt Karlsruhe, Germany
- ³⁵Universit du Maine, France
- ³⁶University of Amsterdam
- ³⁷University of California, Berkeley
- ³⁸University of California, Davis
- ³⁹University of California, San Diego
- ⁴⁰University of Chicago
- ⁴¹University of Houston
- ⁴²University of Illinois
- ⁴³University of Maryland
- ⁴⁴University of Michigan
- ⁴⁵MURR, University of Missouri
- ⁴⁶University of Nancy I, France
- ⁴⁷University of Oslo
- ⁴⁸University of Zaragoza, Spain
- ⁴⁹Ural State University, Russia
- ⁵⁰Westinghouse
- ⁵¹University of Missouri, Columbia
- ⁵²Yamanashi University, Japan
- ⁵³Tohoku University, Japan
- ⁵⁴IBM AdStar
- ⁵⁵IBM Almaden Research
- ⁵⁶Laboratoire Lon Brillouin, France
- ⁵⁷Ris National Laboratory
- ⁵⁸Oxford University, England
- ⁵⁹Lab. for Neutron Scattering, Switzerland
- ⁶⁰Western Michigan University
- ⁶¹Oak Ridge Inst. for Science and Education
- ⁶²Ames Laboratory
- ⁶³CNRS, Meudon, France
- ⁶⁴University of Tsukuba, Japan
- ⁶⁵University of Central Florida
- ⁶⁶Penn State University
- ⁶⁷Ris National Laboratory
- ⁶⁸Royal Institution of Great Britain
- ⁶⁹Sussex University
- ⁷⁰Georgetown University
- ⁷¹University of Pennsylvania
- ⁷²Tel Aviv University
- ⁷³University of California, Berkeley
- ⁷⁴DuPont
- ⁷⁵University of Paris, Sud
- ⁷⁶Max Plank Institute, Germany
- ⁷⁷University of Geneva
- ⁷⁸University of Washington
- ⁷⁹University of West Virginia
- ⁸⁰Philips Laboratory, Eindhoven
- ⁸¹NEC
- ⁸²Lucent Technology
- ⁸³Lousiana State University
- ⁸⁴ISSP, University of Tokyo

Crystallography

Operation of the 32-detector high-resolution powder diffractometer at BT-1 continued smoothly with the reactor operating again at 20 MW. Realignment of the instrument resulted in an increase in diffracted beam intensity of approximately 60% for the Cu311 monochromator, which is by far the most commonly used option. The Cu220 and Si531 monochromators exhibited an increase in diffracted beam intensity of approximately 33%, as would be expected from the increase in reactor power. In a somewhat shortened year of operation, data were collected on over 330 different materials under various experimental conditions resulting in an estimated 1000 or more data sets. This section presents a few highlights of the extremely varied studies using this instrument. Many other crystallographic contributions are covered separately in the sections on Chemical Physics of Materials and Magnetism and Superconductivity, including e.g. crystallographic work on high- T_c superconductors, magnetic materials, metal hydrides, and molecular solids.

Instrumentation and Software

- **Automated Sample Changer**

The design of a three-position automated sample changer for collection of data at room temperature was completed, and a prototype was built and put into operation. Because of the extremely rapid rate of data collection now possible, the sample changer was promptly redesigned to accept up to six samples with computer-controlled changing of samples. The use of this automated sample changer has made possible more efficient use of the instrument.

- **WWW Accessibility**

A system was created and implemented for submission of research proposals for BT-1 via the World-Wide Web (WWW) using a standard Web browser program such as Netscape. This

system is now used for all internal beam-time requests as well. Web submission makes it possible to offer expedited review of proposals on a first-come first-served basis with a deadline occurring shortly before the beginning of each reactor cycle. This speeds access to the BT-1 diffractometer for researchers working on "hot" topics and facilitates access by external users.

A number of WWW pages were added to the CNRF web pages that detail access to BT-1 as well as sample and safety considerations. Some of the topics covered include: the proposal system; proprietary access; preferred sample quantities; why hydrogen or other neutron absorbers in samples is problematic; appropriate containers for neutron diffraction; elements that have significant neutron activation. See <http://rrdjazz.nist.gov/~toby/bt1.html> for further information about the WWW proposal system and links to the other WWW pages. Further work is planned that will allow prospective users to calculate neutron absorption and neutron activation for their samples using Web forms.

Phase Analysis

- **Plasma-Sprayed YSZ**

We have previously reported on the phase analysis of yttria-stabilized zirconia (YSZ) powders used as feedstock for the preparation of ceramic thermal barrier coatings. The addition of yttria (Y_2O_3) to zirconia (ZrO_2) at about 8 wt% Y_2O_3 stabilizes the tetragonal phase relative to the low-temperature monoclinic phase (so-called partially stabilized zirconia); higher amounts of yttria stabilize the cubic phase (fully stabilized zirconia). Plasma spraying is a rapid solidification process that yields a phase composition of the resulting ceramic coating that is different from that of the feedstock powder, and often results in the formation of metastable phases.

Industrial experience with thermal barrier

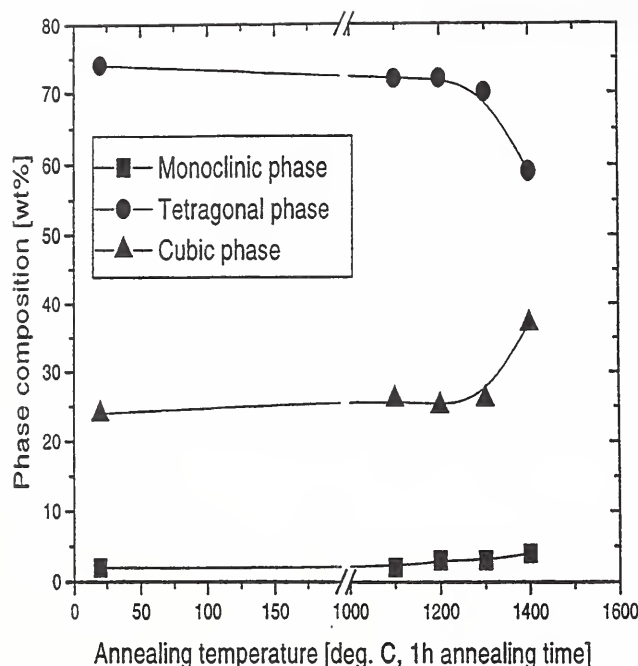


Figure 1. Phase composition of annealed plasma-sprayed YSZ coatings, spray distance 90 mm.

coatings applications has shown that tight control of the coating phase composition is imperative for optimal coating lifetime and survival. Larger amounts of the monoclinic phase in the deposits are considered undesirable, as these transform on heating into the tetragonal phase. Since this transformation is accompanied by a large volume change, stresses are generated in the deposits leading to premature failure. Coatings made of fully stabilized zirconia (cubic phase) have shorter lifetimes and generally inferior properties compared to partially stabilized zirconia coatings.

The zirconia phase analysis is challenging. Whereas the monoclinic phase is easily identified and quantified using X-ray patterns, the tetragonal:cubic ratio is much more difficult since the cubic peaks are all coincident with some of the tetragonal peaks. Previous work has shown that the cubic phase content is often underestimated. Neutron Rietveld refinement provides a superior (albeit inconvenient for the industrial analyst) technique. In addition to yielding more

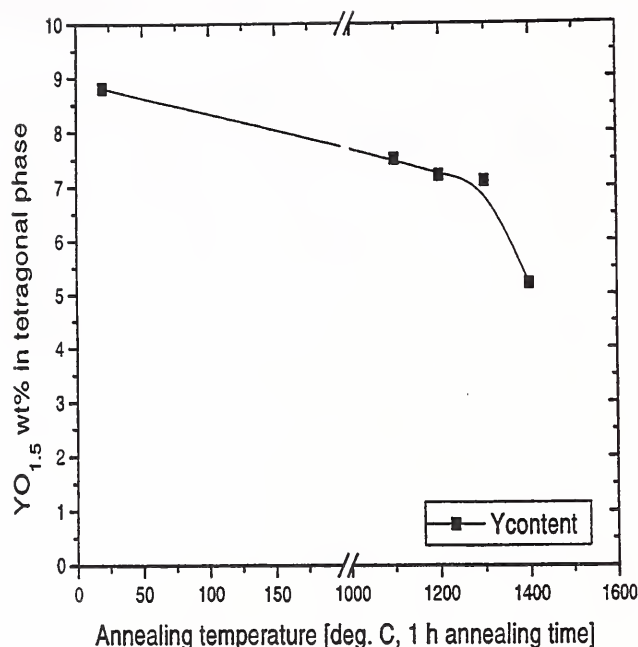


Figure 2. Yttria content of the tetragonal phase of annealed plasma-sprayed YSZ coatings, spray distance 90 mm.

data at higher scattering angle to help differentiate the tetragonal and cubic phases, the neutrons penetrate the entire coating sample and thus give results for the bulk material and make unimportant such X-ray analysis considerations as surface roughness and texture, preferred orientation, and gradations of phase composition through the thickness of the sample.

Deposits made of Sylvania SX233 powder were manufactured at SUNY Stony Brook. The deposits of about 5 mm thickness were sprayed on a steel substrate covered by an Al layer deposited by wire arc spraying. The Al layer was later dissolved using HCl to obtain free-standing deposits. Samples were cut using a diamond saw into 10 mm x 10 mm x 5 mm sections and annealed for one hour in ambient atmosphere at varying temperatures prior to phase analysis.

The results of the neutron Rietveld phase analysis are given in Table 1 and Fig. 1. As can be seen for the samples with a spray distance of 90 mm, little change occurs in the phase composition with heating until 1400 °C, when the com-

Table 1. Phase content and composition of SX233 plasma-sprayed and annealed YSZ coatings

Spray Distance		% Monoclinic	% Tetragonal	% Cubic	wt% YO _{1.5} (tetragonal phase)
Powder	—	25	49	26	8.3
65 mm	as sprayed	3	60	37	8.8
145 mm	as sprayed	2	71	27	9.0
90 mm	as sprayed	2	74	24	8.8
90 mm	1100 °C, 1 h	2	72	26	7.5
90 mm	1200 °C, 1 h	3	72	25	7.2
90 mm	1300 °C, 1 h	3	70	26	7.1
90 mm	1400 °C, 1 h	3	60	37	6.2
65 mm	1400 °C, 1 h	4	59	37	5.9

position reverts to the thermodynamically stable composition, with an increase in the relative amount of the cubic phase as predicted by the phase diagram. For the material sprayed at 65 mm, the as-sprayed phase composition is close to the thermodynamically stable composition, and little change occurs with annealing. In addition, it is possible to calculate the yttria content of the tetragonal phase from the tetragonal lattice parameters. For the materials sprayed at both 65 mm and 90 mm, there is some loss of yttria from the tetragonal phase with annealing even at 1100 °C - 1300 °C, but the loss is accelerated at 1400 °C (Fig. 2). Further work is planned on samples prepared under varying plasma spray and heat treatment conditions.

Crystal Structures

• Colossal Magnetoresistors

Colossal magnetoresistors (CMR) exhibit a very large change in electrical resistance in the presence of magnetic fields. In principle, this phenomenon can be used to design a new generation of devices for reading magnetic media, which has sparked a world-wide industrial quest to understand the prerequisites for CMR and to find new materials. CMR is known to occur in $\text{La}_{1-x}\text{M}_x\text{MnO}_3$ perovskites, but recently it was also demonstrated in $\text{Tl}_2\text{Mn}_2\text{O}_7$, which has a pyrochlore-type structure.

Oxygen deficiencies are known to be essential for CMR in the perovskite materials. In

collaboration with DuPont, we have used neutron Rietveld refinement techniques to determine the level of oxygen vacancies in the pyrochlore $\text{Tl}_2\text{Mn}_2\text{O}_7$. This material is prepared at high pressure, and only a very small amount (0.18 g, or 0.0003 moles!) of sample could be supplied. This amount of sample is two orders of magnitude lower than the amount commonly used for powder neutron diffraction, but using ~24 hr data collection times on the BT-1 diffractometer, the crystal structure was determined.

The results proved that CMR exists in the material without any significant oxygen vacancies, which indicates that a different mechanism for CMR is likely present in this material. This suggests that there may be many more materials that exhibit CMR than previously thought.

• Structure and Magnetic Order in Undoped Lanthanum Manganite

The undoped lanthanum manganite system of nominal composition LaMnO_3 has been analyzed by neutron powder diffraction for different sample heat treatment methods. Four distinct crystallographic phases have been identified: (i) an orthorhombic phase of space group $Pnma$ and lattice parameters (at 300 K) $a = 5.7385(3)$, $b = 7.7024(3)$, $c = 5.5378(2)$ Å, produced by annealing in a reducing atmosphere. The system develops long range antiferromagnetic order below $T_N = 140$ K, with the Mn^{3+} spins coupled ferromagnetically in the ac plane and antiferromagnetically along b , with the spin direction

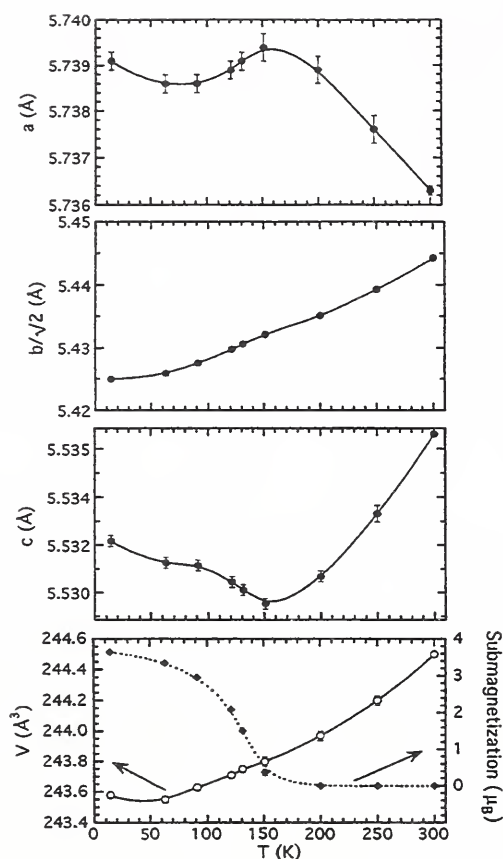


Figure 3. Variation with temperature of the lattice parameters, unit cell volume, and sublattice magnetization obtained from the refinements of the antiferromagnetic orthorhombic phase of sample (i).

along a . The volume of this phase increases monotonically with increasing temperature, but both the a and c lattice parameters exhibit negative thermal expansion in alternate temperature regimes (see Fig. 3). (ii) A second (previously unreported) orthorhombic phase that exhibits a smaller splitting, also of space group $Pnma$ and lattice parameters (at 300 K) $a = 5.4954(3)$, $b = 7.7854(4)$, $c = 5.5355(3)$ Å, produced by annealing in an oxygen (or air) atmosphere. This system orders with a simple ferromagnetic structure at $T_N = 140$ K, with the spin direction along c . Phases (i) and (ii) can be transformed reversibly by suitable heat treatment of the same sample, and exist with a range of lattice parameters and compositions. The unit cell volume for the antiferromagnetic phase is consid-

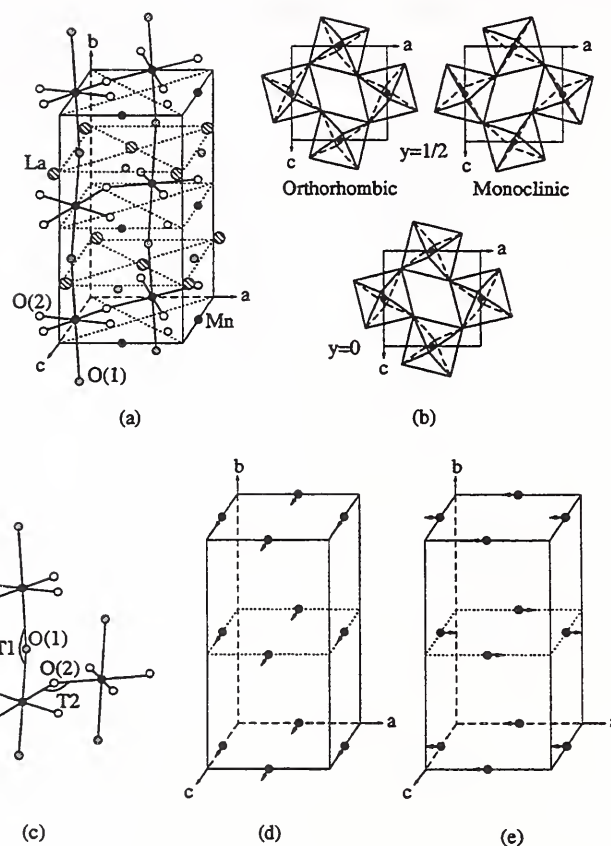


Figure 4. Schematic representation of the nuclear and magnetic structures in the lanthanum manganite system: (a) nuclear structure represented in the $Pnma$ axes; (b) tilting of the MnO_6 octahedra in two successive layers along the c -axis; (c) tilt angles of the octahedra; (d) ferromagnetic structures of phases $P112_1/a$ and $Pnma$; (e) antiferromagnetic structure of phase $Pnma$.

erably larger than for the ferromagnetic phase, which agrees with the double-exchange model proposed for this system. (iii) A monoclinic phase of space group $P112_1/a$ and lattice parameters (at 200 K) $a = 5.4660(4)$, $b = 7.7616(7)$, $c = 5.5241(5)$ Å, $\gamma = 90.909(5)^\circ$ that orders ferromagnetically below 140 K. (iv) A rhombohedral phase of space group $R\bar{3}c$ and hexagonal lattice parameters (at 300 K) $a = 5.5259(2)$, $c = 13.3240(4)$ Å, that is observed only above room temperature.

Occupancy refinements show that phase (i) ideally has the stoichiometric composition

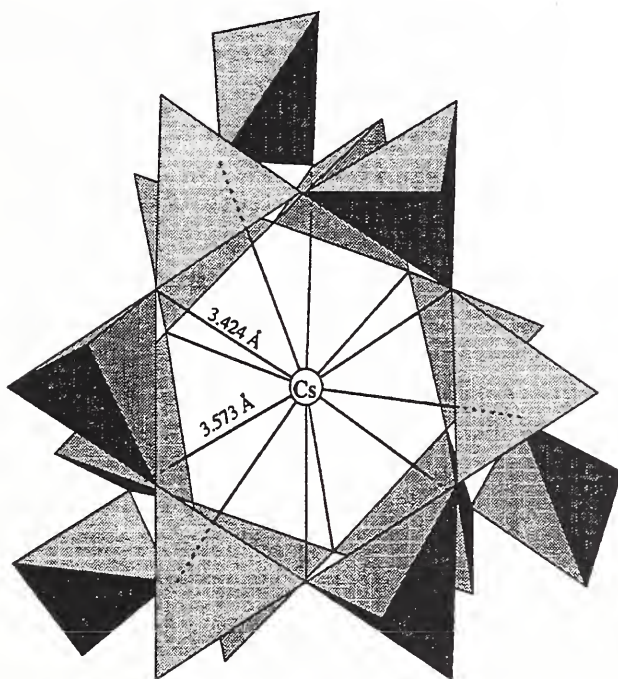


Figure 5. View along one of the $[111]$ axes of the distribution of the TO_4 tetrahedra around a Cs^+ cation. The oxygen atoms bonded to the cesium are indicated by the Cs-O lines.

LaMnO_3 , while the results for the Mn-O bond distances suggest that phases (ii), (iii), and (iv) are progressively richer in oxygen (and thus Mn^{4+}). The results of our study strongly suggest the progressive development of cation vacancies in equal numbers on the La and Mn sites as the oxygen content is increased by heat treatment. In the monoclinic phase the Mn ions occupy two crystallographically independent sites, but no evidence of ordering of Mn^{3+} and Mn^{4+} was observed. The structures of the four phases are closely related to that of perovskite. The MnO_6 octahedra are tilted from the undistorted configuration, the tilt system being $a^-a^-a^-$ in the rhombohedral structure and $a^+b^-b^-$ in both orthorhombic modifications. A schematic representation of the nuclear and magnetic structures of lanthanum manganite is shown in Fig. 4.

- **Neutron and X-Ray Diffraction Study of $\text{CsTiSi}_2\text{O}_{6.5}$**
Silicotitanates are ion exchangers used for re-

moval of cesium from radioactive Na-rich wastes. One compound recently synthesized is a derivative of the cesium aluminosilicate pollucite, $\text{CsAlSi}_2\text{O}_6$, in which titanium replaces aluminum. This substitution requires a mechanism for charge compensation, such as incorporation of oxygen in excess of six atoms per formula unit into the structure, resulting in a composition corresponding to the formula $\text{CsTiSi}_2\text{O}_{6.5}$. The location of such small quantities of extra oxygen requires the use of neutron diffraction techniques. On the other hand, since the scattering amplitude of the atoms occupying the tetrahedral site, $T = 1/3\text{Ti} + 2/3\text{Si}$, is rather small (0.162×10^{-12} cm), these cations can be located precisely using single-crystal X-ray diffraction. The structure of the title compound, therefore, has been analyzed with both techniques.

$\text{CsTiSi}_2\text{O}_{6.5}$ crystallizes with the symmetry of space group $Ia\bar{3}d$ and lattice parameter $a = 13.8417(7)$ Å. There are sixteen formula units per unit cell. The basic structure is similar to that of pollucite and consists of a framework of corner sharing TO_4 tetrahedra forming large voids in which the Cs^+ cations are located (Fig. 5). Titanium and silicon are disordered over the 48g sites of the cubic space group. The eight extra oxygen atoms partially occupy two sets of general sites and are bonded to both the cesium and the T cations of neighboring tetrahedra (Fig. 6), and it is assumed that the extra oxygen is located near the tetrahedra occupied by titanium.

Zeolite SRM Characterization

A long-range study of zeolites and related molecular sieves has been initiated, with particular emphasis of the siting and dynamics of guest molecules and cations. These materials are of great industrial importance in the areas of catalysis, separations, and cation exchange. Zeolites are widely used in the manufacture of gasoline, detergents, gases from air, and other materials. In order to assist industrial and academic researchers, we have cooperated with the NIST Standard Reference Materials program to

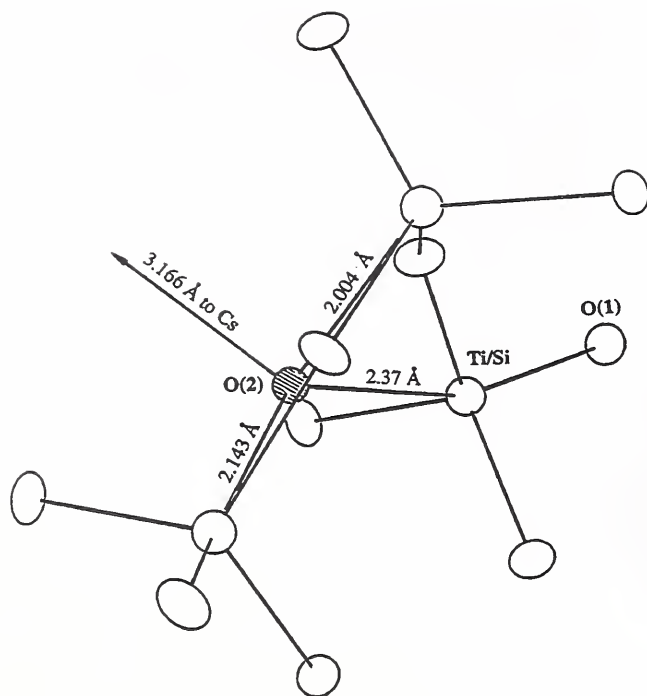


Figure 6. Environment of one of the extra oxygen atoms (shaded circle), showing its relationship to the neighboring TO_4 tetrahedra.

initiate the certification of a series of zeolite SRMs and RMs, providing needed expertise in the handling and characterization of these materials. A procedure was developed for the certification of three zeolite SRM samples by neutron and synchrotron radiation.

In order to facilitate this effort, a collaborative research agreement was initiated with SUNY Stony Brook. As part of this agreement, SUNY has provided a postdoctoral research associate who will participate at NIST in the SRM certification work and will also assist in gas loading studies of zeolites. An *in situ* gas loading cell for these studies has been designed and will be constructed and tested.

Database Activities

The NIST Crystal and Electron Diffraction Data Center is concerned with the collection, evaluation and dissemination of data on solid-state materials. During the year, the master database for the NIST Crystal and Electron Dif-

fraction Data Center was augmented with respect to all classes of materials, and now contains approximately 235,000 entries. In September 1996, updated versions were released of the two distribution databases, the NIST Crystal Data and the Electron Diffraction Database. Also, a Special Issue of the NIST Journal of Research was published in July with manuscripts from the NIST Workshop on Crystallographic Databases which was held in August 1995. This publication reviews the present status and future directions of the crystallographic databases, outlines applications of the databases, summarizes modes of data transfer, and sets the stage for future collaborations and partnerships between NIST and other crystallographic data centers.

• International Tables for Crystallography

During the year, a section entitled 'The space-group distribution of molecular organic structures' has been written for the International Tables of Crystallography. The purpose of this article is not only to present space group statistics, but also to account in a general way for the observed distribution. Ultimately, the space group of a crystal of a particular substance is determined by the minimum of the thermodynamic potential of the van der Waals and other forces, but a very simple model goes a long way towards explaining the relative frequency of the various space groups within a crystal class or larger grouping. The basic idea that space group frequency is determined by packing considerations is discussed, along with the complementary idea that space groups are rare when they contain symmetry elements that prevent molecules from freely choosing their positions within the unit cell. Empirical statistics for the 230 space groups are given for homomolecular organic structures with one molecule in the general position. The frequencies show that most compounds crystallize in a relatively small number of low symmetry space groups and that most space groups have few or no known examples.

By providing the researcher with a summary of what happens in nature, space group statistics may prove useful in the understanding of packing forces and in the *a priori* prediction of crystal structures.

Research Topics

Neutron Powder Diffraction Study of BaND and CaND

F. Altorfer^{30,45} and T. Sichla⁴¹

Crystal Structure Determination of the One-Dimensional Ionic Conductors AgBaLaBr₆ and NaBaLaBr₆

F. Altorfer^{30,45} and M. Wickleder³⁷

Crystal Structure of ZrBeH_{1.5} and ZrBeD_{1.4}

F. Altorfer^{30,45}, T. J. Udovic³⁰, and B. Hauback¹⁶

Crystal Structure of Trioxane Silica Sodalite

F. Altorfer^{30,45}, W. Buehrer¹⁹, and C. Braunbarth⁴⁰

Crystal Structure of Sr(OH)Br

F. Altorfer^{30,45}, W. Buehrer¹⁹, and H. D. Lutz⁴⁸

Neutron Powder Diffraction Study of SrFCI

F. Altorfer^{30,45}, W. Buehrer¹⁹, and H. Bill⁴²

Crystal Structure Determination of the Ionic Conductor Li₃YBr₆

F. Altorfer^{30,45} and M. Wickleder³⁷

Crystal Structure of an Ammonium Nickel Molybdate Prepared by Chemical Precipitation

D. Levin²², S. L. Soled¹², J. Y. Ying²², and J. K. Stalick³⁰

Structural Properties of Ba₂SnO₄ and Sr₂SnO₄

M. A. Green^{31,29}, K. Prassides^{31,50}, P. Day³¹, and J. K. Stalick³⁰

Neutron Investigation of Carbonate-Free BaCuO₂

J. K. Stalick³⁰ and W. Wong-Ng⁸

Structural Studies of Fast-Ion Conductors Y₂(Sn,Ti)₂O₇, (Y,Ca)₂Ti₂O₇, (Yb,Ce)₂Ti₂O₇, and (La,Ca)₂Sn₂O₇

K. Eberman²², B. J. Wuensch²², and J. K. Stalick³⁰

Neutron Structure of LiV₂O₄·D₂O

P. Y. Zavaliy³², M. S. Whittingham³², and J. K. Stalick³⁰

Neutron Investigation of the Crystal Structure of Zr₉Pd₁₁

J. K. Stalick³⁰ and R. M. Waterstrat²³

Quantitative Phase Analysis of ZrO₂ Powders

J. K. Stalick³⁰

Phase Composition of Plasma-Sprayed YSZ Coatings

J. Ilavsky⁸ and J. K. Stalick³⁰

Structural and Magnetic Phase Transitions in KMnF₃

P. M. Gehring³⁰, S. M. Shapiro⁵, and A. Gibaud⁴³

Neutron Powder Diffraction Studies of Sr₇Ti₂Nb₄O₂₁

A. R. Drews³⁰, T. A. Vanderah⁸, R. S. Roth⁸, and A. Santoro³⁰

Cation Vacancies in Ti-doped α-Fe₂O₃

A. R. Drews³⁰ and T. A. Vanderah⁸

Absorption Corrections for Diffraction from Cylindrical Shells

N. Rosov³⁰ and J. W. Lynn^{30,45}

Magnetic Ordering and Structure of PrBa₂Fe₃O₈

N. Rosov³⁰, J. W. Lynn^{30,45}, M. Seyedahmadian³⁴, and T. Yuen³⁴

Magnetic Ordering and Structure of (Pr,Nd)_{1-x}Ce_xSr₂Cu₂(Nb,Ta)O₁₀

N. Rosov³⁰, J. W. Lynn^{30,45}, T. Goodwin³⁹, R. Shelton³⁹, and H. Radousky²⁰

Neutron Diffraction Study of Interstitial Hydrogen in C₆₀

S. A. FitzGerald³⁰, D. A. Neumann³⁰, L. J. Santodonato³⁰, J. R. D. Copley³⁰, T. Yildirim^{30,45} and J. J. Rush³⁰

The Hydration of Cementitious Materials

S. A. FitzGerald³⁰, D. A. Neumann³⁰, J. J. Rush³⁰, and R. Livingston¹³

Neutron Diffraction Study of Na₂C₆₀ as a Function of Pressure and Temperature

T. Yildirim^{30,45}, S. F. Trevino^{30,3}, D. A. Neumann³⁰, and J. E. Fischer⁴⁷

Neutron Diffraction Study of KC₆₀

H. Guerrero²⁸, R. L. Cappelletti²⁸, T. Yildirim^{30,45}, and D. A. Neumann³⁰

- Neutron Diffraction Determination of the Phase Diagram of $\text{Ni}_2\text{Mn}_{1+x}\text{Ga}_{1-x}$**
R. Overholser⁴⁵, M. Wuttig⁴⁵, and D. A. Neumann³⁰
- Order-Disorder Phase Transitions in the Heusler Alloy Ni_2MnGa**
R. Overholser⁴⁵, M. Wuttig⁴⁵, and D. A. Neumann³⁰
- Neutron Diffraction Study of $\text{Ba}_3\text{NiNbO}_7$ and $\text{Sr}_3\text{NiNbO}_7$**
M. Green²⁹, M. Rosseinsky²⁹, and D. A. Neumann³⁰
- Neutron Diffraction Study of $(\text{LaSr})\text{NiO}_4$**
M. Green²⁹, M. Rosseinsky²⁹, and D. A. Neumann³⁰
- Structure of Chromium Jarosite**
N. Lacevic¹⁷, S.-H. Lee¹⁷, C. Broholm¹⁷, C. Kloc⁴⁰, and E. Bucher^{21,40}
- Structure of $\text{ZnGa}_{1-x}\text{Cr}_x\text{O}_4$**
S.-H. Lee¹⁷, S.-W. Cheong²¹, and C. Broholm¹⁷
- Proton Sites in ZSM-5**
A. Peters⁵³, R.-H. Hu⁵³, and B. H. Toby³⁰
- High Dielectric Ba-Fe Titanate Ceramics**
T. Siegrist²¹, T. Vanderah⁸, W. Wong-Ng⁸, and B. H. Toby³⁰
- High Dielectric Ba-Lanthanide Titanate Perovskites**
T. Negas³⁵, C. Rawn⁴⁴, and B. H. Toby³⁰
- Cation Ordering in $(\text{Pb,Ca})\text{TiO}_3$ Perovskites**
B. Burton⁸, E. K. Goo⁴⁹, and B. H. Toby³⁰
- Determination of Amorphous Content in Alumina SRM676**
J. Cline⁸ and B. H. Toby³⁰
- Template Siting in Zeolite CIT-1**
M. Davis⁶ and B. H. Toby³⁰
- A Search for Orthorhombic Forms of Faujasite**
J. B. Higgins¹, J. E. MacDougall¹, and B. H. Toby³⁰
- Proof that the Colossal Magnetoresistor $\text{Ti}_2\text{Mn}_2\text{O}_7$ is Stoichiometric**
M. Subramanian¹⁰, G. Kwei²⁰, and B. H. Toby³⁰
- Characterization of Candidate Materials for Ceramic Membranes**
H. Prask³⁰ and P. Brand³⁰
- Neutron Powder Diffraction Studies of the H_5O_2^+ Ion in Phosphotungstic Acid Hydrates**
N. C. Maliszewskyj³⁰, T. J. Udovic³⁰, and Q. Huang^{30,45}
- Quasi-Laue Neutron Diffraction**
E. Prince^{30,45}, C. Wilkinson¹¹, and M. S. Lehmann¹⁵
- The NIST Crystal and Electron Diffraction Data Center**
V. L. Karen³⁰ and A. D. Mighell³⁰
- Space Group Distribution of Molecular Organic Structures**
A. J. C. Wilson⁷, V. L. Karen³⁰, and A. D. Mighell³⁰
- Neutron Powder Diffraction Study of the Temperature-Dependent Site Occupation of D in YD_2**
T. J. Udovic³⁰, Q. Huang^{30,45}, F. Altorfer^{30,45}, and J. J. Rush³⁰
- Neutron Powder Diffraction Studies of YD_{3-x}**
T. J. Udovic³⁰, Q. Huang^{30,45}, and J. J. Rush³⁰
- Neutron Powder Diffraction Studies of LaD_{2+x}**
T. J. Udovic³⁰, Q. Huang^{30,45}, and J. J. Rush³⁰
- Neutron Powder Diffraction Study of $\text{Pd}_9\text{Si}_2\text{D}_x$**
T. J. Udovic³⁰, Q. Huang^{30,45}, J. J. Rush³⁰, Y. Andersson⁵¹, and T. B. Flanagan⁵²
- Neutron Powder Diffraction Study of Isotope Effects in $\text{La}(\text{H}_y\text{D}_{1-y})_{2.50}$**
T. J. Udovic³⁰, Q. Huang^{30,45}, and J. J. Rush³⁰
- Neutron Powder Diffraction Study of $\text{NbD}(\text{H})_x$ ($0.72 \leq x \leq 0.92$)**
B. Hauer¹⁸, R. Hempelmann³⁶, D. Richter¹⁸, T. J. Udovic³⁰, and J. J. Rush³⁰
- Powder Neutron Diffraction Study of the Nuclear and Magnetic Structures of $\text{YBa}_2\text{Fe}_3\text{O}_{8+w}$ ($-0.24 \leq w \leq 0.11$)**
P. Karen⁴⁶, A. Kjekshus⁴⁶, I. Natali Sora³⁸, Q. Huang^{30,45}, V. L. Karen³⁰, A. D. Mighell³⁰, J. W. Lynn^{30,45}, N. Rosov³⁰, and A. Santoro³⁰
- Neutron and X-ray Powder Diffraction Study of $\text{REBa}_2\text{Fe}_3\text{O}_{8+w}$ Phases**
P. Karen⁴⁶, A. Kjekshus⁴⁶, I. Natali Sora³⁸, Q. Huang^{30,45}, V. L. Karen³⁰, A. D. Mighell³⁰, J. W. Lynn^{30,45}, N. Rosov³⁰, and A. Santoro³⁰

Structure and Magnetic Order in Undoped Lanthanum Manganite

Q. Huang^{30,45}, A. Santoro³⁰, J. W. Lynn^{30,45}, R. W. Erwin³⁰, J. A. Borchers³⁰, J. L. Peng⁴⁵, and R. L. Greene⁴⁵

Structure and Magnetic Order in Ca-Doped Lanthanum Manganite

Q. Huang^{30,45}, A. Santoro³⁰, J. W. Lynn^{30,45}, R. W. Erwin³⁰, J. A. Borchers³⁰, J. L. Peng⁴⁵, and R. L. Greene⁴⁵

Neutron and X-ray Diffraction Study of the Crystal Structure of CsTiSi₂O_{6.5}

M. L. Balmer⁴, Q. Huang^{30,45}, W. Wong-Ng⁸, R. S. Roth⁸, and A. Santoro³⁰

Neutron Powder Diffraction Study of the Nuclear and Magnetic Structures of HoNi_{1.985}Co_{0.015}B₂C and HoNiBC

Q. Huang^{30,45}, J. W. Lynn^{30,45}, A. Santoro³⁰, B. C. Chakoumakos²⁷, R. J. Cava²¹, J. J. Krajewski²¹, and W. F. Peck, Jr.²¹

Crystal Structure of Y_{0.95}Ca_{0.05}CuO_{2.54}: A New Oxygen Deficient Perovskite Chemically and Structurally Related to the 123 Superconductor

I. Natali Sora³⁸, Q. Huang^{30,45}, A. Santoro³⁰, R. J. Cava²¹, J. J. Krajewski²¹, and W. F. Peck, Jr.²¹

Redetermination of the Structure of La₂Cu₂O₅ by Neutron Powder Diffraction

N. Khasanova²⁵, F. Izumi²⁵, Z. Hiroi¹⁴, M. Takano¹⁴, Q. Huang^{30,45}, and A. Santoro³⁰

The Structure of MgC₂

Q. Huang^{30,45}, V. L. Karen³⁰, A. D. Mighell³⁰, P. Karen⁴⁶, A. Kjekshus⁴⁶, and A. Santoro³⁰

Structure and Magnetic Order in La_{1-x}Y_xFeO₃ Solid Solution

Q. Huang^{30,45}, P. Karen⁴⁶, V. L. Karen³⁰, A. D. Mighell³⁰, A. Kjekshus⁴⁶, and A. Santoro³⁰

Structure and Magnetic Order in LnCuGaO₄

Q. Huang^{30,45}, R. J. Cava²¹, J. J. Krajewski²¹, W. F. Peck, Jr.²¹, and A. Santoro³⁰

Nuclear Structure Study of La_{2-x}Sr_xNiO₄

Q. Huang^{30,45} and M. K. Crawford¹⁰

Magnetic Order and Crystal Structure in the Superconducting RNi₂B₂C Materials

J. W. Lynn^{30,45}, S. Skanthakumar^{30,45}, Q. Huang^{30,45}, and S. K. Sinha²

Unconventional Ferromagnetic Transition in La_{1-x}Ca_xMnO₃

J. W. Lynn^{30,45}, R. W. Erwin³⁰, J. A. Borchers³⁰, Q. Huang^{30,45}, and A. Santoro³⁰

Crystal Structure of TlSr₂RECu₂O₇ and Related Compounds

W.-H. Li²⁴, K. C. Lee²⁴, J. W. Lynn^{30,45}, C. C. Lai²⁶, H. C. Ku²⁶, and S. Y. Wu²⁴

Crystal Structure of TbBa₂Cu₃O₇

W.-H. Li²⁴, K. C. Lee²⁴, J. W. Lynn^{30,45}, C. C. Lai²⁶, H. C. Ku²⁶, and S. Y. Wu²⁴

Affiliations

- ¹ Air Products and Chemicals, Inc.
- ² Argonne National Laboratory
- ³ Army Research Laboratory
- ⁴ Battelle Pacific Northwest Laboratory
- ⁵ Brookhaven National Laboratory
- ⁶ California Institute of Technology
- ⁷ Cambridge University, UK
- ⁸ Ceramics Division, NIST
- ⁹ C.N.R.S., France
- ¹⁰ E. I. DuPont de Nemours and Company
- ¹¹ E.M.B.L. Grenoble, France
- ¹² Exxon Research and Engineering Company
- ¹³ Federal Highway Administration
- ¹⁴ Institute for Chemical Research, Japan
- ¹⁵ Institut Laue-Langevin, France
- ¹⁶ Institutt for Energiteknikk Kjeller, Norway
- ¹⁷ Johns Hopkins University
- ¹⁸ KFA Jülich, Germany
- ¹⁹ Lab. for Neutron Scattering, Switzerland
- ²⁰ Lawrence Livermore National Laboratory
- ²¹ Lucent Technologies, Bell Laboratories
- ²² Massachusetts Institute of Technology
- ²³ Metallurgy Division, NIST
- ²⁴ National Central University, Taiwan
- ²⁵ Nat'l. Inst. for Res. in Inorg. Matls., Japan
- ²⁶ National Tsing Hua University, Taiwan
- ²⁷ Oak Ridge National Laboratory
- ²⁸ Ohio State University
- ²⁹ Oxford University, UK
- ³⁰ Reactor Radiation Division, NIST
- ³¹ Royal Institution of Great Britain, UK
- ³² SUNY Binghamton
- ³³ Tata Institute of Fundamental Research, India

- ³⁴ Temple University
- ³⁵ Trans-Tech
- ³⁶ Universität des Saarlands, Germany
- ³⁷ University of Bern, Switzerland
- ³⁸ University of Bressica, Italy
- ³⁹ University of California, Davis
- ⁴⁰ University of Constance, Germany
- ⁴¹ University of Dortmund, Germany
- ⁴² University of Geneva, Germany
- ⁴³ University of Le Mans, France
- ⁴⁴ University of Ljubljana, Slovenia
- ⁴⁵ University of Maryland
- ⁴⁶ University of Oslo, Norway
- ⁴⁷ University of Pennsylvania
- ⁴⁸ University of Siegen, Germany
- ⁴⁹ University of Southern California
- ⁵⁰ University of Sussex, UK
- ⁵¹ University of Uppsalla, Sweden
- ⁵² University of Vermont
- ⁵³ W. R. Grace and Company

Surface and Interfacial Studies

With the liquid hydrogen cold source in operation, an increase in usable flux of almost a factor of five has been realized at the NG-7 reflectometer. In addition, the reflectometer originally located in the confinement building on beam tube BT-7 was moved to the guide hall and installed on guide tube NG-1. A similar increase in flux was also obtained. These substantial increases in flux have significantly enhanced the performance of neutron reflectivity measurements of surfaces and interfaces as illustrated in some of the examples described below.

The New Reflectometer at NG-1

As mentioned in the introduction to this section, the reflectometer originally located inside the confinement building on beam tube BT-7 was moved to the guide hall and installed on guide tube NG-1. For this instrument, the reflecting surface of the sample is vertical, in contrast to the horizontal geometry of the reflectometer at NG-7. In addition, on the NG-1 reflectometer the incident beam can be polarized and the polarization of the reflected beam analysed. Instrumental polarizing efficiencies of 97% are typical for reflection from a non-magnetic sample. The polarizers before and after the sample consist of eight $5 \times 7.5 \text{ cm}^2$ Si plates (0.25 mm thick) with Fe/Si supermirror coatings (on both sides), each having a critical angle for the positive spin state of three times that of ordinary Ni, aligned in series for a total length of 81 cm. The polarizers can be used either in reflection or transmission. The polarizing performance quoted above corresponds to that measured in the transmission geometry. As opposed to operation at 2.35 \AA on BT-7, at NG-1 the wavelength is now 4.75 \AA with a Be filter after the last slit before the detector to suppress higher orders. The monochromator consists of fingers of pyrolytic graphite (PG) mounted on a mechanical cam device for vertical focussing. Each finger has a stack of three individual PG

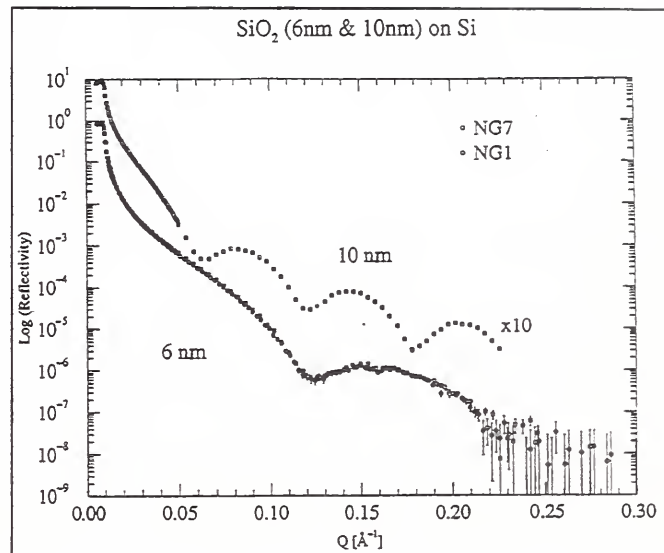


Figure 1. Neutron reflectivity curves for oxide films on Si as measured on NG-7 and NG-1. Note how consistent the data for the same 6 nm oxide film are for the separate instruments. Although measured with the sample in air, reflectivities as low as 1.0×10^{-8} can be measured (the background has been subtracted). With the sample placed in an evacuated environment, the background is reduced by a factor of 20 or more and even lower values of the reflectivity can be measured as shown in Fig. 2.

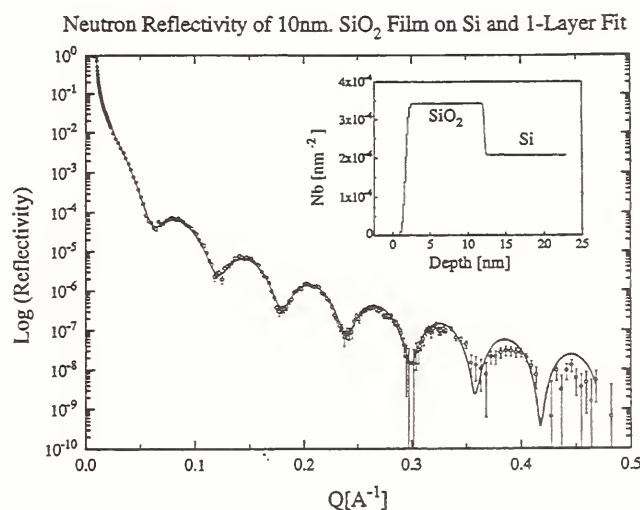


Figure 2. Specular neutron reflectivity data for oxide films on Si as measured on the NG-1 reflectometer with the sample in vacuum.

slabs inclined with respect to one another in a horizontal plane to create an anisotropic mosaic of about one degree so that the wavelength resolution is of the order of a percent. With this vertical focussing and given the twice theta critical angle of Ni coatings on top and bottom guide surfaces, a typical vertical divergence at the sample position is about 2.4 degrees. A pair of slits before and after the sample are fully automated and allow for a constant footprint on the sample as well as a nearly constant resolution dQ/Q as a specular reflectivity scan is performed. The actual beam width at the sample position can be varied from tens of microns up to about 2 cm. Figures 1 and 2 illustrate some of the capabilities of the new reflectometer.

Molecular Beam Epitaxy Chamber for *In-Situ* Neutron Scattering

With the increased flux available from the new liquid hydrogen cold source, reflectivities as low as 10^{-8} have been measured [1], making it practical to investigate reflectivities at higher values of wavevector transfer, Q , with smaller sample volumes, and with higher resolution. This allows studies of thinner films and surface phenomena. As films get thinner, a more significant fraction of the sample volume is contained in the surface contamination layers that occur on all samples exposed to air. Even a monolayer of contamination will disturb many surface phenomena. Thus it is becoming more important to protect a sample's surface using an ultra-high vacuum (UHV) chamber. The Molecular Beam Epitaxy (MBE) Chamber for *In-situ* Neutron Scattering can be used to fabricate single crystal thin films, as a protective UHV environment for both bulk and thin film surfaces, and as an ultraclean environment for loading interstitials, all while performing neutron scattering investigations *in-situ*. MBE is chosen as the thin film growth technique because it produces the purest thin films with the best control of layer thickness and interface widths, and produces the highest quality epitaxial single crystal thin films, heterostructures and su-

perlattices. Although the chamber was designed to go on the NG1 reflectometer, it can also be used on other spectrometers such as triple axis & SANS spectrometers. This is the only combined MBE/neutron scattering chamber in existence. While this chamber has recently been built, and all of its functions are not yet installed, it has already been successfully used for one experiment [2]. A schematic of the chamber appears as Fig. 3.

• Description

Both MBE and neutron reflectivity have very specific and stringent equipment requirements. Also, the types of physics, chemistry, and materials science questions to be investigated add further design constraints. To accommodate these requirements the MBE chamber had to be custom designed with many unique features.

Overall, the chamber has to be light in weight and compact to fit on a variety of spectrometers without overburdening their drive tables. Therefore an ion pump, typical to UHV chambers but very heavy, was replaced by a lighter (2600 L/s) cryopump. With this pump the chamber has achieved a base pressure of 7×10^{-11} torr.

Since the scattered intensity is proportional to sample area, the size of the sample was maximized. The MBE chamber will accept up to 3" diameter samples. The deposition system was engineered to provide better than 2% uniformity in material flux across the substrate to ensure that the thickness of the deposited layers are uniform compared to the resolution of neutron reflectivity. We now have four standard effusion cells that can deposit materials with melting temperatures, $T_m < 1400^\circ \text{C}$. They can be replaced with high temperature effusion cells (providing good flux uniformity of materials with $T_m < 2000^\circ \text{C}$) and electron beam sources (which can deposit higher T_m materials). There is room for 7 effusion cells, or a combination of 5 effusion cells and 2 electron beam sources. Deposition fluxes are monitored with a quartz crystal microbalance. An independent sample

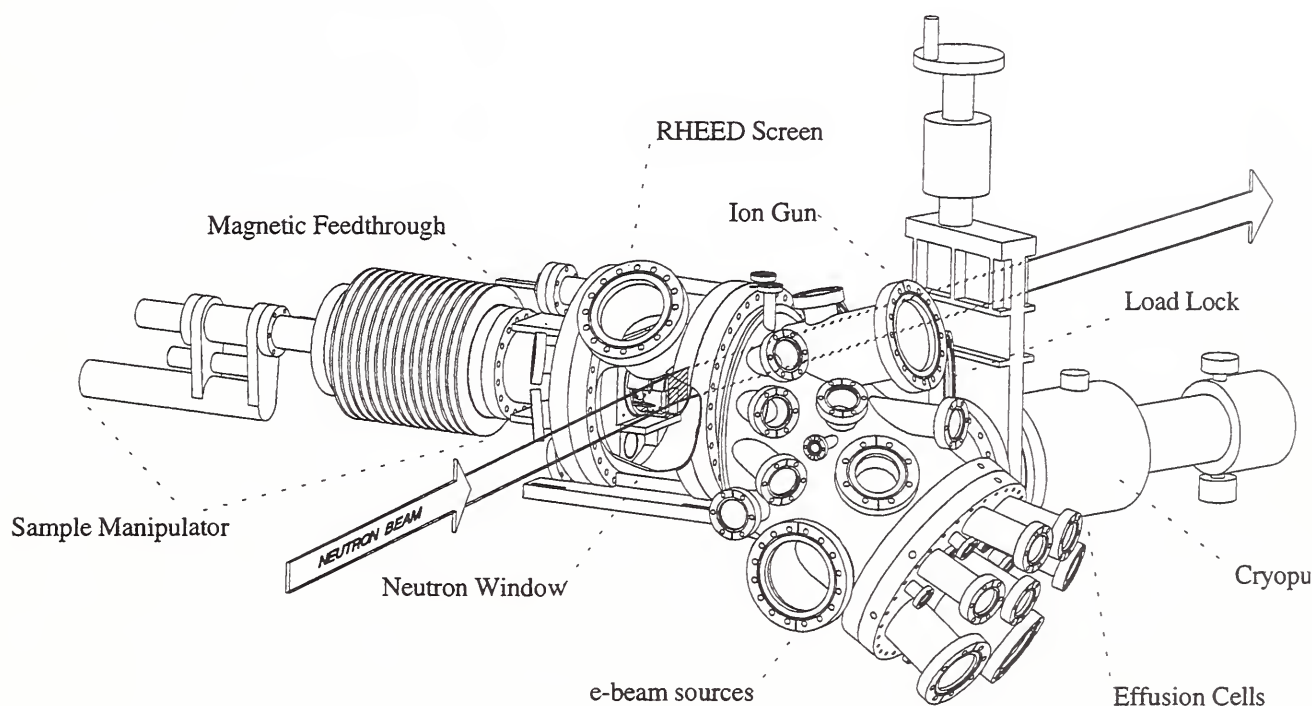


Figure 3. Molecular beam epitaxy chamber for in-situ neutron scattering.

shutter will provide isolation during source calibration, limited sample pattern-masking, and thermal shielding during low temperature operation, and computer controlled source shutters can be used for multilayer growth.

The sample holder is also of custom design, its temperature can be continuously controlled from $\sim 15K$ (to study low temperature magnetic phenomena) to $\sim 1300K$ (required for some substrate preparation and MBE growth). The sample holder is also capable of continuous rotation and *in-situ* 4-point electrical measurements. Various temporary sample holders capable of holding up to 3" diameter substrates and applying temperatures from 77 K - ~ 800 K are currently available.

In addition to growing the samples in the MBE chamber, incompatible samples can be

grown elsewhere and cleaned *in-situ* with a 3 cm flood ion gun. The ion gun will also allow surface cleaning of substrates before growth, dry etching, ion assisted MBE, and reactive growth of oxides, nitrides, etc. The chamber also has a gas loading system with a leak valve and capacitance manometers capable of measuring pressures from $10^3 - 10^{-5}$ torr. Accurate gas introduction will allow *in-situ* intercalation and hydrogen loading.

The neutron window is a 25.4 cm diameter aluminum cylinder. This shape will allow grazing angle neutron diffraction measurements at nearly any azimuthal angle. The length of the cylinder, 11.43 cm, allows an incidence angle of up to 39° , or $Q = 1.66 \text{ \AA}^{-1}$, at the neutron wavelength $\lambda = 4.75$ used at the NG1 reflectometer. A Reflection High Energy Electron Diffraction

(RHEED) system is incorporated in this section. RHEED is used to study surface morphology and crystallography and determine thin film growth rates.

To use polarized neutrons, one must apply a uniform magnetic field at the sample. To move the magnetic field source to outside the vacuum vessel, a pair of ARMCO #1008 steel pole pieces were welded into the sample flange to serve as a "magnetic feedthrough", a device unique to this MBE chamber. A magnetic field is applied to the external portion of the feedthrough. Inside the chamber the pole pieces "dog-leg" toward each other, helping to concentrate the magnetic field lines at the sample position, providing a uniform flux.

The MBE chamber was designed to be very flexible in its uses, and many spare ports were included to allow for future expansion. Expansion possibilities include a quadrupole mass spectrometer (for more accurate flux monitoring and thermal desorption measurements), an optical pyrometer (for more accurate determination of high substrate temperatures), a load lock chamber (allowing quick sample exchange without breaking the vacuum thus eliminating the lengthy bakeout process required for recovery of UHV) and a UHV sample transfer vessel (to allow sample transfer to other growth or analysis chambers). It is also possible to include devices for ellipsometry, SMOKE (surface magneto-optical Kerr effect), low energy electron diffraction with Auger spectroscopy (for in-plane crystallography and surface compositional analysis, respectively), or XPS (x-ray photoelectron spectroscopy).

• Applications

The versatility of both the neutron reflectivity and the MBE techniques as well as the versatility of this combination neutron scattering/MBE chamber lead to a wide variety of possible scientific applications, some of which are listed below:

- Studies of Hydrogen in Materials
- Surface Magnetism and Artificial Magnetic Structures
- Si/SiO₂ Interface Structure And Oxidation
- Epitaxial Growth of Organic Molecules: Biological and Polymer Systems
- Surface Chemistry-Catalysis
- Epitaxial Studies
- Critical Phenomena
- Diffusion Studies
- Direct Inversion of Data (by growth of reference layers on top)
- Studies of Hydrophilic and Other Sensitive Materials

• Conclusion

The MBE Chamber for *In-Situ* Neutron Scattering had to be custom designed due to the specific and stringent requirements of both MBE and neutron reflectivity. Thus, it has a large number of unique features which give rise to numerous new capabilities. The combination of the world class low levels of reflectivity (10^{-8}) achievable at the NG1 reflectometer and the versatility of the MBE chamber will open up a vast array of new opportunities for scientific research.

References

- [1] J. A. Dura, C. A. Richter, C. F. Majkrzak, "Neutron Reflectivity characterization of Thin SiO₂ films for Applications as Next Generation Standard Reference Materials" (work in progress), see also "Vertical Sample Reflectometer" in this volume.
- [2] Hydrogen Induced Changes in the Magnetic Ordering of Fe-V (001) Superlattices in this volume.

Hydrogen Induced Changes in the Magnetic Ordering of Fe-V (001) Superlattices

In some metallic multilayers consisting of thin magnetic layers and non-magnetic spacer layers, the magnetic layers will align either parallel to each other (ferromagnetically) or anti parallel (antiferromagnetically, or AFM), de-

pending on the thickness of the spacer layer. The coupling is RKKY-like and oscillates between these two alignments with a period that is inversely proportional to the fermi wavevector, k_f . However, the basic mechanisms that cause this coupling are still not completely understood. Theoretical models are tested primarily by comparing predictions to measured coupling strengths as a function of the spacing layer thickness, in integral numbers of monolayers (ML), and as a function of the element that comprises the spacer (and thus k_f). Both variables are then discrete. Some measurements have been done on alloys in order to continuously change the composition, and to some degree the thickness of the spacer layer. However, this method is tedious in that it requires the production of a larger number of separate samples, each with the same crystal quality, regardless of the fact that the constituent elements are changing, thereby possibly altering the optimal growth conditions. On the other hand, by using a spacer layer such as vanadium that readily absorbs large quantities of hydrogen thereby expanding its lattice, one can continuously vary the thickness of the spacer layers throughout a range equivalent to more than one monolayer. Also, hydrogen loading has the potential to change the electronic structure. Therefore H-loading is a powerful tool to continuously tune both layer thickness and electronic structure and study their effects on the antiferromagnetic coupling.

Recently, AFM coupled Fe/V (001) superlattice have been produced with a high crystal quality. The hydrogen is found to reside exclusively in the V lattice and is found to cause a completely reversible lattice expansion of the V layers up to 10%. The magnetic character of Fe/V superlattices was determined by SQUID magnetometry measurements. As seen in Fig. 4, for a series of samples in which the Fe thickness was held constant at 3ML and the V thickness varied, the largest AFM coupling strength is found in Fe(3ML)-V(14ML) samples. Considering the lattice expansion effects alone, adding H to the Fe3/V14 sample would diminish the ex-

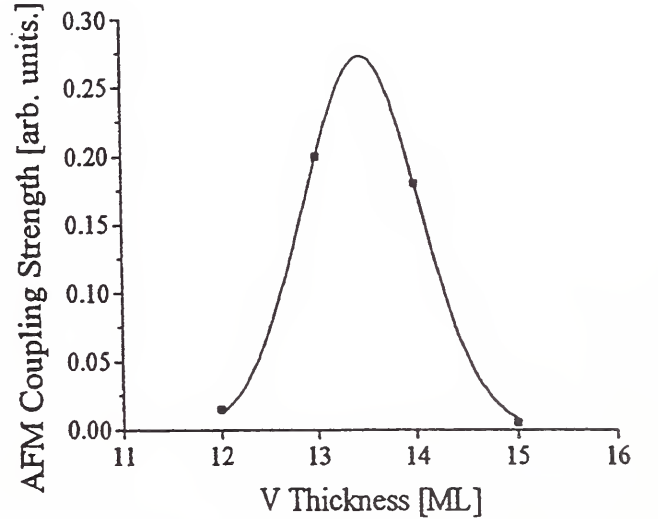


Figure 4. AFM coupling strength at different thicknesses of the spacer layer (in monolayers). The line is drawn to guide the eye.

change coupling while adding H to the Fe3/V12 sample would increase the V thickness toward the ideal 14ML and increase the coupling.

Polarized neutron reflectivity measurements were made on the NG1 Reflectometer on these two samples in the Molecular Beam Epitaxy Chamber for *In-Situ* Neutron Scattering[1]. Measurements were made in a field of ~ 100 Oe, under hydrogen pressures from 700 torr to 10^{-3} torr and under ultra high vacuum, with and without heating (which removes residual hydrogen). For the vacuum and fully loaded cases reflectivity measurements were taken out to a Q beyond the first ferromagnetic peak location. Two features are of interest, and were concentrated on in a majority of the measurements. First, the net magnetization in the direction of the applied field can be inferred from the difference between the $(+,+)$ and $(-,-)$ intensities of the ferromagnetic peak (which occurs at $Q_{FM} = 2\pi$ the superlattice repeat distance). Second, the antiferromagnetic coupling strength is indicated by the intensity of the spin flip components $(+,-)$ and $(-,+)$ of the antiferromagnetic peak, at $Q_{AFM} \simeq Q_{FM}/2$ corresponding to the doubling of the unit cell.

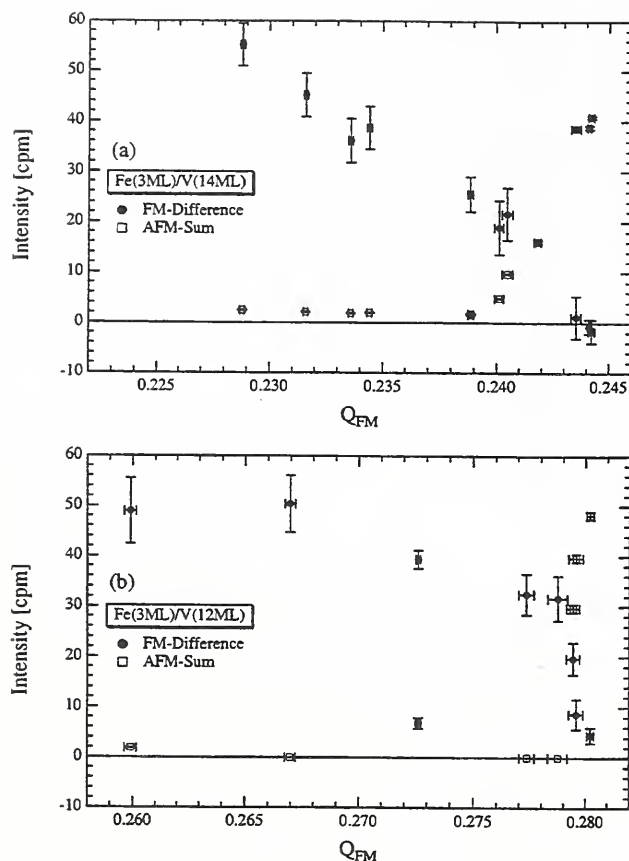


Figure 5. The sum of the intensities of the two spin flip components from the AFM peak and the difference between the non-spin flip components of the ferromagnetic peak as a function of Q of the ferromagnetic peak. Figure 5a is for the Fe3V14 sample and 5b is for the Fe3V12 sample.

In Figs. 5a and 5b we plot both these features for the Fe(3ML)/V(14ML) and Fe(3ML)/V(12ML) samples respectively as a function of Q_{FM} . In these plots, as more H is added the V lattice expands, reducing the Q value to lower values. Therefore the data on the right corresponds to the samples heated under UHV to remove all hydrogen whereas the data on the left of the figure is for a H_2 loading pressure of 700 torr. In both cases a clear transition is seen from an antiferromagnetically coupled state for low H content to one with no antiferromagnetic coupling and a large net magnetization as hydrogen is added. The two samples differ

in that the transition in the Fe(3ML)/V(12ML) sample occurs much more sharply, and at lower H content. The transition occurs at a change in the V layer thickness of 0.58 Å or an H:V ratio of 7.9% in the Fe(3ML)/V(14ML) sample, and a change in the V layer thickness of 0.12 Å or an H:V ratio of 1.8% in the Fe(3ML)/V(12ML) sample. The quicker removal of the antiferromagnetic state in the Fe(3ML)/V(12ML) sample is consistent with the SQUID results which show that the antiferromagnetic coupling is much weaker in this sample. However it is inconsistent with the behavior expected strictly from an expansion of the lattice, which should push the Fe(3ML)/V(12ML) to the left in Fig. 4, toward stronger coupling. Also, in comparison to Fig. 4, the extremely small change in the V spacer layer thickness of the Fe(3ML)/V(14ML) is much less than the amount required to significantly reduce the coupling, and therefore would not account for the loss of the AFM coupling. Alternative explanations for the loss of AFM coupling are: 1) H induced changes in the electronic structure which alter the fermi wavevector; 2) inhomogeneous strain; and 3) H concentration at grain boundaries in the V layers acting as a conductive bridge and directly coupling the ferromagnetic Fe layers. This work is still in progress. We will begin by investigating samples to the right of the resonance in Fig. 4 to probe if explanation #1 is valid. To investigate explanation #3 we can compare the amount of H in the V layers as measured by both the superlattice intensity and nuclear reaction measurements to the amount of H in the V lattice as inferred from the lattice expansion.

[1]B. Hjörvarsson, J. A. Dura, P. Isberg, T. Watanable, T. J. Udovic, G. Andersson, C. F. Majkrzak, in preparation.

Location of Peptides in Alkanethiol/Phospholipid Biomimetic Bilayer Membranes

Neutron reflectivity is being used to probe the structure of peptides associated with biomimetic bilayer membranes in aqueous solu-

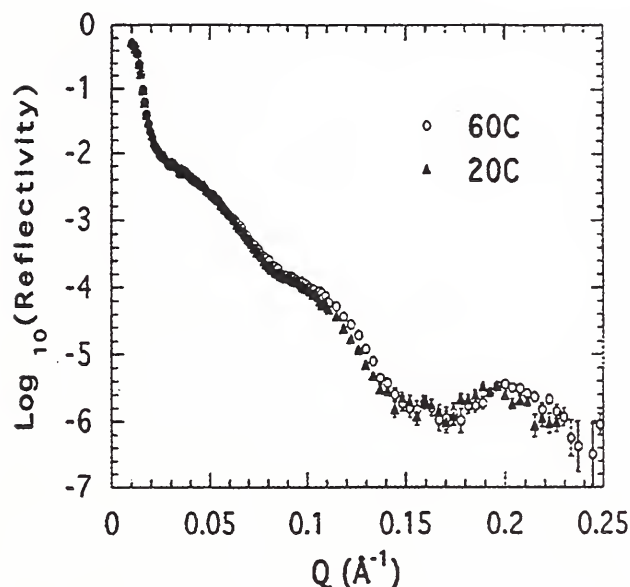


Figure 6. $\text{Log}_{10}(\text{reflectivity})$ vs Q from a $\text{C}_{18}\text{SH}/\text{DPPG}$ HBM in D_2O at 60°C (fluid phase) and at 20°C (gel phase). A small ($1 - 2 \text{ \AA}$) decrease in the DPPC monolayer thickness was detected in the fluid phase.

tion in collaboration with scientists from NIST's Biotechnology Division. A single hybrid bilayer membrane (HBM), consisting of one monolayer of alkanethiol and one monolayer of phospholipid, is formed on a silicon substrate, coated with 50 \AA gold on a chromium adhesion layer, using a modified Langmuir-Blodgett technique. Since the alkanethiol monolayer is strongly bonded to the gold surface, this HBM is more rugged than a conventional supported bilayer, which binds only weakly to a silicon surface. The phospholipid monolayer is in contact with an H_2O or D_2O solution, making it possible for the HBM to support active membrane proteins. Thus, HBMs are commercially significant for a number of applications including biosensors, tissue engineering, bioelectronics and biocatalysis.

Specular reflectivity measurements are sensitive to changes in overall bilayer thickness to within $1 - 2 \text{ \AA}$. To illustrate this, an HBM of octadecanethiol (C_{18}SH) and DPPC was mea-

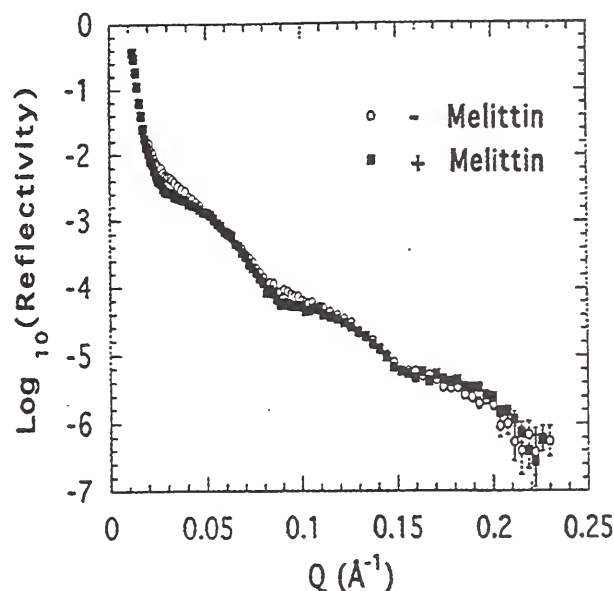


Figure 7. $\text{Log}_{10}(\text{reflectivity})$ vs Q from a $\text{C}_{18}\text{SH}/\text{d}(54)\text{-DMPC}$ HBM in D_2O in the presence (+) and absence (−) of melittin, a pore-forming toxin which is active in HBMs. The data show qualitatively that melittin serves to change the contrast of the HBM relative to the D_2O but has relatively little influence on its total thickness. This suggests that melittin penetrates at least partially into the HBM.

sured at NIST's BT7 reflectometer in D_2O at 20°C , corresponding to DPPC's gel phase, and at 60°C , corresponding to its fluid phase. In the fluid phase, the acyl chains in the DPPC monolayer are disordered and move more freely than in the gel phase. Thus, the DPPC monolayer is less rigid, and possibly slightly smaller by $1 - 2 \text{ \AA}$, in the fluid phase than in the gel phase. Fig. 6 shows that this small change in thickness of the DPPC monolayer is detectable by specular reflectivity measurements. The minimum in the 60°C data is located at a slightly higher Q value than that in the 20°C data, indicating that the HBM is slightly smaller in the fluid phase than in the gel phase.

It is possible to determine from the specular reflectivity measurements the neutron scattering length density (SLD) profile of the HBM as a function of depth perpendicular to the bilayer surface. Since the SLD of both the lipid

head group and the hydrocarbon chain are significantly different from that of most peptides, the insertion of a peptide into the bilayer would change the SLD in the layers in which it is located, thus changing the specular reflectivity curve. Melittin, a pore-forming toxin often used as a model for other similar peptides, was chosen for the initial reflectivity measurements. An HBM of C₁₈SH and d(54)-DMPC was measured in D₂O and in D₂O containing melittin. Changes in the reflected intensity as a function of incident angle were clearly seen with the addition of melittin, as shown in Fig. 7. Since the maxima in the reflectivity curves occur at approximately the same Q - values in both cases, little or no change in bilayer thickness occurs upon the insertion of the melittin. Representative neutron SLD profiles obtained by a model-independent fitting method[1] are shown in Fig. 8. Differences in the SLD profiles indicate that melittin penetrates partially into the HBM, at least as far as the acyl chain region of the d(54)-DMPC monolayer.

Although melittin is often used in model biological membranes, its exact location in the bilayer is not well known. These measurements provide important verification of penetration into the HBM. Higher resolution measurements, which are currently being performed on the new NGI reflectometer, should result in a more exact determination of the location of melittin and other peptides in this model membrane system.

Reference

- [1]N. F. Berk and C. F. Majkrzak, Phys. Rev. B 51, 11296 (1995).

Interlayer Coupling in Annealed Ni-Fe/Cu Multilayers

Recent studies of giant magnetoresistance (GMR) in electron-beam evaporated Permalloy/copper (Ni-Fe/Cu) multilayers suggest that this system may be a viable candidate for ultrahigh density recording applications[1,2]. These multilayers exhibit several desirable properties including low remanence, exceptionally small

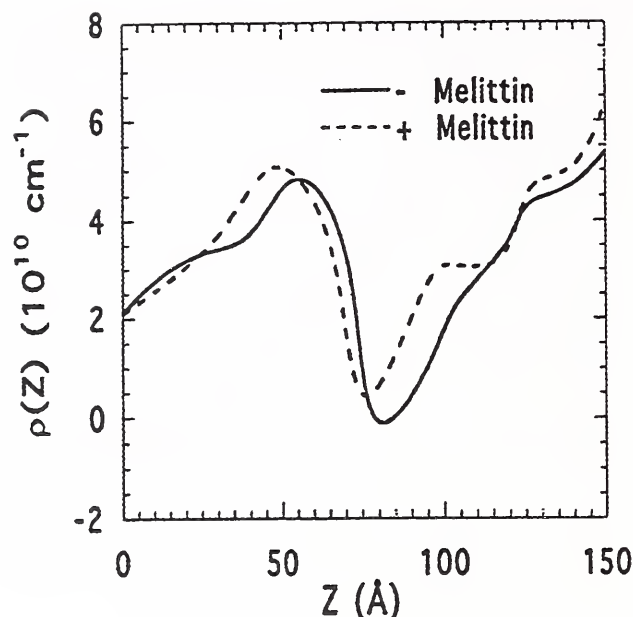


Figure 8. Representative neutron SLD profiles obtained from model-independent fits to the data in Fig. 7. The profiles for the sample with melittin consistently show a higher SLD in the acyl chain region of the d(54)-DMPC, indicating that melittin penetrates at least into this region. High resolution measurements are necessary to further pinpoint its location.

hysteresis, temperature stability up to 350°C, and an insensitivity of the GMR over a broad range of Cu and Ni-Fe layer thicknesses. Resistivity and magnetization measurements show that the magnetoresistance ($\Delta R/R$) increases from < 0.3% to 4.5% following a post-deposition heat treatment at 325°C. Inspection of the hysteresis curves suggests that the interlayer coupling changes from ferromagnetic to antiferromagnetic as a direct consequence of annealing. X-ray diffraction studies of related materials reveal that the interdiffusion at the Ni-Fe/Cu interfaces is more extensive in annealed samples[3,4].

To determine the intrinsic interlayer coupling of these Ni-Fe/Cu multilayers, we performed polarized neutron reflectivity (PNR) experiments on the BT-7 reflectometer and measured all four spin cross sections, (++),

(--), (+-) and (-+) as a function of field applied in-plane. We examined four samples that were diced from one wafer of composition $[\text{Cu}(37\text{\AA})|\text{Ni}_{83}\text{Fe}_{17}(27\text{\AA})]_{10}/\text{SiO}_2(5000\text{\AA})/\text{Si}$ with (111) preferred orientation. Three of these were subjected to different heat treatments (annealing at 275, 300, and 325°C for two hours)[5,6].

We first characterized each sample in a small remanent field. Figure 9 shows PNR data for the 325°C annealed multilayer. The (++) and (--) cross sections are effectively equal at the first-order superlattice peak position, but they differ at the half-order position ($Q_z = 0.056 \text{ \AA}^{-1}$). In addition, a peak is observed at half-order in the (+-) and (-+) data. All of the half-order magnetic scattering disappears upon saturation in a field of 2 kOe. Thus, in low fields, the Ni-Fe layer moments are coupled antiferromagnetically along the growth direction. The presence of magnetic scattering in all four cross sections means that the Ni-Fe moments have projections parallel and perpendicular to the applied field within the sample plane. However, we can only account for roughly one-third of the bulk Ni-Fe moment in our preliminary fits (solid and dashed lines in Fig. 9).

After correcting the reflectivity data for instrumental background contributions and for polarization efficiencies, a smooth ridge of scattering remains at small Q_z in the (+-) and (-+) cross sections (Fig. 9) and may account for some of the "missing" Ni-Fe spins. We can simulate this feature by assuming that the Ni-Fe layer moments are randomly tipped from the antiparallel orientation. In reality, the spins responsible for this scattering may reside only in the interfacial alloy regions.

Low-field (-0.2 Oe) specular data for the 300 °C annealed sample also show an antiferromagnetic reflection, but it is quite broad. This anneal temperature is apparently sufficient to induce short-range antiferromagnetic order along the growth-axis. We do not observe a peak at half-order for the as-deposited and 275 °C annealed samples. These data are suggestive of

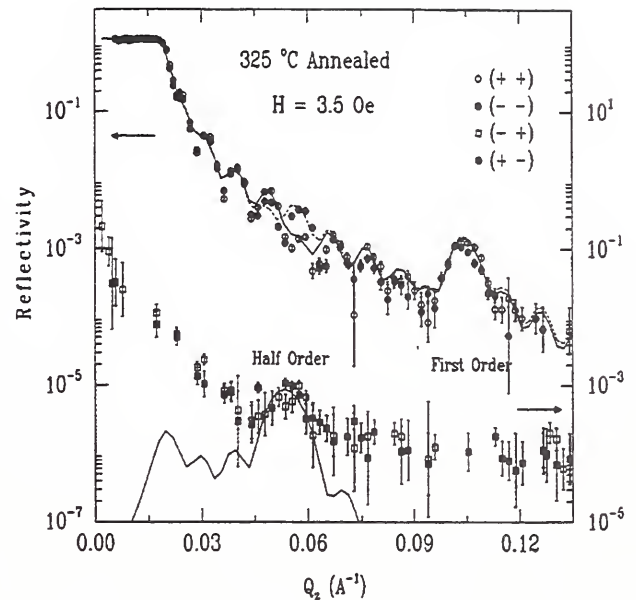


Figure 9. Polarized neutron reflectivity of the 325°C annealed sample in a field of 3.5 Oe after application of a 150 Oe field. The data have been corrected for background contributions and polarization efficiencies. The open and shaded circles designate the (++) and (--) cross section respectively, and the open and shaded squares mark the (+-) and (-+) cross sections. The arrows point to the appropriate vertical axis for each set of cross-sections.)

ferromagnetic interlayer coupling.

Our PNR results demonstrate that the low-field magnetic structures of the as-deposited and 275 °C annealed multilayers are different from those of the 300 and 325 °C annealed samples. Questions remain regarding the mechanism responsible for switching the coupling from ferromagnetic to antiferromagnetic as a consequence of annealing. Cross-sectional TEM analysis shows that the as-grown Ni-Fe/Cu sample is composed of small (150 – 300 Å) grains[2]. It is thus possible that the Cu migrates into the nominal Ni-Fe layers upon heating to form flat Ni-Fe platelets separated by Cu columns, analogous to Ni-Fe/Ag multilayers[5,6]. Theoretical models [5,7] demonstrate that magnetostatic interactions between these platelets could possibly lead to weak antiferromagnetic coupling. Alternately, the as-grown samples might have "pin-

holes" through the Cu that connect the Ni-Fe layers,[8] especially if the evaporated Cu layers are thin[2]. It is possible that annealing reduces the pinhole density, thereby unmasking [9] any intrinsic RKKY-like exchange coupling that may exist between the Ni-Fe layers.

In either case, identification of the interlayer coupling mechanism will require additional characterization of the structural and magnetic properties of these Ni-Fe/Cu multilayers. Specifically, we plan to characterize the diffuse magnetic scattering, evident in preliminary transverse- Q scans, taking advantage of the new, higher-flux NG-1 reflectometer.

Reference

- [1]N. Smith, A.M. Zeltser, and M.R. Parker, IEEE Trans. Mag. **32**, 135 (1996).
- [2]A. M. Zeltser and N. Smith, J. Appl. Phys. **79**, 9224 (1996).
- [3]J.A. Borchers, P.M. Gehring, C.F. Majkrzak, J.F. Ankner, A.M. Zeltser and Neil Smith, J. Appl. Phys. (in press).
- [4]V.S. Speriosu, J.P. Nozieres, B.A. Gurney, B. Dieny, T.C. Huang and H. Lefakis, Phys. Rev. B **47**, 11579 (1993).
- [5]J.A. Borchers, P.M. Gehring, R.W. Erwin, J.F. Ankner, C.F. Majkrzak, T.L. Hylton, K.R. Coffey, M.A. Parker and J.K. Howard, Phys. Rev. B **54**, 9870 (1996); J. Appl. Phys. **79**, 4762 (1996).
- [6]T.L. Hylton, K.R. Coffey, M.A. Parker and J.K. Howard, Science **261**, 1021 (1993); J. Appl. Phys. **75**, 7058 (1994).
- [7]J.C. Slonczewski, J. Mag. Magn. Mater. **129**, L123 (1994).
- [8]B. Dieny, V.S. Speriosu, S. Metin, S.S.P. Parkin, B.A. Gurney, P. Baumgart and D.R. Wilhoit, J. Appl. Phys. **69**, 4774 (1991).
- [9]J.F. Bobo, H. Fisher and M. Piecuch, MRS Sym. Proc. **313**, 467 (1993).

The Magnetic Structure of Cr in Fe/Cr(001) Superlattices

Polarized neutron reflectivity and diffraction measurements, in collaboration with scientists

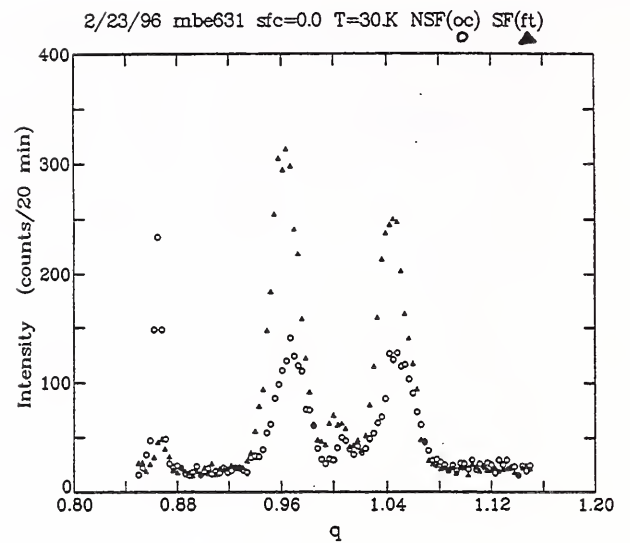


Figure 10. Polarized neutron scattering from the Cr antiferromagnetic structure at high angles, mid-way ($q = 1.0\text{\AA}^{-1}$) between the origin and the (002) Bragg peak in reciprocal space. (The sharp peak to the extreme left is not associated with the Cr magnetic structure.) The non-spin-flip scattering (open circles) is due to projections of the Cr moments parallel to the minimal magnetic field applied vertically and perpendicular to the scattering vector. The spin-flip scattering (filled triangles) arises from the horizontal projections of the Cr moments (but which are also perpendicular to the scattering vector). Two separate peaks appear, split about $q = 1.0\text{\AA}^{-1}$, due to the periodicity of the superlattice.

at the Ruhr-Universitat in Bochum, Germany, have been performed on Fe/Cr superlattices to determine: 1) the magnetic structure of the Cr layers; and 2) whether there exists a correlation between the magnetic state of the Cr and the relative orientation of the ferromagnetic Fe layers which can be parallel, antiparallel, or even non-collinear. The Fe/Cr system is prototypical of multilayers in which the magnetic interlayer coupling between ferromagnetic slabs is associated with a "giant" magnetoresistance effect, of fundamental scientific interest and potential technological application in the magnetic storage of information. The neutron scattering experiments are particularly revealing and straightforward to interpret given that the magnetic configuration of the Fe layers is manifest at low scat-

tering angles whereas that of the intervening Cr is evident at relatively high angles because of the inherent antiferromagnetic coupling between its ferromagnetic (001) atomic planes. With polarized neutron beams, it is possible to determine the relative directions of the Fe and Cr moments and thereby deduce any correlation between the magnetic structures of the two different materials. Polarized neutron diffraction data obtained on SPINS, such as that shown in Fig. 10, have helped demonstrate that the relative orientation of the Fe layers is in fact determined by the magnetic structure of the Cr interlayers. Although much has already been learned about this dependence, more work needs to be done to map out a complete phase diagram for different layer thicknesses as a function of temperature and applied magnetic field.

Block Copolymer Films on Brushes: Controlling Lamellar Wetting

It is well known that thin films of lamellar block copolymers typically form with the lamellae oriented parallel to the substrate and the free surface of the film. One of the two blocks is adsorbed to each interface during the early stages of annealing, and these adsorbed monolayers in turn induce the formation of successive parallel lamellae throughout the film. The total film thickness t is then quantized in integer or half-integer multiples of the bulk lamellar period L , $t = nL$ or $(n + 1/2)L$ (for symmetric and asymmetric boundary conditions, respectively), resulting in the striking and ubiquitous phenomenon of island and hole formation at the free surface.

It is of interest both scientifically and for potential applications to be able to specify at will *which* block of a diblock copolymer will adsorb to a substrate, by modifying the substrate's surface in some fashion. One seemingly obvious way to achieve this is to coat the substrate with a layer of end-grafted chains having the same chemical composition as the block which we desire to adsorb to the substrate, i.e. to form a polymer brush. Neu-

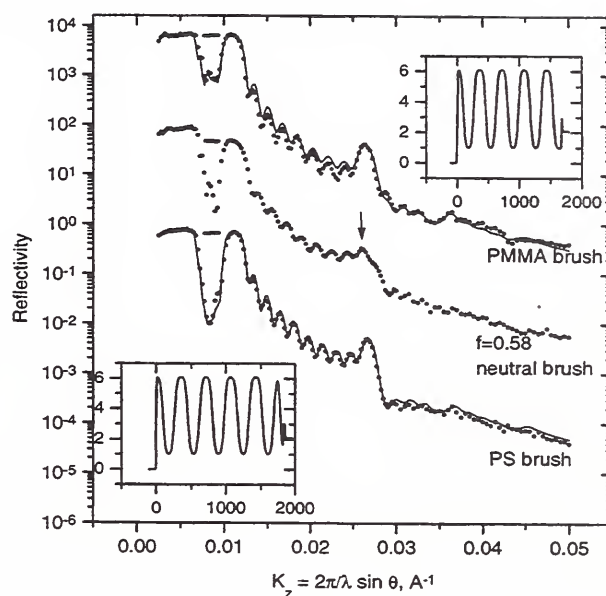


Figure 11. Neutron reflectivity for PS-PMMA films on different brushes.

tron reflectivity and optical microscopy studies show that this technique is indeed effective. Polystyrene and poly(methylmethacrylate) brushes ($M_w = 10,000$ gm/mol) were formed on native oxide-covered silicon wafers by grafting of end-functionalized chains from the melt and rinsing away unreacted chains with toluene. The resulting brushes have a dry thickness measuring 5-6 nm. Films of P(dS-b-MMA) ($M_w = 50,000$ gm/mol) were spin coated on top of these, and the samples were annealed at 170 C for two days.

Figure 11 shows typical neutron reflectivity data for these samples. Clear differences between the data sets (points) are apparent, especially in the region between the critical edge and the first Bragg peak. The data can be quite satisfactorily fit (solid lines) using a simple alternating slab model, with layers of half the usual thickness adjacent to the substrate and free surface. Layers are also included in the model to represent the brush and the native oxide layer. As expected, the fits show that the layer adjacent to the PS brush is composed of dPS, and the layer adjacent to the PMMA brush is composed

of PMMA. The top layer, adjacent to the vacuum interface, is composed of PS in both cases.

A more interesting question is raised when one considers the possibility of tuning the selectivity of the surface in a continuous fashion, from PS-preferential to PMMA-preferential. This can be achieved by grafting P(S-r-MMA) copolymers to the substrate, and controlling the styrene monomer fraction f . Since there is always a preference for PS at the free surface, and it is not possible to create a substrate which is perfectly neutral (although one can get quite close to this situation), one might expect that the lamellae would remain parallel to the substrate for all values of f , and that there would be a sharp transition in the wetting behavior at a critical value of f , from PS adsorption to PMMA adsorption at the substrate.

Experiments yield a quite different result. The data for $f = 0$ and $f = 0.3$ are virtually identical to each other, as are the data for $0.65 < f < 1.0$, and correspond to the simple cases of PMMA and PS adsorption at the substrate, respectively. In the range $0.5 < f < 0.58$, however, the data appear quite different, in that the first and third order Bragg peaks are strongly suppressed. This indicates that there has been a partial (but not complete) loss of ordering in the direction normal to the substrate. When the same set of samples ($0 < f < 1$) are studied by SANS at normal incidence, those samples showing suppressed Bragg peaks in reflectivity show a sharp scattering ring in SANS; while those samples exhibiting strong Bragg peaks in reflectivity give featureless SANS data. This supports the model shown in Fig. 12 for the structure of the samples with $0.5 < f < 0.58$: lamellae are oriented parallel adjacent to the air surface, and perpendicular adjacent to the substrate. The structure of the interface between these two regions is not known, and a possible configuration is shown schematically in the figure. Electron microscopy studies are planned to test the above interpretation of the neutron data.

Alteration of the substrate properties also has a dramatic affect on island and hole forma-

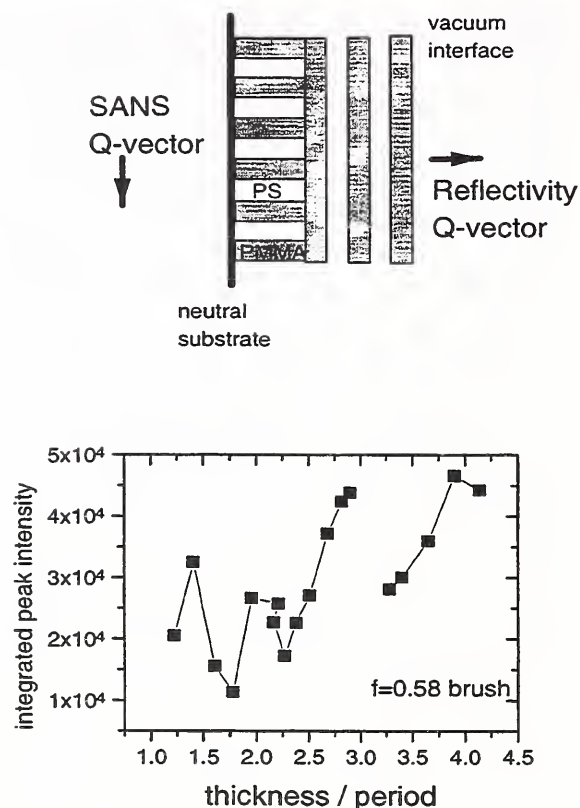


Figure 12. Model for PS-PMMA film on a $f = 0.58$ (PS-r-PMMA) random copolymer brush. Both parallel and perpendicular lamellae are formed. In the bottom portion, intensity of SANS ring as function of sample thickness is shown for $f = 0.58$ sample

tion. Samples which adsorb PS have the thickness quantized as $t = nL$, while those adsorbing PMMA have $t = (n + 1/2)L$. Thus the same initial film thickness will give different surface coverages of islands for these two cases: a film thickness which is perfectly commensurate in one case, yielding a flat surface, is maximally incommensurate in the other case, yielding 50% island/hole coverage. That this is the case can easily be observed in a reflection optical microscope. Optical microscopy also shows that PS-adsorbed and PMMA-adsorbed samples exhibit different sets of interference colors, corresponding to the different sets of allowed thicknesses.

Most striking of all is that copolymer films formed on nearly neutral surfaces, which have lamellae standing on end adjacent to the sub-

strate, *do not exhibit island and hole formation at all* for thickness of about $2L$ or greater. The “extra” thickness beyond a commensurate value is taken up by the layer of vertical lamellae, whose height is unconstrained, rather than being distributed into islands on the surface. Figure 12 shows the intensity of the normal incidence SANS ring as a function of film thickness, for copolymer films on a $f = 0.58$ brush. For $t/L > 2$, the scattering intensity undergoes a series of sawtooth-like oscillations. The height of the vertical lamellae layer increases with the film thickness, until the film is thick enough to accommodate another horizontal layer; at this point, the vertical layer is reduced in thickness by L .

Surface-Induced Phase Segregation in Disordered Diblock Copolymers

Above the order-disorder transition, an A-B diblock copolymer possesses no long range order in the bulk; the average volume fraction of each component is spatially uniform. An interface with the vacuum or a solid surface induces ordering in the vicinity of the surface, via preferential interactions with one of the two blocks. The local volume fraction of component A in a disordered A-B diblock thin film has the form

$$\Phi_A(z) = \langle \Phi_A \rangle + A_1 \exp(-z/x) \cos(2pz/L) + A_2 \exp(-(d-z)/x) \cos(2p(d-z)/L).$$

The amplitudes A_1 and A_2 are the excess volume fraction of component A adjacent to the two surfaces of the film at $z = 0$ and $z = d$. $\Phi_A(z)$ undergoes damped oscillations near the film surfaces, with period L and decay length x . (We are describing the case of films with thickness $d \gg x$, so that the two surfaces are independent). Equation (1) was first derived theoretically by Fredrickson, and has been confirmed by neutron reflectivity for a number of systems. For P(dS-b-MMA) diblocks on silicon oxide substrates, the styrene block segregates to the vacuum interface due to its lower surface tension, while the PMMA block wets the silicon oxide

surface due to its more polar character. Thus the amplitudes A_1 and A_2 have opposite signs.

Fredrickson's calculation also predicts that the oscillation amplitudes A_i are proportional to the strength of the surface potentials which induce the surface ordering. This has not been tested because the degree of segregation is fixed for a given substrate; there has been no method available for varying (and measuring) the surface potential at will. Our group has recently developed a simple but effective strategy for controlling the interactions of polymers with solid substrates. As described in the preceding report, P(S-r-MMA) random copolymers ($M_w = 10,000$ gm/mol) are synthesized with various styrene monomer fractions f , and end grafted to native-oxide covered silicon wafers to form random copolymer brushes 5-6 nm thick. As f is varied from 0 to 1 (PMMA brush to PS brush), the interfacial energies of PS and of PMMA with the modified surface vary in opposite directions, and become equal at approximately $f = 0.55$. The latter case is termed a “neutral surface”. We describe here the results of a neutron reflectivity study of surface induced phase segregation in disordered P(dS-b-MMA) diblock copolymers ($M_w = 32,000$ gm/mol) in contact with random copolymer brushes.

Samples were prepared by spin coating 200 nm films of the diblock onto a series of silicon substrates, which had previously been coated with end-grafted random copolymer layers having styrene fractions f ranging from 0 to 1. The samples were annealed at 150°C in vacuum for one day, and reflectivity measurements were made at room temperature on the NG7 reflectometer. Reflectivity data for the samples prepared on $f = 0$ and $f = 1$ brushes (PMMA and PS, respectively) are shown in Fig. 13. Pronounced differences between the two data sets are apparent, in the vicinity of the quasi-Bragg peak near $K_z = 0.0135$. The points are the data, and the lines are the results of fits done using the model described above; the best-fit scattering length density profiles are shown in Fig. 13. While the composition oscillations at the vac-

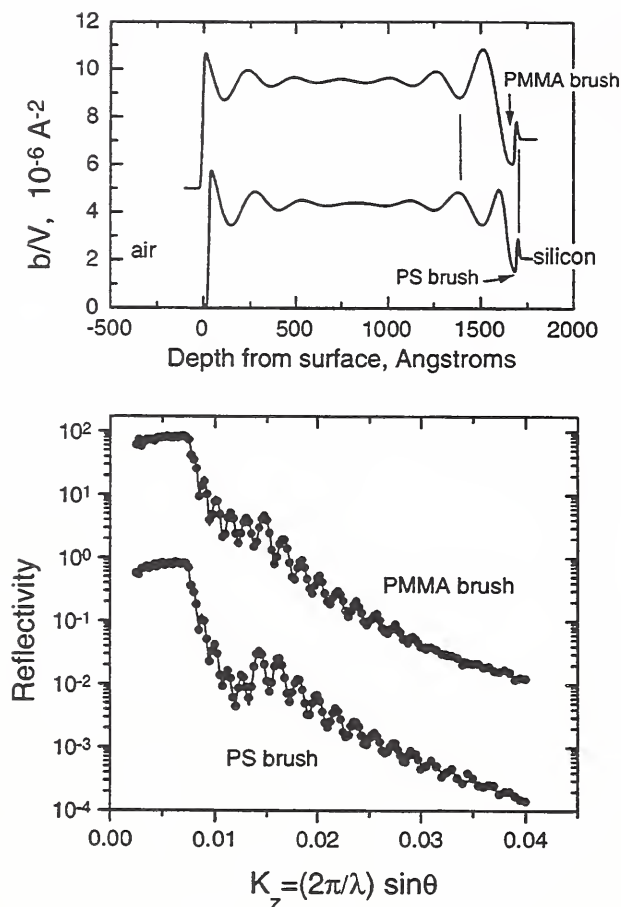


Figure 13. Neutron reflectivity and fits for PS-PMMA films on $f = 0$ and $f = 1$ copolymers brushes. Scattering length densities used to fit the data are shown in the upper portion.

uum interface in both samples are nearly identical, those originating at the substrate are 180 degrees out of phase with each other. This is because the wetting layer adjacent to the brush is composed of the PS block in one case, and the PMMA block in the other.

Fits of similar quality were obtained for all values of f . The fit parameters which we are interested in are the oscillation amplitudes A_1 and A_2 at the free surface and substrate, respectively. These parameters are plotted in Fig. 14 as a function of the brush styrene content f . It can be readily seen that the oscillation amplitude at the free surface, A_1 , is independent of the brush composition. This is expected, since

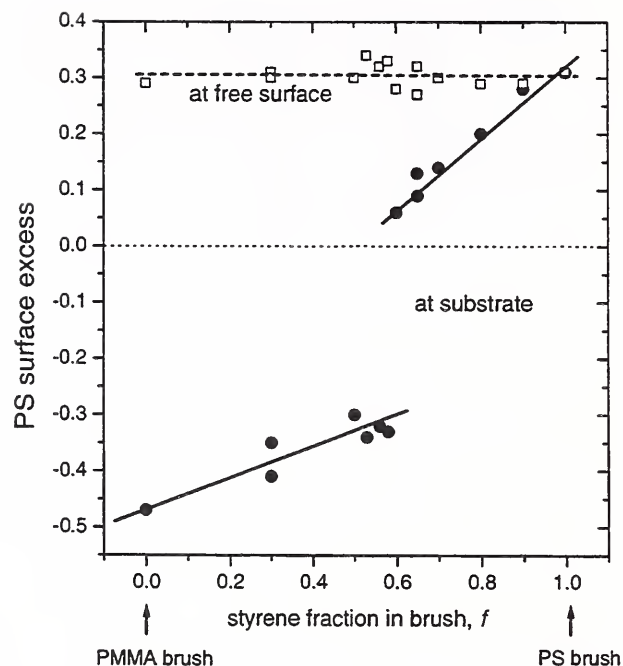


Figure 14. PS surface excess at the substrate and free surface for various (PS-r-PMMA) brushes. Note the jump in the PS excess at substrate near $f = 0.6$.

segregation at the vacuum interface is driven only by the surface tension difference between PS and PMMA. (This is in fact temperature dependent, and more recent studies have confirmed a strong dependence of A_1 on temperature). The oscillation amplitude at the substrate, however, shows a strong variation with f . For $f > 0.6$, A_2 varies approximately linearly with f , in agreement with the prediction of Fredrickson. More interesting is the sharp break in the data between $f = 0.58$ and $f = 0.6$. A 2% change in the styrene content of the brush has induced a tremendous change in the wetting behavior of the copolymer adjacent to the substrate, from very weak styrene segregation to very strong PMMA segregation. We believe that this discontinuous behavior is due to a “tunnelling” effect, driven by the strong attraction of PMMA to silicon oxide. When the barrier posed by the brush becomes sufficiently reduced, by decreasing f , the MMA block of the copolymer penetrates the brush and contacts the substrate,

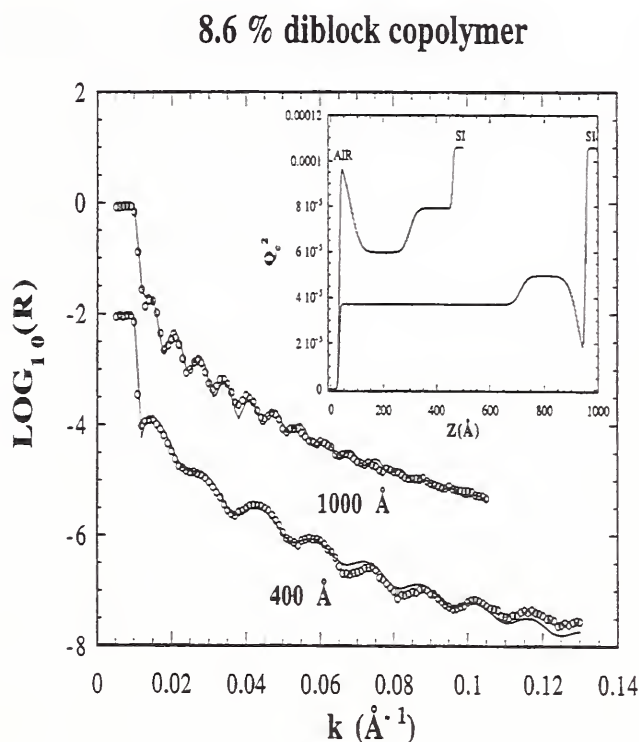


Figure 15. Neutron reflection from a 1000Å and a 400Å blend film of PSM (PSD)PSD-b-PB after several hours from as-cast state. For the 1000Å film, the diblock segregates only to the silicon surface. Moreover, it segregates to both boundaries in the 400 Å film, setting up the boundary conditions for in-plane phase separation

displacing the random copolymer's styrene segments in the process. A similar effect occurring with PMMA homopolymers is described in the previous report in this volume. The reasons for the discontinuous nature of this transition are not fully understood at present. While this is quite interesting in and of itself, it prevents us from controlling the surface potential over the whole range desired: a truly neutral surface or one which weakly wets PMMA is not possible due to the tunnelling effect. Further experiments are in progress to find a way of eliminating penetration of the brush by the PNMA block.

Influence of Diblock Copolymer on Polymer Blend Phase Behavior

To investigate how diblock copolymers af-

fect the behavior of phase separating polymer blends on surfaces, binary homopolymer blend films with small amounts of deuterated diblock copolymer were studied by neutron reflection. The polymers utilized for this study were polystyrene (PSH), polybutadiene (PB) and the diblock copolymer (PSD-b-PB). Previously we have observed, utilizing optical microscopy (OM) and atomic force microscopy (AFM), a strong suppression of surface morphology of phase separating polymer blend films with addition of small amounts of block copolymer. Recent studies have also indicated that surfactant impurities may alter the spinodal wavelength (L_c), affecting the thickness cross-over regime from 3-d to 2-d phase separation kinetics observed when $L \ll L_c$ [1]. We anticipate that the diblock copolymer acts similarly to surfactants in decreasing L_c . This assumption is consistent with results from temperature jump light scattering measurements for which q_{max} ($t = 0$) changes from 0.0018 to 0.002 \AA^{-1} with the addition of only 3% diblock.

Fig. 15 shows the neutron reflectivity from a 1000Å film of PSH(3k)/PB(3k)/PSD-b-PB (5k-5k) (45.7/45/8.6) after incubation times of 30 hours at room temperature. A fit to the data indicates that the diblock is enriched at the silicon surface, more initially and somewhat less at much longer times. OM revealed that the film surface was smooth even a week later. Given that the pure homopolymer blend film would have phase separated into droplets (late-stage of phase separation) in the same time [1], the diblock is evidently very effective in suppressing the lateral surface pattern formation. However, another blend film of the same composition, but with a thickness of 400Å exhibits a very different depth profile. In this "thinner" film, the diblock is enriched at both the air and the silicon surface within 15 hours of casting (see Fig.15) and a spinodal surface pattern appeared a week later. This result is consistent with the hypothesis that the surface patterning occurs in samples which exhibit symmetric boundary segregation, i.e. the same polymer component is present at

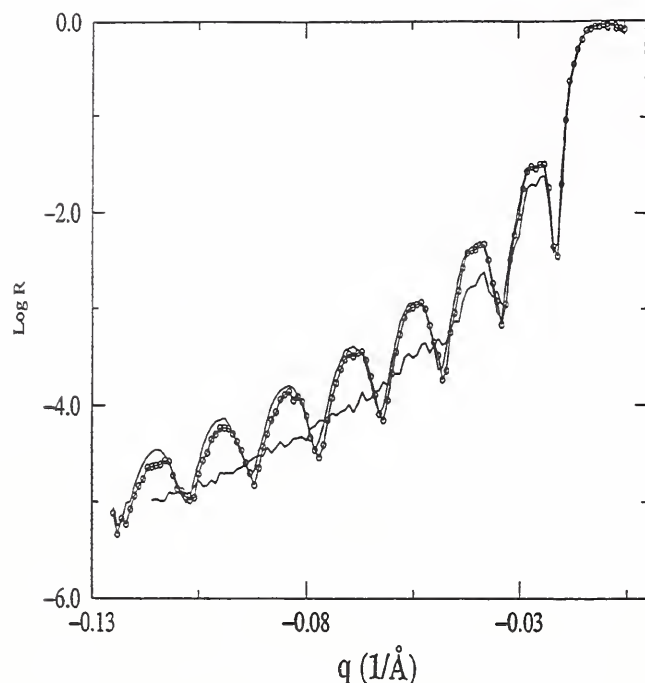


Figure 16. This figure illustrates the effect of annealing a bilayer of 10K/1000K (hPS/DPS) system at 60°C and 90°C (damped and highly damped state) compared to the as-cast profile (solid line). These sub T_g (glass transition temperature) measurements relate to relaxation at polymeric interfaces in contrast to interdiffusion at $T > T_g$.

both boundaries. Further neutron reflection and optical microscopy work is in progress to study the influence of diblock copolymers on thin film blend phase separation.

Reference

- [1] L. Sung, A. Karim, J.F. Douglas, C.C. Han, *Phys. Rev. Lett.* **76**, 4368 (1996).

Relaxation of Polymeric Bilayers below the Bulk Glass Transition Temperatures

We have previously observed a rapid relaxation at the interface of a bilayer of regular and deuterated polystyrene (hPS/dPS) on the order of 40-50Å when it was heated at a temperature just above the bulk glass transition temperature ($\sim 100^\circ\text{C}$) of the polymer. It was speculated that

this “burst effect” was induced by a rapid relaxation of the interface between the two layers since the surface tension between the two layers was no longer present after a bilayer is created. (The bilayer is prepared by spin coating the bottom layer and floating on the top layer.) To investigate this phenomena in more detail, two sets of samples were prepared. In the first set, the bottom layer was dPS of $\sim 450\text{\AA}$ and the top floated layer was $\sim 1000\text{\AA}$, while in the second set, the top layer was of similar thickness but the bottom layer was on the order of 150\AA . The first set comprised a batch of four different matched molecular weights (from 50k to 1000k), one highly asymmetric system (10k/1000k) and one for which the lower layer was end-grafted (EG85k/100k). All samples of this set were identically treated thermally. Fig. 16 shows the as-cast and annealed reflectivity profile of one such bilayer (10k/1000k), annealed for 1 hour at 60°C and at 90°C . A damping of oscillations is seen to occur upon annealing at a temperature of 60°C , that is well below the bulk T_g of the polymer of $\sim 100^\circ\text{C}$. At temperatures below 60°C , the damping was substantially less in all of the samples, while it did not relax significantly more at temperatures between 60 and 90°C . Additionally, it was established that further annealing much longer at any temperature in this range did not produce any further changes in the reflectivity, suggesting a relaxation type mechanism for the limited interfacial mixing. However, Fig. 16 also shows that the reflectivity is quite significantly damped for the annealing temperature of 90°C . Now, the samples of set 1 showed stronger damping of oscillation, as if indicative of interdiffusion above “ T_g ” of the bilayer film. The asymmetric system showed in Fig. 16 interdiffused significantly more than the other molecular weights. Thus, there appears to be a strong molecular weight effect to the phenomena, for molecular weights above and below the entanglement molecular weight. The samples of the second set, where the bottom layer was much thinner showed a continuous relaxation all the way up to 87.5°C , in contrast to the first set. Further

experiments are required to pin down the details of the relaxation phenomena and the transition from relaxation to interdiffusion in thin polymer bilayer films.

Research Topics

Field Dependence of the Magnetic Coupling Angle in a Fe₂₅Co₇₅/Mn Superlattice

J. A. Borchers¹², J. F. Ankner³³, M. E. Filipkowski³⁴, C. J. Gutierrez³⁵, C. F. Majkrzak¹², J. J. Krebs⁹, and G. A. Prinz⁹

Temperature and Field Dependence of the Fe Moment Orientation in a Fe/Al/Fe Trilayer

J. F. Ankner³³, J. A. Borchers¹², M. E. Filipkowski³⁴, C. J. Gutierrez³⁵, C. F. Majkrzak¹², J. J. Krebs⁹, and G. A. Prinz⁹

Polarization of Pd Interlayers in Fe/Pd Superlattices

J. A. Dura¹², J. A. Borchers¹², J. F. Ankner⁷, J. R. Childress¹⁵, C. F. Majkrzak¹², and R. W. Erwin¹²

Origin of Low-Field Giant Magnetoresistance in Ni₈₀Fe₂₀/Ag Multilayers

J. A. Borchers¹², P. M. Gehring¹², J. F. Ankner³³, C. F. Majkrzak¹², T. L. Hylton³⁷, K. R. Coffey³⁷, M. A. Parker³⁷, and J. K. Howard³⁷

Magnetization Profile of Co/Pt Superlattices

J. F. Ankner³³, J. A. Borchers¹², C. F. Majkrzak¹², R. F. C. Farrow⁵, and R. F. Marks⁵

Polarized Neutron Reflectivity Studies of Co/Cu and Co/Ag Multilayers

J. A. Dura¹², T. Wantanabe³⁸, J. A. Borchers¹², C. F. Majkrzak¹², and J. Bass³⁹

Antiferromagnetic Spin Ordering and Interlayer Magnetic Correlations in MnTe/CdTe Superlattices

T. M. Giebultowicz⁴, W. Faschinger¹⁸, G. Bauer¹⁸, V. Nunez^{19,12}, P. Klosowski¹², and J. K. Furdyna²⁰

NiC/Ti Supermirror Coating Reflectivity

J. Wood¹¹ and C. F. Majkrzak¹²

Fe/Si Supermirror Polarizer Efficiency

J. Wood¹¹ and C. F. Majkrzak¹²

Co/Cu Superlattices: Polarized Neutron Reflectometry Study

A. Schreyer¹³, H. Zabel¹³, J. F. Ankner⁷, and C. F. Majkrzak¹²

Analyzing Specular Reflectivities with Parametric B-Splines

N. F. Berk¹² and C. F. Majkrzak¹²

Magnetic Critical Scattering in Single Crystal Tb: Skin Effects

P. M. Gehring¹², H. Hirota¹, G. Shirane¹, and C. F. Majkrzak¹²

Fe/Cr Superlattices: Polarized Neutron Study of Interlayer Coupling

A. Schreyer¹³, J. F. Ankner⁷, H. Zabel¹³, and C. F. Majkrzak¹²

Neutron Reflectivity Studies of Biological Membrane Films

K. Gawrisch⁸, B. Koenig⁶, S. Krueger¹², N. F. Berk¹², and C. F. Majkrzak¹²

Proteins in Thin Films

A. Liebmann¹⁶, H. Wu¹⁶, M. Foster¹⁶, and C. F. Majkrzak¹²

Structure and Diffusion in Langmuir-Blodgett Films

L. A. Feigin²³, H. Kepa, N. Berk¹², L. Kleinwaks⁴⁵, and C. F. Majkrzak¹²

Block Copolymers in Confined Geometries

P. Lambooy⁵, T. P. Russell⁵, G. Kellogg²⁴, A. Mayes²⁴, S. K. Satija¹², and P. D. Gallagher¹²

Interfacial Structures of Electrically Conducting Adsorbed Multilayers

G. Kellogg²⁴, A. Mayes²⁴, W. Stockton⁵, M. Ferreira²⁴, M. F. Rubner²⁴, and S. K. Satija¹²

Structure of a Bimodal Polymer Brush

M. S. Kent³⁰, B. J. Factor²², G. S. Smith³¹, and S. K. Satija¹²

Selective Solvation in Lamellar Block Copolymer Thin Films

R. Levicki²⁵, N. Koneripalli²⁵, M. Tirrell²⁵, F. S. Bates²⁵, and S. K. Satija¹²

Wetting on Polymer Surfaces by Critical Binary Fluids

P. D. Gallagher¹², S. K. Satija¹², A. Karim²², and L. Fetters²

Surface Segregation in Thin Polymer Films

N. Singh²⁵, M. Sikka²⁵, F. S. Bates²⁵, S. K. Satija¹² and P. D. Gallagher¹²

Surface and Phase Behavior of Thin Polymer Blend Films

- T. Slawewski²⁶, S. K. Kumar²⁶, A. Karim²², and S. K. Satija¹²
- Effect of Solvent on Surface Induced Diblock Copolymer Ordering**
H. Lin²⁷, A. Steyrl²⁷, A. Karim²², T. P. Russell⁵, and S. K. Satija¹²
- Adsorption of Surfactants at a Hydrophobic Surface Near the Solid-Liquid Interface**
D. C. McDermott²⁸, R. Thomas²⁸, A. R. Rennie²⁹, S. K. Satija¹², and P. D. Gallagher¹²
- Development of Molecular Beam Epitaxy Chamber for Neutron Scattering**
J. A. Dura¹²
- Effects of H Loading on Magnetic Properties of Fe/V Superlattices**
J. A. Dura¹², B. Hjorvarsson⁴⁴, T. J. Udovic, T. Watanabe, and C. F. Majkrzak¹²
- Thermal Degradation of Co/Cu Spin Valves**
B. McMichael⁴⁵, T. Watanabe¹², J. A. Dura¹², and J. A. Borchers¹²
- Effects of Field Cycling on Co/Cu and Co/Ag Multilayers**
J. A. Borchers¹², J. A. Dura¹², T. Watanabe¹², and C. F. Majkrzak¹²
- Exact Determination of the Giant Fe Moment in FeN₁₆ Films**
T. Watanabe¹², Y. Sugita⁴⁶, J. A. Borchers¹², J. A. Dura¹², and C. F. Majkrzak¹²
- Polarization of the Rh Layer in Fe/Rh Superlattices**
Gerry Harp⁴⁷, T. Watanabe¹², J. A. Borchers¹², J. A. Dura¹², and C. F. Majkrzak¹²
- Fe/Cr Superlattices**
A. Schreyer¹³, C. F. Majkrzak¹², J. A. Dura¹², and T. Watanabe¹²
- Reflectivity Investigations of Electronic Device Structures**
J. A. Dura¹², J. G. Pellegrino⁴⁸, and C. A. Richter⁴⁸
- Neutron Reflectivity Characterization of SiO₂ on Xerogels**
N. C. Maliszewskyj¹², J. A. Dura¹², and W. W. Lee⁴⁹
- Selective Transmutation Doping in Silicon Epilayers**
J. A. Dura¹², T. Golding⁵⁰, and R. Lindstrom¹²
- UHV Ion-Beam Etching Investigations of the Origin of Two Length Scales**
J. A. Dura¹², P. M. Gehring¹², C. F. Majkrzak¹², and G. Shirane¹
- Location of Peptides in Alkanethiol/Phospholipid Biomimetic Bilayer Membranes**
S. Krueger¹², A. Plant⁶⁰, K. Meuse⁶⁰, C. F. Majkrzak¹², and J. A. Dura¹²
- Studies of Magnetic Critical Scattering in Strained and Lattice-Matched (Y/Lu)|Ho|(Y/Lu) Films**
P. M. Gehring¹², C. F. Majkrzak¹², L. D. Gibbs¹, A. Vigliante¹, A. C. Lake²⁸, J. Goff²⁸, and R. A. Cowley²⁸
- Magnetic Structure Determination in Annealed Ni₈₀Fe₂₀/Cu Multilayers**
J. A. Borchers¹², P. M. Gehring¹², J. F. Ankner³³, Y. Ijiri¹², C. F. Majkrzak¹², A. Zeltser⁵³, and N. Smith⁵³
- Magnetic Homogeneity of a Fe₃O₄ Film Capped with Co**
R. W. Erwin¹², J. A. Borchers¹², C. F. Majkrzak¹², D. Marguiles⁵⁴, and A. E. Berkowitz⁵⁴
- Structural Characterization and Magnetism of Fe/Tb Multilayers**
N. S. Rosov¹², J. A. Borchers¹², A. Freitag⁵⁵, A. R. Chowdhury⁵⁵
- Polyimide Foam Films**
J. Fodor¹⁹, and R. Briber¹⁹
- Crosslinked Polymer Interdiffusion**
W-L. Wu²², and W. Wallace²²
- Branched Linear Polymer Blends**
D. Walton²⁴ and A. Mayes²⁴
- Polyelectrolyte Brushes**
D. Irvine²⁴ and A. Mayes²⁴
- Surface Segregation of Polymers**
N. Pellgrini⁵⁶ and K. Winey⁵⁶
- Langmuir Films of Block Copolymers**
M. Kent³⁰ and G. Smith³¹
- Lamellar Surfactant Phases at Solid-Liquid Interface**
G. Salamat⁵⁸ and K. Wong⁵⁸
- Adsorption of Surfactants on Hydrophobic Surfaces**

A. Rennie²⁹, P. Thirtle²⁸ and R. Thomas²⁸

Nickel Oxide Electrochemistry

R. Hillman⁵⁹

Affiliations

- ¹Brookhaven National Laboratory
- ²Exxon Research and Engineering Co.
- ³Florida State University
- ⁴George Mason University
- ⁵IBM Almaden
- ⁶Johns Hopkins University
- ⁷MURR, Columbia, MO
- ⁸National Institutes of Health
- ⁹Naval Research Laboratory
- ¹⁰Oak Ridge National Laboratory
- ¹¹Ovonics Company
- ¹²NIST-Reactor Radiation Div.
- ¹³Ruhr University, Germany
- ¹⁴Rutgers University
- ¹⁵Thomson-CSF, France
- ¹⁶University of Akron
- ¹⁷University of Arizona
- ¹⁸University of Linz, Austria
- ¹⁹University of Maryland
- ²⁰University of Notre Dame
- ²¹NIST-Ceramics Division
- ²²NIST-Polymers Division
- ²³Russian Academy of Science
- ²⁴MIT
- ²⁵University of Minnesota
- ²⁶Penn State University
- ²⁷University of Rhode Island
- ²⁸University of Oxford
- ²⁹University of Cambridge
- ³⁰Sandia National Laboratory
- ³¹Los Alamos National Laboratory
- ³²University of Illinois
- ³³University of Missouri Research Reactor
- ³⁴University of Arkansas
- ³⁵Southwest Texas State
- ³⁶University of Florida
- ³⁷IBM Storage Systems Division
- ³⁸Sandia University
- ³⁹Michigan State University
- ⁴⁰NIST-Inorganic Analytical Research Div.
- ⁴¹University of Leicester

- ⁴²University of Bath
- ⁴³Georgetown University
- ⁴⁴Uppsala University
- ⁴⁵NIST-Metallurgy Div.
- ⁴⁶Hitachi
- ⁴⁷Ohio University
- ⁴⁸NIST-Semiconductor Electronics Div.
- ⁴⁹Texas Instruments
- ⁵⁰University of Houston
- ⁵¹ILL, Grenoble, France
- ⁵²IBM Storage Systems, San Jose, CA
- ⁵³Kodak, Rochester, NY
- ⁵⁴University of California, San Diego
- ⁵⁵University of Alaska
- ⁵⁶University of Pennsylvania
- ⁵⁷University of Delaware
- ⁵⁸CEN, Saclay, France
- ⁵⁹University of Leicester, U.K.
- ⁶⁰NIST-Biotechnology Div.

Macromolecular and Microstructure Studies

Two high resolution, 30 m long, small angle neutron scattering (SANS) instruments, and a moderate resolution 8 m SANS instrument, are the principal tools used at the CNRF to characterize the nanoscale structure (~ 1 to 400 nm) of a wide variety of materials including polymers, colloids and microemulsions, microporous media, biological macromolecular complexes, nanocrystalline metals and ceramics, molecular composites, and many others. A record number of researchers, over 250, carried out experiments on these instruments during the year covered in this report, the first full year of operation of the CNRF's new liquid hydrogen cold source. The titles of the SANS studies conducted in the past year (except for those listed elsewhere in this report) are listed at the end of this section. Summarized below are highlights of some of this work in which Reactor Division staff scientists have played a leading role.

Complex Fluids

• Supercritical CO₂-Based Microemulsions

Carbon dioxide, because of its low cost, low toxicity, and readily accessible critical point is the ideal solvent for use in supercritical fluid extraction techniques. Unfortunately, hydrophilic solutes are only sparingly soluble in carbon dioxide. Therefore, a mechanism for enhancing their solubility in CO₂ is necessary to make CO₂ extraction of hydrophilic solutes commercially feasible. Recently, ammonium carboxylate perfluoropolyether (PFPE) has been shown to dissolve in CO₂ and enhance the solubility of water in CO₂. Several observations and measurements suggest that the added water is encapsulated in inverse micelles[1]. However, none of the previously used techniques allow quantitative determination of the micellar size, structure, or intermicellar interactions. SANS is an ideal technique for quantitatively measuring the structure

and interactions in inverse micellar solutions because the length scales probed include both the size of the aggregate and the interaggregate distance.

This investigation, carried out in collaboration with Prof. E. Kaler's group at the University of Delaware, focused on PFPE/D₂O/CO₂ microemulsions as a function of D₂O concentration and pressure, clearly showing that water swollen reverse micelles form in supercritical CO₂ [2]. Phase behavior and small angle neutron scattering (SANS) experiments were performed on D₂O-in-CO₂ microemulsions as a function of pressure (192 - 287 bar) and D₂O composition (0.8-2.0 wt%). For these microemulsion droplets the scattered intensity is dominated by the D₂O core, which has a neutron scattering contrast $(\Delta\rho)^2$ nearly two orders of magnitude larger than the CO₂-rich PFPE shell surrounding the core. Sample temperature was maintained at 35°C, above the critical temperature of CO₂ ($T_c = 31^\circ\text{C}$). The view cell used for the phase behavior study and sample preparation is based on a prior design [3], and was connected to the NIST SANS high pressure cell. The NIST pressure cell has been previously used for liquid and semi-solid materials and has proved versatile and reliable for use with supercritical fluids.

The prepared microemulsion sample was transferred from the view cell to the SANS cell nearly instantaneously by using nitrogen as the pressurizing fluid in the view cell. Sample transfer was accomplished by opening a valve between the view and SANS cells, allowing the sample to flow rapidly into the SANS cell. Concurrent with the sample flowing into the SANS cell, a self-venting pressure control valve allowed additional nitrogen to flow into the pressurizing side of the view cell, thereby maintaining a constant sample pressure.

SANS measurements were made on mixtures of PFPE, CO₂, and D₂O in the one-phase re-

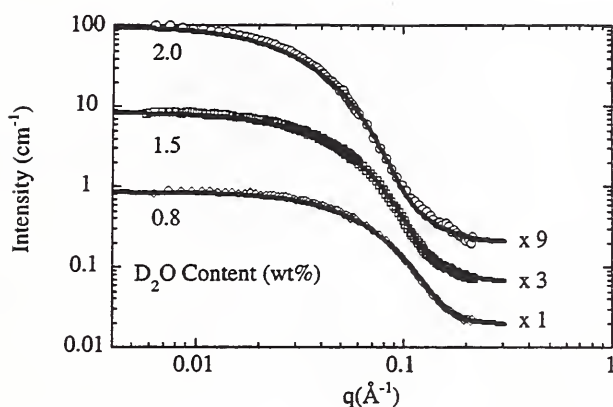


Figure 1. SANS spectra of 0.8, 1.5, and 2.0 wt% D₂O in CO₂ / PFPE mixtures at 35°C and 287 bar. The PFPE concentration is 2.1 wt %. The 1.5% and 2.0% D₂O data sets are shifted up by scale factors of 3 and 9 respectively for clarity. Note the changes at both low and high q in these spectra reflecting the change in micelle size. Lines represent model fits to the data for polydisperse spheres (standard deviation 25%) of radius 20, 27, and 35 Å respectively as the D₂O concentration is increased.

gion in the CO₂-rich corner of the phase diagram (2.1 wt% PFPE on a D₂O-free basis). Figure 1 shows the SANS spectra for a series of microemulsions with increasing concentrations of D₂O, at a constant pressure of 287 bar. Note the increase in the magnitude of the scattered intensity at low q , as well as changes in the shape of the scattered intensity in the higher q portions of the spectra. This change in scattering at higher q qualitatively indicates changes in microemulsion droplet size. To quantify these changes, the spectra were fit to a model of polydisperse spherical droplets.

The D₂O core radius remains essentially unchanged with changes in pressure at 20 Å for the 0.8 wt% D₂O samples, 27 Å for the 1.5 wt% D₂O samples and 35 Å for the 2.0 wt% D₂O samples. The constant core radius is consistent with the lack of change in water solubility in CO₂ with pressure, maintaining a constant partitioning of water between the core of the micelle and the bulk solvent. There are also relatively weak changes in the interfacial tension forces acting

to drive changes in droplet size, as measured in similar CO₂ and PFPE mixtures. However, increasing the water content of the microemulsion results in a significant increase in the droplet radius as the added water enters the micelles. At lower pressures, near the phase boundary, critical fluctuations contributed to the scattering. The compressibility and the correlation length were found to increase with decreasing pressure, as expected for samples approaching a phase boundary. These CO₂-based microemulsions contain aqueous regions large enough to solubilize biological molecules such as proteins, with potential use in industrial-scale separations. A supercritical CO₂ microemulsion with a significantly reduced level of incoherent scattering may also provide a unique and advantageous SANS environment for biological molecules.

• Structure and Interactions in Binary Colloidal Mixtures

The growing interest in colloidal mixtures has prompted many investigations of their equilibrium and non-equilibrium behavior, and a fundamental understanding of the interactions that control the stability and phase behavior of colloidal mixtures is of significant practical importance. One underlying theme in the study of colloidal mixtures is the effect that any 'microstructure' in the solvent has on a dispersion. The oldest example of this phenomena is the depletion attraction induced by the addition of soluble polymer to an otherwise stable colloidal dispersion [4]. Information about the three pair interactions present in such a bimodal colloidal mixture can be determined through properly designed small-angle scattering experiments. A recently developed optimization regularization (OR) technique [5] provides quantitative partial structure factors for bimodal colloidal mixtures through the inversion of a set of solvent contrast variation SANS measurements.

This study, also in collaboration with Prof. Kaler's group at the University of Delaware, focuses on the behavior of aqueous mixtures of colloidal silica and an oil-in-water microemulsion

comprised of AOT, decane, and brine [6]. Microemulsions are thermodynamically stable, and through changes in temperature or composition a variety of microstructures can be formed using the same set of microemulsion components. This added degree of flexibility is not found in other colloidal mixtures. One challenge is that kinetically stable solid dispersions are sensitive to the nature of their chemical environment, and this sensitivity to aggregation imposes severe constraints on the formulation of a compatible microemulsion. Despite these constraints, the wealth of data concerning microemulsion behavior makes it relatively easy to tailor a microemulsion for such an application.

Microemulsion - silica mixtures were prepared at three different oil concentrations of $\alpha = 5, 10$, and 15 at a constant silica concentration. α is defined as the weight percent of decane in the brine and does not include the surfactant. At each value of α , SANS measurements were performed on mixtures with solvent (brine) scattering length densities of $3.80, 4.10, 4.40$, and $4.80 \times 10^{10} \text{ cm}^{-2}$. The OR method was applied to these sets of scattering data, extracting partial structures at each oil concentration, α .

The three experimental partial structure factors for a mixture $\phi_{mem} = 0.29$ (corresponding to $\alpha = 15$) and $\phi_{silica} = 0.071$ are shown in Fig. 2. The microemulsion droplet volume fraction, ϕ_{mem} , includes both the decane and the hydrocarbon tails of the AOT. The experimental values are shown as points, and the error bars shown are derived from a sensitivity analysis and represent the relative error associated with each partial structure factor, rather than absolute error. The solid lines through the data are the best-fit partial structure factors calculated using a multicomponent sticky hard sphere (SHS) model.

The data analysis reveals that the silica-silica (SLL) interaction potential remains nearly constant at $2.0 \pm 0.1kT$ for all three microemulsion compositions. The microemulsion-silica ($S\mu L$) interactions are also constant and equal to zero, so these are hard sphere-effective hard sphere

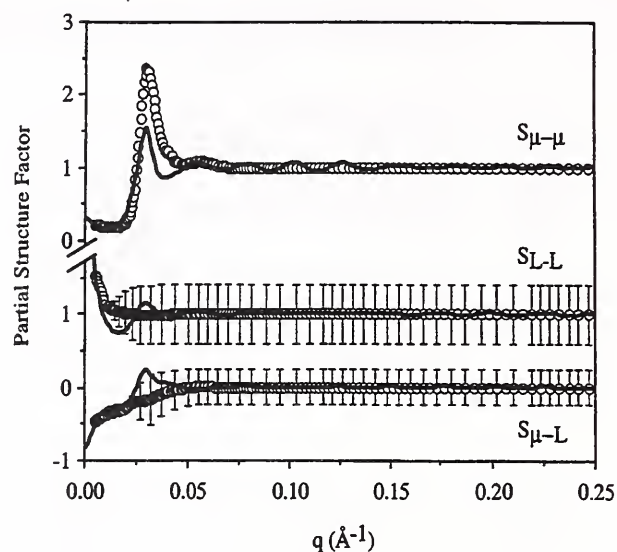


Figure 2. Optimized partial structure factors from a colloid-microemulsion mixture of $\phi_{mem} = 0.29$ and $\phi_{silica} = 0.071$. The experimental partial structure factors are shown as open circles with the microemulsion-microemulsion partial structure factor offset for clarity. The solid lines are best-fit partial structure factors calculated for a multicomponent mixture of sticky hard spheres.

interactions. Some level of repulsive interactions remain between the charged microemulsion droplets, so the microemulsion-microemulsion ($S\mu\mu$) interactions are modeled as effective hard sphere interactions. More appropriate theoretical models are necessary to correctly describe the interactions present in these mixtures, but are not currently available.

Modeling of the partial structure factors yields the three binary interaction potentials in the mixtures as a function of the decane concentration in the microemulsion, permitting characterization of the microemulsion-induced depletion attraction as the size ratio in the colloidal mixture changes. Results show convincingly that the addition of oil to a droplet microemulsion does not adversely affect the stability of colloidal silica particles, even at the large volume fraction (ca. 40%) of dispersed structures present in these mixtures. These results contrast with the results for a similar mixture of colloidal silica and sodium dodecyl sulfate mi-

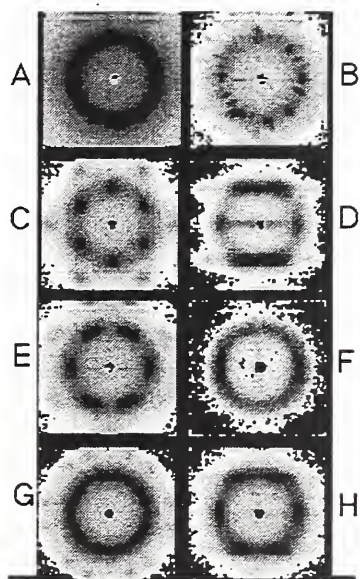


Figure 3. SANS patterns from a 25 weight % aqueous solution of the triblock copolymer $\text{PEO}_{25}\text{-PPO}_{40}\text{-PEO}_{25}$ in radial geometry (A) at 32°C , (B) at 35°C , (C) at 40°C , 20 Hz steady shear; (D) same as C in tangential geometry; (E) radial geometry at 40°C , 0 Hz; (F) same as E in tangential geometry; (G) radial geometry at 40°C , during and post-oscillatory shear; (H) tangential complement of G. The scattering vector Q ranges from 0.13 nm^{-1} near the beam stop, to 0.95 nm^{-1} at the edges.

celles. In that study [7] the attractive silica-silica interaction potential increased in strength as more micelles were added, resulting in the irreversible flocculation of the silica particles.

• Shear-Induced Structural Transitions in Polymer Micelle Solutions

The solution behavior of triblock copolymers is of intense industrial and academic interest due to the technological promise for applications including colloid stabilization, viscosity control, preventing damage to microorganisms in bioprocessing, and controlled drug release [8]. Aqueous solutions of the commercially-available, nonionic, symmetric triblock $\text{PEO}_n\text{-PPO}_m\text{-PEO}_n$, show particularly rich phase behavior, from Gaussian polymer chains at low temperatures and micelles at higher tempera-

tures, to an “inverse melting transition” to form a micellar crystalline phase upon further heating [9].

SANS was used to study the micellar structures formed in a 25 weight % solution of $\text{PEO}_{25}\text{-PPO}_{40}\text{-PEO}_{25}$ in D_2O , which is known to form a micellar crystalline phase upon heating and upon subjecting it to shear [10]. Samples were studied in the NIST-Boulder couette-type shear cell with a 0.5 mm gap between the inner cylindrical stator and outer cylindrical rotor. This assembly was then heated *in-situ* on the 30m SANS instrument where the samples were observed in both radial (incident beam perpendicular to shear direction (\mathbf{v}), parallel to shear gradient ($\nabla\mathbf{v}$)) and tangential (beam parallel to \mathbf{v} , perpendicular to $\nabla\mathbf{v}$) geometries.

As has been reported in the literature [10], the triblock copolymer solution gradually forms micelles upon heating, until all of the polymer chains are hydrodynamically and thermodynamically driven to form spherical micelles, as evident by the well-defined SANS ring pattern in Fig. 3A. Further heating through the inverse-melting transition induces a large-grain, polycrystalline structure (Fig. 3B). Under shear a single crystal-like structure forms which is most highly oriented at shear rates of $\sim 20\text{ Hz}$. The diffraction spots seen at 20 Hz in the radial (Fig. 3C) and tangential (Fig. 3D) geometries correspond to close-packed planes of micelles that are parallel to the walls of the shear cell and which have a predominantly ABABAB... stacking (hcp structure) in the shear gradient direction. Remarkably, upon the cessation of shear, a transformation to a different oriented structure [11] occurs within 100 seconds as evidenced by the patterns seen in Fig. 3E and Fig. 3F for the radial and tangential geometries, respectively.

The observed shear-induced structural transformation was found to be reversible and reproducible upon repeated application and removal of steady shear and has not been previously reported. We have found, in addition, that the transformation to the structure at 0 Hz can be inhibited by subjecting the sample to a strong

oscillatory shear. Figures 3G and 3H show the radial and tangential (respectively) SANS patterns of the sample being subjected to 200% strain at a frequency of ~ 4 Hz (maximum shear rate of ~ 120 Hz). The patterns resemble those of the 20 Hz steady shear except that each of the visible spots is now split—indicative, perhaps, of twinning in the crystal. What is most striking about this structure, compared with the steady shear behavior, is its persistence; cessation of the applied oscillatory shear has no further effect on it. It was found that only significant temperature change or subjecting the sample again to steady shear could disrupt this oscillatory shear-induced structure.

These results indicate that the rich phase behavior observed in this system as a function of temperature becomes even more complex with the application of shear. New theories and models for the “soft sphere” interactions in polymer micelle solutions will need to be developed to account for all of the observed phenomena.

Polymers

• Early Stages of Nucleation and Growth in a Polymer Blend

Over the past few years, substantial effort has been devoted to the understanding of the demixing process in polymer blend mixtures. The thermodynamics of phase separation proceed either through a homogeneous spinodal decomposition (sinusoidal density wave across the sample) or through the formation of nucleation centers. Whereas spinodal decomposition is well understood and has been investigated at length using scattering methods, the nucleation-and-growth process in polymers has not received much attention. The nucleation-and-growth region of the phase diagram constitutes a narrow strip between the binodal and spinodal lines and is therefore harder to access than the much larger spinodal region.

SANS is well suited for investigations of the kinetics of phase decomposition in polymer blends in the early-to-intermediate stages. Fol-

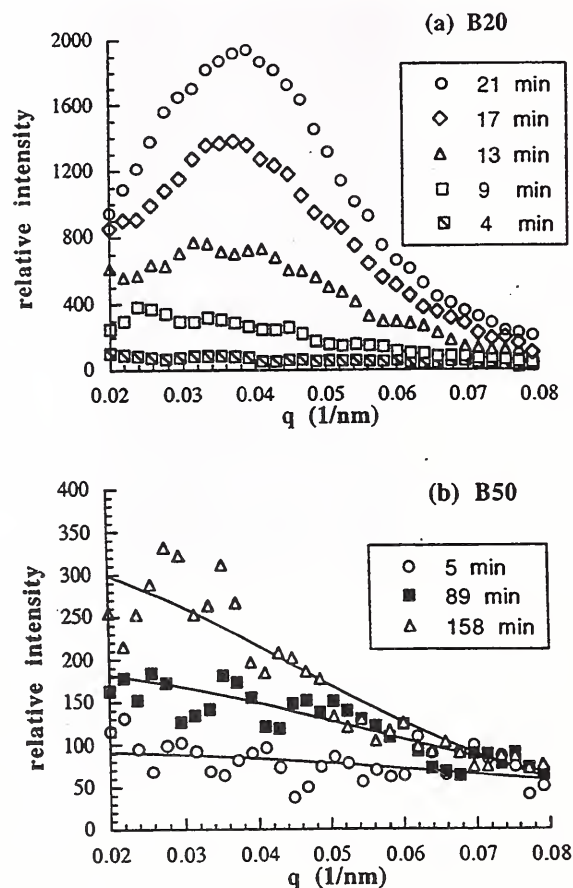


Figure 4. Variation of SANS profiles from polymer blend samples of polyethylbutylene (PE) and polymethylbutylene (PM) (with added diblock copolymer PE-PM) with time after a temperature jump (a) for sample B20 (spinodal decomposition process) and (b) for sample B50 (nucleation-and-growth region). Samples B20 and B50 contain 20% and 50% copolymer respectively.

lowing a temperature jump from the one-phase to the two-phase region, SANS can be used to monitor structural changes in real time. In collaboration [12] with N. Balsara (Polytechnic University, Brooklyn, NY), two blends of polyethylbutylene (PE), polymethylbutylene (PM) and a diblock copolymer (PE-PM) with compositions (by volume) of 27% PE, 53% PM, 20% PM-PE (sample B20), and 17% PE, 33% PM, 50% PM-PE (sample B50), corresponding to the spinodal and the nucleation-and-growth regions (at 25°C), respectively, were used to compare

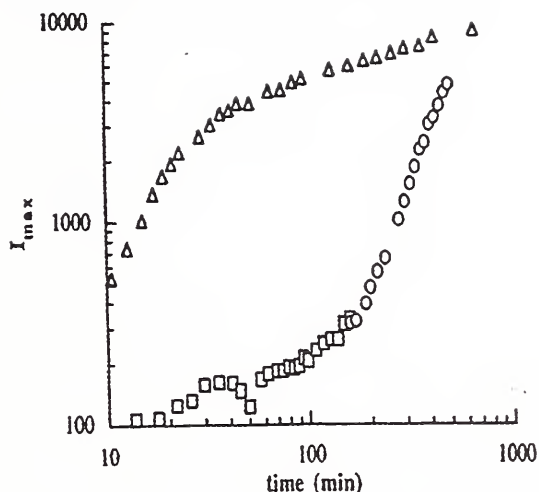


Figure 5. Variation of the SANS peak intensity with time showing the difference between the two phase separation processes: spinodal decomposition (top curve) and nucleation-and-growth (bottom curve).

these two forms of phase separation. The PE polymer was deuterium labeled in order to enhance the neutron contrast. Since the molecular size and the relative concentration of the PE and PM homopolymers were nearly the same in both samples, the time scale for molecular motion at a particular temperature is expected to be the same. Therefore any difference in the evolution of structure in these blends can be directly attributed to differences in "location" of the blend relative to the phase boundary.

SANS kinetics were monitored for many hours following a temperature jump from 250°C to 25°C for each sample. The early stage of phase separation for the two samples was completely different (Figures 4a,b). The first sample (B20) showed typical spinodal decomposition behavior where a spinodal peak appears almost instantly then moves to lower Q 's with time while its intensity builds up. The second sample (B50) does not show any peak in the scattering intensity for the first 2 hours; this is believed to be the signature of a nucleation process. Average nucleation cluster sizes and number of chains/cluster were estimated and found to in-

crease with time. Comparison of the variation of the SANS intensity with time over the first few hours shows the difference between the two kinds of phase separation for the two samples. In the spinodal decomposition case, the intensity grows rapidly from the beginning whereas in the nucleation-and-growth case, there is an initial slow "incubation" period when clusters are formed (see Fig. 5) before the intensity starts growing.

The results for the early stages of nucleation and growth obtained in this study are not understood. Hence further study is needed using a variety of techniques to verify that the novel technique used to access this region of the phase diagram does not introduce unintended effects.

• SANS from Pressurized Polyolefin Blends

The SANS technique is developing into an effective tool to study pressure effects on the miscibility of polymer blends. Pressure is an important thermodynamic parameter which enters in most forms of polymer processing and influences many polymer properties such as mixing/demixing, morphology and texture, etc. In previous work, blends that phase separate upon heating (LCST) were investigated and found to undergo pressure-induced phase mixing; presumably due to the reduction of free volume with increasing pressure. Over the past year, blends that phase separate upon cooling (UCST) have been investigated under pressure in collaboration with N. Balsara (Polytechnic University, Brooklyn, NY) and are described here.

A polyolefin blend of polyethylbutylene (PE) and polymethylbutylene (PM) characterized by a low glass-rubber transition temperature has been measured under pressure and temperature control. One component was deuterium labeled (DPM) in order to enhance the SANS signal and a diblock copolymer (PE-PM) was added in order to adjust the phase transition temperature to easily reachable values. The effect of pressure was seen to shift the phase boundary lines upward in temperature, i.e., pressure favors demix-

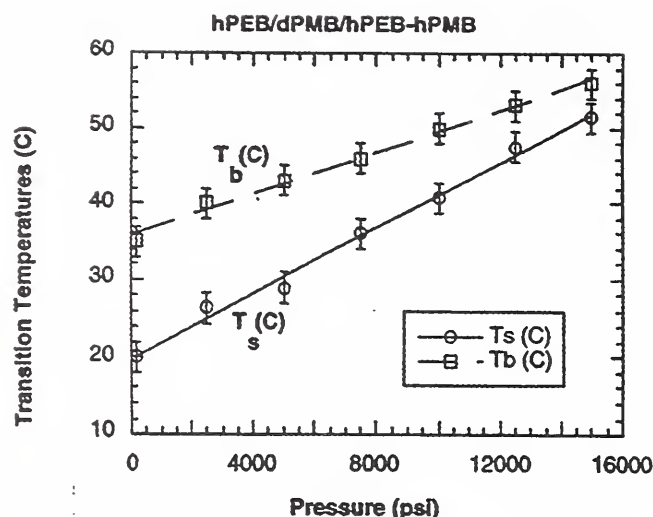


Figure 6. Estimated variations of the spinodal temperature (T_s) and binodal temperature (T_b) with pressure, for a polymer blend with a UCST, derived from SANS measurements.

ing in this UCST system.

Careful monitoring of the SANS intensity (when the sample is in the one-phase region) is a good indicator of the proximity of phase transition lines. A conventional method (extrapolation of $1/I_0$ vs $1/T$ where T is the absolute sample temperature and I_0 is the SANS intensity in the forward direction) was used to determine the spinodal temperature reliably. Moreover, $1/I_0$ (intercept of Zimm Plot) becomes negative when the sample phase separates; i.e., when it crosses the binodal line. These two methods were used to map out the spinodal and binodal temperatures and monitor their variation with pressure (see Fig. 6). It is interesting to see that in our sample, the nucleation-and-growth region narrows down under pressure. SANS is the only method that can give such results.

Pressure jumps (at fixed temperature) from the one-phase region to the two-phase region have been performed for the first time. The kinetics of phase separation have been followed for many hours whereby a spinodal peak appeared, then built up while moving to lower Q values (Fig. 7). Reverse pressure jumps (two-phase region to one-phase region) have also been

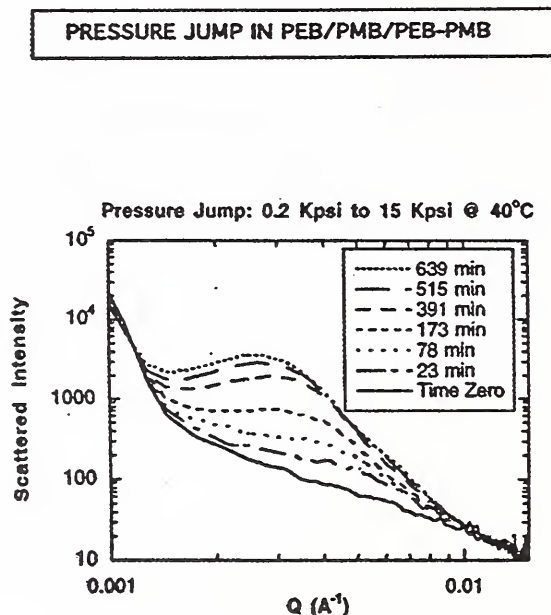


Figure 7. The time evolution of the small angle scattering from a polymer blend following a pressure jump from ambient pressure to 1 kBar at a fixed temperature (40°C) corresponding to a jump from the one-phase region to deep within the spinodal region.

performed and the kinetics of dissolution of the formed structure have been investigated. In this dissolution process, the peak intensity decreases while the peak position moves (also) to lower Q 's.

Quantitative analysis of our observations remains to be performed. At the present time, the observed trends appear reasonable and this novel use of pressure changes with scattering measurements appears to be an effective method of probing and elucidating polymer blend phase behavior. Pressure jumps are easier to realize experimentally than temperature jumps and may also prove to be useful in the processing of polymer mixtures.

References

- [1] K. P. Johnston, K. L. Harrison, M. J. Clarke, S. M. Howdle, M. P. Heitz, M. P. F. V. Bright, C. Carlier, and T. W. Randolph, *Science* 271, 624 (1996).
- [2] R. G. Zielinski, S. R. Kline, E. W. Kaler, and

- N. Rosov, to be submitted to *Langmuir*.
- [3] J. M. Ritter, A. M. F. Palavra, C. P. C. Kao, and M. E. Paulaitis, *Fluid Phase Equil.* 55, 173 (1990).
- [4] S. Asakura, and F. J. Oosawa, *Chem. Phys.* 22, 1255 (1954).
- [5] S. R. Kline, and E. W. J. Kaler, *Appl. Cryst.* 29, 427 (1996).
- [6] S. R. Kline and E. W. Kaler, to be submitted to *Langmuir*.
- [7] S. R. Kline, and E. W. Kaler, *J. Chem. Phys.* 105, 3813 (1996).
- [8] Y. C. Yun, S. H. Chen, J. S. Huang, *Phys. Rev. E* 54, 1698 (1996); P. Alexandridis, J. F. Holzwarth, and T. A. Hatton, *Macromol.* 27, 2414 (1994), and references therein.
- [9] K. Mortensen, W. Brown, and B. Norden, *Phys. Rev. Lett.* 68, 2340 (1992).
- [10] K. Mortensen, *Europhys. Lett.* 19, 599 (1992).
- [11] Very similar to the unidentified structure observed in a diblock copolymer melt by K. Almdal, K. A. Koppi, F. S. Bates, and K. Mortensen, *Macromol.* 25, 1743 (1992).
- [12] N. P. Balsara, C. C. Lin, and B. Hammouda, *Phys. Rev. Lett.* 77, 3847 (1996).
- D. Perahia³² and B. Hammouda²⁷
- Non-Mean Field Effects on the Phase Separation in Polystyrene/Polyvinylmethylether Blends**
R. M. Briber⁴⁷, S. Choi⁴⁷, D. Schwann¹⁸ and B. Hammouda²⁷
- Order-Disorder Transition in Polystyrene-Polyisoprene Diblock Copolymer**
N. P. Balsara⁶ and B. Hammouda²⁷
- Aggregation and Microstructure of Random Copolymers in Organic Solvents: Effects on Viscosity**
H. D. Ou-Yang²¹ and M. F. Islam²¹
- Pressure Effects on Blend Miscibility in PEB/PMB Polymer Mixtures**
N. Balsara⁶, J.-H. Lee²⁷, A. Lefebvre⁶ and B. Hammouda²⁷
- Pressure Dependence of the Lower Critical Ordering Transition in Diblock Copolymers**
T. P. Russell¹⁷ and A. M. Mayes²⁴
- Isotope Effects in PDMS Blends**
G. Beaucage⁴², S. Rane⁴² and S. Sukumaran⁴²
- SANS Studies on the Orientation of Thin Film Symmetric Diblock Copolymers**
G. J. Kellogg²⁴, A. M. Mayes²⁴, D. G. Walton²⁴, T. P. Russell¹⁷ and P. A. Mansky¹⁷

Research Topics

POLYMERS

Block Copolymer Films on Neutral Surfaces: Controlling Lamellar Orientation

P. Mansky¹⁷, T.P. Russell¹⁷, C. Hawker¹⁷ and J. Mayes⁴⁰

Characterization of Nanofoams Formed by Thermal Treatment of Tri-Block Copolymer Films

R.M. Briber⁴⁷, J.S. Fodor⁴⁷ and T.P. Russell¹⁷

Characterization of Polymer Fifth Generation Dendrimers - Size as a Function of Solvent

S.F. Trevino² and N. Beck-Tan²

Early Stages of Nucleation and Growth in Polyolefin Polymer Blends

N. P. Balsara⁶, C. Lin³² and B. Hammouda²⁷

Effect of Pressure on Phase Transitions in Polystyrene-Polyisoprene Block Copolymers in Decane

Measurement of Molecular Alignment of Liquid Crystalline Polymers and Microfibrillated Composites Containing LCPs under Flow

N. J. Wagner⁴⁴, W. Kernick⁴⁴ and M. Rivera⁴⁴

Shear Effects on Block Copolymer Solutions

N. P. Balsara⁶, H. J. Dai⁶, H. S. Jeon⁶ and B. Hammouda²⁷

Scattering Properties of Swollen Polymer Networks

F. Horkay²⁷ and B. Hammouda²⁷

Polymer Chain Conformations in Melt Inter-calated Polymer-Silicate Nanocomposites

R. Krishnamoorti⁹, R. A. Vaia⁶² and E. P. Giannelis⁹

Microphase Separation in Random Copolymers

A. M. Mayes²⁴ and D. G. Walton²⁴

In-situ Polymer/Liquid Crystal Network FormationT. P. Russell¹⁷, R. J. Twieg¹⁷ and R. D. Miller¹⁷**Determination of Void Morphology in Polyethylene Composites via Neutron Scattering**D. Marr⁸ and M. Wartenberg³³**Use of Small Angle Neutron Scattering to Probe the Chain Conformation of Heat Resistant, High Modulus Resins in the Melt**R. A. Vaia⁶² and R. Krishnamoorti⁹**Polymer Chain Dimensions in Porous Media**R. M. Briber⁴⁷ and I. Teraoka⁶**SANS Studies of Acrylic Coatings Derived from Latex Blends**A. Biswas¹⁰, S. Mazur¹⁰ and C. J. Glinka²⁷**Effect of Film Thickness on the Phase Separation Temperature of Confined Ultrathin Film Polymer Blends**R. L. Jones³¹, S. K. Kumar³¹, R. M. Briber⁴⁷, J. S. Fodor⁴⁷, T. M. Slaweki²⁷ and T. P. Russell¹⁷**Small Angle Neutron Scattering Studies on Ionomer Blends**R. A. Weiss¹⁴ and R. Xie⁴³**Thermodynamics of Polyolefin Blends Polymerized by Metallocene Catalysts**W. W. Graessley³², G. C. Reichart³², C.-C. Lin³² and D. Lohse¹²**Pressure Dependence of the Lower Critical Ordering Transition in Diblock Copolymers**T. P. Russell¹⁷ and A. M. Mayes²⁴**Polystyrene-Carbon Dioxide and Polystyrene-Toluene Mixtures to 100 bar Pressures**J. H. van Zanten¹⁹ and M. E. Paulaitis¹⁹**BIOLOGY****Conformation of D-Rubisco in its Native State and Bound to GroEL**P. Thiagarajan¹ and C.-Y. Ku¹**Magnetic Alignment of F-Actin**R. Ivkov⁴⁷, J. Forbes⁴⁷, A. Drews²⁷ and J.G. Barker²⁷**Solution Structure of Cyclic AMP Receptor Proteins as a Function of cAMP Binding**S. Krueger²⁷, F. Schwartz^{7,27}, I. Gorshkova^{7,47}, J. Brown⁴⁷ and K. McKinney²⁷**Solution Structure of Hemoglobin in Different Oxygenation States**S. Krueger²⁷, G. Vasquez⁷ and G. Gilliland^{7,27}**Determination of the Molecular Size and Mass of Murine Monoclonal Immunoglobulin M Antibody (T₁₀B₉)**Z.-H. Li²⁵, M. Schenerman²⁵ and M. Lin¹²**GAPDH/PGK Binding and Conformational Changes in Citrate Synthase**S. Henderson⁵⁰, E. Serpersu⁵⁵ and L. Kurz⁴⁹**SANS Studies of Actin Polymerization**R. Ivkov⁴⁷, S. C. Greer⁴⁷ and A. Drews²⁷**Neutron Scattering Studies of Calmodulin/Myosin Light Chain Kinase Interactions**J. Trehella²², J. Krueger²² and J. Stull⁵⁶**Membrane Active Peptides: Phase Transitions and Supramolecular Assemblies of Peptides in Membranes**H. W. Huang³⁴, W. Heller³⁴, T. Harroun³⁴ and L. Yang³⁴**SANS from DNA in Semidilute Solutions**R. Borsali³⁸ and R. Pecora³⁸**COMPLEX FLUIDS AND GELS****Phase Behavior and Structure of a Water-in-Supercritical Carbon Dioxide Microemulsion**S. R. Kline²⁷, N. Rosov²⁷, R. G. Zielinski⁴⁴ and E. W. Kaler⁴⁴**Shear-Induced Structure in Dilute Aqueous Solutions of Thread-like Surfactant Micelles**T. M. Slaweki²⁷ and C. J. Glinka²⁷**Pressure-Induced Interdigitated Phase in Phospholipid Bilayers**D. Worcester⁴⁹ and B. Hammouda²⁷**Surface Fluctuations and Phase Separation in Lipid-Cholesterol Vesicles**B. Frisken³⁷, A. Drews²⁷, J. G. Barker²⁷ and S. Krueger²⁷**Structure and Interactions in Binary Colloidal Mixtures: Microemulsions and Colloidal Silica**S. R. Kline²⁷ and E. W. Kaler⁴⁴**Characterization of the Structure of Humic Acid**D. Wirtz¹⁹ and A. Penisson¹⁹

Microstructure of Shear Thickening and Shear Thinning Suspensions

N. Wagner⁴⁴, J. Bergenholtz⁴⁴ and R. Butera¹¹

Structure of Polyelectrolyte Solutions in Equilibrium and Under Flow Conditions

D. Wirtz¹⁹, A. Silva¹⁹ and A. Palmer¹⁹

Partial Structure Factors in Sheared Bimodal Particulate Dispersions

R. H. Ottewill² and A. R. Rennie^{6a}

SANS Studies of the Structural Evolution of Micelles Formed by Tri-block Copolymers (Pluronic and Pluronic-R) in Aqueous Solution

Y. Liu²⁴ and S.-H. Chen²⁴

Shear-Induced Structural Transitions in Polymer Micelle Solutions

T. M. Slaweki²⁷, B. Hammouda²⁷ and C. J. Glinka²⁷

SANS Study of Shear Flow in Free-Standing Liquid Films

X.-L. Wu⁵², M. Rutgins⁵² and B. Martin⁵²

The Structure of Highly Associated Fluids: AOT Microemulsions with Triblock Copolymers

U. Batra³², J. S. Huang¹² and M. Lin¹²

Evolution of Microstructure during Microemulsion Polymerization

E. W. Kaler⁴⁴, C. Co⁴⁴, D. Iampietro⁴⁴, G. Salamat⁴⁴ and R. Zielinski⁴⁴

SANS Study of Micelle to Vesicle Transitions in Mixed Surfactant Systems

E. W. Kaler⁴⁴, L. Brasher⁴⁴, K. Lusvardi⁴⁴ and S. Kline²⁷

Kinetics of Alignment and Decay in Viscoelastic Solutions of Threadlike Micelles

P. Butler²⁹, W. Hamilton²⁹, L. Magid⁵⁵ and Z. Han⁵⁵

Rheology and Microstructure of Dense Colloidal Suspensions

W. B. Hunt⁴⁶, G. Flickenger⁴⁶, S. Jogun⁴⁶, K. Miller⁴⁶ and C. F. Zukoski⁴⁶

Mixed Colloidal Crystals

H. J. M. Hanley²⁷, G. C. Straty²⁷, W. B. Hunt⁴⁶ and C. F. Zukoski⁴⁶

Characterization of Flocs in Concentrated Colloidal Suspensions and Sediments

P. A. Smith³⁰, P. J. Brunsima³⁰ and J. Phillips³⁰

Tandem Small Angle and Contrast Variation Neutron Scattering from Osmotically Stressed Unilamellar Vesicles

J. Pencer⁴⁵ and R. Hallet⁴⁵

Kinetics of Poiseuille Shear Induced Structures in Solutions of Threadlike Micelles

W. A. Hamilton²⁹, P. D. Butler²⁹, L. J. Magid⁵⁵ and Z. Han⁵⁵

Tuning of Micelle Morphology: Electrostatic and Counterion-Specific Contributions

L. J. Magid⁵⁵, P. D. Butler²⁹, W. A. Hamilton²⁹ and Z. Han⁵⁵

Block Copolymer Micelle Structure near the Critical Micellisation Temperature

I. Goldmints²⁴, F. von Gottberg²⁴ and T. A. Hatton²⁴

SANS Study of Nonionic Surfactant Molecules at the Water-Oil Interface

T. Sottmann²³, R. Strey²³ and H.-S. Chen²⁴

Block Copolymer Micelle Solutions

E. Sheu³⁹, I. Goldmints²⁴ and L. Molnar²⁴

Effects of Shear on the Formation of Ordered Mesopores in the MCM-41 Class of Silica Molecular Sieves

J. W. White³ and K. Edler³

Scaling Behavior in the Structural Evolution in Dense Silica Gels

H. J. M. Hanley²⁷, B. D. Butler²⁷, C. D. Muzny²⁷ and G. C. Straty²⁷

Reversible Gel Formation in Organic Liquids

R. G. Weiss¹⁴, O. Schurr¹⁴, E. Ostuni¹⁶ and C. J. Glinka²⁷

Structure of Surfactant/Polymer Systems in Equilibrium and in Shear Flow

A. Palmer¹⁹, S. Amin¹⁹ and D. Wirtz¹⁹

Adsorption of Surfactants on a Trioctahedral Smectite Mineral

H. J. M. Hanley²⁷, B. Butler²⁷, C. Muzny²⁷, G. Straty²⁷ and L. Aldridge⁵

Surface Enrichment in Ultrafine Aerosols

R. Strey²³, B. Wyslouzil⁶¹, J. Cheung⁶¹ and G. Wilemski²²

MATERIALS SCIENCE

Contrast Matching Phase Analysis of RuO₂/TiO₂ AerogelsC. Merzbacher²⁶, K. Swider²⁶ and J. G. Barker²⁷**Determination of the Size Distribution of Oxide Particles in an Internally Oxidized Platinum/Aluminum Alloy**J. G. Barker²⁷ and T. Flanagan⁵⁷**Low Temperature Magnetic Scattering for SrCr_{9p}Ga_{12-9p}O₁₀**S. H. Lee²⁷ and C. Broholm¹⁹**Magnetic Scattering from Nanocrystalline Nickel**J. Weismüller⁵³ and J. G. Barker²⁷**Determination of the Size Distribution of Oxide Particles in an Internally Oxidized Platinum/Aluminum Alloy**T. Flanagan⁵⁷ and J. G. Barker²⁷**Structural Framework Stability of Silica Aerogels Rewetted with Water**C. Merzbacher²⁶, K. Swider²⁶ and J. G. Barker²⁷**Fractal Behavior of MgAl₂O₄ Ceramics**S. F. Trevino², G. Gilde² and A. J. Allen²⁷**Microstructure of Silica Fume Cements**A. J. Allen²⁷ and R. Livingston¹³**SANS Studies of Irradiation Induced Microstructural Evolution in Pressure Vessel Steels**B. Wirth⁴¹, D. Klingensmith⁴¹ and G. R. Odette⁴¹**Hydrogen Trapping at Lattice Defects in Palladium**B. Heuser⁴⁶ and J. S. King⁴⁸**Effect of Grain Size, Annealing, and Warm Compaction on the Pore Distribution in Nanocrystalline Copper and Palladium**P. G. Sanders²⁸, J. R. Weertman²⁸ and J. G. Barker²⁷**Morphological and Kinetic Study of Early Calcium-Silicate-Hydrate Gel Development during the Hydration of Cement and Tricalcium Silicate**H. M. Jennings²⁸, J. J. Thomas²⁸ and A. J. Allen²⁷**Effect of Grain Size, Annealing, Compaction Pressure, and Warm Compaction on the Pore Distribution and Sintering Behavior of Nanocrystalline Nickel**B. R. Elliott²⁸, J. R. Weertman²⁸ and J. G. Barker²⁷**Correlating Toughness and Microhardness of MoSi₂ with Microstructural Evolution during Pressure Sintering**R. Suryanarayanan⁶⁰ and A. J. Allen²⁷**In situ SANS of Alloy Corrosion**S. G. Corcoran²⁶, K. Sieradzki⁴ and D. Wiesler¹⁵**Correlation between the Electrical and Structural Properties of RuO₂-TiO₂ Aerogels**C. I. Merzbacher²⁶, K. E. Swider²⁶ and J. G. Barker²⁷**Defect Structure in Plasma Sprayed Ceramic Coatings**J. Ilavsky²⁷, A. Allen²⁷ and G. Long²⁷**Small Angle Neutron Scattering by Activated Carbons**P. Pendleton⁵⁴ and C. Howard⁵**Structural Properties of Silica-Aerogel Sensor Materials**R. F. Reidy³⁶, A. J. Allen²⁷ and S. Krueger²⁷**Micro-Porosity in Amorphous Carbons and Li-Carbons**J. E. Fischer⁵¹, P. Zhou⁵¹, Y. Sorek⁵¹ and W. Kamitakahara²⁷**Defects in Sapphire Windows**S. F. Trevino², B. Forch² and D. Mildner²⁷**Diffuse Scattering from Co/Ti, Fe/Si and Fe/Ge Polarizer Supermirrors as a Function of Magnetic Guide Field**N. Rosov²⁷ and J. G. Barker²⁷**Affiliations**¹Argonne National Lab²Army Research Lab³Australian National University⁴Arizona State University⁵Australian Nuclear Sci. & Tech.⁶Brooklyn Polytechnic University^{6a}Cavendish Laboratory, UK⁷CARB⁸Colorado School of Mines⁹Cornell University¹⁰Dupont Central R&D¹¹Dupont Marshall Laboratory

- ¹²Exxon Research and Engineering Co.
- ¹³Federal Highway Administration
- ¹⁴Georgetown University
- ¹⁵George Washington University
- ¹⁶Harvard University
- ¹⁷IBM Almaden Research Laboratory
- ¹⁸Inst. für Festkörperforschung, Germany
- ¹⁹Johns Hopkins University
- ²⁰Lawrence Livermore Laboratory
- ²¹Lehigh University
- ²²Los Alamos National Laboratory
- ²³Max Planck Inst., Goettingen, Germany
- ²⁴MIT
- ²⁵MedImmune
- ²⁶Naval Research Laboratory
- ²⁷NIST
- ²⁸Northwestern University
- ²⁹Oak Ridge National Laboratory
- ³⁰Pacific Northwest Laboratory
- ³¹Pennsylvania State University
- ³²Princeton University
- ³³Raychem Corporation
- ³⁴Rice University
- ³⁶Rothe Development, Inc.
- ³⁷Simon Fraser Univ., BC
- ³⁸Stanford University
- ³⁹Texaco R&D
- ⁴⁰University of Alabama
- ⁴¹Univ. of California at Santa Barbara
- ⁴²University of Cincinnati
- ⁴³University of Connecticut
- ⁴⁴University of Delaware
- ⁴⁵University of Guelph, Canada
- ⁴⁶University of Illinois
- ⁴⁷University of Maryland
- ⁴⁸University of Michigan
- ⁴⁹University of Missouri
- ⁵⁰University of Oklahoma
- ⁵¹University of Pennsylvania
- ⁵²University of Pittsburgh
- ⁵³Univ. Saarlandes, Germany
- ⁵⁴University of South Australia
- ⁵⁵University of Tennessee
- ⁵⁶University of Texas
- ⁵⁷University of Vermont
- ⁵⁸University of Waterloo
- ⁵⁹University of Bristol, UK
- ⁶⁰Washington University, Saint Louis
- ⁶¹Worcester Polytechnic Institute
- ⁶²Wright Patterson Air Force Base

Neutron Beam Applications

Neutron Diffraction Measurement of Residual Stress

Considerable progress has been made in the last five years at NIST in a number of areas relating to the neutron diffraction measurement of residual stress. This includes the development of new methods of sample alignment ("ALIGN"), and the development of a comprehensive data reduction program ("STRESS"). The most significant accomplishment in FY96, however, is the completion of construction, installation, and initial utilization of a new multipurpose double-axis diffractometer, "DARTS", with a number of state-of-the-art features specifically for improved residual stress measurement. The software with which data from this instrument is analyzed ("CONVERT") has been developed.

Applications of the neutron diffraction technique to engineering applications, particularly weldments, have resumed.

- **A New Double-Axis Spectrometer for Residual Stress, Texture, and Single-Crystal Analysis ("DARTS")**

A new multipurpose neutron diffraction instrument for residual stress, texture and single-crystal diffraction studies at the NIST Reactor became operational in March of 1996. The principal features are summarized below and pictured on the WWW (at <http://rrdjazz/bt8.html>).

Features:

- Large take-off angle range ($15^\circ \leq 2\theta_m \leq 120^\circ$)
- Large specimen size range (0 to 50 kg)
- x,y,z translation (15 cm \times 15 cm \times 20 cm)
- Remote control monochromator exchange
- Variable beam apertures (position and size)
- Pre-monochromator beam limitation
- PG filter toggle
- "Quick shutter" (beam photography)
- Position sensitive detector

A number of the items listed above are

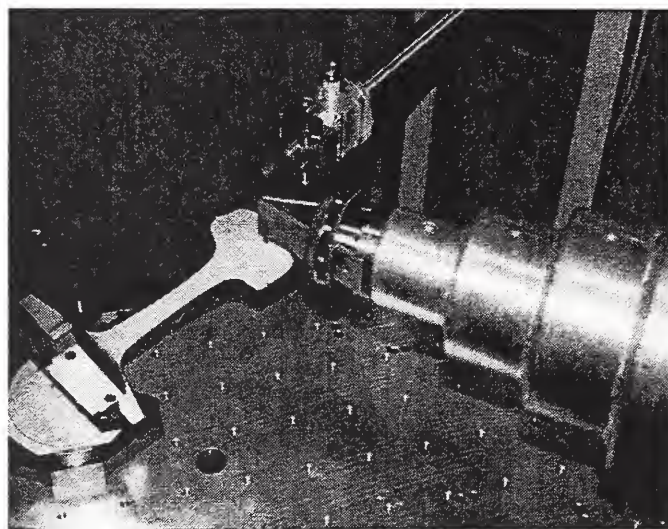


Figure 1. Determination of the residual stresses in a slice of rail by means of the new, state-of-the-art residual stress diffractometer at BT-8 of the NIST Research Reactor.

unique to DARTS and have proved to be enormously important in facilitating sample handling, in maximizing the quality of data (e.g. signal/noise), and increasing "thru-put" relative to the instrument at BT-6 previously used for these measurements. In particular, the capability of accommodating large, heavy specimens is facilitated by the ability to withdraw the pre- and post-sample apertures (shown in Fig. 1), rotate and translate the sample, and then reposition the apertures *all under computer control, programmable in a command file*. This feature significantly reduces the number of times that a specimen must be removed from the sample table, which always requires a time-consuming re-alignment. Also, a number of safety features, unique to DARTS, have been incorporated, including carefully-integrated shielding which minimizes neutron background even up to the reactor face.

Comparison of measurements at DARTS and the BT-6 instrument on comparable steel samples indicate that a "target" $\Delta d/d$ sensitivity

(e.g. 5×10^{-5}) can be achieved ≈ 5 times faster on DARTS than on the old instrument. The planned addition of focussing monochromators should increase this even more.

• Residual Stress Measurements

Railroad rails. The John A. Volpe Center of the Federal Railroad Administration (FRA) has been conducting a long term research project on rail integrity. A damage tolerance basis for frequency of in-service-inspection of railroad rail was developed by Orringer [1], and the FRA Office of Safety has incorporated elements of that work in a rule-making now in progress. The research included development of a fracture mechanics model for estimating the propagation lives of internal transverse fatigue cracks in rail heads, commonly referred to by industry track engineers as detail fracture (DF) [2].

A sensitivity study conducted with the DF model brought to light the fact that the axial residual stress in the rail head is one of the strongest influences on DF slow crack growth life [3]. Parallel studies led to the development of a theoretical method for estimating rail residual stresses, based on a hypothesis that there exists a shakedown stress state independent of the axial coordinate [4], and also led to an investigation of numerous methods for experimental determination of rail residual stress.

From the experimental investigations there has now emerged an approach believed to possess a combination of accuracy and economy suitable for a standard technique. This approach, known as the Transverse/Oblique Slice Thermal Moire method (TOSTM) [5], involves both measurement and data reduction procedures. The measurement procedure consists of removal of transverse and oblique slices approximately 10 mm thick from the rail sample, face grinding and plating with a heat resistant cladding, photo-etching of a cross grating on the clad surface, stress relief at 482°C, and determination of the associated in-plane displacements by means of grating interferometry ("Moire"). The data reduction procedure involves the ap-

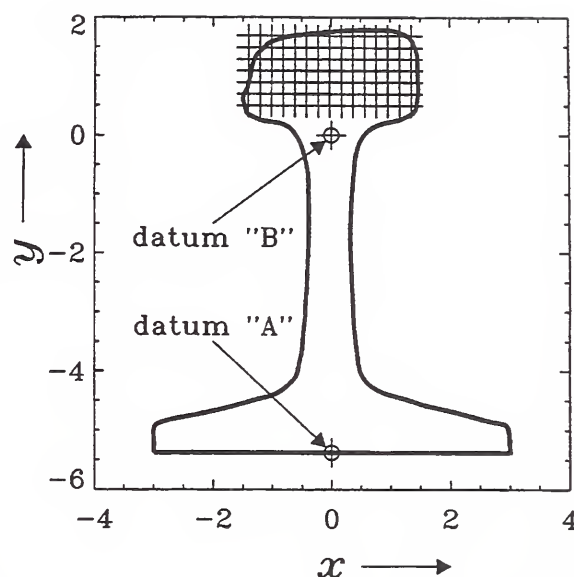


Figure 2. Residual stress measurement mesh. The measurement points are at the intersection points of the mesh. The points are 5 mm apart in both the x and y directions. The depth location of the points is 3.175 mm ($1/8''$) below the surface. The relative location of the mesh is determined by so called entering curves on the outer circumference of the part. The size of the probe volume is approximately $2 \times 2 \times 2 \text{ mm}^3$ (somewhat bigger due to some divergence of the primary and diffracted beams). The x and y dimensions are given in inches, commensurate with DOT documents ($25.4 \text{ mm} = 1''$).

plication of solid mechanics principles to reconstruct, from the transverse and oblique slice in-plane measurements, the axial component of residual stress which was completely lost from the transverse slice when it was removed from the rail sample, as well as Poisson effect losses from in-plane components.

To date it has not been possible to obtain comparative results with two or more of the independent measurement methods on the same rail sample. Difficult logistics ended a previous attempt at the Institute Laue Langevin [6] to compare some of the destructive techniques with neutron diffraction results. Despite the fact that the TOSTM method has since emerged as the best destructive approach, it is still important to establish a base of comparison between

the results obtained by this method and results obtained by an in situ measurement technique such as residual stress measurements by means of neutron beam diffraction.

DARTS has been used to complete the first phase of the needed measurements under Agreement Number DTRS-57-95-X-00075 76-0813. The specimen was a 6.35 mm transverse slice of railroad track shown on DARTS in Fig. 1. This slice is taken from a track section that has been subjected to a specified load in the Volpe Test Center's High Tonnage Loop. It is obvious that the residual stress field in such a thin slice is not the same as in the completely intact railroad section. In particular, the stress in the longitudinal direction of the rail (perpendicular to the section lines) will be almost completely relieved. A nominal sampling volume of 2 mm \times 2 mm \times 2 mm was used. However, horizontal and vertical divergence of the beam make the true sampling volume \approx 2.4 mm \times 2.4 mm \times 2.4 mm. In Fig. 2 a tracing of the 6.35 mm thick rail slice is depicted. Superimposed on the picture is the mesh of positions at which stress measurements have been performed. The mesh is built of points that are separated 5 mm in both the x and y directions.

The relationship between the rail outline and the measurement mesh is established through so called "entering curves". The entering curve technique [7] has proved very useful for positioning this class of specimens. It is based on the detection of (diffracted) neutron intensity as a function of specimen position, which in turn is determined by the amount of sample from which the scattered neutrons can reach the detector. For a given type of geometry (reflection, transmission, etc.) the intensity as a function of the relative specimen position can be easily modeled based on straightforward geometry. Every time the specimen is remounted to achieve a different orientation of \mathbf{Q} (the momentum transfer or probe direction) this positioning of the specimen has been repeated to ensure that the subsequent strain measurements are done on the same mesh. Strain measurements in the rail slice are

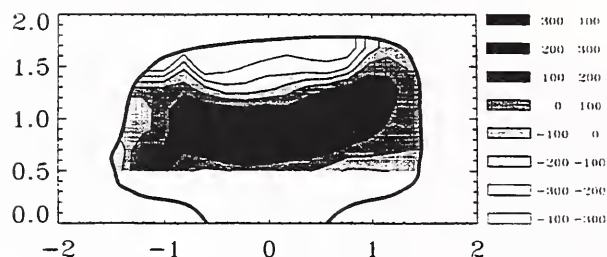


Figure 3. Contour map of the residual stresses σ_{xx} in the rail head. The origin position $(x, y) = (0, 0)$ corresponds to datum "B" in Fig. 2. The x and y dimensions are given in inches, commensurate with the DOT agreement (1" = 25.4 mm).

performed at 5 different orientations of \mathbf{Q} . This particular set of orientations allows us to extract σ_{xx} , σ_{yy} , σ_{zz} and σ_{xy} from the data without assumptions. No information about σ_{xz} and σ_{yz} can be obtained using the chosen set of orientations.

The stress free lattice parameter d_0 was obtained from the extremities of the base region of the rail slice. It was confirmed independently by changing the orientation of the sample and measuring d again that this region was very close to stress free so that we could forego the process of cutting little coupons out of the rail slice. The value for the stress free lattice parameter that was found this way was $d = 2.03218 \pm 0.00010$ Å (standard uncertainty). The diffraction elastic constants that were used in this evaluation were: $S_1(110) = -1.3 \times 10^{-6}$ MPa $^{-1}$ and $S_2(110)/2 = 5.87 \times 10^{-6}$ MPa $^{-1}$. These values have been obtained from a previous calibration on a different steel sample. They are appropriate for this steel as well.

The five different d -spacings obtained at five different orientations at every point of the mesh yield, via least squares fits σ_{xx} , σ_{yy} , σ_{zz} , and σ_{xy} . The particular choice of mesh points lends itself very well to the presentation of the data in the form of contour plots, an example of which is shown in Fig. 3. Overall, the present results show that with DARTS very precise measure-

ments of the residual stress state in the rail head can be made. The comparison with modeling efforts and the TOSTM method will be done at a later date when phase 2 results are obtained. From the present data we can say the following [8]:

1. The σ_{zz} data are consistent with the expectation that the stresses perpendicular to the thin slice would be relieved (i.e. would have become equal to zero). Finding σ_{zz} to be this close to zero throughout the rail head supports the assumption that the stress free lattice parameter d_0 obtained from the base part of the slice is the correct one. This opens the possibility to do measurements on similar rail slices made of this material without the need for extracting coupons out of the material for d_0 determination.

2. σ_{xx} and σ_{yy} both show compressive stresses at the top surface of the rail head. These are balanced by tensile stresses in the bulk. This is in agreement with the notion that the top surface has been plastically deformed under the pressure load of the train wheel, not unlike what happens in a process like shot peening. In the beginning of the rail life this is a process that will protect the top surface of the rail against crack initiation. This "rotection" is at the expense of the high tensile stresses in the interior. There is reason to believe that in the intact rail (i.e. a non sectioned one) the stresses in the longitudinal direction (here σ_{zz}) will also be tensile. If this is the case a hydrostatic tension situation might develop in the interior of the rail head. This would eventually lead to cracking of the rail head from the rail interior on outward.

Bent Pipes. Two mild steel tubes, of outside diameter 168 mm, wall thickness 7 mm and length 1000 mm, were subjected to four-point bends. Tube I is seamless, tube II has a weld parallel to the cylindrical axis. After bending, the central 260 mm, together with end pieces, were cut out of the tubes for neutron diffraction measurements (Fig. 4). Using a nominal $2 \times 2 \times 2 \text{ mm}^3$ gauge volume, strain components were measured as a function of depth beneath

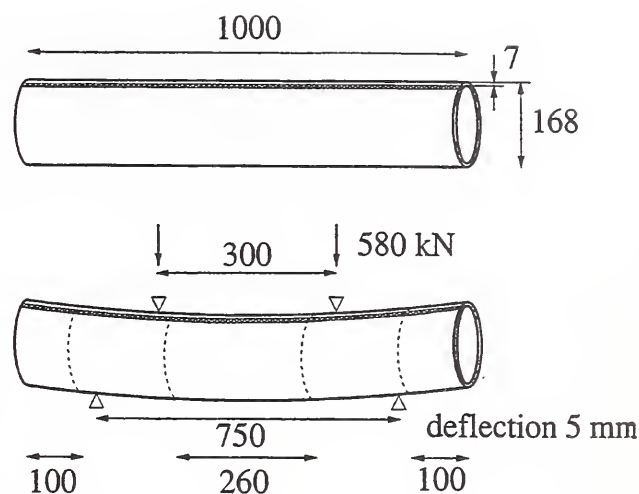


Figure 4. Schematic of the bent tube before bending and cutting. The weld parallels the cylinder axis. The central 260 mm and the outer 100 mm portions are cut out and used for the neutron measurements.

the surface at 22.5° intervals around the circumference of the unwelded tube at the mid-plane, and with higher density around the weld on the bent tube.

At each measurement point, five Q -directions were examined in the r - θ plane, and one along the axial direction. The value of d_0 was obtained from the average of several position and orientation measurements on the tube end pieces. Diffraction elastic constants for the [110] reflection in steel were obtained—as for the rail head—from earlier measurements. In the upper part of Fig. 5 results are shown for the axial residual stresses for the region between 2 and 5 mm of the 7 mm thick wall. The lower part of the figure shows the measured axial residual stresses measured along a line 3.9 mm in from the inner surface (i.e. corresponding to the horizontal line in the contour plot). Each plot covers the full 360° around the tube.

It should be noted that the four point bending fixture was positioned along 0 and 180° on the tube and that the measured stresses are essentially mirror symmetric about the plane passing through these positions. It is also of interest that at $\sim 90^\circ$ away from the bend points a sharp compressive to tensile transition occurs in the

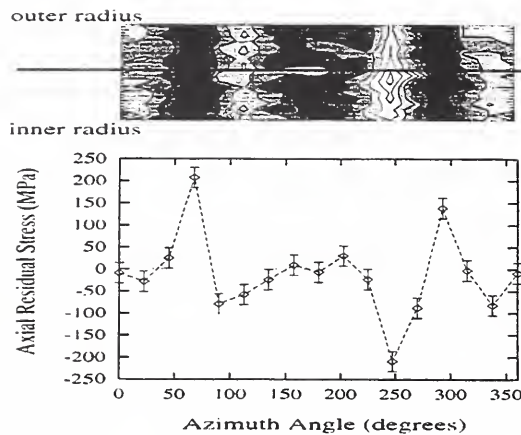


Figure 5. The measured axial residual stress distribution for the bent, unwelded tube. The contour plot shows the region from ~ 2 mm to ~ 5 mm of the 7 mm thick wall. The lower plot shows the measured axial residual stress distribution at 3.9 mm from the inner surface corresponding to the horizontal line in the contour plot.

stress profile. We expect to compare this with an FE calculation and with results obtained with magnetic probes.

Other Studies

1) As reported previously, the confirmation that d_0 can be correlated with the FWHM is key to the truly non-destructive determination of residual stresses around weldments by neutron diffraction. If not correlatable, coupons for d_0 determinations will have to be extracted from specimens at the gauge-volume positions. This project has been resumed, but larger EDMed coupons ($> 2 \times 2 \times 2$ mm³) in which the whole gauge volume would be contained appear to be needed.

2) The determination of residual stresses in structural members of bridges (DOT sponsored) has been undertaken. This work is being performed in collaboration with Materials Reliability Division (NIST/Boulder) and seeks to provide reference results which can be used to test and/or calibrate field-portable techniques. Initial efforts—now completed—have focussed on determination of residual stresses in pieces cut from large eyebars taken from bridge structures.

3) Two projects are underway in the area of the determination of residual stresses in surface coatings. One is partially supported by ATP funding and is collaborative with Prof. H. Herman and a Ph.D student of SUNY/Stony Brook; the second involves specimens which have been prepared and FE modeled at the Idaho National Engineering Laboratory. In both projects the interest is in ceramic coatings such as alumina attached to metal substrates such as aluminum via graded interfaces. DARTS measurements on an aluminum/alumina sample from INEL have been completed; the analysis of the data was in progress at the end of FY96.

4) Two projects on determining the residual stress distribution in aluminum-alloy bars were completed. The first, with scientists at Alcoa, was not successful because of the very large grain size of the experimental alloy used. Some progress was made in developing methodology to determine stresses in such a specimen, and will be continued in the future. The second project, with scientists at Boeing/Wichita, was successful because of the fine grain of the 7050-T7451 plate examined. The neutron results are being compared at Boeing with results of FE calculations.

References

- [1] O. Orringer, DOT Transportation Systems Center, Cambridge, MA, DOT/FRA/ORD-90/05, June 1990.
- [2] O. Orringer, Y.H. Tang, J.E. Gordon, D.Y. Jeong, J.M. Morris, and A. B. Perlman, DOT Transportation Systems Center, Cambridge, MA, DOT/FRA/ORD-88/13, October 1988.
- [3] O. Orringer, Proc. International Symposium on Rail Steels - Developments, Performance and Manufacturing, (B.L. Bramfitt, R.K. Steele, and J.H. Martens, ed.), AIME Iron and Steel Society, 149-159 (1993).
- [4] J. Orkisz and M. Holowinski, Rail Quality and Maintenance for Modern Railway Operation, (J. J. Kalker, D.F. Cannon, and O. Orringer, ed.), Kluwer Academic Publishers, Dordrecht, The Netherlands, 1993, pp. 273-296.

- [5] Y. Y. Wang, X. Shen, and F. P. Chiang, Proc. 4th International Conference on Contact Mechanics and Wear of Rail/Wheel Systems, Vancouver, BC, 1994 (in press).
- [6] G. A. Webster et al., Residual Stress in Rails, *ibid.*, pp. 143-152.
- [7] P. C. Brand and H. J. Prask, Journal of Applied Crystallography, 27, 164-176, 1994.
- [8] P. C. Brand, H. J. Prask and G. E. Hicho, NISTIR 5912, October 1996, 27pp.

Neutron Diffraction Measurement of Texture

DARTS has been utilized for texture (or similar) determinations in several projects. The characterization of structural members of bridges (DOT sponsored) includes texture studies in parallel with the residual strain measurements. This work is being performed in collaboration with Materials Reliability Division (NIST/Boulder) who are characterizing the same specimens by magnetic and ultrasonic measurements. Neutron texture measurements have been completed on three pieces cut from large eyebars taken from bridge structures.

Neutron diffraction has been investigated as a possible technique for assessing the quality of sapphire single crystals used as windows in an Air Force missile system.

Neutron Autoradiography Program

- **Autoradiography Study of Rembrandt's *An Old Man in Military Costume***

The J. Paul Getty Museum in Los Angeles has in its collection a striking portrait by Rembrandt known as *An Old Man in Military Costume* (Fig. 6) which, in the past, has been the subject of considerable debate concerning both its attribution and dating. The picture had been traditionally dated to around 1629, and was generally accepted as being by Rembrandt himself. However, when the Rembrandt Research Project published the picture in its *Corpus of Rembrandt Paintings* the attribution was questioned due to some apparent dissimilarities in the handling of

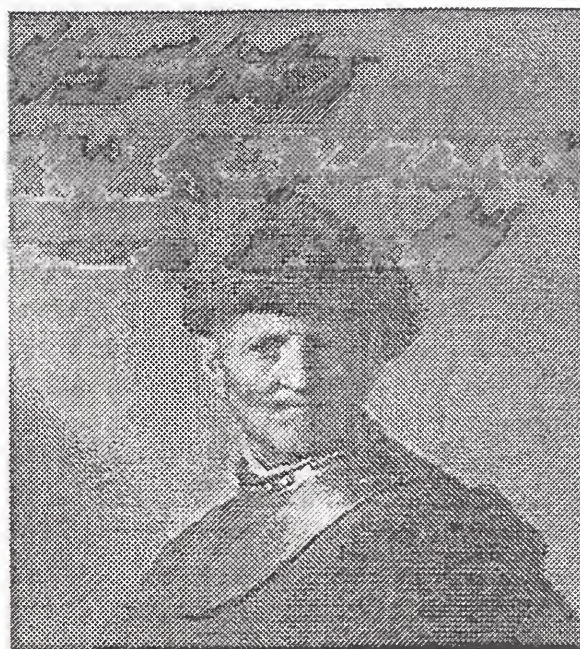


Figure 6. *An Old Man in a Military Costume.* The actual size is approximately 66 cm high by 51 cm wide.

the portrait with other autograph pictures from the late 1620's. Most recently, Walter Liedtke of the Metropolitan Museum of Art published an article re-affirming Rembrandt's authorship of the picture, but suggested a later date, to 1631 or 1632. This change in dating answered some of the stylistic anomalies which had been noted by earlier attempts to date the picture to the late 1620's.

When the painting was first acquired by the Museum (in 1978) an x-ray was taken which revealed the presence of another portrait underneath the visible surface. The underlying portrait was visible as a ghostly, upside-down image in the radiograph; the image was very difficult to read, however, because of interference from the additional layers of paint (most of which contained some degree of lead white) which had been used in the portrait of *An Old Man in Military Costume*. It was always hoped that autoradiography might provide some more legible images of the underlying portrait, and that this might help resolve some of the questions concerning attribution and dating.

In the Spring of 1996, the painting was brought to the Reactor Radiation Division at NIST for autoradiographic study. As hoped, a series of images were produced which provided a legible impression of the underlying portrait. The most useful images in this autoradiographic series were produced on imaging plates. The digital image produced by these re-usable plates could be enhanced and manipulated in such a way that the underlying portrait became even more legible than it was on the traditional autoradiographic films. Not only were the features of the face, ear and hair clearly visible, but the simple costume of the underlying figure was legible as well (Fig. 7). Details of the brushwork in the underlying portrait were found to be very close in form and feeling to Rembrandt's paintings of the early 1630's. The underlying portrait also appeared to have many stylistic similarities to several other Rembrandt portraits, some of which are signed and dated 1631 or 1632. This new information will be of considerable importance to art historians in their future studies of the painting.

Several of the technical details relating to the methodology are worth noting. For example, this painting contains unusually low quantity of elements such as iron, cobalt, or antimony in its pigments that would have produced relatively long lived radioactive isotopes in neutron activation. The radioactivity generated in the painting was decayed to practically background level in just one day. The traditional film method only registered the initial radioactivity distribution in the painting and was not sensitive enough to produce any subsequent autoradiographs from longer lived isotopes. The digital storage photostimulable phosphor (SPP) imaging plates which are 100 times more sensitive than x-ray films, on the other hand, produced useful autoradiographs.

The digital autoradiographic images of the painting generated by the SPP imaging plates are compiled in CD-ROM form and can be readily accessed and analyzed on a PC. The advantages of increased sensitivity, which can be used

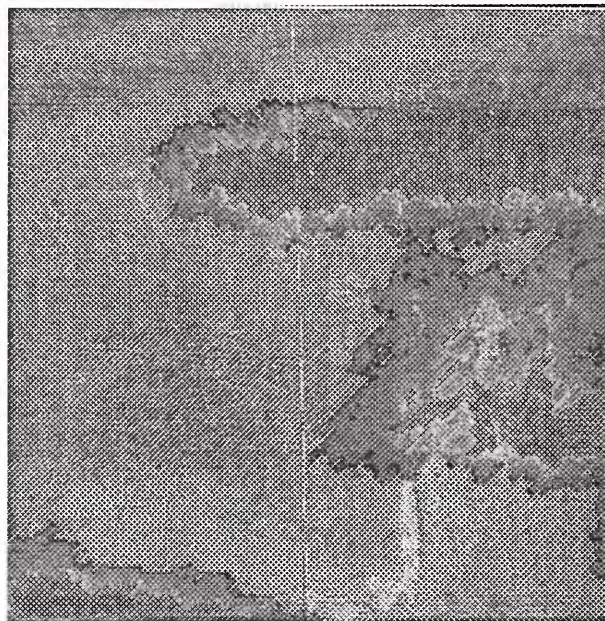


Figure 7. An SPP image plate autoradiograph of the central portion of the painting of Fig. 6. This image corresponds to the central $\approx 20 \text{ cm} \times 20 \text{ cm}$ of the painting and is rotated 180° with respect to the painting. The vertical line is the boundary between two plates.

to reduce reactor activation time or to generate more autoradiographs for detailed study, readily accessible computer processing of a digitized image and the elimination of the need for labor intensive film development can greatly enhance the utility of the autoradiography technique.

• Detector Development

The SPP technology is being applied in the design of a sensitive, high resolution neutron area detector which is free of gamma and x-ray interference and is not count rate limited. A two-step process is utilized in which a large-area metal converter foil is first activated in a neutron field followed by an autoradiography procedure to transfer the neutron field information from the foil to an imaging sensor. The autoradiography is done outside of the neutron field with either of the two new charged-particle imaging technologies, the SPP imaging plates and the micro-channel array detector. Both imaging sen-

sors exhibit linear response over a wide dynamic range ($\geq 10^5$). Compared to conventional neutron detectors the inherent high resolution of the new imaging sensors ($\geq 25 \mu\text{m}$ for SPP imaging plates) will allow the converter foil to be placed much closer to the neutron scattering sample without compromising measurement precision. This—coupled with the fact that no shielding is required for the foil—results in a compact, low-cost detector for scattering or diffraction measurements. This allows multiple experiments to share the same beam line, increasing the utilization of neutrons. The foil can be of any size and can be formed into different shapes to cover *all* solid angles of interest without detector movement. This two-step approach eliminates any non-neutron radiation interference and offers the flexibility to tailor the type, shape and size of converter, and the activation and imaging procedures to specific experimental conditions. It can significantly reduce the size, cost, and complexity of neutron detectors, while improving precision and throughput. A sensitivity of $1 \text{ n/cm}^2/\text{s}$ is anticipated with this new approach. The measurement time for mapping a complete scattering or diffraction profile may be in terms of minutes, thus offering the potential for measurements under dynamic conditions.

Research Topics

Evaluation of New Neutron Area-Detectors
Y. T. Cheng^{7,8}

“DARTS”: A New Neutron Diffractometer for Residual Stress Measurement, Texture Determination, and Single Crystal Diffraction
P. C. Brand⁸, C. S. Choi⁸, and H. J. Prask⁸, S. Allah⁹ and A. Sangariyavantich¹¹

“CONVERT”: A New Code for Data Reduction in Neutron Diffraction Residual Stress Measurements
P. C. Brand⁸

Software Development for Texture Studies on “DARTS”
P. C. Brand⁸ and C. S. Choi⁸

Possible Correlation of FWHM and d_o for Dif-

fraction Peaks in Weldments
P. C. Brand⁸ and H. J. Prask⁸

Evolution of Residual Stresses Around a V-notch Multipass Weld in a Steel Plate
J. Blackburn¹⁴, P. C. Brand⁸, R. J. Fields⁸ and H. J. Prask⁸

Fabrication and Characterization of Standard Reference Specimens for Residual Stress Measurement Techniques
H. J. Prask⁸ and P. C. Brand⁸

Spot Welded High-Strength Low Alloy Steel: Measurement and Modeling of Residual Stresses
P. C. Brand⁸, J. Blackburn¹⁴, R. J. Fields⁸, H. J. Prask⁸, Z. Feng⁵, Y. Y. Zhu¹⁰ and T. Zacharia¹⁰

Determination of Residual Stresses in an Al plate with Very Large Grains
P. C. Brand⁸, H. J. Prask⁸ and H. Weiland²

Residual Stresses in 7050-T7451 Aluminum Plate
P. C. Brand⁸, H. J. Prask⁸ and D. Burford³

Using Neutron Depth Profiling to Orient a Single Crystal Invisible in a Boule
N. Rosov⁸ and P. C. Brand⁸

Residual Stresses in a Weld in Inconel-617
P. C. Brand⁸, H. J. Prask⁸, T. N. Crump⁴ and E. Drescher-Krasicka⁸

Residual Stresses in Welded Aluminum Plates
P. C. Brand⁸ and A. Stern⁸

Residual Stresses around Welds and Cracks in Infrastructure Components
P. C. Brand⁸, H. J. Prask⁸, R. Livingston¹⁶ and D. McColskey^{8a}

Residual Stress Measurements on Railroad Rails
P. C. Brand⁸, O. Orringer¹⁵, G. M. Hitcho⁸ and H. J. Prask⁸

Residual Stress Analysis of Bent Steel Pipes
P. C. Brand⁸, J. Goff¹², M. T. Hutchings¹, D. J. Buttle¹ and H. J. Prask⁸

Residual Stresses in Al-Metal-Matrix Composites
H. J. Prask⁸, P. C. Brand⁸ and H. M. Ledbetter^{8a}

Neutron Diffraction Validation of Residual Stress Measurements by Scanning Acoustic Imaging

P. C. Brand⁸, H. J. Prask⁸ and E. Drescher-Krasicka⁸

Neutron Autoradiography of Paintings

Y.-T. Cheng^{7,8} and J. Olin¹³

Neutron Autoradiography of Rembrandt's

"An Old Man in a Military Costume"

Y.-T. Cheng^{7,8}, J. Olin¹³, M. Leonand⁶ and H. J. Prask⁸

Affiliations

¹A.E.A. Technology, Harwell, U.K.

²Alcoa Tech. Center

³Boeing Comm. Airplane Grp. I

⁴Dupont

⁵Edison Welding Inst., Ohio

⁶The J. Paul Getty Museum

⁷Neutek Inc.

⁸NIST

^{8a}NIST-Boulder

⁹Nuclear Res. Center, Egypt

¹⁰Oak Ridge National Lab.

¹¹Office of Atomic Energy for Peace, Thailand

¹²Oxford Univ., U.K.\

¹³Smithsonian Institution

¹⁴U.S. Navy david Taylor Res. Center

¹⁵U.S. Dept. of Transportation

¹⁶Federal Highway Administration

Analytical Chemistry

Nuclear Methods Group

The development and application of nuclear analytical techniques for elemental compositional analysis with greater accuracy, higher sensitivity and better selectivity are the goals of the Nuclear Methods Group (NMG). A high level of competence has been developed in both instrumental and radiochemical neutron activation analysis (INAA and RNAA). In addition, the group has pioneered the use of neutron beams as analytical probes with both prompt gamma activation analysis (PGAA) and neutron depth profiling (NDP). PGAA measures the total amount of an analyte present throughout a sample by the analysis of the prompt gamma-rays emitted during neutron capture. NDP, on the other hand, determines concentrations of several important elements (isotopes) as a function of depth within the first few micrometers of a surface by energy analysis of the prompt charged-particles emitted during neutron bombardment. These techniques (INAA, RNAA, PGAA, and NDP) provide a powerful combination of complementary tools to address a wide variety of analytical problems of great importance in science and technology. During the past several years, a large part of the Group's efforts has been directed at the exploitation of the analytical applications of the guided cold-neutron beams available at the new Cold Neutron Research Facility (CNRF) at the NIST reactor. The Group's involvement has been to design and construct state-of-the-art instruments for both PGAA and NDP using cold neutrons, while retaining and utilizing our existing expertise in INAA and RNAA. During the previous year the NIST reactor had been shut down for major improvements. These included the installation of new heat exchangers, a new (liquid hydrogen) cold source and refrigerator, and completion of the installation of the neutron guides into the guide hall. The reactor resumed full 20 MW power in September 1995. The major im-

provement for our beam operations has been the increase in the cold-neutron current density of a factor of four or more delivered to the analytical instruments.

• SRM Analysis and Certification

The nuclear analytical methods have continued to contribute to the Standard Reference Material (SRM) certification effort; this year's efforts include measurements performed on a number of SRMs including: Highly Contaminated Sediment, two soils, two Petroleum Cokes, three Zeolites, an Arsenic Implant in Silicon, and two Mussel Tissues. Group members are serving as Technical Champions for several of these new SRMs, and as such are responsible for scientific decisions made throughout the production and certification processes of these materials.

• Neutron Activation Analysis Method Development

Although NAA has been in use for many years, new developments continue to provide improvements in detection sensitivities, elemental specificity, precision, and overall accuracy. Particularly in the last few years, the NAA technique has become one of the primary analytical techniques for the certification of elemental concentrations in biological SRMs. One important reason is that NAA has unique quality assurance characteristics that provide accurate analyses and often allow the analytical values obtained to be internally evaluated and cross checked. In addition, the capability of INAA for nondestructive analyses (eliminating dissolution errors) and for homogeneity determinations at the $\mu\text{g/kg}$ level for sample sizes as low as 100 mg has made this technique an integral component of trace element analyses at NIST. Furthermore, the relative matrix independence of NAA has resulted in applications to a wide variety of materials including high temperature superconductors, soils, fly ash, rocks and ores, foods, and

a many types of biological materials.

Optimizing the gamma-ray counting conditions for the various forms of NAA can generally improve precision, increase sample throughput, or both. This is especially important when counting the very small amount of radioactivity produced by ultratrace quantities of impurities, for example, in semiconductor silicon or (after radiochemical separations) noble metals in human tissue. Sensitivity can be gained by using high-efficiency, low-background detectors; a subsidiary benefit is that less radioactive material needs to be generated, handled, and discarded. The sources of background in gamma-ray detectors have been reexamined at NIST and elsewhere in recent years, resulting in improved understanding. It is now clear that with care in the selection of the materials from which the detector and the shielding are constructed, the only important source of gamma-ray background is the interaction of cosmic ray particles with the shield and the detector itself. Experiments are underway to reduce this component by active, anti-cosmic ray shielding.

A new rapid pneumatic tube system was recently designed, constructed, and inserted into the NIST nuclear reactor this year. This new computer controlled facility uses CO₂ at 35 lbs. pressure to propel the irradiated sample out of the irradiation terminal and into the counting station approximately 10 feet away in 475 ± 10 milliseconds (precision), with an estimated accuracy of ± 3 ms. Infrared sensors are used to measure the location and travel speed of the irradiated capsule, thus providing the required exact irradiation and decay times needed for the calculation of chemical concentrations in the irradiated samples. This new pneumatic tube, designated RT-2, has a highly thermalized neutron spectrum like our other, slower pneumatic tube systems, and a neutron fluence rate of $5.0 \times 10^{13} \text{ n}\cdot\text{cm}^{-2}\text{s}^{-1}$, somewhat higher than the RT-4 pneumatic tube facility but less than RT-1. Characterization measurements are currently being carried out on this facility, which when completed will allow for its routine use. The

application of short half-life activation products in this facility will allow the determination of nuclides with half lives as low as one second. This will provide NIST with the capability for accurately determining, for example, fluorine through ²⁰F ($t_{1/2}=11.00$ s) at low levels. Another new capability will be the improved determination of selenium through use of ^{77m}Se ($t_{1/2}=17.4$ s). A new possibility is the determination of lead (at elevated levels) using ^{207m}Pb ($t_{1/2}=0.8$ s). A future modification is planned to provide a second position located in an area with a highly epithermal component to the neutron spectrum. This second location will offer the possibility of substantially improving sensitivity for the determination of iodine and other elements with high resonance integrals. Final approval for routine use of this facility in its current configuration is expected in FY97.

A new radiochemical separations project has been initiated to develop methods to measure additional elements, such as phosphorus and sulfur, which do not decay with the emission of characteristic gamma rays. Quantitation is accomplished by beta counting the isolated activation products of interest. Efforts are currently underway to develop a radiochemical procedure for the measurement of P in steels. Preliminary analyses of P in existing Steel SRM are in agreement with certified values, while the detection limit for the method is $< 10 \text{ ng/g}$.

• Specimen Bank Research

The NMG continues to support the National Biomonitoring Specimen Bank (NBSB) research programs through analyses of selected banked materials and by providing quality assurance (QA) for the laboratories of other agencies that analyze banked materials. These programs have included the EPA Human Liver Project (HLP), the NOAA National Status and Trends (NS&T) program, the NCI Micronutrient Program, the IAEA/NIST/FDA/USDA Total Diet Study, the two NOAA marine mammal tissue banks are under the Marine Mammal Health and Stranding Response Program. In addition, the NIST

participation in intercalibration exercises with the project laboratories and the development of QA materials for various marine analyses have helped to enhance the quality of the analytical results used in the assessment of the environmental health of the nation.

- **Superconductivity Research**

The Group has undertaken an active role in the NIST program on high-temperature superconductivity research. In cooperation with materials scientists at NIST and elsewhere, we are measuring impurities in superconductor starting materials and final products, as well as determining the stoichiometry of major constituents. The needs of the superconductivity program have stimulated the development of methods for accurate, rapid analysis of these materials by both NAA and PGAA. In particular, an effort is underway to establish monitor-activation analysis techniques at NIST. Conventional NAA requires the irradiation and counting of a standard for each element to be determined in a given sample. Preparing numerous standards requires much labor, and the accurate quantitation of unanticipated activities in the gamma spectrum is not possible. An elegant solution has been pioneered in Europe, which uses a dimensionless compound nuclear constant called k_0 , which can be measured far more accurately than the cross sections and other constants that comprise it. We have begun to apply this approach to cold-neutron PGAA, which is especially subject to systematic errors from neutron scattering effects, and have found that the k_0 approach for determining element ratios offers all the advantages that internal standards offer other methods. We intend to apply the k_0 formalism to traditional NAA as well.

- **Neutron Depth Profiling**

NDP is a nondestructive analytical technique which measures the concentrations, and determines the near surface distributions, of selected elements. Increasingly, manufacturers of semiconductor components are finding NDP to be

an important tool for calibration, quality control and basic research. The NDP instrument is located at the end of the new NG-0 cold neutron curved guide which has a coating of nickel-titanium supermirror. This gives an increase of about a factor of 3 in neutron current density relative to a ^{58}Ni guide. The two-meter long curved section has a radius of curvature of 57 m, which is sufficient to remove line-of-sight fast neutrons and gamma rays from the cold neutron beam. The beam area at the guide exit is 3 cm x 5 cm and the neutron fluence rate is $2.45 \pm 0.05 \times 10^9 \text{ n} \cdot \text{cm}^{-2} \text{ s}^{-1}$.

Current experiments of interest at the NDP instrument include the measurement of nitrogen profiles in thin TiN films in conjunction with Intel Corp., and the measurement of lithium migration in electrochromic films in cooperation with SAGE Electrochromics. Depth profiling of nitrogen is based on the measurements of the proton from the $^{14}\text{N}(n,p)^{14}\text{C}$ reaction. These nitrogen measurements are the first quantitative evaluation of nitrogen concentrations since the instrument was reconfigured and placed on the curved neutron guide. The advantages of this new arrangement are apparent in the higher signal rate and the lower background rate compared with nitrogen measurements made at the previous instrument location.

The lithium profiles are based on the measurement of the energy of alpha particles from the $^6\text{Li}(n,\alpha)^3\text{H}$ reaction. The energy of the detected particle provides a direct measurement of the depth of the originating lithium nucleus. In this case, in situ measurements were taken with different bias voltages on the film layers. The bias causes the lithium to migrate between different layers and changes the optical transparency of the film.

- **Prompt-Gamma Activation Analysis**

PGAA allows accurate, nondestructive measurements of a number of elements, including H, B, C, N, S and Cd. Recent improvements to the cold neutron prompt gamma activation analysis (CNPGAA) instrument, con-

structed as part of the CNRF, have greatly improved its measurement capabilities. Furthermore, both the CNPGAA and University of Maryland-NIST thermal-neutron PGAA instruments have found research applications in many diverse areas within chemistry, physics, and materials sciences.

During the reactor shutdown considerable effort was directed toward the upgrade of the CNPGAA instrument in the Cold Neutron Research Facility. The installation of the new liquid hydrogen cold source and the increase in reactor power from 15 to 20 MW have resulted in a factor of 6 improvement in neutron capture rate at the PGAA station, while PGAA sensitivities ($\text{counts}\cdot\text{mg}^{-1}\cdot\text{s}^{-1}$) for most elements are a factor of 3-4 better than measured before the shutdown. The addition of shielding boxes filled with poured lead and steel shot results not only in a lower gamma-ray background for measurements but in decreased radiation exposure for users of the instrument. The shielding walls serve to reduce gamma-ray background from capture of Si and H in a one meter section of neutron guide previously visible to the PGAA detector. As a result of the improvement in sensitivities and lower background, elemental detection limits have improved by up to a factor of 2.

Additional modifications to the instrument have improved measurement accuracy and have yielded a more user-friendly instrument. The addition of redesigned gamma-ray and neutron collimators with different sized apertures allows better control of the gamma-ray signal reaching the detector. Reproducible counting geometry is achieved by mounting sample and detector together on a moving plate, with the sample at a fixed distance from the detector. The moving plate rides on a pair of high precision rails to ensure accurate positioning of the sample in the neutron beam. A stepping motor drives the plate forward (toward the neutron guide) to position the sample in the beam and back again for sample mounting, with a reproducibility better than $50\text{ }\mu\text{m}$ on all these axes.

Recent measurements by CNPGAA involve

both continuing and new applications. The determination of hydrogen in titanium alloys continues to be an important application due to the ability of H to embrittle Ti and other metals. We have recently determined H at levels below 100 mg/kg in a new set of Ti-alloy jet-engine turbine blades, and in the Ti Al V (alloy) sheet metal which will be used to prepare a series of prototype standard reference materials. Other continuing applications of PGAA involve the measurement of H in a wide variety of materials including: nanocrystalline metals; hydrofluorocarbons; solid acid catalysts (along with other elements of interest); solid proton conductors, and amorphous carbons. New applications include measurement of boron in samples of high-purity quartz and in tree rings from Brazil, nitrogen in reference materials, chlorine in highway materials, and trace pollutants in marine sediments.

• Focused Neutron Research

A long-range program to explore and develop the analytical applications of focused beams of cold neutrons continues within the Group. The goal of this research is to produce beams of neutrons which have intensities several orders of magnitude greater than previously available. The new hydrogen cold source has given the neutron beams an increase of up to six times in the current densities delivered by neutron guides at longer wavelengths. This enables neutron absorption measurements on samples with fine (submillimeter) spatial resolution, by increasing the current densities even further using focusing techniques. Such beams will greatly enhance the capabilities of both PGAA and NDP and increase their elemental sensitivities, and may ultimately lead to a neutron probe for microanalysis.

Grazing-angle reflective optics involving multiple mirror reflection from smooth surfaces offers the best method of transporting and focusing a white beam of long wavelength neutrons. Neutrons from the macroguide enter the narrow channels of polycapillary glass fibers which act as miniature versions of neutron guides com-

monly used at research reactors. A typical lens contains over a thousand fibers of diameter 0.5 mm, each with over a thousand hollow capillaries of diameter 10 μm . The advantage of the narrow ($\approx 10 \mu\text{m}$) channels is that the neutron beam can be bent more sharply than for the wide ($\approx 50 \text{ mm}$) guides. The fibers are curved such that the neutron trajectories are directed towards a common focus. The high intensity beam is placed on a small sample area for improvement of both the spatial resolution and the detection limits of individual elements of neutron absorption measurements in analytical research.

In conjunction with X-Ray Optical Systems, Inc. we have designed a polycapillary bender-focuser lens that not only focuses but also bends the beam downward out of the shadow of the incident beam in order to improve the signal-to-noise ratio. The glass fibers are accurately guided by six stainless steel meshes in frames that hold the fibers in position. The fibers point towards the common focus 95 mm away from the exit and a distance 42.5 mm below the incident beam centerline, 20 mm below the bottom edge of the beam. There is also ^6Li glass shielding around the lens. The lens itself is enclosed for protection with silicon windows. The lens can be moved out of the beam by computer control when not needed.

The transmission characteristics of this lens have been analyzed using a video radiation detector at the focal plane to measure the spatial intensity distribution. The focused beam has a FWHM of 0.65 mm, and the current density gain over the area for this diameter is a factor of 20. Further measurements have been performed using a dysprosium foil and a photostimulable luminescent imaging plate. This imaging system has a wide (10^5) linear dynamic range and can analyze over a much greater area. The results show that the background adjacent to the focus is reduced by a factor of 16 relative to the background in the direct beam. Although the complex curvature of the fibers have allowed only a gain of about 20, the lower background levels provide significantly better detection limits than

the previous lens. Further PGAA measurements are underway.

A monolithic lens consisting of a fused tapered bundle of polycapillaries has been shown to provide a smaller focus of about 0.16 mm (FWHM at the focal spot), with a focal length of 20 mm, and gains in neutron current density gain of ~ 60 , comparable with the polycapillary lenses. Each optic contains many thousands of 10 μm channels occupying 50% of the entrance area, and proportionately tapered towards the exit. The physical dimensions of these devices (at present the maximum entrance diameter is less than 10 mm) is much smaller than for the polycapillary lenses, and so monolithic lenses are particularly useful for the NDP instrument with its more constrained space. The goal is to perform three dimensional compositional mapping of thin-film semiconductor materials using NDP with the monolithic tapered lens to achieve greater lateral resolution and higher sensitivity.

The transmission of neutrons through a tapered channel has been analyzed using the relationships among the various parameters such as the distance between reflections, and the polar and grazing angles of a trajectory at each reflection. These results have been used in a simulation to study the transmission characteristics of a cylindrical channel. The transmission, the transmitted beam angular divergence and the number of reflections are determined for different values of the taper angle and the incident beam divergence. The results for the tapered channel can be described using the same analytic expressions derived for the straight channel but with an effective lower critical angle.

• Detector Imaging Research

The Nuclear Methods Group, working through a CRADA with CID Technologies Inc. and with the Surface and Microanalysis Science Division, have developed a video radiation detector (VRD) based upon a charged injection device (CID) camera and image processing system. The process is somewhat analogous to the nuclear track technique, and applications of the

two methods do overlap; however, the VRD system allows real-time high resolution imaging of neutron and charged particle fields. The VRD system is essentially 100% efficient for the detection of alpha particles above a few MeV energy; emission rates as small as 10^{-5} Bq have been localized. The system allows discrimination between tritons, alpha particles, and fission fragments. Spatial resolution of less than 11 μm is achieved by interpolating between camera pixel elements. Because the charge injection device is sensitive to visible, X-ray and UV photons, charged-particle images can be correlated with optical images of the sample. As an example, it has been used for detecting spontaneous emission of naturally radioactive materials from minerals or contaminants in the analysis of environmental samples.

By adding a thin ^6Li converter, we have adapted the VRD for the characterizing neutron focusing components for neutron intensity, focal plane location, and analysis of individual elements in the focusing device. Neutron field maps obtained by using the VRD have been indispensable for the focused neutron project. The location and size of the focus can be determined much more quickly with the VRD than by using a large series of photographic films. Thus the VRD system provides a more rapid, and higher resolution image in electronic format, and provides data of a greater dynamic range than photographic film.

• Group Interactions

The strong interaction with industrial scientists using NDP, PGAA, and NAA has continued during the year with a growing number of guest workers, research associates, and joint publications. For example, working this year with researchers from SEMATECH, we have used NDP to study various aspects of quality control using CVD (chemical vapor deposition) reactors. These measurements will be useful in optimizing process yield and reliability as well as establishing confidence for the industrial in-house analytical techniques.

Smithsonian Institution

The Conservation Analytical Laboratory of the Smithsonian Institution maintains an INAA research facility within the Nuclear Methods Group at NIST. This facility, which consists of two automated sample changers and four gamma detectors with associated electronics, provides high precision multielement chemical data for use in a wide range of Smithsonian and Nuclear Methods Group research projects. In the past year over 1500 archaeological samples have been analyzed in support of 6 Smithsonian research projects. The projects include studies of Classic Maya pottery, prehistoric Pueblo pottery, Bronze and Iron age ceramics from ancient Gordian and Hacinebi in Turkey, obsidian artifacts from Yemen, and lead glazed ceramics from French Colonial sites around Mobile Bay, Alabama..

One highlight of this year's research, has involved a study of the chemical characterization of 216 lead glazed earthenwares recovered in excavations of French colonial sites in southern Alabama. These sites date from the early through mid 18th century and include Old Mobile, the first capital of the French colonial effort in the Gulf region. This research was undertaken to compliment the stylistic classification of these ceramics and to identify the sources of supply of ceramics to the French colony.

Two basic types of glazed earthenwares were examined: lead glazed wares with non-calcareous clay bodies and tin opacified lead glazed wares with calcareous clay bodies - Faience. Chemical analysis of the non calcareous ceramics showed that the green glazed variety was all manufactured at a single location, thought to be in France, while the red glazed variety was manufactured at an other location, possibly in France, Spain or Mexico. Three samples of a stylistically different redware could be readily distinguished chemically from the green and red wares and is thought to have been made in New England or French Canada. The calcareous ceramics proved to have a much more complicated chemical profile. Several sherds were

stylistically identified as Mexican productions and all these matched, chemically, with previous analysis of ceramics from Puebla, Mexico. The French faience samples, however, fell into nine chemically distinct groups, all presumed to represent different production locales in France. Comparable data is not, at present, available from production centers in France and these samples must be collected and analyzed before a final assignment can be made.

Food and Drug Administration

The Food and Drug Administration (FDA) maintains a neutron activation analysis (NAA) facility in the reactor building of the National Institute of Standards and Technology (NIST). This facility is directed by FDA's Center for Food Safety and Applied Nutrition and provides agencywide analytical support for special investigations and applications research. NAA complements other analytical techniques used at FDA and serves as a reference technique and confirmatory quality assurance (QA) tool. Instrumental, neutron-capture prompt- γ , and radiochemical NAA procedures (INAA, PGAA, and RNAA, respectively) continue to be the prime nuclear analytical approaches. Radioisotope X-ray fluorescence spectrometry (RXRFS) provides support for FDA programs that monitor potentially toxic elements in housewares (e.g. Pb, Cd and Ba). A low-level γ -ray counting facility developed by the Nuclear Methods Group of the NIST Inorganic Analytical Research Division is used to determine radioactivity concentrations of ^{137}Cs , ^{40}K , and other γ -ray emitters in foods. This combination of analytical techniques enables diverse multielement and radiological information to be obtained for foods and related materials.

Annually, FDA's facility at NIST performs multielement analysis with INAA (60 foods) and radionuclide analyses (15 foods) for quality assurance (QA) in conjunction with the Agency's Total Diet Study (TDS) Program. Another important QA task undertaken is the development of in-house food reference materials. Two ma-

terials that have been developed for use in FDA programs are soy-based infant powder and cocoa powder. Preliminary work has also begun towards the development of a seafood reference material. As a third part of FDA's QA effort, four NIST food Standard Reference Materials (SRMs), 1566 (Oyster Tissue), 1567 (Wheat Flour), 1568 (Rice Flour), and 1570 (Trace Elements In Spinach), are being analyzed by INAA and PGAA. The results will be used to revalidate or reestablish element concentrations for these materials. This study is valuable because FDA can continue to use a supply of 17 to 20-year old materials, which it maintains, as analytical controls, even though the original certificates have expired. These results are valuable to the analytical community because of the information generated by the study relevant to long-term stability of reference materials. Portions are being analyzed from bottles that have been stored under a variety of conditions. These include bottles that have never been opened, bottles that have been opened several times (over a number of years) to remove analytical portions, and some that have undergone long-term desiccation. Based on analyses performed to date, the original certificates values for Na, Al, K, Ca, V, Mn, Cu, and Cd still represent accurate concentrations. In addition, concentrations determined for H, B, C, N, Mg, S, Cl by INAA and PGAA agree well with literature values.

An interlaboratory trial on the ability of three different commercial lead test kits to measure lead in solder was conducted at FDA's NIST facility and two other FDA laboratories. One set of 15 solder test coupons and blanks (prepared at FDA's NIST facility) was tested by each laboratory. The test coupons contained a variety of solders, including NIST SRMs, commercial products, and laboratory preparations. PGAA and RXRFS were used to establish or verify Pb, Sn, Sb, and Bi concentrations. The trial, whose procedures were based on the draft FDA Laboratory Information Bulletin (LIB) "Identification of Lead Solder on a Metal Can Seam", focused on lead and demonstrated that

the lowest concentration that can be reliably measured by using the commercial test kits and the LIB was about 20% Pb. The final procedure was issued as FDA LIB No. 4041.

University of Maryland

The University of Maryland (at College Park, UMCP) aerosol chemistry group has used the NBSR reactor for instrumental neutron activation analysis to characterize atmospheric aerosol particles and gases for more than 20 years. Detailed and accurate multielement analyses are routinely achieved, nondestructively, for up to 40 elements in samples collected for periods of several hours to a few days on various types of filters and in cascade impactors which size fractionate the aerosol into as many as 10 size domains. Some of the elements measured, e.g., As, Se, and Hg, are highly toxic and are, therefore, of epidemiological interest, especially in the Chesapeake Bay and Coastal Marine environments. Equally important is that information on elemental constituents remains a powerful, fundamental tool with which atmospheric sources, transport, and processes may be elucidated. Current projects are discussed below.

• Characterization of Submicrometer Aerosol Particles

Detailed investigations of the size distribution and composition of urban aerosols are important to the scientific community because they contain information about the formation, sources, transport, and atmospheric behavior of particles containing toxic and nutrient substances, and respiratory irritants. This work extends measurement to very small (often < 100 μg) samples of submicrometer aerosol particles size fractionated with low-pressure-drop Micro-Orifice Impactors (MOI). In a recently completed study, size-segregated aerosol samples were collected at three sites near Washington, DC, an area influenced largely by emissions from motor vehicles, utility coal and oil combustion, and municipal incineration; and at two

sites in the heavily industrialized Philadelphia area, to determine the spatial variability in elemental size spectra and relationships between modal diameter and atmospheric aerosol origin and age, including hygroscopic growth functions.

Samples were collected daily from 7 am to 6 pm EST at the three Washington sites in mid August to late September, 1990; and at the Philadelphia area sites from mid October to mid November using 10-stage MOI which provided 7 size fractions in the range < 0.06 to 3 μm . INAA have now been completed for up to 40 elements on 74 MOI sets, representing > 600 individual samples, laboratory blanks, and field blanks.

The results of this study confirm the existence of fine structure in submicrometer aerosol and suggests that particles from various sources remain separated, i.e., unmixed over urban transport scales. In the heavily industrialized Philadelphia area, the size spectra show individual accumulation aerosol peaks for elements such as Zn, Ti, and V at modal diameters of approximately 0.1 μm . These clearly represent the influence of plumes from a municipal incinerator, titanium pigment plant, and residual oil combustion, i.e., sources in close proximity to the sampling sites. Elements such as As, Se, and S, which have strong components from distant sources and occur in much wider peaks with modal diameters near 0.5 μm and represent what receptor modelers have termed "regional" sulfate. Whereas classical receptor modeling employs statistical techniques to resolve the contributions of generic source types from ambient measurements of unfractionated fine particles, our results demonstrate the resolution of individual sources. This is a degree of resolution not previously attained by statistical analysis of unfractionated fine aerosol particles.

In addition, by fitting spectra containing single peaks and correlating the fitted mass median aerodynamic diameters against water activity, we have developed the first hygroscopic growth function for V in ambient aerosol particles. As discussed below, growth functions for various elements are sorely needed to predict their dry

deposition fluxes, especially to natural waters.

- **Chesapeake Bay Atmospheric Deposition Study**

Atmospheric deposition by wet and dry processes is known to be an important source of several anthropogenic, particulate-bound metals in critically important waters such as the north atlantic Ocean, the coastal mid-Atlantic waters, and the Great Lakes. The Chesapeake Bay, perhaps the world's most productive bay, is especially subject to deposition of anthropogenic air pollutants as it lies in close proximity to heavily polluted urban areas, e.g., Baltimore, MD, Washington, DC, Norfolk, VA, and receives polluted air masses from the heavily industrialized Ohio Valley.

We are now in the third year of a project to characterize the spatial and temporal variations in the concentrations of various elements in aerosol particles depositing on the Chesapeake Bay. Aerosol particles with diameters smaller than 10 μm are sampled weekly at three rural shoreline sites, one at the Wye Research Institute in the northern Bay, a second near the Elms educational institute in the middle Bay, and the third at Haven Beach located near Gloucester Point in the south Bay.

Analyses have been completed for more than 450 samples, field blanks, and laboratory blanks. In addition to INAA, inductively-coupled plasma-atomic emission spectrometry (ICP-AES), and graphite furnace atomic absorption spectrometry with Zeeman background correction (GFAAS) were also used. Analyses for Al, As, Cd, Cr, Cu, Fe, Ni, Pb, S, Se, and Zn have been used to estimate aerial dry deposition fluxes to Bay surface waters as the product of the annual average concentrations and deposition velocities (Vds) determined from limited experimental measurements on other waters reported in the literature. The results indicate that dry deposition fluxes for many elements emitted from high-temperature combustion sources are comparable to wet fluxes. The dry deposition fluxes of elements associated with

large particles of coal or crustal materials typically exceed the wet fluxes for these elements.

Deposition models suggest that particle size is extremely important in determining deposition velocities. Size is governed by the nature of the source, coagulation, cloud processing, and hygroscopic growth. Over large distances, atmospheric processes tend to homogenize separate particle populations. However, on the urban scale, our submicrometer aerosol studies have shown that aerosol particle populations from individual sources remain discrete, i.e., unmixed. Thus, particle size, hygroscopic growth, and deposition of various elements will differ for particles emitted from different sources. To investigate the importance of these effects, we have collected size segregated aerosol samples with micro-orifice impactors on the pier at the Matapeake Police Station on Kent Island, and on the Pier at the Chesapeake Biological Laboratory in Solomons, MD. INAA of 15 sets of these samples are in progress. Preliminary results show that most of the deposition occurring under neutral conditions at wind speeds of 5 m/s (the mean Bay wind speed) is accounted for by the fraction of the elemental mass associated with large particles, i.e., particles $> 5 \mu\text{m}$, aerodynamic diameter. For example, at Matapeake, particles collected on stages 0 and 1 (diameters 21 and 7 μm) accounted for 85% of the deposition of S and V, despite the fact that only 10% of their mass resides in these particles.

Research Topics

Certification of Standard Reference Materials by Neutron Activation Analysis

D. A. Becker¹, R. Demiralp¹, R. R. Greenberg¹, R. M. Lindstrom¹, E. A. Mackey¹, B. R. Norman¹ and R. Zeisler¹

Improvements to INAA Methodology

D. A. Becker¹, R. Demiralp¹, R. R. Greenberg¹, R. M. Lindstrom¹, E. A. Mackey¹ and R. Zeisler¹

Quality Assurance Improvements for NAA

D. A. Becker¹, R. Demiralp¹, R. R. Greenberg¹, R. M. Lindstrom¹, E. A. Mackey¹ and R. Zeisler¹

Development of Radiochemical Separation for

NAA

D. A. Becker¹, R. R. Greenberg¹, E. A. Mackey¹
and B. R. Norman¹

Reactor Characterization for NAA

D. A. Becker¹

Evaluation of Errors and Interferences in NAA

D. A. Becker¹, M. J. Blackman¹, R. R. Greenberg¹, R. M. Lindstrom¹ and R. Zeisler¹

Determination of Phosphorus via RNAA with Beta Counting

R. L. Paul¹

Trace Elemental Characterization of Silicon Semiconductor Materials

D. A. Becker¹ and R. M. Lindstrom¹

Improvements to PGAA Methodology

D. L. Anderson², R. M. Lindstrom¹, E. A. Mackey¹ and R. L. Paul¹

Evaluation of Accuracy and Precision in INAA of Botanical Materials

D. A. Becker

Neutron Scattering Effects on PGAA

R. M. Lindstrom¹, E. A. Mackey¹ and R. L. Paul¹,

New Developments in Monitor Activation Analysis

G. P. Lamaze¹, R. M. Lindstrom¹, E. A. Mackey¹
and R. L. Paul¹

Bio-analytical and Specimen Bank Research

K. A. Fitzpatrick¹, R. R. Greenberg¹, G. V. Iyengar¹, B. J. Koster¹, J. K. Langland¹ and E. A. Mackey¹

Studies in Elemental Speciation

D. A. Becker¹, E. A. Mackey¹

Multielement Analysis of Foods and Related Materials by NAA

D. L. Anderson² and W. C. Cunningham²

High Sensitivity Gamma-Ray Spectrometry

R. M. Lindstrom¹

Application of Radioisotope-Induced X-Ray Emission to the Identification of Lead and Other Elements in Ceramic Glazes and Housewares

D. L. Anderson² and W. C. Cunningham²

Elemental Characterization of High Temperature Superconductors

D. A. Becker¹, R. R. Greenberg¹, R. M. Lindstrom¹ and R. L. Paul¹

New Developments in NDP

H. Chen-Mayer¹, G. P. Lamaze¹ and J. K. Langland¹

Comparison of Nuclear Reactors for Analytical Chemistry

D. A. Becker¹

Determination of Hydrogen by PGAA

R. R. Greenberg¹, R. M. Lindstrom¹, E. A. Mackey¹ and R. L. Paul¹

Analytical Applications of Cold Neutrons

H. H. Chen-Mayer¹, R. Demiralp¹, R. R. Greenberg¹, G. P. Lamaze¹, J. K. Langland¹, R. M. Lindstrom¹, E. A. Mackey¹, D. F. R. Mildner¹, R. L. Paul¹ and V. A. Sharov³

Nitrogen Profiling of Thin Titanium Nitride Films

G.P. Lamaze¹, H. H. Chen-Mayer¹ and N. Cox⁴

Lithium Migration in Electrochromic Thin Films

G.P. Lamaze¹, H. H. Chen-Mayer¹ and M. Badding⁵

Test of a Novel High Sensitivity Neutron Detector

B. Feller⁶, H. H. Chen-Mayer¹ and G.P. Lamaze¹

Neutron Focusing for Analytical Chemistry

H. Chen-Mayer¹, G. P. Lamaze¹, J. K. Langland¹, D. F. R. Mildner¹ and V. A. Sharov³

Metal Capillaries for Neutron Lenses

H. H. Chen-Mayer¹, V.S. Fokin⁷, D.F.R. Mildner¹, P.L. Reeder⁷ and V.A. Sharov³

Neutron Transmission through Curved Capillaries

H. H. Chen-Mayer¹, V. S. Fokin⁷, D. F. R. Mildner¹ and V. A. Sharov³

Neutron Imaging with Scintillating Fiber Faceplates

H. H. Chen-Mayer¹, V. S. Fokin⁷, D. F. R. Mildner¹, P. L. Reeder⁷ and V. A. Sharov³

Neutron Transmission through Tapered Capillaries

H. H. Chen-Mayer¹, D. F. R. Mildner¹ and V. A. Sharov³

Applications of Neutron Laue Diffraction Focusing Methods

H. H. Chen-Mayer¹, V. V. Kvardakov⁸, J. W. Lynn¹, D. F. R. Mildner¹ and V. A. Sharov³

Focusing Methods for Radiography and Topography

H. H. Chen-Mayer¹, D. F. R. Mildner¹, K. M. Podurets⁹ and V. A. Sharov³

Neutron Beam Spatial Distributions using Imaging Plate Technology

H. J. Bahre¹⁰, H. H. Chen-Mayer¹, Y. T. Cheng¹, D. F. R. Mildner¹ and V. A. Sharov³

Hydrogen Detection in Industrial Materials by Incoherent Neutron Scattering

H. H. Chen-Mayer¹, V. V. Kvardakov⁸ and D. F. R. Mildner¹

A Bender-Focuser for Prompt Gamma Activation Analysis

H. H. Chen-Mayer¹, R. M. Lindstrom¹, D. F. R. Mildner¹, R. L. Paul¹, Q.-F. Xiao¹¹ and V. A. Sharov³

Low-Angle Neutron Diffraction from Polycapillary Fibers

M. Agamalian¹² and D.F.R. Mildner¹

Development of a Position-Sensitive Video Radiation Detector

H. Chen-Mayer¹ and C. J. Zeissler¹

Chesapeake Bay Atmospheric Deposition Study

Z. C. Lin¹³, J. M. Ondov¹³ and A. Suarez¹³

Characterization of Submicrometer Aerosol Particles

J. M. Ondov¹³

Archeological Applications of NAA

R. Bishop¹⁴, M. James Blackman¹⁴ and J. E. Myers¹⁴

Radionuclides in Foods

D. L. Anderson² and W. C. Cunningham²

Quality Assurance Programs

D. L. Anderson² and W. C. Cunningham²

Revalidation of Food SRMs

D. L. Anderson² and W. C. Cunningham²

Bromation in Breadmaking

W. C. Cunningham² and C. R. Warner²

Affiliations

¹NIST, Nuclear Methods Group

²Food and Drug Administration

³X-Ray Optical Systems, Inc., Albany, NY

⁴Intel Corporation

⁵SAGE Electrochromics

⁶Nova Scientific

⁷Pacific Northwest Natl. Lab., Richland, WA

⁸Russian Sci. Center, Kurchatov Inst., Moscow

⁹Russian Sci. Center, Kurchatov Inst., Moscow

¹⁰Fuji Med. Systems USA, Inc., Stanford, CT

¹¹X-Ray Optical Systems, Inc., Albany, NY

¹²Oak Ridge National Lab.

¹³University of Maryland

¹⁴Smithsonian Institution

¹⁵University of Michigan

¹⁶Neutek, Inc., Darnestown, MD

¹⁷Russian Academy of Sci., Moscow

Neutron Interactions and Dosimetry

This group provides measurement services, standards, and fundamental research in support of NIST's mission as it relates to neutron technology and neutron physics. The industrial sectors served include materials development, scientific instrument calibration, electric power production, radiation protection, national defense, and radiation therapy.

This project maintains, develops, and applies well-characterized neutron fields for detector development, methods evaluation, and standardization as needed for materials dosimetry in nuclear reactor applications and for personnel dosimetry in radiation protection. These neutron fields include thermal neutron beams, "white" and monochromatic cold neutron beams, a thermal-neutron-induced ^{235}U fission neutron field, and ^{252}Cf fission neutron fields, both moderated and unmoderated. The calibration of these neutron fields is derived from related artifacts, facilities, and capabilities maintained by the project: the national standard neutron source NBS-I, a manganous sulfate bath for neutron source comparisons, a collection of fissionable isotope mass standards (FIMS), a collection of boron and lithium isotopic standards, spectroscopy facilities for both gamma rays and alpha particles, and a capability to perform radiation transport calculations. The group also performs experimental tests of critical neutron transport data and computation methods.

The group carries out forefront research at the CNRFB in neutron physics and tests of fundamental symmetry principles, develops advanced measurement techniques in neutron interferometry, and is developing neutron spin filters based on laser polarization of ^3He .

Highlights of activities are given below.

Fundamental Neutron Physics

- Neutron Interferometry and Optics

Since September 1996, the Neutron Interferometry and Optics Facility (NIOF) in the NIST Cold Neutron Guide Hall has been fully operational as a national users' facility, and it has a crowded schedule of experiments as far as can be seen into the future. One third of the beam time is reserved for NIST staff research, focused primarily on development of new techniques for materials research. The remainder of the beam time is allotted to outside users by an advisory committee, based on the merit of research proposals submitted. Experiments have already been done involving researchers from the University of Missouri-Columbia, Exxon, the Hahn-Meitner Institute (Berlin), and the Atom Institute (Vienna). These experiments have given preliminary results in phase-contrast imaging, high-resolution two-dimensional absorption imaging, neutron scattering length measurements, and testing of very large scale interferometer crystals. Most of these experiments are expected to be concluded in the next few months after receiving additional beam time.

The very keen interest of the national and international user community in this facility arises from the unique capabilities of this new facility. Two new large interferometers of NIST design have been fabricated and are being used to carry out experiments. These interferometers have novel design features allowing elimination of second order beam contamination and operation at low neutron energies (~ 4 meV) which are advantageous for materials science and solid state physics research. These are the first neutron interferometers in the world that have been successfully operated at such low neutron energies. When operated at slightly higher energies, one of these interferometers achieved fringe visibility as high as 88% at its best spot and had a large area with fringe visibility exceeding 70% everywhere within. At 4 meV the fringe visibility is about 40% at the best spots. Phase sta-

bility is of the order of a few milliradians per 24 hours. The special foundation under the facility, robust vibration isolation systems, an active position stabilization system, and the special characteristics of the new NIST design interferometer crystals all contribute toward the achievement of these unprecedented performance characteristics.

In addition, exploration of the possibilities and preliminary design work have been done toward development of a large scale (~ 20 cm diameter) neutron radiography/tomography capability.

• Development of Neutron Spin Filters by Laser Polarization of ^3He

The developmental program to produce polarized neutron beams using a ^3He spin filter at NIST has seen major advances during the last two years. This method should yield efficient, broadband neutron polarizers that will have several advantages over conventional polarizers, both for condensed matter studies and for fundamental physics. In addition, the technology for polarizing the ^3He gas is applicable to the newly emerging medical field of polarized gas magnetic resonance imaging (MRI), as well as applications in basic nuclear physics.

The spin filter is based on the spin-dependent absorption of neutrons by polarized ^3He in the reaction $^3\text{He}(n,p)^3\text{H}$. We have parallel programs to produce polarized ^3He either by (1) spin-exchange with optically pumped rubidium vapor or (2) by direct optical pumping of metastable ^3He followed by mechanical or cryogenic compression of the low pressure gas. Progress in each program will be discussed separately below.

Spin-Exchange Based Spin Filter: Milestones passed in the last two years include optimization of ^3He polarization using the Ti:Sapphire laser, conversion to use of inexpensive diode laser arrays for optical pumping of Rb, construction of a cell filling station, production of cells with properties required by a real polarizer, and initial testing of cells on a neutron

beam. Work has begun on a medical imaging spin-off of this technique.

A ^3He polarization of 25% was measured in the spin-exchange setup early in 1995 using the Ti:Sapphire laser. Later in 1995 we measured 15% polarization using a laser diode array. The diode laser requires higher density ^3He for optimal performance, so we have constructed a cell filling system and a new oven to better match the properties of the diode laser. The filling system was commissioned in April of this year, and we have produced multiple cells with long lifetimes (some near 200 hours). In the summer of 1996 we tested some of the cells on the polarized neutron beam at the end of NG-6 at the Cold Neutron Research Facility. Results from these tests are guiding the design of improved cells and the choice of cell materials. The new materials have been ordered and we expect to have a viable spin filter cell within the next few months.

In April 1996 we were contacted by a researcher at the University of Pennsylvania regarding magnetic resonance imaging (MRI) of lungs using polarized ^3He . In collaboration with the Medical Imaging group at Pennsylvania, we have produced multiple cells containing roughly one liter of polarized ^3He , and produced initial images of a volunteer's lungs, which are almost impossible to image using traditional MRI techniques.

Metastability-Exchange Based Spin Filter: In the metastable method, the gas is polarized at a pressure of ~ 1 torr, and then must be compressed up to a pressure of ~ 1 bar for use as a neutron polarizer. Maintaining the polarization during compression is a technical challenge, but has been achieved by a group in Mainz, Germany using a two-stage piston compressor. We are developing a similar compressor in collaboration with Indiana University. Our collaborators at Indiana have designed this apparatus, and NIST is assisting with the construction of their optical pumping system. In addition, we are investigating an alternate compression apparatus based on modification of a commercial

diaphragm pump. Success in this alternate approach could yield a compact, simple apparatus that would allow very economical development of the metastable method for neutron polarizers and other applications. The apparatus for optical pumping of ^3He at low pressure has been constructed and 80% polarization has been obtained.

- **The Neutron Lifetime and Asymmetries of the Weak Interaction**

The NG6 End Station in the Cold Neutron Guide Hall is operated as a national users' facility for fundamental neutron physics, under the supervision of the same advisory committee mentioned above in regard to the NIOF. Experiments at this beam station are focused on testing aspects of the standard model of particle interactions which are accessible from precise measurements of neutron interactions and decay.

For a number of reasons, including two longer-than-expected shutdowns of the NIST research reactor, the neutron lifetime experiment had to be taken off-line temporarily to allow beam time for two other weak interaction experiments which were ready to run. The neutron lifetime experiment at NIST collected data during two separate periods 10/93 - 5/94 and 11/95 - 5/96. This difficult experiment which had run with some success in Grenoble previously, has had more serious difficulties in the attempts to improve on or even reproduce the Grenoble results at NIST. Investigations of several possible causes of these difficulties are in progress off-line while the initial runs are made for the two other experiments: Parity-Non-conserving Spin Rotation in Liquid Helium and the *emiT* Experiment, a search for time-reversal asymmetry in neutron beta decay.

Parity-Non-conserving, Neutron Spin Rotation in Liquid Helium: This experiment concerning details of parity violation is primarily the work of a team from the University of Washington, Seattle (D. Markoff, S. Penn, B. Heckel, and E. Adelberger). NIST physicists have been involved in preparation of the supermirror po-

larizer and analyzer for this experiment, as well as other aspects of beamline preparation and shielding; the polarization achieved was 96%. This experiment collected useful data intermittently during 9/96 - 11/96, but suffered frequent outages for recovery from cryostat problems. The data obtained will be marginal statistically for setting a significant bound on the spin rotation per unit length of travel. A future run with an improved cryostat is expected.

The emiT Experiment: This very large collaboration involves physicists and engineers from the Univ. of Washington, University of Notre Dame, the Lawrence Berkeley Laboratory, the Univ. of Michigan, Los Alamos National Laboratory, and NIST. This experiment uses the same supermirror polarizer arrangement as the spin rotation experiment. The experiment will run for about 20 weeks beginning in 12/96.

Two more experiments besides conclusion of the beam-type neutron lifetime experiment are in the planning stages for 1997. An ultracold neutron, bottle-type lifetime experiment with collaborators at Harvard University is in preparation, with an initial run expected in 1997. A repeat of a Russian spin-antineutrino asymmetry experiment is also likely to be allocated beam time. NIST staff participated in an initial run of this experiment in Grenoble in the summer of 1996.

Neutron Fields and Standards

- **Neutron Dosimetry for Reactor Safety Assessment**

Through a cooperative agreement with the Office of Nuclear Regulatory Research, NIST provides measurement assurance services and consultation related to neutron dosimetry and nuclear reactor safety. After many years of NIST consultation with experts from industry and national laboratories, the Draft Regulatory Guide DG-1053 (formerly DG-1025), *Calculational and Dosimetry Methods for Determining Pressure Vessel Neutron Fluence*, was issued in essentially final form with very little objection from the ma-

for reactor vendors or regulated utilities. NIST will continue to support the measurement assurance steps called for in this guide to keep the national measurement system on track in this field. Consultation issues have begun to go from the generic case to plant specific cases, as aging nuclear electric power plants are nearing levels of cumulative neutron radiation exposure which could be of concern regarding the risk of brittle fracture of a pressure vessel under certain extreme conditions. NIST also has carried out and published research on fission neutron transport through thick steel sections to test the relevant nuclear data files employed in calculations for assessment of reactor safety.

• Nuclear Cross Section Standards

Nuclear cross section data standards are important for nuclear reactor safety and performance calculations, for development of fusion energy, for understanding accelerator neutron source dosimetry, and for basic studies in astrophysics. The NIST program in support of these nuclear data standards has been substantially reduced in scope in recent years, and the emphasis of the remaining program has shifted from measurements to evaluation and international coordination of standards efforts. NIST performs its role in motivating and coordinating new standards measurements by examining the standards data base, pursuing the extension of the standards over a larger energy range, and leading efforts directed toward new evaluations of the standards. These efforts have taken place largely through participation in the Cross Section Evaluation Working Group and our international involvement through the Nuclear Energy Agency Nuclear Science Committee and the International Nuclear Data Committee. Continuing experimental collaborations include an effort at the Ohio University Tandem Accelerator to refine the angular distribution data for the very important hydrogen scattering cross section standard.

• Calibrations, Irradiation Services, and Special Tests

The demand for routine calibrations of instruments and dosimeters for radiation protection has recently dropped off somewhat as secondary calibration laboratories have opened across the U.S., but assuring the quality the measurements at the secondary laboratories remains a fully supported, high priority activity. NIST calibrations are still performed for instrument manufacturers who need direct NIST traceability for international trade purposes. NIST continues to directly calibrate 10-20 neutron sources per year, because there is not enough demand in this area to stimulate development of secondary laboratory capabilities. We continue to satisfy requests for a variety of special tests of instruments and samples in NIST standard neutron fields.

Research Topics

Neutron Interferometry and Optics

M. Arif⁸, D. Jacobson⁸, D. Brown¹¹, R. Clothier³, A. Thompson⁸, S. Werner¹⁶, A. Ioffe⁴, A. Zeilinger¹⁴, K. Raum¹⁷, B. Schillinger¹⁷ and C. Rausch¹⁷

Determination of the Neutron Lifetime

M. S. Dewey⁸, G. L. Greene¹⁰, D. Gilliam⁸ and W. M. Snow⁶

Accurate Determination of Neutron Capture Flux

M. S. Dewey⁸, M. Arif⁸, D. Gilliam⁸, G. L. Greene⁸, W. M. Snow⁶, J. Pauwels⁷, C. Inglebrecht⁷ and R. Scott¹¹

Study of Time Reversal Invariance in Neutron Beta Decay

J. Wilkerson²⁰, E. Wasserman⁹, J. Nico⁸, R. G. H. Robertson¹⁰, S. Freedman⁹, A. Garcia¹⁸, T. Chupp¹⁵, K. Coulter¹⁵, M. S. Dewey⁸, G. L. Greene¹⁰, A. Thompson⁸, B. Fujikawa⁹, G. L. Jones⁸, J. Adams⁸, F. Wietfeldt⁸, L. Lising⁹, S. Hwang¹⁵ and T. Steiger²⁰

Parity Non-Conserving Neutron Spin Rotation

B. Heckel²⁰, D. Markoff²⁰, E. Adelberger²⁰, S. Penn²⁰ and F. Wietfeldt⁸

Highly Accurate Neutron Wavelength Measurements

M. S. Dewey⁸, K. Coakley¹³, W. M. Snow⁶ and M. Arif⁸

LASER Polarization of ³He for Neutron Spin Filters and Medical MRI

A. Thompson⁸, T. Gentile⁸, M. S. Dewey⁸, G. L. Jones⁸, F. Wietfeldt⁸, W. M. Snow⁶ and R. Rizi¹⁹

Trapping of Ultra Cold Neutrons

J. Doyle⁵, S. Lamoreaux¹⁰, R. Golub⁴, G. L. Greene¹⁰ and M. S. Dewey⁸

Utilization of the Materials Dosimetry Reference Facility - Tests of New IRMM ²³⁷Np and ²³⁸U Fast Neutron Dosimeters

E. D. McGarry⁸, J. Grundl⁸, C. Eisenhauer⁸, D. Gilliam⁸, J. Adams⁸ and P. Simpson¹⁵

Benchmark Measurements and Calculations of Neutron Transport

D. Gilliam⁸, M. S. Dewey⁸, J. Nico⁸, C. Eisenhauer⁸ and J. Grundl⁸

Neutron Fluence Rate Measurements

D. Gilliam⁸, J. Nico⁸ and J. Adams⁸

Defined-Geometry Alpha Counting

D. Gilliam⁸ and J. Nico⁸

Certified Neutron Fluence Standards from the Cavity Fission Source

E. D. McGarry⁸, J. Grundl⁸ and J. Adams⁸

Quality Assurance Checks on Masses and Impurities in Neutron Dosimeters for NRC Reactor Pressure Vessel Embrittlement Surveillance

E. D. McGarry⁸, J. Grundl⁸ and J. Adams⁸

Measurement of LET Spectra

R. Schwartz⁸, H. Gerstenberg¹, P. Lamperti⁸ and A. Thompson⁸

Intercomparison of NIST and PNL Calibration Facilities

R. Schwartz⁸, J. McDonald², M. Murphy² and A. Thompson⁸

Response of Albedo Dosimeters Versus Distance from a Neutron Source

R. Schwartz⁸ and A. Thompson⁸

Response of Albedo Neutron Dosimeters as a Function of Angle

R. Schwartz⁸

Affiliations

¹Armed Forces Radiobiology Research Institute

²Battelle Pacific Northwest Laboratory (PNL)

³Bethany College

⁴Hahn-Meitner Institute

⁵Harvard University

⁶Indiana University

⁷Inst. for Ref. Matls. & Meas., (CEC), Belgium

⁸Ionizing Radiation Division, NIST

⁹Lawrence Berkeley Lab., Univ. of Cal.-Berkeley

¹⁰Los Alamos National Laboratory

¹¹Northern Illinois University

¹²Scottish Universities Research and Reactor Centre

¹³Statistical Engineering Division, NIST

¹⁴University of Innsbruck

¹⁵University of Michigan

¹⁶University of Missouri-Columbia

¹⁷University of Munich

¹⁸University of Notre Dame

¹⁹University of Pennsylvania

²⁰University of Washington

Polymer Division Programs

Interfaces and Thin Films

- **Polymer Interdiffusion Near an Attractive Interface**

Fundamental knowledge about the polymer dynamics near an impenetrable surface is important in a number of technological areas including adhesion, electronics packaging, and composite materials. The nature of the polymer-substrate interaction plays an important role in the polymer properties. For example, it has been observed that the coefficient of thermal expansion changes with film thickness and also increases or decreases with different polymer-substrate interaction energies [1-3].

In this project, we apply neutron reflectivity to measure the dynamics of the Interdiffusion between polymer bilayers where the polymer-polymer interface is placed at different distances from an attractive solid surface. The system that we study are bilayers of deuterated ($M_w = 135,000$) and hydrogenated poly(methyl methacrylate) (PMMA) ($M_w = 143,000$) on the native oxide surface of silicon wafers. The silicon oxide surface has an attractive interaction energy with PMMA and is expected to retard the interdiffusion dynamics for chains "stuck" to the interface. The neutron results suggest that the interface retards the polymer chain dynamics at distances up to 3 radii of gyration, R_g , of the polymer (for this polymer, $R_g = 93 \text{ \AA}$). This relatively long length scale indicates that the presence of the substrate affects polymer chains not directly in contact with the surface. Currently, we continue to explore the polymer chain dynamics using other lower layer thicknesses, different molecular weight polymers, and different substrates.

References

- [1] J. H. van Zanten, W. E. Wallace and W. L. Wu, "Effect of Strongly Favorable Interactions on the Thermal Properties of Ultrathin

Polymer Films", *Phys. Rev. E*, **53** (3), 2053 (1996).

- [2] W. E. Wallace, J. H. van Zanten, and W. L. Wu, "Influence of an Impenetrable Interface on A Polymer Glass-Transition Temperature", *Phys. Rev. E*, **52**(4), 3329 (1995).
- [3] E. K. Lin, S. K. Satija and W. L. Wu, "Polymer Interdiffusion Near an Attractive Interface", in review.

- **Thermal Expansion of a Buried Interfacial Layer**

In this project, we use neutron reflectivity to measure the coefficient of thermal expansion for a labeled polymer layer near an attractive interface inside of a bulk polymer film. Following the interdiffusion experiment of PMMA polymer films described above, the density profile of the deuterated lower layer does not appear to change with additional annealing. Using this profile as a label, we measure the density profile as a function of temperature to determine the coefficient of thermal expansion.

From the experimental data, we obtain information about the thermal expansion for both the interfacial layer and the overall polymer film. The coefficient of thermal expansion for the overall film is the same as that for bulk PMMA polymers with a distinct change near the glass transition temperature (T_g) of the bulk polymer. Within the current accuracy of our measurement, the interfacial layer appears to also follow the bulk thermal expansion values, but with a transition temperature above that of the bulk T_g . This behavior is in agreement with measurements of the thermal expansion using ultrathin one-component PMMA films. Greater resolution is required to gain a better understanding of this phenomena. Toward this end, we are incorporating the use of higher molecular weight polymers to mark the interfacial layer more clearly.

- **Mass Density of Polymer Thin Films Measured by Symmetric Neutron Reflectivity**

In recent years there has been much interest in the physical behavior of polymer thin films. A wide variety of polymer thin film physical phenomena have been investigated including thermal expansion, glass transition temperature, diffusion, and wetting, just to cite a few representative examples. However, one fundamental property of polymer thin films, upon which many of the other properties depend, remains unmeasured. This property is mass density and this is a difficult quantity to measure with an accuracy on the order of 1% or better.

The mass density of ultra-thin polystyrene films supported on silicon substrates was measured by neutron reflectivity [1]. To account for possible sample misalignment that may lead to spurious results, the reflectivity was measured from the free surface side of the thin film and from the silicon substrate side. This new approach has been termed "symmetric", or "twin", reflectivity. The films ranged from 72.5 to 6.8 nanometers in thickness. All except the very thinnest films showed a mass density very close to that of the bulk. Those that were less than about 7 nanometers in thickness showed a decrease in density. The films were prepared by spin coating onto two different silicon surfaces: the native oxide and the monohydride-terminated surface. The character of the silicon surface did not affect the film density.

Reference

- [1] W. E. Wallace, N. C. Beck Tan, S. K. Satija and W. L. Wu, "Mass Density of Polymer Thin Films Measured by Symmetric Neutron Reflectivity", in review.

Blends

- **Polystyrene/Polybutadiene/Polystyrene-Polybutadiene Blends Under Shear**

The effect of a diblock copolymer on the phase behavior of polymer blends under shear

flow was examined by SANS. In quiescent condition, the phase diagram of the PS/PB/PS-PB blend shifts linearly downward with PS-PB diblock concentration and the kinetics of spinodal decomposition slows down in the presence of diblock copolymer, which serves as a compatibilizer in the blending process. In addition, a finer and more dispersed morphology was observed with increasing copolymer concentration, and the molecular weight and architecture of the copolymer also have a strong impact on the phase behavior of the blend. The influence of simple shear fields on the mixing/demixing behavior (in the one-phase and two-phase regions) of the polymer blend with various copolymer concentration was studied. Preliminary results showed that suppression of concentration fluctuations along the flow direction as well as along the vorticity axis was observed, however the suppression rate decreases with increasing copolymer concentration. More experiments will be conducted on the blend with only the diblock polymers are labeled to investigate the role and conformation of the diblock copolymer of the blend under the steady shear flow.

- **Hydrogen Bonded Polymer Blend**

SANS was used in the study of the polymer blends made miscible by a dilute, random distribution of hydrogen bonds between the two components. The material used was a binary mixture of deuterium-labeled polystyrene with a low mole fraction (0.5 mole % to 10 mole %) of hexafluoro-isopropylol modification, and poly(butyl methacrylate). The OH group of the modified polystyrene is capable to form hydrogen bonding with the carbonyl group of the poly(butyl methacrylate). The model of two lengths distribution with the hydrogen bonding forms a potential barrier to inhibit the long-wavelength instability was studied by varying the co-monomer composition (OH containing monomer) of the polystyrene component. The SANS static structure factor at various temperatures are analyzed by the two lengths model.

- **Small Angle Neutron Scattering Characterization of Silicone Polymer/Filler Blends**

The focus of this project will be for Dow Corning to prepare deuterated poly(dimethyl siloxane) (PDMS) and trimethyl treated silica filler materials for utilization in small angle neutron scattering (SANS) studies to characterize component molecular dimensions, domain sizes, and interaction parameters of the PDMS/filler blends. Monte Carlo simulations have predicted the polymer chain dimensions in the absence and presence of silica fillers as a function of filler size. Tests of these predictions are not yet available and the proposed studies will provide a more thorough understanding of the PDMS chains and the filler particles and the domain sizes of the filler components in the blends. Initial experiments have been conducted on unlabelled materials in solvents with sufficient differences in the scattering cross sections to probe the experimental conditions which will be required in this study.

- **Compatibilizers made from Copolymers that Exhibit Strong Interactions**

Blends of immiscible polymers often require the addition of a block polymer that improves the dispersion and adhesion of the phases. The blocks are usually the same types as the two polymers to be blended. If the blocks contained a polymer that had a strong, favorable interaction with one of the blended polymers, the effect of the block copolymer may be much stronger than the athermal case.

Random copolymers of poly(methyl methacrylate- d_8) (PMMA) and poly(methacrylic acid) (PMAA) were synthesized and blended with polyethylene oxide (PEO), and SANS was used to estimate the strength of interaction between the various polymer pairs. Scattering from PEO/PMMA was typical of an athermal blend, and the calculated interaction parameter was negative, but small in magnitude. As the PMAA content was increased, the scattering became very weak and flat, indicating that the PEO/PMAA inter-

action was very favorable thermodynamically.

Block copolymers were synthesized and blended with PEO and polystyrene. Copolymers made with PMAA showed very favorable effects, giving very fine dispersions of the phases.

- **Polystyrene-Poly(ϵ -caprolactone) Diblock Copolymer and the Blends**

Block copolymer with one crystalizable block and the corresponding blends will be studied by SANS with and without the external shear flow. Currently SANS experiment of polystyrene-poly(ϵ -caprolactone) under shear flow is being carried out. The effect of crystallization on the micro-phase separated block copolymer structure is being measured.

Melts and Solutions

- **Micellization of Model Ionic Graft Copolymers**

This study includes characterization and experimental investigations of polymers interacting by way of strong ionic interactions to form ionic micelles. Light scattering, neutron scattering, and TEM are used to characterize solubility, size, structure, and interactions of model polymers with specific interacting groups incorporated as ionic grafted copolymers. This project will encompass applications of these materials for water recovery, drug delivery, and rheologically modified solutions.

Model graft copolymers made up of neutral backbones and ionic grafts have been synthesized and characterized as a function of backbone grafting density. Small angle neutron scattering, dynamic light scattering, TEM, and computer modeling are used to characterize the solubility, size, shape, and specific interactions of self-assembled micelles that form from these copolymers in selective solvents as a function of grafting density, concentration, solvent composition, ionic strength, and charge density.

Selective solvents have been identified for PS/PMAA- Na^+ and PS/P4VPBz+ Br^- graft copolymers and micellization has been observed and characterized in three samples using dy-

namic light scattering and small angle neutron scattering. Structures observed in these systems include multi-molecular spherical micelles with core-shell morphology as well as intramolecular cylindrical micelles. With changes in solvent composition, we have observed structural changes in micelles of PS/PMAA graft copolymer micelles including reverse micellization. With changes in ionic strength we have observed changes in micelle dimensions and chain extension. Using SANS and solvent contrast matching, the preferential absorption of small organic molecules into the interior of the micelles has been investigated as a function of micellar geometry. The inter-particle structure factor which quantifies the interactions between particles in solution has been measured at higher concentrations of copolymers for both spherical and cylindrical micellar systems and modeled as a function of ionic strength, solvent composition and concentration.

- **Examination of Cylindrical Diblock Copolymer Melts During Shear**

The morphology of a diblock copolymer of (deuterated) styrene-butadiene at rest and under shear has been investigated using SANS. The goal of this study was to examine the shear effects on the order-disorder (microphase separation) temperature of copolymer as a function of temperature, shear rate and strain. The dynamics of the structural changes during and after cessation of shear were also examined. Prior evidence of a martensitic-like transformation in a triblock copolymer of similar molecular weight motivated these studies on the diblock copolymer to provide insight into the relationship between the martensitic-like transition and copolymer architecture.

Using a specially designed shear cell, scattering data from the copolymer during shear in two scattering planes was obtained: the "through" position, normal to the shearing plane of the material and the "tangential" position, giving a view of the materials in the direction of flow. The martensitic transformation found for the

triblock copolymer was not observed in the diblock indicating unique flow mechanisms for each copolymer chain architecture despite similar microstructural morphologies. Furthermore, we have observed that shearing may be disruptive to the long range order of the diblock copolymer but that a high degree of order is regained upon cessation of shear.

- **Examination of Lamellar Diblock Copolymer Solutions**

Order-disorder transitions (ODT's) of symmetric styrene-2-vinylpyridine diblock copolymers in a common good solvent and melts were determined by dynamic rheological measurements (DRM) and small angle neutron scattering (SANS) measurements. The ODT conditions determined by DRM and SANS coincide with each other and the degree of polymerization dependence of the critical volume fraction in solutions at almost constant temperature agrees with the theoretical prediction for semidilute solutions. However, the semidilute behavior holds in a much wider concentration range than that of ordinary polymer solutions and the crossover from semidilute to concentrated regions is not clear.

Rheological properties and structural changes under steady shear flow were studied for poly(styrene- d_8 -*b*-2-vinylpyridine) in α -chloronaphthalene at 13 wt %. The structural changes were observed by measuring small angle neutron scattering (SANS) from a flow cell of the couette type. The order-disorder transition (ODT) temperature in the quiescent state was determined to be 55-60°C by dynamic mechanical measurements and the solutions assume lamellar structures in the ordered quiescent state. In the ordered state, both the shear stress and the first normal stress difference change their shear rate dependencies at certain critical shear rates in the same manner as immiscible polymer blends. It was found that the critical shear rate for the change in the shear stress is always smaller than that for the change in the first normal stress difference.

SANS measurements revealed that steady shear flow causes the lamellar orientation at certain critical shear rates. Lamellar normals are preferentially oriented along the vorticity direction at very high shear rates. Comparison between rheological and SANS data indicates that the shear stress and first normal stress difference change their shear rate dependencies after the lamellae are preferentially oriented.

• Hybrid Linear-Dendritic Block Copolymers

Associative polymers have hydrophylic and hydrophobic blocks that form hydrophobic complexes in water based solvent mixtures. The rheological properties are strongly effected by the types of associations which can be probed by small angle scattering.

The hybrid linear-dendritic ABA copolymers consist of stiff dendritic aromatic polyethers as block A that are connected via a flexible linear block B of Polyethylene oxide (PEO). Six samples were studied that were built by a combination of dendrons ([G2] or [G3]) and linear PEO (Mw, 11 k, 15 k, and 23 k). Two different solvents were used, one of which (THF-d4) is a good solvent for the dendrons and a bad solvent for the PEO chain. The other solvent used is a mixture of 1:1 (v:v) CD₃OD/D₂O. This mixture is known to be a good solvent for PEO, but is a nonsolvent for the dendrons.

The ABA copolymers dissolved in THF-d4 form a solution of single particles. This indicates a formation of intramolecular micelles formed by the dendrons (blocks A) that are surrounded by freely soluble PEO chains (block B). In contrast to the THF-d4 solutions, the copolymers form gels in the mixture CD₃OD/D₂O for concentrations $c = 3$ wt%. For concentrations of $c = 15$ wt% the gels are macroscopically stable and do not flow over a time period of days. All gelled samples show a very intense peak in the scattering function $I(q)$ as shown in Fig.1. The peak reflects a regular ordering of micelles formed by the dendrons. The formation of micelles is due to their hydrophobic interactions

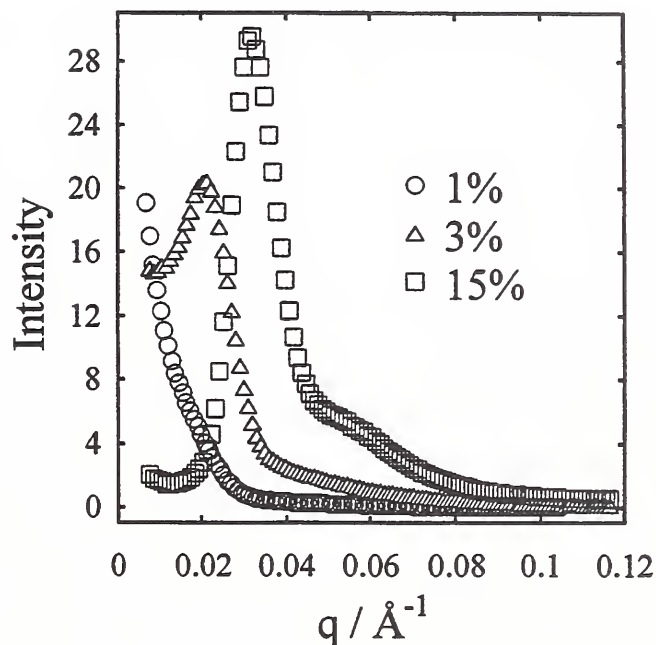


Figure 1. Plot of the scattering intensity from solutions of hybrid linear-dendritic block copolymers (type ABA; A, aromatic polyester dendron [G3]; B, linear PEO, 23 k) for different concentrations in a 1:1 (v:v) CD₃OD/D₂O mixture.

in the solvent mixture. The strongly uniform spacing between the micelles, as indicated by the narrowness of the observed peak, and the presence of a higher order shoulder, can be explained by a simple model consisting of dendrons of one ABA copolymer that are located in different micelles that are bridged by the PEO chain.

• Location of Counterions in Solutions of Polyelectrolyte Dendrimers

The location of the terminal groups of dendrimers and the location of associated counterions of protonated terminal groups is of major importance to applications of dendrimers. SANS of dendrimers with labeled counterions can be compared to the scattering of the whole dendrimer to compare their relative radii-of-gyration.

Eighth generation polyamidoamine dendrimers were protonated with acetic acid-d3 and SANS was done in pure D₂O and in D₂O/H₂O mixtures that were a contrast match to the

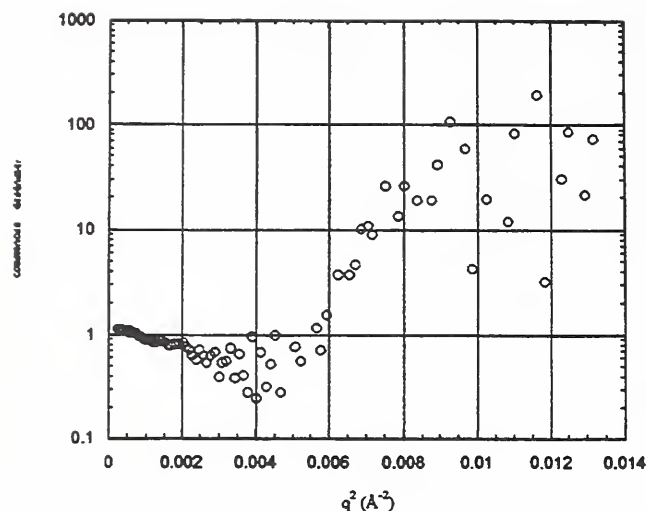


Figure 2. The downward slope indicates that the counterion cloud has a larger radius of gyration than the dendrimer itself. The increase at higher q is an indication that the counterion cloud forms a narrow band around the dendrimer.

dendrimers. In the first case, scattering was from the whole dendrimer, and in the second case, the scattering was from only the counterion cloud. Figure 2 shows a plot of the ratio of the two scattered intensities vs the scattering vector squared. The slope of this modified Guinier plot gives the difference in the radii of gyration of the two species.

Pressure Studies

• Diblock Copolymers Under Pressure

This work examined the effect on pressure of the order-disorder transition in block copolymers. The results were that shifts of 15 degrees centigrade are achievable through the application of pressure. Additionally, the neutron scattering data was shown to agree with data taken through optical birefringence.

• Polyolefin Blends Under Pressure

This work examines the effect of pressure on polyolefin blends. The recent commercialization of metallocene based polyolefin materials creates a need for the understanding of the miscibility of these materials under conditions encoun-

tered in polymer processing conditions. We are examining the shifts in the interaction parameter in both LCST and UCST type blends of both model and commercial materials. Recent results show significant increases in transition temperatures as a function of pressure, as well as small shifts in the radius of gyration.

Research Topics

Diffusion of Linear Chains into Crosslinked Networks

W. L. Wu¹⁴, B. J. Bauer¹⁴, W. E. Wallace¹⁴ and S. K. Satija¹⁴

Interdiffusion Mechanism between Linear Polymers

K. A. Welp⁶, R. P. Wool⁶ and W. L. Wu¹⁴

Segregation of Amine/Epoxy Mixtures near Silicon Oxide Surfaces

N. C. Beck Tan³, P. Giuseppe⁶, S. K. Satija¹⁴ and W. L. Wu¹⁴

Off-Specular Reflectivity Measurements of Polymer Blends

W. L. Wu¹⁴ and C. F. Majkrzak¹⁴

Polymer Interdiffusion Near an Attractive Interface

E. K. Lin¹⁴, S. K. Satija¹⁴ and W. L. Wu¹⁴

Polymer Thin Film Density

W. E. Wallace¹⁴, N. C. Beck Tan³ and W. L. Wu¹⁴

Examination of the Flow Induced Structure in a Thermotropic Polyether by Neutron Scattering

M. D. Dadmun¹⁵, S. Clingman¹⁸, C. K. Ober¹⁵, A. I. Nakatani¹⁴ and C. C. Han¹⁴

Surface Layering in Polymer Blends with Added Diblock Copolymers

A. Karim¹⁴, L. Sung¹⁰, C. Han¹⁴ and N. Balsara¹³

Interface Development in Strongly Interacting PPO/SAN Systems

A. Karim¹⁴, D. Majumdar⁹ and D. Paul¹⁶

Interdiffusion in Thin Film Polystyrene Bilayers Below the Bulk T_g

A. Karim¹⁴, G. Felcher² and J. Koberstein⁴

Polystyrene/Polybutadiene/Polystyrene-Polybutadiene Blends Under Shear

L. Sung¹⁴, A. I. Nakatani¹⁴ and C. C. Han¹⁴

Hydrogen Bonded Polymer BlendC. Zhou¹⁴, B. Bauer¹⁴ and C. C. Han¹⁴**Micellization of Model Ionic Graft Copolymers**C. L. Gettinger¹⁴, C. L. Jackson¹⁴, C. C. Han¹⁴,
M. Pitsikalis¹, J. W. Mays¹ and H. Chanzy⁵**Examination of Cylindrical Diblock Copolymer Melts During Shear**K. A. Barnes¹¹, F. A. Morrison¹¹ and A. Nakatani¹⁴**Examination of Lamellar Diblock Copolymer Solutions**S. Kitade¹², N. Ochiai¹², Y. Takahashi¹², I. Noda¹², Y. Matsushita¹⁴, M. Imai¹⁷, A. Karim¹⁴,
A. I. Nakatani¹⁴ and C. C. Han¹⁴**Small Angle Neutron Scattering Characterization of Silicone Polymer/Filler Blends**R. G. Schmidt⁷, W. Chen⁷, G. Gordon⁷ and A. I. Nakatani¹⁴**Hybrid Linear-Dendritic Block Copolymers**A. Topp¹⁴ and B. Bauer¹⁴**Compatibilizers made from Copolymers that Exhibit Strong Interactions**B. J. Bauer¹⁴ and D.-W. Liu¹⁴**Location of Counterions in Solutions of Polyelectrolyte Dendrimers**D. Valachovic¹⁴, B. Bauer¹⁴ and E. Amis¹⁴**Polystyrene-Poly (ϵ -caprolactone) Diblock Copolymer and the Blends**L. . Sung¹⁴, M. Nakatani¹⁴ and C. C. Han¹⁴**Diblock Copolymers Under Pressure**K. Migler¹⁴ and C. C. Han¹⁴**Polyolefin Blends Under Pressure**K. Migler¹⁴, M. Rabeony⁸, Garner⁸ and D. Lohse⁸**Model Polyelectrolytes in Non-Aqueous Solutions**E. J. Amis¹⁴ and B. D. Ermi¹⁹**Polyelectrolyte Dendrimers**E. J. Amis¹⁴ and D. E. Valachovic¹⁹**Domain Structure in Polyelectrolyte Solutions**E. J. Amis¹⁴, B. D. Ermi¹⁹ and D. E. Valachovic¹⁹**Affiliations**¹University of Alabama²Argonne National Laboratory³Army Research Laboratory⁴University of Connecticut⁵CNRS, FRANCE⁶University of Delaware⁷Dow Corning Corporation⁸Exxon Co.⁹GE Corp¹⁰University of Maryland¹¹Michigan Technological Univ¹²Nagoya University¹³New York State University¹⁴NIST¹⁵University of Tennessee¹⁶University of Texas¹⁷Tokyo University¹⁸Cornell University¹⁹University of Southern California

EXXON Research at the CNRF

Exxon Research and Engineering Company is a member of the Participating Research Team (PRT) that operates, maintains and conducts neutron-related research activities on CNRF's NG7-30m SANS instrument. Most experiments are in the fields of polymers, complex fluids and petroleum mixtures, using SANS as a tool to study their structure-property relations. We also participate in other type of activities at CNRF, for example, neutron imaging, neutron reflectivity. The following short reports briefly describe some of the programs, while a more complete list of the programs and their collaborators can be found at the end of this Section in Research Topics.

Pure Component Properties and Mixing Behavior in Polyolefin Blends

This work summarizes extensive investigation of the thermodynamic interactions that govern phase behavior in blends of polyolefins and examines their relationship to pure component PVT properties. Interaction strengths, obtained by SANS measurements, are classified as regular or irregular according to their consistency with a solubility parameter formalism. Characteristic pressure P^* and temperature T^* are obtained from PVT data on the pure components with various liquid-state models. For the regular blends, a close correspondence is found between the SANS-based and PVT-based solubility parameter assignments, the latter being closely related to P^* , as expected. The pattern of deviations for the irregular blends, positive in some and negative in others, effectively ruled out equation-of-state contributions as a general explanation. However, the results suggest that mismatches in both P^* and T^* play some role, and we offer some tentative attempts at generalization.[1]

Blends of Block Copolymers with Homopolymers

A morphological study is performed with symmetric diblock ethylene-propylene copolymer (DEP) and the binary blends made from DEP and atactic polypropylene (APP) by use of small angle X-ray, light and neutron scattering, and also scanning and transmission electron microscopy. DEP contains a crystallizable polyethylene block and an amorphous atactic polypropylene block. Quenching the blends in liquid nitrogen preserves the morphology in the melt state. This quenching technique reveals that DEP forms a lamellar microdomain structure and blending DEP and APP includes morphological changes in the microdomain structures as well as macrophase separation. When the APP chain is shorter than the APP block, the addition of APP changed the morphology from a lamellar to a bicontinuous cylindrical and then a discrete cylindrical and finally to a spherical structure. On the other hand, when the APP chain is longer than the APP block, macrophase separation is observed and only a transition from a lamella to a bicontinuous cylinder occurred. These morphological transitions in the melt state can be correlated to differences in the crystallization kinetics of the blends.[2]

Microstructure and Rheology of Polymeric Micellar Solutions

We study the relationship between microstructure and rheology of spherical micelles formed by a triblock copolymer consisting of polyethylene oxide and polypropylene oxide in aqueous solutions. SANS is used to determine the self-association and hydration of the micelles at various polymer concentrations and temperatures. The intermicellar interaction can be described as a hard core repulsion with surface attraction. At elevated temperatures, the polymeric micelles exhibit a higher degree of association, dehydration, and surface adhesion. The

low shear viscosity of the micellar solution is evaluated as a sum of the hydrodynamic contribution from the interparticle interaction. The latter part is calculated based on the formula proposed by deShepper et al. We adopt Baxter's model of a hard sphere with an adhesive surface to evaluate the interparticle structure factor and find that the surface attraction effectively increases the viscosity at high volume fractions. To calculate the relative viscosity at low shear rate of the polymeric micellar solutions, we use the volume fractions and intermicellar interaction potentials extracted from SANS data analysis. We obtain excellent agreement between the calculated viscosity values and the experimental measurements.[3]

Simultaneous Measurements of Viscosity and Structure for Rod-like Micelles

The structure-rheology property relation is an important issue in understanding complex fluids. For example, the macroscopic viscosity is an ultimate function of the microstructure of the fluids including volume fractions, molecular weights, particle size, shape and distribution, and interactions among various constituents of the fluids. Conventionally, however, the two aspects are measured separately, due to experimental difficulties. With a rheometer-modified SANS cell, we study a model rod-like micellar solution where we measure the viscosity while monitoring the microstructure with SANS as a function of shear stress. The system slightly below the overlapping concentration c^* would go through a phase transition at a certain critical shear rate when both the viscosity and structure undergo a dramatic change. In contrast, above c^* such a transition never happens. With this highly correlated study, we can understand the physics underlining the transition observed. The modified rheometer-SANS cell can be used to carry out similar studies on other complex fluids where rheology is a key issue. In addition, the understanding of the rod-like particles in solution drawn from this study can be applied to

other anisotropic systems.

Structure and Flow Properties of Rod-like Micelles with Associating Polymers

The structure and alignment of rod-like micelles in aqueous solutions in shear flow are investigated by SANS. Micellar rods in dilute concentrations are formed from an equimolar mixing of cetyltrimethylammonium bromide and sodium salicylate. With increasing shear rate, the scattering patterns went from spherical to elliptical and later to butterfly-like ones. Increasing anisotropy signifies the alignment and eventually the growth of micelles. The effect of hydrophobic interactions with associating or hydrophobically modified polymers on micellar alignment and growth is then studied. Hydroxyethylcellulose with and without C16 grafts in semidilute concentrations is added. With non-associating polymer, a similar trend in scattering is seen but with a shift in the anisotropy to lower shear rates due to an increase in solvent viscosity. With associating polymer, stronger anisotropy is observed at low shear rates from better alignment. However, at high shear rates the patterns, surprisingly, become more isotropic again from the lack of micellar growth and the loss of alignment. It is likely that the associations prevent the rods from coming together and growing and that the disruption of interactions leads to micellar breakup.

High Resolution SANS Characterization of Asphaltene Particles

Asphaltene is the heaviest components of a petroleum liquid. We use SANS to characterize its particle size and distribution, as well as their change under various concentrations and temperatures. Typical SANS curves from dilute to semi-dilute solutions of asphaltene in an aromatic solvent (1-methylnaphthalene) are shown in Fig. 1. Conventional SANS (or SAXS) probes a Q range of only larger than $\sim 0.007 \text{ \AA}^{-1}$. To that extent, the curves can be fit with models of various shape and size distribution, and the

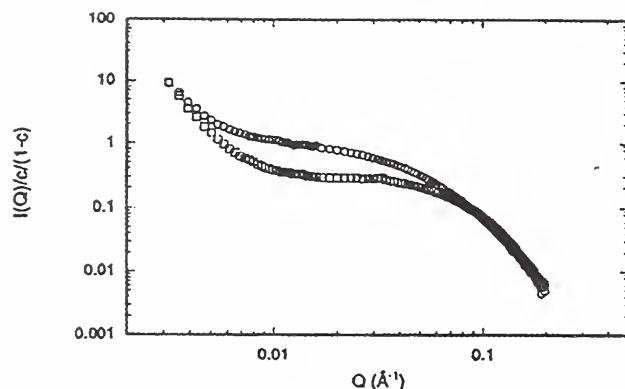


Figure 1. SANS intensity normalized by the volume fraction c for 2 asphaltene solutions in 1-methylnaphthalene- d_{10} (circles: 5%; squares: 15%).

average size is typically no larger than 100 Å. This basic particle size has been found in asphaltene solutions of many different petroleum origins. The high resolution SANS can extend the Q range to close to 0.002 Å^{-1} . An uprising in intensity towards the lowest Q probed can be seen in this range. So far, it is generally considered as a signal of the interactions between the basic particles and lacks analytical interpretation due to its limited Q range. However, we propose that it actually represents an important gradient in the asphaltene solutions, which could be more responsible for the macroscopic behavior (e.g., rheological properties) than the basic particles. With data obtained under various concentrations and temperatures, we can use scaling arguments to quantitatively characterize this new group of particles. We found that these particles have much large sizes, in the range of microns. They are formed by the aggregation of the basic particles when temperature is lowered or when concentration increases. Filtering experiments also confirm our predictions.

References

- [1] Krishnamoorti, R., Graessley, W.W., Gregory, T.D., Walsh, D.J., Fetters, L.J., Lohse, D.J., "Pure Component Properties and Mixing Behavior in Polyolefin Blends", *Macromol.*

29, 367 (1996).

- [2] Sakurai, K., MacKnight, W.J., Lohse, D.J., Schulz, D.N., Sissano, J.A., Lin, J.S., Agamalyan, M., "Blends of Amorphous-Crystalline Block Copolymers with Amorphous Homopolymers. Morphological Studies by Electron Microscopy and Small Angle Scattering", *Polymer* 37, 4443 (1996).
- [3] Liu, Y.C., Chen, S.H., Huang, J.S., "Relationship between the Microstructure and Rheology of Polymeric Micellar Solutions", *Phys. Rev. E* 54, 1698 (1996).

Research Topics

Poly(ethylene oxide) Chain Dimension in Water Approaching Theta Temperature

M.Y. Lin² and K. Charil⁸

Polystyrene in Theta Solvents

L.J. Fetters², J.S. Huang² and M.Y. Lin²

Polymer Adsorption on Hydrate Surfaces

H. E. King², T. Sun² and M.Y. Lin²

Mixing in Blends of Saturated Hydrocarbon Polymers

G. Reichart⁵, W.W. Graessley⁵, C.-C. Lin⁵, R.T. Garner² and D. J. Lohse²

Pure Components Properties and Mixing Behavior in Polyolefin Blends

R. Krishnamoorti⁴, W.W. Grassley⁵, L. J. Fetters² and D. J. Lohse²

Diblock Copolymer in Selective Solvents

J. S. Huang², L. J. Fetters², Y. C. Liu⁶ and M.Y. Lin²

Diblock Polymer-Polyelectrolytes Interactions

J. S. Huang², Y. C. Liu⁶, Z. H. Li² and M.Y. Lin²

Microstructure and Rheology of Polymeric Micellar Solutions

Y. C. Liu⁶, S. H. Chen⁶ and J. S. Huang²

In-Situ Rheology and Microstructure of Rod-Like Micelles under Shear

M.Y. Lin², C. Munzy³, G. C. Straty³, H. J. M. Hanley³, T. M. Slaweki⁷ and S. K. Sinha¹

Structure and Flow Properties of Rod-Like Micelles with Associating Polymers

S. Panmai⁵, G. Wu⁵, R. Prud'homme⁵, D. J. Peiffer² and M. Lin²

Temperature and Shear Dependence of Crude Oils

M.Y. Lin², G. Hu² and E. B. Sirota²

Asphaltene in Mixed Solvents

M.Y. Lin² and E. B. Sirota²

Alcohol-Paraffin Mixtures

E. B. Sirota² and M.Y. Lin²

Fuel Cell Radiography

J. H. Dunsmuir², M.Y. Lin² and R. J. Bellows²

Affiliations

¹Argonne National Lab.

²Exxon

³NIST, TPD

⁴University of Houston

⁵Princeton University

⁶MIT

⁷NIST, RRD

⁸Kodak

The University of Minnesota

The University of Minnesota, through its Center for Interfacial engineering, is a member of CNRF's participating research teams (PRT) in small-angle neutron scattering (SANS) (with NIST, Exxon Research and Engineering Company, and Texaco R & D) and reflectometry (with NIST and IBM). During the past year the research emphasis was on polymeric materials with participation by ten graduate students, two post-docs, three faculty members, eight staff scientists located at four National Laboratories, and one industrial scientist. Work performed at NIST plays an integral part in a comprehensive research program at the University of Minnesota that addresses fundamental and applied aspects of soft materials science and engineering.

Research Projects

- **Polypropylene Blends**

Isotactic polypropylene (iPP) is now the second largest volume commodity plastic with annual US sales in excess of 10 billion pounds. Continued growth in applications requires methods for blending this saturated hydrocarbon polymer with other plastics. Recently, the Univ. of Minn. group discovered that certain poly(ethylene/ethylene) random copolymers were melt miscible with commercial iPP. SANS experiments at NIST have aided in establishing the composition and temperature range where this occurs, thereby providing a quantitative framework for designing homopolymer and block copolymer additives.

- **Lifshitz Behavior in Block Copolymer**

Mean-field theory predicts that a symmetric A-B diblock copolymer and equal amounts of the corresponding A and B homopolymers will be characterized by a multicritical Lifshitz point when $N_A = N_B < N_{A-B}$ where N is the degree of polymerization. Previous experiments with high molecular weight polyolefins demon-

strated close agreement between experiment and theory. During the past year we designed two lower molecular weight systems in order to make contact with the related field of surfactancy. Poly(ethyleneoxide)-poly(ethylene) (PEO-PE), and poly(dimethylsiloxane)-poly(ethylene) (PDMS-PEE) diblocks, and the corresponding homopolymers were synthesized and combined to yield two sets of symmetric mixtures. The PEO-PE diblock had a molecular weight of just $M = 1,600$ g/mol while the PDMS-PEE had $M = 12,000$ g/mol. Comprehensive SANS experiments provided clear evidence of a systematic departure from the mean-field prediction as M decreased. Mixtures of PEO-PE with PEO and PE oligomers displayed phase behavior that was remarkably similar to that found in oil-water-nonionic surfactant systems.

- **Polymer-Polymer Thermodynamics**

Most theories that attempt to predict polymer-polymer phase behavior account for segment-segment interaction energy effects using the classic Flory-Huggins χ parameter. This term is frequently associated with local interactions that are assumed to be unaffected by molecular architecture. Therefore, both block copolymers and homopolymer blends should be described by a common value of χ . A model set of polyolefins was prepared to evaluate this common assumption. A symmetric poly(ethylene)-poly(ethylenepropylene) (PE-PEP) diblock copolymer and equal molecular weight PE and PEP homopolymers were synthesized, and the phase behaviors characterized by rheological and SANS experiments. SANS determined $\chi(T)$ expressions were found to be strongly dependent on the molecular architecture contrary to our expectation.

- **Order and Disorder in Block Copolymer Melts**

The Polymer Group at the University of Minnesota continued to explore various aspects of order and disorder in undiluted block copolymers during the past year. SANS experiments on PEO-polyalkane diblock copolymers demonstrated complex phase formation at unprecedented low molecular weights. A new category of molecules, tetrablock copolymers, was synthesized for the purpose of studying the role of variations in monomeric friction factors, on melt state mobility. SANS measurements provided a crucial assessment of the thermodynamic state of the materials as a function of temperature. Correlation hole scattering obtained at elevated temperatures was extrapolated to estimate the order-disorder transition temperatures, an important parameter in designing the diffusion experiments.

- **Solvent Distribution in Block Copolymers**

Many industrial applications of block copolymers involve addition of low molecular weight modifiers. For example, pressure sensitive adhesives (PSA), a multibillion dollar industry, are typically 30% to 50% tackifier, a complicated mixture of oligomers. In order to better understand the properties of such mixtures the Polymer Group has been investigating how solvent quality and concentration affect the partitioning of low molecular weight diluents in block copolymers. By taking advantage of the contrast matching technique the (weak) localization of solvent at the interface between styrene and isoprene microdomains has been documented using SANS. These experiments rely on subtle variations in local scattering length density, that produce a weak signal on a substantial incoherent background intensity. Our recent success in documenting this effect was facilitated by the enhanced flux made available by the cold source upgrade.

- **Polymer Coil Dimensions**

One of the most fundamental polymer structural characteristics, which influences melt and solution state thermodynamics and dynamics, is the coil conformation. Routine measurements of coil dimensions is a crucial component of the Univ. of Minn. Polymer Group effort at NIST. During the past year several projects have relied on such determinations including a variety of hydrogenated polybutadienes, and a commercial isotactic polypropylene.

- **Confinement Effects in Diblock Copolymer Thin Films**

Block copolymers are strongly affected by symmetry-breaking interfaces, particularly in thin-film form. Two classes of neutron reflection (NR) experiments have been conducted during the past year with poly(styrene)-poly(vinylpyridine) (PS-PVP) diblock copolymers, cast onto large silicon wafer substrates. First, blends of two PS-PVP diblocks with different compositions, and controlled levels of deuterium labeling, were used to evaluate self-consistent mean-field theory (SCFT) predictions regarding chain localization and stretching in the lamellar morphology. Nearly quantitative agreement was found. The second type of experiment exploited a confinement technique developed in our laboratory. PS-PVP layers were restricted between two hard walls, and the stability of the lamellar morphology evaluated by NR and transmission electron microscopy. As the space allotted to the molecules was reduced, packing frustration led to a morphological transition producing a new in-plane structure. NR confirmed the viability of this method for producing conformationally strained films that could be liberated by stripping one of the confining walls.

- **Swelling Lamellar Thin Films**

The thin film geometry affords an ideal sample arrangement for evaluating the effects of preferential solvent swelling of the lamellar block copolymer morphology. PS-PVP diblocks are

an excellent material for this purpose since methanol is a non-solvent for PS but swells PVP at ambient conditions. The PVP domain confined between the PS domains typically swell by about 500% relative to their dry state thickness. NR data analysis reveals a structure consistent with a pair of opposing polymer brushes in the methanol swollen PVP domains.

Research Topics

Polypropylene Blends

P. Wiemann², M. Hillmyer², T. Jones², K. Chaffin², F. S. Bates², K. Almdal², J. D. Londono¹, Y. Melnichenka¹ and G. D. Wignall¹

Lifshitz Behavior in Block Copolymer-Homopolymer Mixtures

M. Hillmyer², W. Maurer², Y. Y. Won², T. P. Lodge², F. S. Bates² and K. Almdal¹

Polymer-Polymer Thermodynamics

W. Maurer², T. P. Lodge², F. S. Bates² and K. A. K. Mortensen⁶

Order and Disorder in Block Copolymer Melts

M. Hamersky², B. Chapman², T. P. Lodge², D. Hajduk², M. Hillmyer², F. S. Bates² and S. Smith⁵

Solvent Distribution in Block Copolymers

M. Hamersky², K. Hanley² and T. P. Lodge²

Polymer Coil Dimensions

H. Tao², T. Jones², P. Weimann², F. S. Bates² and T. P. Lodge²

Confinement Effects in Diblock Copolymer Thin Films

N. Koneripalli², R. Levicky², F. S. Bates², J. Ankner³, H. Kaiser³ and S. K. Satija⁴

Swelling Lamellar Thin Films

P. R. Levicky², N. Koneripalli², M. Tirrell² and S. K. Satija⁴

Affiliations

¹Oak Ridge National Lab.

²University of Minnesota

³University of Missouri

⁴NIST

⁵Procter & Gamble

⁶Risø National Lab., Denmark

Instrumentation Development

High-Flux Backscattering Spectrometer

The High-Flux Backscattering Spectrometer (HFBS), which will occupy the end position on guide NG-2, is still under development. This new instrument will enable scientists to perform ultra-high energy resolution studies of the low-frequency dynamics of a large variety of systems. Applications of backscattering spectroscopy are numerous and include studies of rotational tunneling, molecular reorientations, diffusion, dynamics of liquids, and critical scattering near phase transitions.

The primary limitation of backscattering spectroscopy is the low neutron flux that results from having such a sharp energy resolution. Therefore the goal of the HFBS is to maximize the neutron flux as much as possible using state-of-the-art neutron optics while providing an energy resolution of less than $1 \mu\text{eV}$ full width at half maximum (FWHM). To this end, the instrument design incorporates several flux-enhancing elements including a 4 m long converging guide, a large spherically-focussing monochromator and analyzer, and a novel device known as a phase-space transformation (PST) chopper.

A backscattering spectrometer can be viewed most simply as a special case of a triple-axis spectrometer in the limit where the scattering angles of both the monochromator and analyzer are 180° . In keeping with this analogy, the HFBS will operate in a fixed final-energy mode with $E_f = 2.08 \text{ meV}$. This energy corresponds to a wavelength of 6.271 \AA , which is set by the d -spacing between the (111) lattice planes of the silicon analyzer. The incident neutron energy E_i cannot be varied in the traditional way, i. e. by changing the scattering angle of the monochromator, as this would cause the instrument to move out of the backscattering condition. Instead, E_i will be varied using a Si(111) monochromator attached to a Doppler drive which,

when running at full speed, will give users access to a maximum neutron energy transfer of $\Delta E = \pm 60 \mu\text{eV}$. The target energy resolution for the HFBS is $\sim 0.75 \mu\text{eV}$ FWHM with a Q -range of 0.15 to 1.8 \AA^{-1} .

It is hoped that the HFBS will provide a significant increase in flux beyond what is presently available at other backscattering facilities. This flux increase is achieved in several stages. Starting with the converging guide, the entire $15 \text{ cm} \times 6 \text{ cm}$ neutron beam from NG-2 will be focussed down to $2.8 \text{ cm} \times 2.8 \text{ cm}$ over a distance of 4 meters. The interior surfaces of this guide are coated with $2\theta_c^{\text{Ni}}$ supermirrors, and should increase the outgoing flux by a factor of 3. The outgoing beam divergence will increase accordingly, as required by Liouville's Theorem.

The PST chopper, which immediately follows the converging guide, is perhaps the most intriguing component of the HFBS as it exploits the physics of Bragg diffraction from moving mosaic crystals. The chopper consists of a 1 m diameter disk that is divided into six sectors. The periphery of alternate sectors is covered with highly-oriented pyrolytic graphite (HOPG) crystals 3.5 cm high, 2.8 cm wide, and 0.15 cm thick which are mounted inside magnesium cassettes. The (002) lattice planes of the HOPG crystals are aligned parallel to the axis of rotation of the chopper disk so that when spinning, the crystals are moving perpendicular to the scattering vector.

Neutrons that are Bragg diffracted from the rotating PST chopper are Doppler-shifted up or down in energy depending on whether they are less than or greater than 2.08 meV , respectively. This corresponds to a tilting of the outgoing Bragg-diffracted phase space element with respect to the nominal final neutron wavevector \vec{k}_f . Monte Carlo simulations suggest that, with the PST chopper spinning at 4700 rpm, the phase-space transformation process should enhance the flux of 2.08 meV neutrons incident

on the monochromator by a factor of 5 – 6 relative to that diffracted from a stationary chopper. The total diffracted flux, however, will depend directly on the reflectivity of the HOPG crystals.

An additional flux increase is obtained by spherically bending the silicon crystals used to monochromate and analyze the incident and scattered neutrons. The bending introduces a small lattice gradient along the [111] direction, thereby increasing the bandwidth of neutron energies that satisfy the backscattered Bragg condition. In the case of the analyzer, this bending is achieved by gluing thin Si(111) wafers onto spherically cut aluminum backing plates. The flux increase that results from this bending scales with the FWHM of the energy resolution, assuming a constant reflectivity. The finished analyzer will stand 2 meters tall, span 165° in scattering angle, and cover 20% of 4π steradians, nearly 70% more than that on IN16 at Grenoble.

In the past year, a liquid nitrogen cooled Be/Bi filter has been installed on NG-2 with a total filter capacity of 16 inches. A neutron velocity selector has been installed just after the filter. All of the electrical, vacuum and water connections have been made and tested. Nearly all of the glass for NG-2 has been installed and leak tested. Only the converging guide section remains to be mounted. In addition, all of the corresponding guide shield walls and roofs have been put into place. Construction of a thermal shutter mechanism is nearly complete. This shutter will be placed just before the converging guide.

The internal cadmium shielding for the large vacuum chamber shown in Fig. 1 has been installed, and the external high density polyethylene shielding has been cut and is being mounted into place. A dedicated crane is being purchased to lift sample dewars and cryogenic equipment off the experimental floor and onto the chamber roof. This crane will be bolted to the top of the chamber. Both stairs and railings for the chamber have been designed and sent out for bids.

Progress on the PST chopper has also con-

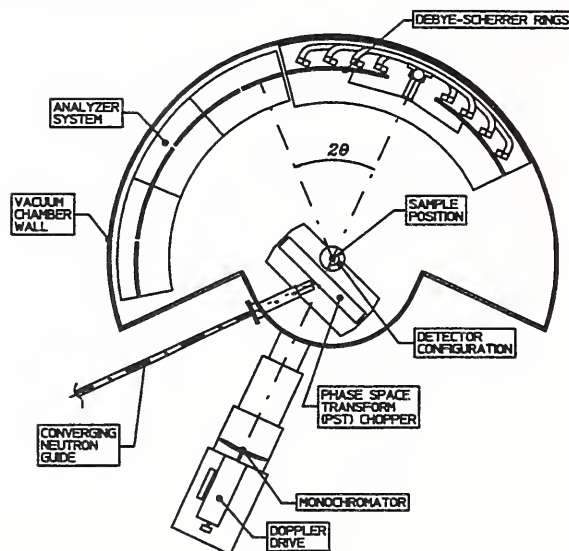


Figure 1. Schematic diagram of the CNRF backscattering spectrometer.

tinued. The last of the 180 HOPG crystals needed for the PST chopper have been tested and loaded into the Mg cassettes. The measured mosaic spread of each crystal lies between 2.25° and 3.00° FWHM. The crystals were stacked in groups of three, separated by Be wedges, in order to obtain an effective mosaic spread of 7.5° FWHM, a value that was chosen on the basis of detailed computer simulations. The PST chopper has been statically balanced, and is awaiting a final dynamical balancing before it is mounted inside the vacuum chamber.

Tests of the Doppler drive were performed using a laser-based vibrometer. The results of these tests indicate the need for significant design review and rework as the velocity profile of the drive exhibited numerous glitches near the maximum speeds where the cam follower bearings were apparently bouncing from one side of the cam surface to the other. This has serious implications for both bearing wear and data acquisition. Two promising alternative design options have been identified and are being pursued.

Delivery of the analyzer has been delayed by unforeseen difficulties in machining the large

rectangular aluminum backing structures to the high surface tolerance required for optimal performance. Delivery is now scheduled for February of 1997. This will be the last component of the HFBS to arrive. Calibration and testing of the HFBS should begin during the fall of 1997.

Neutron Spin Echo Spectrometer

The Neutron Spin Echo (NSE) spectrometer is being built and will be operated as a PRT facility involving NIST, KFA-Jülich, and Exxon Research and Engineering Co. The KFA-Jülich has recently finished construction of a similar spectrometer for which operational testing began in March 1996. The NSE spectrometer will be installed in the end position on guide NG-5. The instrument is optimized to maximize the neutron flux on the sample by keeping the length as short as possible, while achieving as high a resolution as practicable. The maximum Fourier time is expected to be at least $9.2 \times 10^{19} \lambda^3 \text{ s m}^{-3}$ (*i.e.* 47 ns for 8 Å neutrons). This design attempts to reduce the magnetic field coupling between the two main coils in order to allow access to large momentum transfers (up to 2 Å^{-1}).

The incident beam will be monochromatized to 10% by a mechanical velocity selector, and polarized by a transmission cavity similar to that developed for SANS. Provisions have been made for the possible use of a reflection polarizer at longer wavelengths or a Drabkin flipper for better monochromatization of the beam. An optical filter, similar to that designed for the NG-4 Disk Chopper Spectrometer has been designed. This optical filter will eliminate the requirement for a Bi/Be filter, and so increase the flux on the sample by 40%. The flux transmission through the optical filter is estimated to be 75% at 6 Å and 100% above 8 Å.

Correction elements have been designed (at the KFA-Jülich) that will allow not only off-axis neutrons to satisfy the echo condition but also divergent neutrons. Tests performed at Jülich have shown that the echo condition at 30 ns (70% full power) can be satisfied over an area of at least 12 cm in diameter on the detector.

Unlike SANS, where the polarization analysis can be performed anywhere along the scattered flight path, the polarization analysis for NSE can only be performed just before the detector. In order to satisfy the demands on mechanical stability for good polarization efficiency, a monolithic array of polarizing supermirror elements has been designed that will allow all neutrons from a sample of up to 5 cm in diameter to be analyzed and detected.

The NSE spectrometer will move on air pads, thereby requiring the construction of a suitably smooth and level floor: a tanzboden. We have successfully tested an epoxy tanzboden with a test bed bearing loads of up to 8 tons. Construction of the NSE tanzboden is underway and will be completed in early 1997.

The main coils for the spectrometer were delivered in November 1994. The remaining electronics and carriers for the coils were delivered in July 1996. Operational testing is expected to begin in the summer of 1997.

Disk Chopper Time-of-Flight Spectrometer

The Disk Chopper Spectrometer (DCS), at the NG-4 neutron guide, will be used for a variety of experiments such as studies of magnetic and vibrational excitations, tunneling spectroscopy, and quasielastic neutron scattering investigations of local and translational diffusion. One of the challenges in designing this instrument has been to provide a high energy resolution option, albeit at the expense of intensity, without having to resort to neutron wavelengths which severely limit the range of available wave vector transfers. The instrument promises to be versatile, popular, and fully competitive with similar instruments in Europe.

The NG-4 guide has been installed to a point just short of the first chopper housing position. Measured fast neutron and gamma-ray intensities at the end of the guide are reasonably consistent with estimates based on extensive analytical and Monte Carlo numerical calculations performed by J.M. Rowe and N. Rosov (private

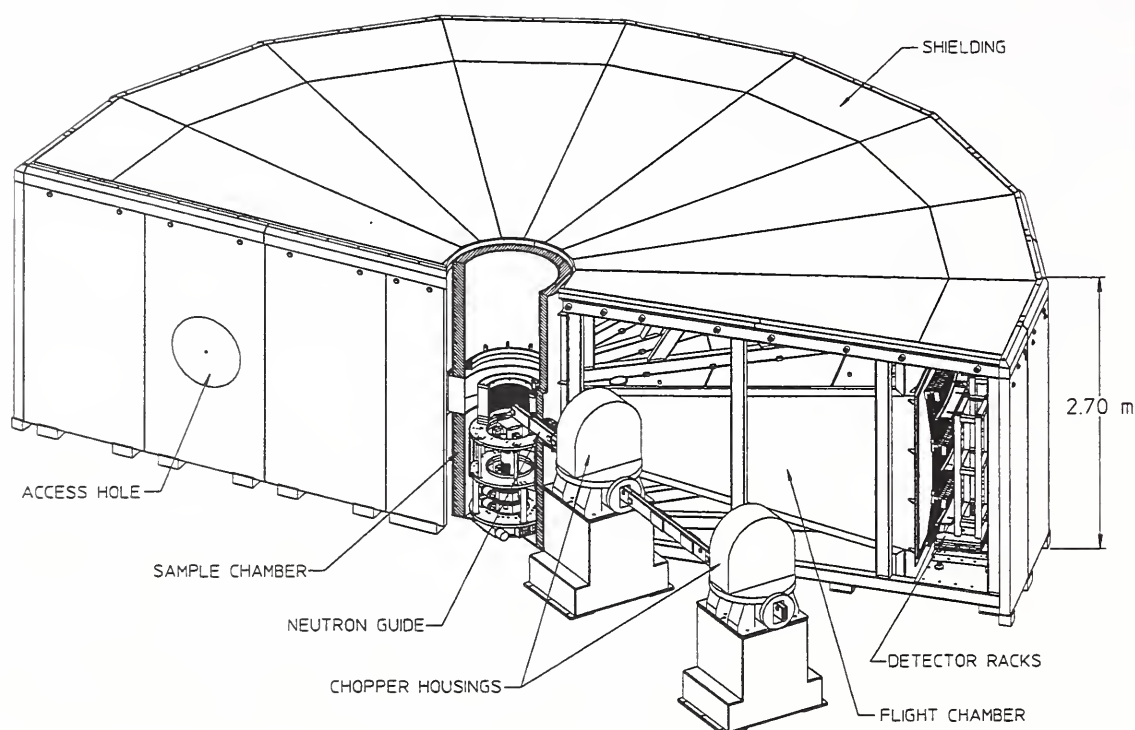


Figure 2. The engineering design of the flight chamber for the Disk Chopper Spectrometer, showing a detector rack, the sample chamber, and some external shielding. Also visible are the last two chopper housings, and several neutron guide sections. The distance from the sample axis to the detectors is 4 meters.

communication). The results also imply that the optical filter will reduce fast neutron and gamma-ray intensities to sufficiently low levels that we will not need an additional filter in the guide. Nevertheless we shall install an extra short section of guide in front of the first chopper housing; this guide will be removable to permit installation of an additional crystal filter in the unlikely event that this proves necessary.

The DCS uses a set of seven chopper disks and a partitioned guide to produce monochromatic pulses of neutrons at the sample position. The first and last chopper pairs determine the incident wavelength and the three intermediate choppers remove contaminant wavelengths and unwanted pulses [1]. There are three slots, with different angular widths, in each of the disks belonging to the first and last counter-rotating chopper pairs. By appropriately phas-

ing these disks the instrument can be operated in one of three distinct "resolution modes", without having to change the incident wavelength or the speed of the choppers. During the past year we have continued to test and debug the chopper system, in close collaboration with our colleagues Stephan Polachowski and Jürgen Rübiger (KFA Jülich). Future plans include replacement of the analog magnetic bearing control modules with newly designed digital modules; the new modules dramatically improve the mechanical stability of the disks with respect to axial disturbances.

The channeled guides which pass through the chopper housings will be enclosed in metal casings. This approach has the advantage that the guides will be protected from shocks which could conceivably break the vacuum, causing catastrophic damage to one or more choppers.

The casings have been designed and detailed, and manufacturing will begin shortly.

The mechanical design of the rest of the instrument has advanced rapidly in the past twelve months. The detector racks, which can accommodate more than 900 ^3He proportional counters placed 4 meters from the sample, were described in last year's progress report [2]. They are presently being fabricated in the shops, and delivery of the first completed rack is anticipated in January 1997. The flight chamber, support structure and associated shielding have been fully designed and are now being detailed (Fig. 2). The nature and thickness of the shielding materials were decided using results from a series of background measurements under different shielding conditions. The sample chamber, which will accept a variety of cryostats and furnaces, is at an advanced stage of design. An important feature is a removable guide section which will bring the beam close to the sample, minimizing losses associated with beam divergence. The various positioning devices that go inside the sample chamber have been assembled, and the radial collimator has been received from the manufacturer.

There has been major progress in the design and construction of the 32-input boards that form the heart of the data acquisition system. The discrete TTL integrated circuit design has been transformed into a 10ns programmable logic device which is the equivalent of more than 100 discrete integrated circuits. Extensive simulations of this device indicate that timing requirements will be fully realized and that setup times are sufficient to ensure reliable operation. The design has been checked using internal diagnostic programs and has been compiled without error. A six layer printed circuit board which will hold the chip, two memory chips and two "AND" gates, has been designed and is being fabricated. A system to test this board has been assembled using a 32-output detector pulse simulator and a 32-input digital data acquisition board in a PC. A test program is being written, and tests will begin shortly. A pro-

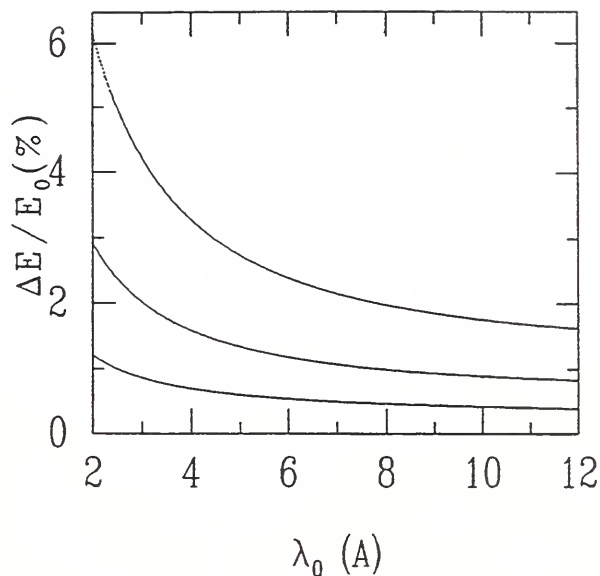


Figure 3. The calculated FWHM elastic energy resolution for the three resolution modes, with the choppers spinning at 20,000 rpm.

gramable logic device will also be used for the interface between the data acquisition boards and the data acquisition slave computer; the design of this interface will begin shortly. Considerable effort has been devoted to the design of low and high voltage distribution/monitoring systems for the amplifiers and detectors. The circuit boards for distribution of $\pm 12\text{V}$ power to the amplifier/discriminators have been manufactured, tested, and assembled into a chassis with a silk screen front panel. Three boards will be mounted and tested when we receive the first complete detector rack.

Following our decision to manage data acquisition and instrument control using a high speed personal computer running the Linux operating system, we have purchased a suitable computer which currently serves as the development platform for spectrometer software. Central to the data acquisition system is a card-based slave computer resident on the host bus. The slave will map and histogram event words read from the data acquisition boards, and will transfer histograms to the host through shared memory.

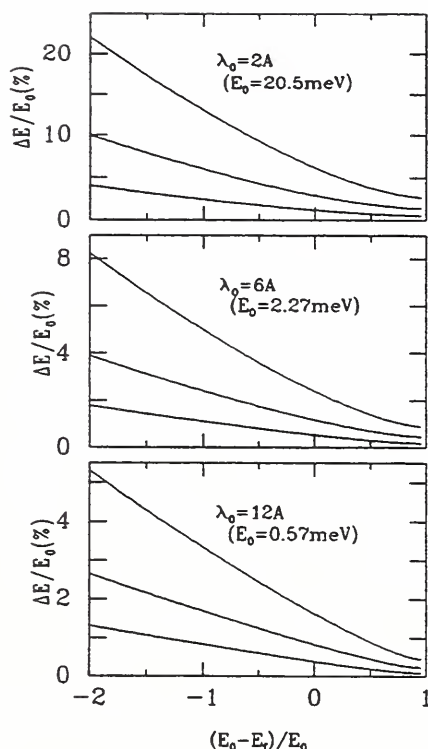


Figure 4. The calculated FWHM inelastic energy resolution for the three resolution modes and three incident wavelengths, with the choppers spinning at 20,000 rpm.

Control of CAMAC devices such as scalers and I/O registers has been achieved using a GPIB card in the PC, a GPIB crate controller, and a set of GPIB routines developed for Linux by Claus Schröter at the Free University of Berlin [3]. Standard serial ports and protocols will be used to communicate with the chopper control computer, motor controllers and devices such as temperature and pressure sensors.

In order to implement the concept of an autonomous core program which is responsible for all communications with spectrometer hardware, interprocess (TCP/IP) routines have been written and demonstrated to work reliably. The core program will consist of a series of routines written in the Tcl scripting language and as C extensions of Tcl. Our intent is to store experimental data in the self-describing hierarchical data format HDF [4].

Estimated fluxes at the DCS sample position, and energy resolutions for elastic scattering, are given in ref.[5], with a discussion of the assumptions that went into these calculations. The anticipated energy resolution for elastic scattering is shown in Fig. 3 as a function of wavelength, and the inelastic scattering energy resolution at three different wavelengths is shown in Fig. 4, for the three resolution modes of the instrument with the choppers spinning at 20,000 rpm.

References

- [1] J. R. D. Copley and T. J. Udovic, J. Res. NIST 98, 71 (1993).
- [2] "NIST Reactor: Summary of Activities, October 1994 through September 1995" ed. L. K. Clutter, NISTIR 5829 (1996), p. 98.
- [3] Available from <http://obelix.chemie.fu-berlin.de>
- [4] Consult <http://rrdjazz.nist.gov/NEXUS-proposal/NEXUS-proposal.html>
- [5] F. B. Altorfer, J. C. Cook and J. R. D. Copley, Mat. Res. Soc. Symp. Proc. Vol. 376, 119 (1995).

New Filter Analyzer Neutron Spectrometer (FANS)

The increasing complexity of new materials and processes is an important factor driving the development of new characterization tools. The traditional vibrational spectroscopies, infrared absorption and Raman scattering, have long played a central role. In principle, neutrons are a more versatile dynamical probe than photons because the fundamental nature of the neutron-nucleus interaction permits the observation of *all* the vibrations, not just those which satisfy appropriate symmetry-based selection rules. Furthermore the output of an inelastic neutron spectrum can be directly related to the vibrational density of states, providing a powerful testing ground for theoretical modelling of materials as well as a means to design materials with specific thermal properties. However inelastic neutron scattering has long suffered from

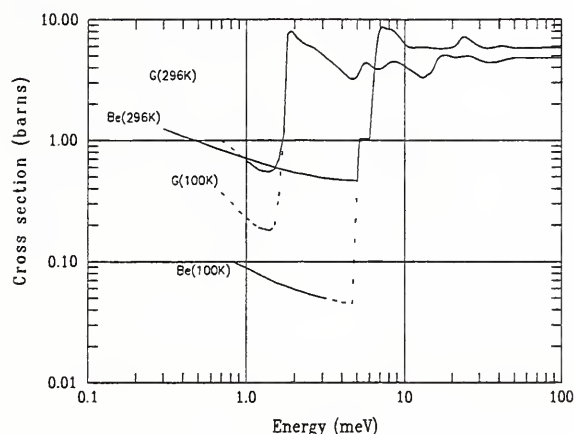


Figure 5. The total cross sections of polycrystalline beryllium (Be) and graphite (G) as a function of neutron energy for 100 and 296 K. Continuous lines represent smoothed experimental results. Broken lines represent estimates based on interpolations or extrapolations of the experimental results. The 100 K cross section for graphite is no more than a very crude estimate.

the rather low intensity. To address this, a new high intensity filter-analyzer neutron spectrometer (FANS) is being designed and constructed for installation in the reactor hall by a consortium of scientists from the University of Pennsylvania, the University of California at Santa Barbara, NIST, Hughes Aircraft, and DuPont. The throughput and sensitivity of FANS will exceed by a factor of at least 50 that of the heavily oversubscribed filter analyzer option currently in use on the BT4 spectrometer. This will provide opportunities for new users and new kinds of experiments. For instance FANS will be used to study intra- and intermolecular vibrations in molecular crystals and liquids, polymers, guest-host systems (hydrogen in metals, hydrocarbons in zeolite catalysts, sorbed gases on surfaces etc.), to characterize novel forms of carbon (fullerenes, tubules, foams and aerogels, amorphous carbons, fibers, etc.), novel candidate molecules for environmentally acceptable refrigerants, gas separation materials, aging of cements etc.

The operation of FANS is conceptually sim-

ple [1]. Monochromatic neutrons of variable energy E_i are inelastically scattered from the sample and are then detected at a fixed final energy E_f after they pass through a low-pass Bragg cutoff filter consisting of a cooled polycrystalline material (lattice constant d) which transmits only those neutrons with wavelengths longer than $2d$. E_f is defined by the cutoff wavelength, ~ 3 meV for beryllium and ~ 1.1 meV if powdered graphite is placed in series with the Be (see Fig. 5). Inelastic spectra are recorded by scanning the incident energy and detecting all scattered neutrons with $E_f < E_{\text{cutoff}}$. The accessible range of ΔE is limited on the high end to 200 meV (1600 cm^{-1}) by the anticipated beam divergence which places a lower limit on the monochromator angle and on the low end to 10 meV (80 cm^{-1}) by leakage of short-wavelength neutrons from higher-order monochromator diffraction.

The primary spectrometer of BT4 will be replaced with a new monochromator drum, new monochromators, and new double focussing monochromator devices. The detailed engineering design of the drum is now essentially complete and the construction should begin soon. The new monochromators will be Ge(311) and Cu(311). In the last year, we have developed a procedure to hot press Ge in order to achieve the desired mosaic. Procedures for cold working Cu have been in use at NIST for many years. Thus it appears to be straightforward to obtain suitable monochromator crystals. However we are also pursuing the new technology developed at Brookhaven whereby wafers are individually bent, reflattened, and then stacked in order to create an anisotropic mosaic. This leads to improved vertical focussing and therefore improved intensity for small (short) samples.

Most of the gain of FANS compared to the current filter analyzer option on BT4 arises from the much larger solid angle covered by the secondary spectrometer (9% of 4π steradian compared to 0.2%). Thus most of the work to date has been directed toward the filter system (see Fig. 6). During the past year the design of the

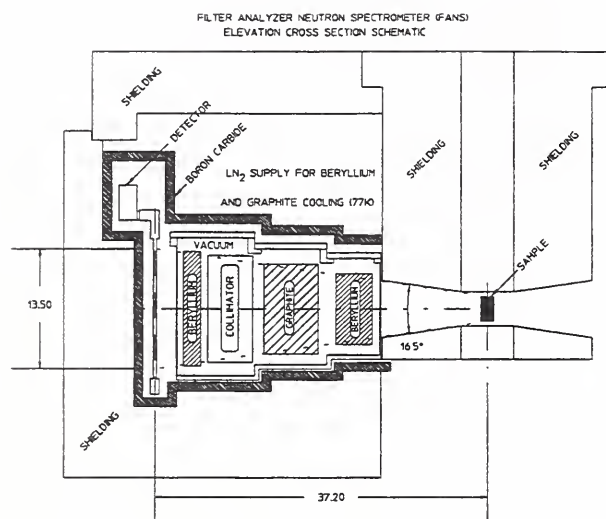


Figure 6. Cross-sectional view of the FANS analyzer. Dimensions are in inches.

Be wedges has been finalized and the Be has been ordered. Delivery of the first test piece is anticipated shortly. Detailed calculations of the thermal diffuse cross-section for graphite have demonstrated that there is no significant advantage in cooling the material below the boiling point of nitrogen. Therefore the entire filter system will be cooled with liquid nitrogen leading to a substantial simplification in the mechanical design of the analyzer system. Detailed calculations of the expected heat load are currently underway and finite element calculations of the vacuum chamber which encloses the filter system have been completed. Note that all of the filters on a given side of the sample will be located within a single vacuum in order to minimize radiative heating.

We have ordered and received approximately 140 ^3He detectors with a fill pressure of 3 atm. The background tests of these detectors along with the associated electronics have been completed. In addition we have used these detectors to measure the background near the reactor as a function of shielding thickness in order to determine the required thickness of the shielding. It is currently anticipated that the entire secondary spectrometer will be moved using air pads. Tests

of the loading appropriate for FANS were made using the epoxy test floor constructed for the spin echo spectrometer. These tests showed that the epoxy should be able to withstand the expected loading. During the next year we anticipate that the mechanical design of the analyzer will continue and that construction of some components will begin.

Reference

- [1] J. R. D. Copley, D. A. Neumann, and W. A. Kamitakahara, *Can. J. Phys* **73**, 763 (1995).

Monochromator Development

The intensity limited science of neutron diffraction constantly calls for instrumental developments that provide an increase of flux at the sample; the fabrication of an instrument specific, fully optimized neutron monochromator to make efficient use of the incident white beam is of primary concern in any instrument design or upgrade. Recent efforts in monochromator development at NIST include: mechanical deformation of bulk copper and germanium single crystals to increase the mosaic width, the examination of simultaneous reflection effects and how to avoid this potential neutron loss through careful crystal orientation, and the investigation of new monochromator materials such as stacked sheets of fluorinated mica.

Copper (220) and (311) single crystals have been successfully cold pressed from their original mosaic width of several thousandths of a degree up to 0.25 and 0.33 degrees. Cu single crystals are first cooled in liquid nitrogen, and then quickly pressed to introduce the necessary disorder. This process is repeated at increasingly higher pressures to sneak up to the desired mosaic, since the FWHM of an overpressed crystal cannot be brought back down to the desired width. The copper crystals for a (311) monochromator to be installed in the new Filter Analyzer Spectrometer will soon arrive to be characterized and squashed.

Bulk germanium (311) and (511) single crystals have been hot pressed to induce mosaic

widths from 0.15° to 0.3° . Germanium crystals are brought to approximately 90% of their melting temperature in a vacuum press, and then squeezed at 2530 psi. The temperature and pressure can be altered to achieve the desired mosaic. The absolute reflectivity of these pressed germanium samples is still scheduled to be measured.

A new vertically focusing Ge (311) monochromator for the BT-1 powder diffractometer is currently under construction, and crystal orientation was carefully considered to ensure maximum performance. Simultaneous reflection positions were calculated for a fixed wavelength of 1.077 \AA (germanium (311) at 37.5°), and initial experimental data supports the calculations. The monochromator crystals were oriented to have both a (311) face, and the $(02\bar{2})$ direction rotated 110° azimuthally about the scattering vector. This orientation positions the crystals for maximum reflected intensity by avoiding any parasitic neutron loss. The BT-1 monochromator is scheduled to be built, aligned, and operational by the end of January, 1997.

The characteristics of fluorophlogopite, a synthetic fluorinated mica, as a neutron monochromator are also under study. The large d-spacing (9.98 \AA) provides a low takeoff angle, and the material has an intrinsic mosaic width on the order of 0.08° . Thin sheets of the material can be stacked and misoriented with aluminum shims to "build" a crystal mosaic up to 0.5° . We are currently working with Brookhaven National Laboratory in investigating the optimum crystal thickness, the neutron absorption cross section, and the incoherent scattering cross section of fluorophlogopite. If it proves an efficient material, we intend to build a vertically focusing monochromator made of individual "fingers" of fanned sheets of this synthetic mica for several instruments at NIST.

Perfect Crystal SANS Diffractometer

Development of a Perfect Crystal SANS Diffractometer (PCD) has progressed to the stage of final testing of components (crystals and mo-

tion controls) and preparation of the beam port is set to begin in the next few months.

The PCD is a Bonse-Hart double-crystal diffractometer that utilizes the narrow Darwin reflection width of perfect crystals to study SANS in the ultra-high resolution regime (0.1 nm^{-1} to 0.001 nm^{-1}). This instrument will be built at thermal neutron beam port (BT-5) to take full advantage of the high flux at short wavelengths and large beam divergence available there. Our simulations show that we can achieve a flux on the sample of approximately $6 \times 10^4 \text{ n/cm}^2\text{s}$ over a $5 \text{ cm} \times 5 \text{ cm}$ beam area using Ge (220) crystals and approximately $4 \times 10^4 \text{ n/cm}^2\text{s}$ using Si (220). The performance of any PCD instrument is ultimately determined by how well the scattered flux in the Q-region of interest compares to the background. This background can be dominated by an instrumental background that results from the "wings" of the Darwin reflection. To suppress these wings, multiple reflections are needed in both the monochromator and analyzer. In theory, a triple-bounce monochromator and analyzer will suppress the wings to Q^{-6} . In practice, this has not been demonstrated for neutrons until very recently. An extra instrumental background source term has limited the performance of PCDs at high Q values. A recent study from ORNL [1] suggests that this extra background results from reflection from the back side of the crystals or rescattering of the neutrons that form an internal current down the length of the crystals. The ORNL group has found that these effects can be suppressed with appropriate placement of an absorbing material. We expect to use a similar approach to enable us to reach near-theoretical performance. With the high flux that we can obtain from a thermal tube and a triple-bounce monochromator and analyzer set, our instrument is expected to offer a several orders-of-magnitude improvement over existing PCD-SANS instruments world-wide.

Before the construction of the instrument can be started, the beam port needs to be fitted with a new shutter. A design for this com-

ponent is now ready for final approval and construction. Two triple-bounce channel-cut silicon crystals have been purchased and will be tested for the suppression of the "wings" of the Darwin reflection they produce and their reflectivity. A detailed design of the instrument is being completed for submission to the Safety Evaluation Committee. Once approved, the major components of the instrument will be fabricated and preparations begun for installation. These major components will include new external shields, a vibration isolation table to support the crystals and a detector array. Other components will include a temperature control hutch for the instrument and a experiment-area enclosure to limit access to the sample area.

Reference

- [1] Agamalian, M., Wignall, G. D., Triolo, R., "Optimization of a Bonse-Hart Ultra-Small Angle Neutron Scattering Facility by Eliminating the Rocking Curve Wings," (submitted to *J. Appl. Cryst.*, 1996).

Implementation of Polarized Neutron SANS

The option of using polarized neutrons for small-angle neutron scattering measurements has been implemented on the NIST/NSF 30 m SANS instrument on guide NG-3. The essential component for this option is a transmission polarizing guide based on the same type of Fe/Si supermirror coatings that have been developed for the transmission polarizers for the NG-1 reflectometer and the SPINS spectrometer. The polarizing guide for the SANS instrument, fabricated by CILAS, France, consists of an array of 1 mm thick silicon plates, with Fe/Si supermirror coatings, aligned to form a V inside a section of copper-coated neutron guide. The large difference in the critical angles of the supermirror coating for the two spin states approximately $\frac{1}{2}\theta_c^{Ni}$ and $3\theta_c^{Ni}$ for the "down" and "up" spin states respectively allows a relatively large convergence angle to be used to polarize a large beam cross section beam ($4 \times 5 \text{ cm}^2$ in the

present case) over a range of wavelengths (5 to 15 Å) with a guide of moderate length (1.2 m).

The polarizing cavity is installed on one of the movable tables in the pre-sample flight path of the CHRNS SANS instrument for easy insertion when needed. Immediately following the cavity is a standard flat coil spin flipper for reversing the direction of polarization. Permanent magnets magnetize the iron layers of the supermirror coating and provide a guide field to maintain the polarization up to the sample position. Computer control of the insertion of the polarizing guide, associated guide field magnets, and current to the flipper coils have been added to the instrument's user friendly data acquisition software.

Test measurements at a typical wavelength of 8 Å yielded a beam polarization of 89%. This is close to the expected polarization of 90-95%. Further tests are planned to map out the spatial variation of the polarization over the beam area to try to determine if the polarization can be improved. With this degree of polarization, combined with the measured 94% flipping efficiency of the spin flipper, flipping ratios (ratio of the beam intensity with flipper current off to that with the current on) between 10-15 are obtained, depending on wavelength and sample size. This level of performance provides a significant enhancement in sensitivity to SANS from ferromagnetic inhomogeneities which is not available on any other SANS instrument in the U.S. Efforts will continue to reach flipping ratios > 20 , the original design goal for the apparatus.

Research Topics

The Disk Chopper Time-of-Flight Spectrometer

J. R. D. Copley⁶, F. B. Altorfer^{6,8}, N. C. Maliszewskyj⁶, C. W. Brocker^{6,8}, H. P. Layer⁶, and J. C. Cook^{6,8}

Performance Tests of the Choppers for the Disk Chopper Time-of-Flight Spectrometer

F. B. Altorfer^{6,8} and J. R. D. Copley⁶

Acceptance Tests of Detectors and Amplifiers for the Disk Chopper Time-of-Flight Spec-

trometer

P. C. Tobin⁶

Mechanical Design of the Disk Chopper Time-of-Flight Spectrometer

C. W. Brocker^{6,8}

Design of the Data Acquisition System for the Disk Chopper Time-of-Flight Spectrometer

H. P. Layer⁶

Software Development for the Disk Chopper Time-of-Flight Spectrometer

G. C. Greene⁶, N. C. Maliszewskyj⁶ and P. Klosowski^{6,8}

Ray-Tracing Calculations of Neutron Focusing Properties of Toroidal Mirrors

J. R. D. Copley⁶ and C. Hayes⁴

Calculations of Fast Neutron and Gamma-ray Dose Rates Exiting a Neutron Optical Filter

N. Rosov⁶, J. M. Rowe⁶ and J. R. D. Copley⁶

Backscattering Tests of Variable Thickness Si(111) Analyzer Plates

P. M. Gehring⁶, D. A. Neumann⁶, B. F. Frick⁴, C. H. Appel¹⁰ and M. D. Shaw³

Mosaic Measurements of ZYH Grade Highly-Oriented Pyrolytic Graphite

P. M. Gehring⁶, K. T. Forstner^{8,6}, D. A. Neumann⁶, and A. W. Moore⁹

Construction of an Epoxy Tanzboden

R. Williams⁶

Field Dependence of Diffuse Scattering from Polarizing Supermirrors

N. Rosov⁶ and J. Barker⁶

Construction of a New Sample Furnance

A. Clarkson⁶ and N. Rosov⁶

Development of Perfect Crystal SANS Diffractometer

A. Drews⁶, J. Barker⁶, J. Moyer⁶, M. Agamalian⁷ and C. Glinka⁶

SANS Polarized Beam Development

J. Barker⁶, D. Fulford⁶, B. Hammouda⁶ and C. Glinka⁶

Pressed Cu for Neutron Monochromators

T. Forstner^{8,6} and S. F. Trevino^{6,1}

Pressed Ge for Neutron Monochromators

T. Forstner^{8,6}, S. F. Trevino^{6,1}, D. A. Neumann⁶, J. Blendell⁶ and B. Chakomakos⁸

Synthetic Mica for Neutron Monochromators

T. Forstner^{8,6}, C. F. Majkrzak⁶, L. Passell² and D. A. Neumann⁶

Design of the New Filter Analyzer Neutron Spectrometer (FANS)

P. Papanek^{6,11}, D. A. Neumann⁶, R. Christman⁶, D. Pierce⁶, J. E. Fischer¹¹, J. J. Rush⁶, M. L. Klein¹¹ and A. K. Cheetham¹²

Hydrogen Cold Source Development

R. E. Williams⁶, P. A. Kopetka⁶ and J. M. Rowe⁶

Monte Carlo Methods for Nuclear Applications

R. E. Williams⁶

Affiliations

¹Army Research Lab.²Brookhaven National Lab.³Eagle-Picher Research Labs.⁴Institute Laue-Langevin, France⁵Johns Hopkins University⁶NIST, Reactor Radiation Division⁷ORNL⁸Univ. of Maryland⁹UCAR Co.¹⁰SFA Inc.¹¹Univ. of Pennsylvania¹²Univ. of California-Santa Barbara

MSEL Programs

The Reactor Radiation Division's research projects fall almost entirely within two MSEL program areas: Neutron Facility Operation and Neutron Characterization. Some of the work described in the previous sections of this report fall into four other MSEL program areas. These programs are described below.

Biotechnology

The Neutron Scattering Facilities at the NIST Research Reactor offer a unique opportunity in the US for studying the structure and dynamics of biological macromolecules and biomimetic systems as a function of chemical or biological environment. Two 30m small-angle neutron scattering (SANS) instruments and reflectometers provide the country's best combined capabilities for surface and structural studies. Both SANS and reflectometry are well-suited for in situ structural studies of macromolecules in solution ranging in size from 1 nm to 100 nm. In addition, a wide range of dynamic processes encompassing the 10^{-7} to 10^{-12} s timescales will soon be accessible with the completion of three state-of-the-art neutron spin-echo, high-resolution time-of-flight and backscattering spectrometers. These techniques provide information on macromolecular dynamics which is complementary to, and in many cases more direct than, that obtained from NMR and electron spin resonance and which can be directly compared with molecular dynamics computer simulations. Thus, both structure and dynamics studies are being pursued, using this unique variety of measurement capabilities, to probe structure-function relationships in macromolecules and other biologically and technologically important systems. The program is being carried out with close collaboration and support from NIST's Biotechnology Division. Strong collaborations are also underway with NIH and the University of Pennsylvania.

Ceramic Coatings

The Ceramic Coatings Program is a measurement and characterization effort which addresses the processing reproducibility and performance prediction issues associated with, primarily, thermal-spray deposited ceramic coatings. The program focuses on plasma-spray-deposited ceramic thermal barrier coatings used in aircraft gas turbines and expected to be used in land-based turbines and diesel engines. Sales in the thermal-spray industry are currently valued at over one billion dollars annually, a significant portion of which is ceramic thermal-barrier coatings. Collaborations have been established with industrial organizations including Pratt and Whitney, General Electric, Caterpillar, METCO, MetTech and Zircoa as well as the Thermal Spray Laboratory at the State University of New York at Stony Brook and the Thermal Spray Laboratory at Sandia National Laboratory. The program includes collaboration with the National Aerospace Laboratory and the National Mechanical Engineering Laboratory, both in Japan, to examine functionally gradient materials. Research is also conducted on the processing and properties of chemical-vapor-deposited (CVD) diamond films in collaboration with Westinghouse, an Advanced Technology Program (ATP) awardee, and on Physical Vapor Deposited (PVD) ceramic coatings in collaboration with Praxair, another ATP awardee.

Participants in the NIST program are located in the Ceramics, Materials Reliability and Reactor Radiation Divisions of the Materials Science and Engineering Laboratory as well as the Chemical Science and Technology Laboratory.

The approach taken in the plasma-spray (PS) research has been to build on the analytical capabilities at NIST and the material processing capabilities of collaborators. The program has the following elements:

- development of techniques for character-

ization of physical and chemical properties of stabilized zirconia feedstock to provide data for increased processing reproducibility as well as data required for production of a Standard Reference Material suitable for calibration of light-scattering size distribution instruments used in industry for analysis of PS powder:

- development of scattering techniques to determine the quantity, size and orientation of porosity and microcracks in PS ceramic coatings suitable for use in modeling the thermomechanical behavior of these materials;

- development of methods to measure chemical, elastic modulus, and thermal properties on a scale suitable for use in microstructural models of behavior;

- development of techniques to model thermomechanical behavior of thermal-barrier coatings to enable more reliable performance prediction; and

- development of techniques for accurate measurement of the thermal conductivity of PS coatings, by use of the guarded hot-plate technique suitable for incorporation in ASTM standards and by the pulsed laser heating technique, to provide a method for comparison with routine industrial techniques.

- development and refinement of more sensitive methods for accurate analysis of oxide phases and residual stresses which affect performance and durability of coatings.

Research on chemical mapping of powders and microstructures is conducted in the Microanalysis Division of the Chemical Science and Technology Laboratory. Thermal property research is conducted in the Materials Reliability and Metallurgy divisions and the Reactor Radiation Division participates in both the powder analysis and scattering projects. A strong attribute of the PS coatings research is the use of common materials for which complementary data can provide a more complete understanding of processing-microstructure-property relationships.

Evaluated Materials Data

The objective of the Data Technologies Program is to develop and facilitate the use of evaluated databases for the materials science and engineering communities. Both research- and application-directed organizations require readily available evaluated data to take advantage of the large volume of materials information developed on public and private sponsored programs. This information, particularly numeric data, is available in an ever increasing number of publications published worldwide. The necessity to consolidate and allow rapid comparison of properties for product design and process development underlies the database projects.

Evaluated databases are developed in cooperation with the NIST Standard Reference Data Program Office and, often, coordinated with the activities of other laboratories and scientific/technical societies. Research consists of the compilation and evaluation of numeric data as well as recently initiated efforts directed at more effective distribution and use of data. Database activities reflect laboratory programs with scientific capabilities required for appropriate data evaluation.

Database projects in MSEL include:

- Phase Diagrams for Ceramists (PDFC), conducted in cooperation with the American Ceramic Society;

- the Structural Ceramics Database (SCD), a compilation of evaluated mechanical and thermal data for nitrides, carbides, and oxides of interest to engineers and designers;

- a ceramic machinability database, coordinated with the Ceramic Machining Research Program;

- a high T_c superconductivity database developed in cooperation with the Japanese Agency for Industrial Science and Technology (see superconductivity);

- development and implementation of the STEP protocol for the exchange of materials data, under the auspices of the ISO 10313 activity;

- the NACE/NIST Corrosion Performance

Database developed to provide a means to select structural alloys for corrosive applications; and

- the Crystal Data Center which provides fundamental crystallographic data on inorganic materials.

High Temperature Superconductivity

A significant program in critical transition temperature superconductivity is being conducted in MSEL and other Laboratories at NIST. The primary focus of the MSEL program is on bulk superconducting materials for wire and magnet applications. In carrying out this program, researchers in MSEL work closely with their counterparts in other NIST Laboratories, and collaborators in U.S. industry, universities, and other National Laboratories.

The primary thrusts of the program are as follows:

- Phase equilibria - Work is being performed in close collaboration with the U.S. Department of Energy (DOE) and its national laboratories to provide the phase diagrams necessary for processing these unique ceramic materials. A prime objective is the development of the portions of the phase diagram for the Pb-Bi-Sr-Ca-Cu-O system relevant to production of the high T_c materials.

- Flux pinning - Use is made of a unique magneto-optical imaging facility to examine flux pinning in a variety of materials, with much of this work being conducted in collaboration with American Superconductor Corporation. In addition techniques for better interpretation of magnetic measurements are being developed. Structure and dynamics of flux lattices and melting phenomena, critical to applications, are investigated with small-angle neutron scattering techniques.

- Damage mechanisms - Work is being carried out under a joint CRADA (cooperative research and development agreement) with American Superconductor Corporation as part of the "Wire Development Group" which involves a number of DOE National Laboratories and the

University of Wisconsin to elucidate the effects of strain on the loss of current in superconducting wires. The primary tool being employed is the use of microfocus radiography available at the NIST beamline at the Brookhaven National Laboratory.

- Database - A high temperature superconductor database has been developed in collaboration with the National Research Institute for Metals (NRIM) in Japan. The High Temperature Superconductor Database (HTSD) includes evaluated open-literature data on numerous physical, mechanical, and electrical properties of a variety of chemical systems. The first version of the database is now for sale by the Office of Standard Reference Data.

- Crystal structure - Thermal neutron scattering techniques and profile refinement analyses are being utilized to investigate crystal and magnetic structures, composition, dynamics and crystal chemical properties. This research is being carried out in collaboration with a number of industrial and university experts and researchers at National Laboratories.

Reactor Operations and Engineering

In spite of furloughs, snow storms and electric power interruptions, last year was a good year and the first full year at full power of 20 MW since 1991. The reactor was on-line 72% of the time equivalent to 70% at 20 MW which is about 94% of available time. Both the reactor and the cold neutron facility were essentially trouble free. Most of the time, the reactor has been operating on a regular seven-week schedule; five and a half weeks at power and one and a half weeks for refueling, maintenance, and installation and reconfiguration of experiments. Average fuel utilization reached almost 70% which is significantly better than any other research reactor.

Major efforts this year were concentrated on updating the safety analysis report, operating procedures and drawings. Plans are continuing to upgrade reactor systems and components in preparation for relicensing beyond 2004. Many of these improvements are underway and all should be completed by the time application for a 20-year license renewal is made to the Nuclear Regulatory Commission.

Guest Researchers and Collaborations

The NBSR provides some of the nation's most advanced capabilities in the area of neutron beam research. A major role of the division is to make these capabilities available to all qualified U.S. researchers – from universities, industry, and government laboratories. Scientists from other institutions, or other divisions of NIST, are thus involved in nearly all of the ongoing research activities of the division.

The number of NBSR research participants is plotted against time in Fig. 1. This figure shows the strong, steady growth over the past decade. Figure 1 also shows the predominance of outside user participation in experiments performed at the NBSR. The rightmost column represents participants from 54 U.S. industrial laboratories, 92 universities, 33 other government institutions, and over 100 foreign institutions. Participants include those who were at the facility at least once for an experiment or by collaborating in other ways (e.g. sample, co-authors on publications).

The development of new instrumentation at the NBSR over the years represented in Fig. 1 is certainly the most important factor contributing to the increasing number of facility users. During the past fiscal year (FY96), several experimental stations have come into routine operation, or have had major improvement in their measurement capability. A new state-of-the-art residual stress diffractometer, located at beam port BT-8 in the reactor confinement building, enables experimenters to determine stress fields within samples with a spatial resolution of about 1 mm. The method is one of the most advanced techniques available for non-destructive evaluation of materials in engineering applications. A polarized beam reflectometer has been relocated from the reactor confinement building to a position on neutron guide NG-1. In the new position, the reflectometer can collect data much faster with lower background, and longer wavelengths may be more effectively employed.

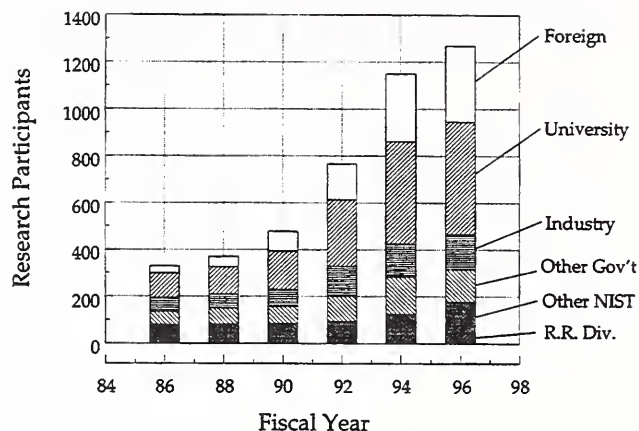


Figure 1. Research Participants at the NBSR

Equipped with state-of-the-art transmission supermirror polarizers which may be inserted in either the incident or reflected beams, it is currently among the most advanced instruments of its type. While it is useful for mapping profiles below a smooth surface in samples of many kinds, it excels in the examination of magnetic systems, such as the giant magnetoresistive materials used in magnetic sensors and read heads for computer hard disks. The neutron interferometer station is now in routine operation. Developed and operated by NIST, it is a national user facility for both fundamental physics experiments and materials science applications.

Facility users obtain access to NBSR instrumentation in several ways. The first and most straightforward route is through a formal research proposal system, as described in a following paragraph. A second avenue lies in direct collaborations between external facility users and NIST scientists, involving experiments of limited duration on specific research topics. A third, also very important, mode of access involves more formal collaborations of longer duration with larger groups, i.e., research consortia, rather than with individual scientists. The third mode has been used to build and operate

several new instruments.

In the formal research proposal system, calls for proposals are issued at a six- or seven-month interval. During FY96, one call for proposals was issued, with the subsequent call to be made at the beginning of FY97. Approximately 110 proposals were received in response to the last call, requesting in excess of 400 instrument-days. The instruments in greatest demand were the small-angle neutron scattering (SANS) diffractometers, which accounted for 59 proposals, and the neutron reflectometers, which attracted 28. While 80% of the proposals were approved, only about 50% of the time requested could be granted. Significant opportunity for growth lies in the area of cold-neutron inelastic neutron scattering. At present, there are only two instruments at the CNRF, the Fermi-chopper time-of-flight spectrometer and the spin-polarized cold-neutron triple-axis spectrometer (SPINS), which are routinely scheduled from formal proposals. In a year's time, three major new instruments are expected to become operational – the backscattering spectrometer, the disk-chopper time-of-flight spectrometer, and the spin-echo spectrometer. These will significantly extend the high-resolution inelastic scattering capability in the U.S., and greater user demand for inelastic neutron scattering is anticipated.

We rely on a peer review system for evaluation of proposals for instrument time. Final decisions about the allocation of beam time are made by the Program Advisory Committee (PAC), which is a group of seven prominent scientists appointed by NIST management. The PAC membership represents a wide range of expertise in neutron beam research, and advises NIST on many aspects of the research activities and instrumentation at the reactor, especially those concerning user interaction. In their regular meeting, i.e., once every proposal cycle, the PAC considers the peer reviews of proposals that have been sent to expert referees, technical reviews made by NIST scientists, reviews for safety, and the proposals themselves, in order to approve or reject proposals, and to allocate

specific amounts of instrument time.

Direct collaborations remain a common way in which facility users obtain access to the instruments at the NBSR, accounting for approximately 60% of the number of instrument-days. The thermal-neutron scattering instruments, i.e., triple-axis spectrometers in the reactor confinement building and the high-resolution powder diffractometer, were mainly scheduled in this way.

Access to instruments may also be obtained through research consortia, in the third method by which beam time is allocated. For example, the 30-meter SANS diffractometer on neutron guide NG-7 was built and is operated by a group consisting of NIST, Exxon Research and Engineering Co., the University of Minnesota, and Texaco R & D. Three-quarters of the beam time on the instrument is reserved for the consortium, and the remaining time is allocated to general user proposals. Similar arrangements involving other consortia apply for the horizontal sample reflectometer and the high-resolution powder diffractometer.

Several of the experimental stations at the NBSR are wholly or partially operated by personnel from other organizational units of NIST. In particular, chemical analysis by nuclear methods is carried out by a group from the Analytical Chemistry Division. There are several experimental stations operated by this group. For example, cold-neutron prompt-gamma neutron activation analysis (PGAA), an in-beam method, is offered directly to users through proposals, while instrumental (i.e., conventional, *ex-situ*) activation analysis is an in-house activity offered to users through collaborations.

Services such as irradiation, radiography, and materials characterization are provided to other government agencies using the facilities at the NBSR. The FDA and Smithsonian have maintained long-term, continuing associations, while other institutions receive services at the NBSR on a short-term, case-by-case basis. Such services are provided to non-government agencies as well.

In some cases, industrial R&D of a proprietary nature are carried out at the NBSR, provided that appropriate beam-time charges are paid on a full-cost-recovery basis to the U.S. government.

Several meetings and workshops were arranged during FY96. The Neutron Scattering Satellite Meeting to the XVII Congress of the International Union of Crystallography was held at NIST during Aug. 5-7, 1996. Approximately 130 scientists from 15 countries attended this general meeting on neutron scattering science and instrumentation. A meeting of the CNRF Researchers' Group was held on the evening of Aug. 5, during which the users of the facility had an opportunity to exchange ideas on the operation of the CNRF. In recent years, we have run an annual summer school workshop, with the purpose of educating new users, primarily graduate students and younger scientists in neutron scattering techniques at the research level. This year's summer school, held June 3-6, 1996, was devoted to small angle scattering and reflectometry methods. A workshop on high resolution neutron spectroscopy is planned for the summer of 1997, in anticipation of the user interest in the new spectrometers to be commissioned in the CNRF guide hall.

We, working with the researchers group, plan to make greater efforts to obtain feedback from facility users. In addition to the annual CNRF researchers' group meeting, small seminar-type meetings are being held at NIST, in order to sample the experiences of users who have come to use the facility, while they are on site. A more formal survey of users, through electronic and/or regular mail, will be carried out during the coming year. Plans are also being made to track in more detail the use of all the instruments at the NBSR. A comprehensive data base will be implemented to provide detailed information on investigators, proposals, and experimental stations.

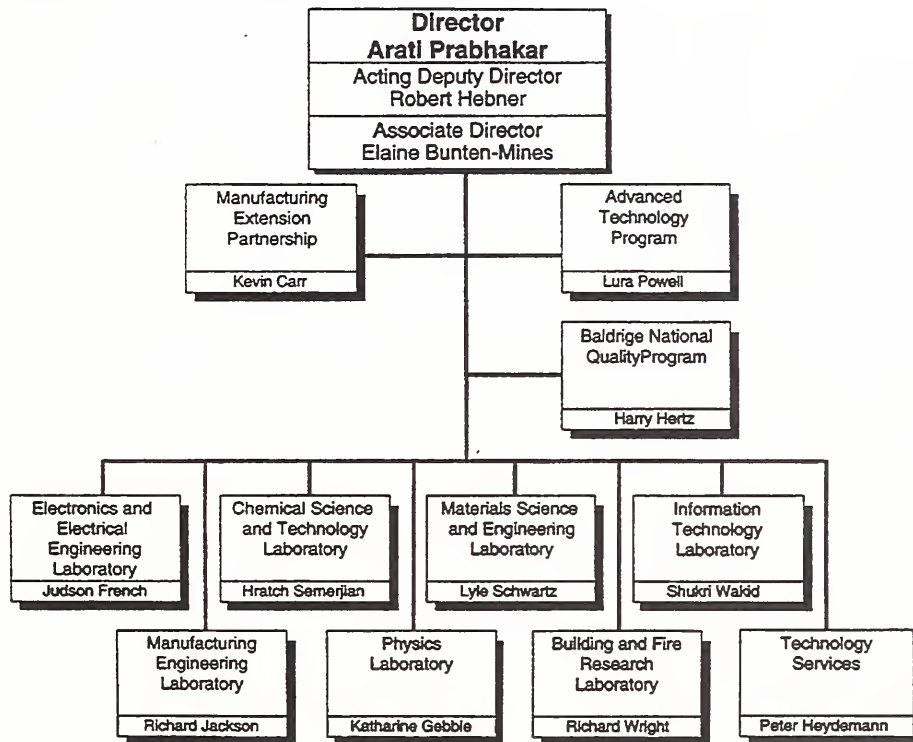
The World Wide Web at <http://rrdjazz.nist.gov> is rapidly becoming the standard method for users to obtain in-

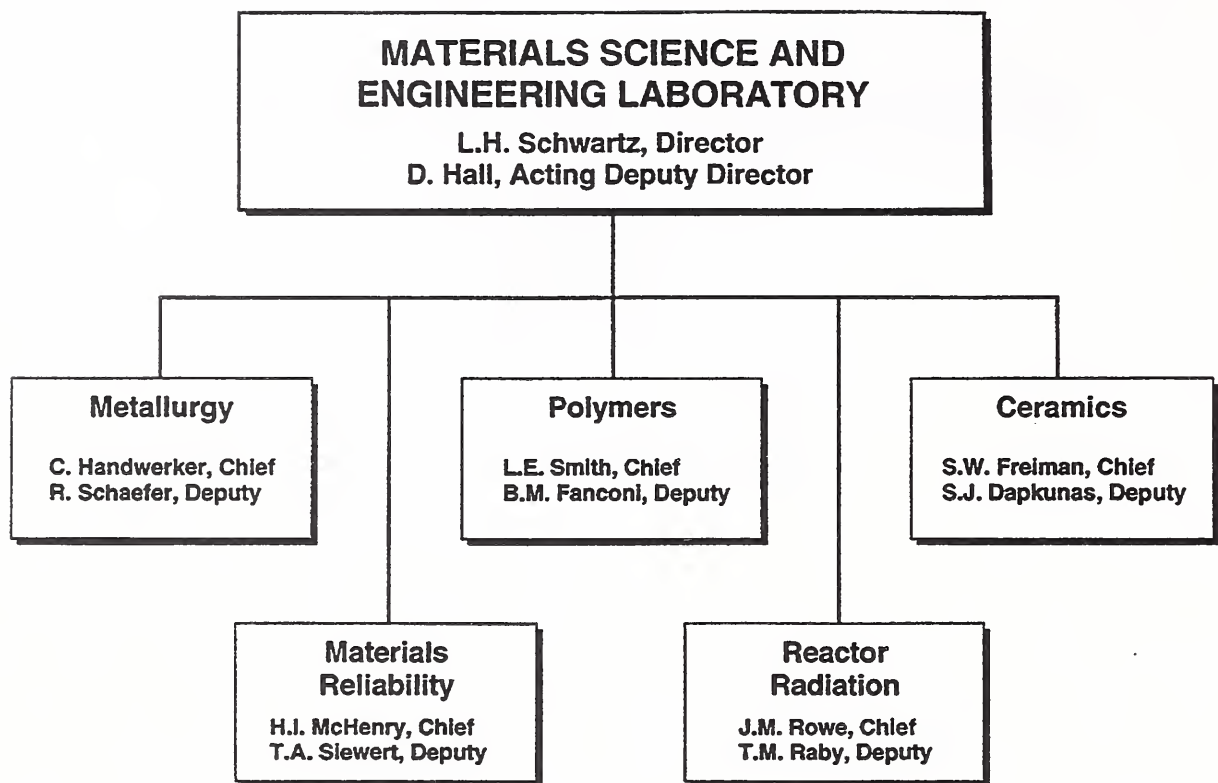
formation about the facility. Submission of beam-time proposals from a Web page form is now possible. For further information on the NBSR, its instrumentation and the guest researcher program, interested parties should examine the division's pages on its Web site, or contact Bill Kamitakahara at (301) 975-6878, billk@rrdstrad.nist.gov. Inquiries about specific techniques or instruments may be directed to any appropriate RRD staff member. Names, telephone numbers, and e-mail addresses may be found on the list of instrument scientists on a Web page.

Organizational Charts

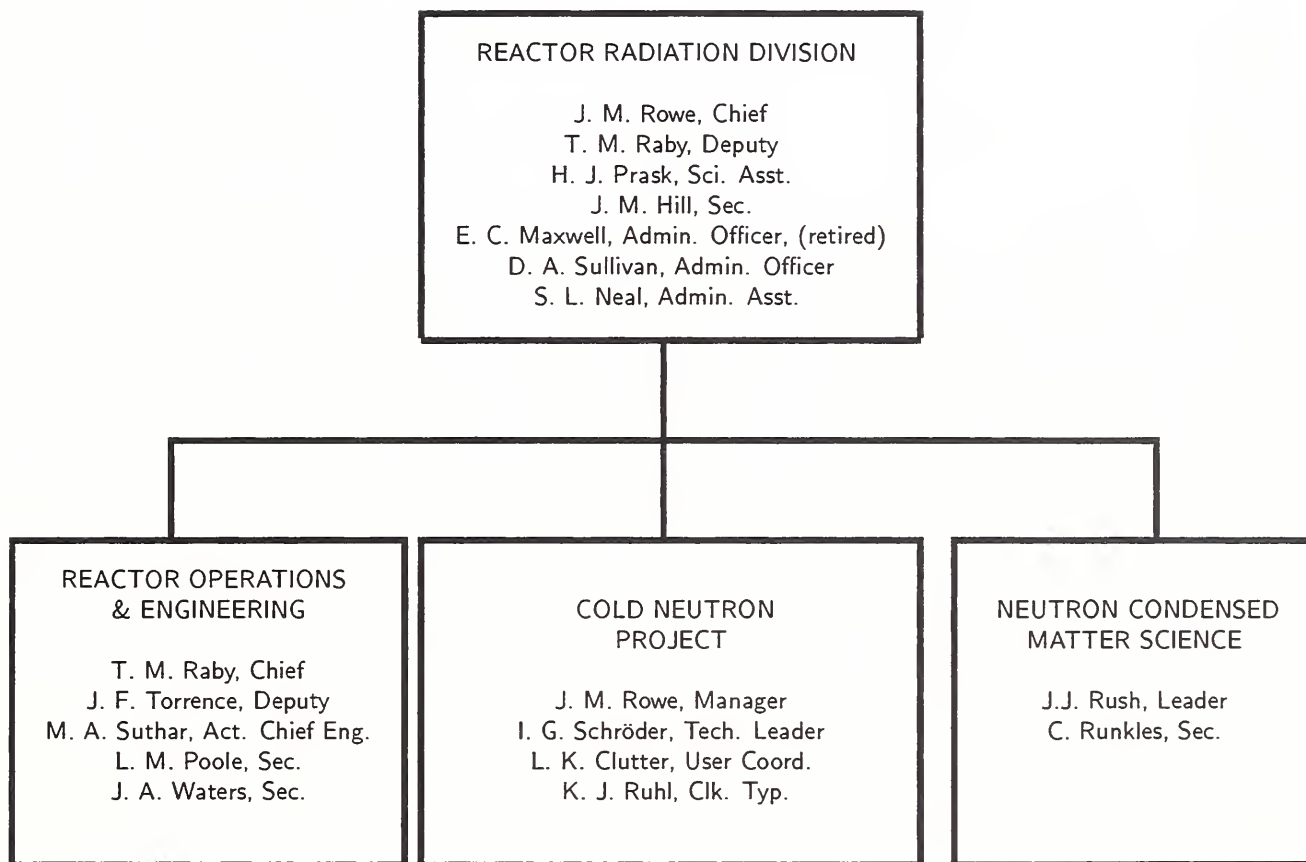
National Institute of Standards and Technology

Organizational Chart





Personnel Roster



The Division staff is organized formally into three groups, as shown in the chart above; however, staff are utilized where necessary, irrespective of group. Below the group level of organization, personnel are grouped into research teams according to their predominant interest. Once again, these groupings are not hard and fast; there are many overlapping interests. These teams, including long-term guest researchers, are shown in Table 1. A number of "non-resident" Ph.D. students and continuing collaborators from universities and industry are not

listed. It should be noted that scientific contributions to the Cold Neutron Project are included in the teams by scientific interest, even though in most cases, their predominant responsibility is for CNRF instrument building and/or operation. In fact, they have only 30% of their time given to the conduct of research, while 70% is dedicated to the facility. Likewise, many members of the Neutron Condensed Matter Science Group have sizable CNRF responsibilities, which may amount to as much as $\frac{1}{2}$ time when needed.

Table 1. NBSR and CNRF Resident Staff**ADMINISTRATIVE - DIVISION 856**

Rowe, J. M., Chief
 Maxwell, E. C., Admin. Off. (retired)
 Sullivan, D. A., Admin. Off.
 Neal, S. L., Admin. Asst.
 Hill, J. M., Secretary
 Prask, H. J., Sci. Asst.
 Barker, J. G., Matls. Sci.

REACTOR OPERATIONS & ENGINEERING

Raby, T. M., Chief
 Torrence, J. F., Deputy
 Poole, L. M., Secretary
 Waters, J. A., Secretary

Operations

Beasley, R.D.
 Bickford, N. A.
 Bobik, P. A.
 Cassells, M. G.
 Clark, F. C.
 Dilks, H. W.
 Flynn, D. J.
 Guarin, E. L.
 Lindstrom, L. T.
 McDonald, M. J.
 Mueller, W. W.
 Myers, T. J.
 Ring, J. H.
 Sprow, R. P.
 Stiber, R. F.
 Toth, A. L.
 Wilkison, D. P.
 Wright, K. D.

Engineering

Suthar, M. A., Act. Chief
 Poole, L. M., Secretary
 Beatty, J. A.
 Brady, D. E., Inst. Supv.
 Hall, K. D.
 Liposky, P. J.
 Shuman, L.A.
 Thompson, R. G.

Research Associates

Anderson, D. A. (FDA)
 Billos, J. (Montg. College)
 Cunningham, W. C. (FDA)
 Heine, C. J.
 Olin, J.(Smithsonian)

NEUTRON CONDENSED MATTER SCIENCE GROUP

Rush, J. J., Leader
 Runkles, C. L., Secretary
 Berk, N. F.
 Borchers, J. A.
 Brand, P.
 Copley, J.R.D.
 Drews, A. R.
 Dura, J. A.
 Erwin, R. W.
 Forstner, K. T.
 FitzGerald, S. A.
 Fulford, D. B.
 Gehring, P. M.
 Glinka, C. J.
 Hammouda, B.
 Ijiri, Y.
 Karen, V. L.
 Kline, S. R.
 Krueger, S. T.
 Lynn, J. W.
 Majkrzak, C. F.
 Maliszewskyj, N. C.
 Mighell, A. D.
 Neumann, D. A.
 Robeson, L. A.
 Santodonato, L. J.
 Santoro, A.
 Satija, S. K.
 Slaweck, T. M.
 Stalick, J. K.
 Toby, B. H.
 Udovic, T. J.

Guest Scientists

Altorfer, F. B.
 Chang, Y.-T.
 Cook, J.
 Doloc, L.

Huang, Q. Z.
 Kepa, H.
 Klosowski, P.
 Lee, S.-H.
 Lin, M. Y.
 Mrose, M.
 Papanek, P.
 Prince, E.
 Skanthakumar, S.
 Sung, L.
 Tobias, D. J.
 Trevino, S. F.
 Watanabe, T.
 Yildirim, T.
 Zaliznyak, I.

COLD NEUTRON PROJECT

Rowe, J. M., Leader
 Clutter, L. K., User Coord.
 Hill, J. M., Secretary
 Ruhl, K. J., Clerk Typist
 Baltic, G. M.
 Bostian, C. D.
 Clarkson, A.
 Clem, D. L.
 Clow, W. R.
 Dickerson, W. E.
 Fravel, D. H.
 Gallagher, P. D.
 Green, T. A.
 Greene, G. C.
 Heald, A. E.
 Kamitakahara, W. A.
 Knill, W. C.
 Kopetka, P. H.
 Kulp, D. L.
 LaRock, J. G.
 Layer, H. P.
 Pierce, D. J.
 Rinehart, M. J.
 Rosov, N. S.
 Schroder, I. G.
 Thai, T. T.
 Tobin, P. J.
 Williams, R. E.

Guest Engineers

Brocker, C. W.
 Christman, R.
 Moyer, J. J.
 Williams, R. H.
 Wrenn, C. W.

NEUTRON INTERACTIONS - 846

Gilliam, D. M., Leader
 Rhodes, S. E., Secretary
 Adams, J.
 Arif, M.
 Carlson, A. D.
 Dewey, M. S.
 Eisenhauer, C. M.
 Gentile, T. R.
 Jacobson, D. L.
 Jones, G. L.
 Nico, J. S.
 Thompson, A. K.
 Weitfeld, F. E.

HEALTH PHYSICS -DIVISION 354

Slaback, L. A., Leader
 Thomas, C. L., Secretary
 Brown, D. R.
 Campbell, C. D.
 Cassells, L. H.
 Clark, J. S.
 Deardorff, G. E.
 Fink, L. E.
 Mengers, T. F.
 Shubiak, J. J.

NUCLEAR METHODS GROUP- DIVISION 839

Greenberg, R. R., Leader
 Wilson, J. M., Secretary
 Becker, D. A.
 Benenson, R. E.
 Bishop, R. L.
 Blackman, M. J.
 Chen-Mayer, H. H.
 Demiralp, R.
 Fitzpatrick, K. A.
 Fokin, V. S.
 Iyengar, G. V.

Lamaze, G. P.
Langland, J. K.
Lindstrom, R. M.
Mackey, E. A.
Mildner, D.F.R.
Norman, B. R.
Paul, R. L.
Porter, B. J.
Sharov, V. A.
Welsh, J. F.
Zeisler, R. L.

Research and Engineering Staff

J. G. Barker	SANS instrumentation and research Microstructure of materials
N. F. Berk	Condensed matter theory Scattering theory for microstructure analysis Computer software for graphics and data analysis
N. A. Bickford	Reactor operations Reactor irradiations Reactor utilization
J. A. Borchers	Thin-film analysis Artificially modulated materials Magnetism
D. E. Brady	Electrical/electronic engineering Nuclear reactor instrumentation
P. Brand	Materials research engineer NDE diffraction methods
J. R. D. Copley	Time-of-flight spectrometer development Neutron instrumentation conceptual design Condensed matter physics
W. E. Dickerson	Neutron scattering instrumentation Microcomputer interfacing Nuclear and engineering physics
A. R. Drews	Perfect Crystal Diffractometer Development Condensed Matter Physics
J. A. Dura	Combined molecular beam epitaxy and neutron reflectivity/ diffraction instrumentation Surface, interfacial, and epitaxial physics Metastable phases in artificial materials
R. W. Erwin	Magnetic materials Phase transformations Cryogenics
S. A. FitzGerald	Neutron and optical spectroscopy Condensed matter physics Fullerenes and cements

K. T. Forstner	Instrumentation Monochromator development
D. B. Fulford	SANS equipment development and maintenance Mechanical engineering
P. D. Gallagher	Neutron reflectometry instrumentation Interfacial phenomena in polymer systems and complex fluids Phase transitions and critical phenomena
P. M. Gehring	Neutron backscattering instrumentation Magnetic and structural phase transitions in disordered systems Dynamics of high T_c materials
C. J. Glinka	SANS microstructure of metals and porous media CHRNS project director Cold neutron instrument development
G. C. Greene	System and user software for cold neutron instrumentation Spectrometer and data acquisition systems interfaces
B. Hammouda	SANS from polymers, liquid crystals, and colloids Dynamics of polymers in solution Scattering from sheared fluids
A. E. Heald	Design engineering Neutron instrumentation Shielding
Y. Ijiri	Magnetic materials Analysis of thin films & multilayers Triple-axis diffraction & reflectometry
W. A. Kamitakahara	The CNRF guest researcher program Dynamics of disordered solids Condensed matter physics
V. L. Karen	Crystallographic database development Theory of lattices and symmetry Neutron and x-ray diffraction
S. R. Kline	Microstructure of colloids and microemulsions Novel surfactant systems SANS instrumentation
P. Klosowski	Scientific data visualization Numerical computer modeling Data acquisition software and hardware

P. A. Kopetka	Mechanical engineering Cold source design Electro-mechanical systems
S. T. Krueger	SANS instrumentation Microstructure of materials Biological problems
J. G. LaRock	Mechanical engineering Neutron instrumentation design
H. P. Layer	Electronics and data processing Advanced instrumentation Fundamental physics
P. J. Liposky	Design engineering Nuclear systems and components
J. W. Lynn	Condensed matter physics Magnetic and superconducting materials Neutron scattering methods
C. F. Majkrzak	Condensed matter physics Polarized neutron scattering and instrumentation development Neutron reflectivity measurements
N. C. Maliszewskyj	Time-of-flight instrumentation Condensed matter physics Computer software development
A. D. Mighell	Crystallographic database development Single crystal and powder diffraction Theory of lattices
T. J. Myers	Reactor operations Nuclear engineering Safety analysis
D. A. Neumann	Molecular and layered materials Condensed matter physics Neutron and x-ray scattering instrumentation
D. J. Pierce	Mechanical engineering Neutron instrumentation design
H. J. Prask	Residual stress measurement methodology Neutron NDE applications Neutron NDE instrumentation

T. M. Raby	Reactor operations Nuclear engineering Reactor standards
G. Reilly	Design engineering Nuclear systems and components
N. Rosov	Spin echo techniques Phase transformations Magnetic materials
J. M. Rowe	Orientationally disordered solids Cold source development Cold neutron research and instrumentation
J. J. Rush	Catalysts and molecular materials Hydrogen in metals Inelastic scattering methods
L. Santodonato	Condensed matter physics Cryogenics
A. Santoro	Structure of electronic and structured ceramics Theory of crystal lattices Powder diffraction methods
S. K. Satija	Low-dimensional molecular systems Fractal aspects of microporous media Neutron reflectometry
I. G. Schröder	Cold neutron instrumentation development Nuclear and engineering physics Optical devices for neutron transport
T. M. Slaweki	SANS and reflectometry from polymers Complex fluid microstructure SANS instrumentation
J. K. Stalick	Neutron and x-ray diffraction Inorganic chemistry Crystal database development
M. A. Suthar	Design engineering Nuclear systems and components
B. H. Toby	Neutron and synchrotron diffraction Zeolite crystallography Structure determination methods

J. F. Torrence	Reactor supervision Reactor maintenance Nuclear engineering
T. J. Udovic	Neutron time-of-flight instrumentation Properties of catalysts and adsorbates Hydrogen in metals
R. E. Williams	Cold neutron source development Nuclear engineering

Technical Staff

Reactor Operations

Richard D. Beasley	William W. Mueller
Mark G. Cassells	John H. Ring
Forrest C. Clark	Ricky P. Sprow
Howard W. Dilks	Robert F. Stiber
Daniel J. Flynn	Attila L. Toth
Enrique L. Guarin	Daniel P. Wilkison
Larry T. Lindstrom	Kevin D. Wright
Michael J. McDonald	

Reactor Engineering

James A. Beatty
Keith Hall
Lynn A. Shuman

Cold Neutron Project

George M. Baltic	Wayne C. Knill
C. Douglas Bostian	Doris Kulp
Andrew Clarkson	Michael J. Rinehart
David Clem	Lewis P. Robeson
William R. Clow, Jr	Thuan T. Thai
Donald H. Fravel	Patrick J. Tobin
Thomas A. Green	Robert H. Williams (U. of MD)

Technical and Professional Committee Participation and Leadership

American Chemical Society

A. D. Mighell, Division of Chemical Information

American Crystallographic Association

A. D. Mighell, A.I.P. Crystal Data Committee

E. Prince, Publication Committee

American Physical Society

J. A. Borchers, Session Co-Chairman

J. R. D. Copley Co-Organizer, Focused Session on Fullerenes and Fullerene-Related Materials

J. W. Lynn, Symposium Chairman

J. W. Lynn, Organizer, Topical Group on Magnetism and ITS Applications

American Nuclear Society/American National Standards Institute

T. M. Raby, Standards Steering Committee

National Chairman, N-17

Working Groups, Chairman ANS-15.1, ANS-15.4, ANS-15.11

National Standards Service Award

J. F. Torrence, Working Groups, ANS-15.1

N-17 National Committee Member

Atomic Energy of Canada Limited (AECL)

J. J. Rush, Technical Review Committee for Condensed Matter Science

BESAC Panel on a New Spallation Neutron Source

D. A. Neumann, Member

Brookhaven National Laboratory

C. G. Glinka, HFBR Proposal Review Sub-Committee in Materials Science

C. F. Majkrzak, Chairman, HFBR Program Advisory Committee

J. M. Rowe, Co-Chairman, Physics Visiting Committee

J. J. Rush, Neutron Scattering Facility Scheduling Committee

Council on Materials Science and Engineering of the Southeastern Universities Research Association

J. W. Lynn

Department of Commerce

Silver Medal Award

J. K. Stalick

Department of Energy

T. M. Raby, Member, Basic Energy Sciences Sub-committee

J. J. Rush, Member, BESAC Panel on LANSCE Upgrade Proposal

Review Panel Members for DOE Enhanced Research Capabilities Program

C. J. Glinka

W. A. Kamitakahara

Gordon Research Conference on Disorder in Materials

D. A. Neumann, Vice-chairman

Graduate Texts in Contemporary Physics (Springer-Verlag)

J. W. Lynn, Series Editor

International Advisory Committee, Conference on Strongly Correlated Electron Systems (SCES'98)

J. W. Lynn, Member

International Advisory Committee for Fifth Conference on Applications of Nuclear Techniques

H. Prask, Organizer

International Advisory Council of the Canadian Journal of Physics

J. M. Rowe

International Conference on Neutron Scattering, Sendai, Japan

C. J. Majkrzak, International Advisory Committee

International Conference on Neutron Scattering (Toronto, Canada - 1997)

J. W. Lynn, Organizing Committee

Treasurer, ICNS'97

C. J. Majkrzak, Publications Co-chair

C. J. Glinka, Program Committee

D. A. Neumann, Program Committee

International Conferences on Hydrogen in Metals

J. J. Rush, Advisory Committee

International Symposium on Nondestructive Characterization of Materials (Prague, June 1995)

H. Prask, Session Chairman

International Union of Crystallography

E. Prince, Commission on International Tables

Commission on Neutron Scattering

Commission on Crystallographic Nomenclature

A. Mighell, Data Commission

B. H. Toby, Commission on the Crystallographic Information File

IUCr, Seattle, Aug. 1996

C. F. Majkrzak, Session Chairman

International Workshop on Itinerant Electron Magnetism (Moscow)

J. W. Lynn, Program Committee

Journal of Neutron Research

C. F. Majkrzak, Editorial Board

JCDDS-International Centre for Diffraction Data

A. D. Mighell, Crystal Data Management Board

Crystal Data Committee

Data Subcommittee

Electron Diffraction Subcommittee

Technical Committee

J. K. Stalick, Chairman, Neutron Powder Diffraction Subcommittee

B. H. Toby, Chairman, PDF Database Subcommittee

Los Alamos National Laboratory

J. M. Rowe, Chairman, Advisory Board on LANSCE

Magnetism and Magnetic Materials Conference

J. L. Borchers, Program Committee

J. W. Lynn, Symposium Chairman

Advisory Committee

Massachusetts Institute of Technology

J. M. Rowe, Visiting Committee, Nuclear Engineering Department

NAS/NRC

J. J. Rush, Solid State Sciences Committee

National Organization of Test, Research and Training Reactors

T. M. Raby, Past Chairman and Member of Executive Committee

National Science Foundation

W. A. Kamitakahara, Review Panel Member for Small Business Innovation Research

J. W. Lynn, Member of Evaluation Panel for International Program

National Science and Technology Council

J. J. Rush, Subcommittee on Research Infrastructure

National Standards Service Award, Nov. 1996

T. M. Raby

National Steering Committee for the NSNS (National Spallation Neutron Source)

J. W. Lynn, Member

Neutron Scattering Satellite Meeting to the XVII IUCr Congress

S. Krueger, Local Chairman

E. Prince, Program Committee

Neutron Scattering Society of America

C. F. Majkrzak, Secretary (prior to Aug. '96)

W. A. Kamitakahara (Aug. '96)

NIST/NSF Center for High Resolution Neutron Scattering (CHRNS)

C. J. Glinka, Project Director

NIST Strategic Planning Workshop - Magnetism: Measurement Challenges and Opportunities at Small Length Scales

J. A. Borchers

J. A. Dura

J. W. Lynn, Organizing Committee

NSF Materials Research Science and Engineering Center (through Univ. of MD)

J. W. Lynn, Member, Board of Directors

Rare Earth Research Conference

J. W. Lynn, Session Chairman, Member of the Board of Directors

Second Workshop on Software Development at Neutron Scattering Sources (Softness '95)

J. R. D. Copley, Organizer

P. Klosowski, Organizer

Steering Committee for the National Spallation Neutron Source

J. W. Lynn, Member

Summer School on Neutron Small Angle Scattering and Reflectometry from Submicron Structures (June 3-6, 1996)

C. J. Glinka, Co-organizer

B. Hammouda, Co-organizer

C. F. Majkrzak, Co-organizer

S. K. Satija, Co-organizer

Surfactancy and Self-Assembly Technical Advisory Committee for the University of Minnesota's Center for Interfacial Engineering

C. J. Glinka

University of Michigan Reactor Review

J. M. Rowe, Member

T. M. Raby, Member and Chairman

University of Missouri, External Safety Review Committee

T. M. Raby

Workshop on High Resolution Cold Neutron Spectroscopy

C. J. Glinka, Organizer

J. R. D. Copley, Organizer

D. A. Neumann, Organizer

Publications

- Allen, A. J., Berk, N. F., Krueger, S., Long, G. G., Kerch, H. M., Ilavsky, J., "New Developments in Multiple Small-Angle Neutron Scattering Studies of Advanced Ceramics," in *Neutron Scattering in Materials Science II*, edited by D. A. Neumann, T. P. Russell, B. J. Wuensch, Materials Research Society Symposium Proceedings, Vol. 376, (MRS, Pittsburgh, 1995), p. 347.
- Allen, A. J., Krueger, S., Long, G. G., Kerch, H. M., Hahn, H., Skandan, G., "Small-Angle Neutron Scattering Studies of Ceramic Nanophase Materials," *Nanostru. Matls.* **7**, 113 (1995).
- Allen, A. J., Krueger, S., Skandan, G., Long, G. G., Hahn, H., Kerch, H. M., Parker, J. C. and Ali, M. N., "Microstructural Evolution During the Sintering of Nanostructured Ceramic Oxides," *J. Amer. Ceram. Soc.* **79**, 1201 (1996).
- Allen, A. J., Long, G. G., Kerch, H. M., Krueger, S., Skandan, G., Hahn, H., Parker, J. C., "Sintering Studies of Nanophase Ceramic Oxides Using Small-angle Scattering", in *Ceramics: Charting the Future*, edited by P. Vincenzini, Proceedings 8th CIMTEC World Ceramics Congress and Forum on New Materials, Vol. C, (CIMTEC, Faenza, Italy, 1995).
- Allen, A. J., Long, G. G., Kerch, H. M., Krueger, S., Skandan, G., Hahn, H., Parker, J. C., "Sintering Studies of Nanophase Ceramic Oxides Using Small-angle Scattering", in *Ceramics International* **22**, 275 (1996).
- Altorfer, F. B., Cook, J. C., Copley, J. R. D., "The Multiple Disk Chopper Neutron Time-of-flight Spectrometer at NIST," in *Neutron Scattering in Materials Science II*, edited by D. A. Neumann, T. P. Russell, B. J. Wuensch, Materials Research Society Symposium Proceedings, Vol. 376 (MRS, Pittsburgh, 1995), p. 119.
- Ankner, J. F., Gallagher, P. D., Schreyer, A., Zhang, H., Majkrzak, C. F., Satija, S. K., Zabel, H., Matheny, A., Flynn, C. P., "Polarized Neutron Glancing-Angle Diffraction Study of Magnetic Structure at the Y/Gd[0001] Interface," in *Neutron Scattering in Materials Science II*, edited by D. A. Neumann, T. P. Russell, B. J. Wuensch, Materials Research Society Symposium Proceedings, Vol. 376 (MRS, Pittsburgh, 1995), p. 573.
- Avelar, J. M., Mason, P. C., Gaulin, B. D., Copley, J. R. D., "Small Angle Neutron Scattering at McMaster University," in *Neutron Scattering in Materials Science II*, Materials Research Society Symposium Proceedings, edited by D. A. Neumann, T. P. Russell, B. J. Wuensch, Vol. 376 (MRS, Pittsburgh, 1995), p. 83.
- Averitt, R. D., Pippenger, P. M., Papanyan, V. O., Dura, J. A., Nordlander, P., Halas, J. J., "Photoluminescence Spectra of Epitaxial Single Crystal C₆₀," *Chem. Phys. Lett.* **262**, 592 (1995).
- Balmer, M. L., Huang, Q., Wong-Ng, W., Roth, R. S., Santoro, A., "Neutron and X-Ray Diffraction Study of the Crystal Structure of CsTiSi₂O_{6.5}," *J. Sol. State Chem.*, in press.
- Balsara, N. P., Lin, C., Hammouda, B., "Early Stages of Nucleation/Growth in a Polymer Blend," *Phys. Rev. Lett.* **77**, 3847 (1996).
- Barker, J. G., Mayes, A. M., Briber, R. M., Orts, W. J., "Radius of Gyration Scaling in the Semidilute Regime," in *Neutron Scattering in Materials Science II*, Materials Research Society Symposium Proceedings, edited by D. A.

- Neumann, T. P. Russell, B. J. Wuensch, Vol. 376, (MRS, Pittsburgh, 1995), p. 291.
- Barker, J.G., Pedersen, J.S., "Instrumental Smearing Effects in Radially Symmetric Small-Angle Neutron Scattering by Numerical and Analytical Methods," *J. Appl. Crystallogr.* **28**, 105 (1995).
- Bendersky, L. A., Stalick, J. K., Portier, R., Waterstrat, R. M., "Crystallographic Structures and Phase Transformations in ZrPd," *J. Alloys Comp.*, **236**, 19 (1996).
- Benmouna, M., Briber, R., Hammouda, B., "Polymer Blends, Copolymers and Networks," *Mac. Chem. Phys.*, in press.
- Berk, N. F., Majkrzak, C. F., "Analyzing Specular Reflectivities with Parametric B-Splines," in *Neutron Scattering in Materials Science II*, Materials Research Society Symposium Proceedings, edited by D. A. Neumann, T. P. Russell, B. J. Wuensch, Vol. 376, (MRS, Pittsburgh, 1995), p. 187.
- Berk, N. F., Majkrzak, C. F., "Inverting Specular Neutron Reflectivity from Symmetric, Compactly Supported Potentials," *J. Phys. Soc. Jpn.*, in press.
- Birch, W. R., Knewton, M. A., Garoff, S., Suter, R. M., Satija, S., "The Structure of Precursing Thin Films of an Anionic Surfactant on a Silicon Oxide/Silicon Surface," *Langmuir*, in press.
- Bodeker, P. Sonntag, P., Schreyer, A., Borchers, J. A., Guthoff, F., Zabel, H., "Spin Density Waves in Epitaxial Fe/Cr Films," *J. Appl. Phys.*, in press.
- Borchers, J. A., Gehring, P. M., Erwin, R.W., Ankner, J. F., Majkrzak, C. F., Hylton, T. L., Coffey, K. R., Parker, M. A., Howard, J. K., "Antiferromagnetic Interlayer Correlations in Annealed Ni₈₀Fe₂₀/Ag Multilayers," *Phys. Rev. B* **54**, 9870 (1996).
- Borchers, J. A., Gehring, P. M., Erwin, R.W., Majkrzak, C. F., Ankner, J. F., Hylton, T. L., Coffey, K. R., Parker, M. A., "Nature of the Interlayer Coupling in Annealed Ni₈₀Fe/Ag Multilayers," *J. Appl. Phys.* **79**, 4762 (1996).
- Borchers, J. A., Gehring, P. M., Majkrzak, C. F., Ankner, J. F., Hylton, T. L., Coffey, K. R., Parker, M. A., Howard, J. K., "Magnetic Structure Determination for Annealed Ni₈₀Fe₂₀/Ag Multilayers Using Polarized-Neutron Reflectivity," in *Neutron Scattering in Materials Science II*, Materials Research Society Symposium Proceedings, edited by D. A. Neumann, T. P. Russell, B. J. Wuensch, Vol. 376 (MRS, Pittsburgh, 1995), p. 577.
- Borchers, J. A., Gehring, P. M., Majkrzak, C. F., Zeltser, A. M., Smith, N., Ankner, J. F., "Dependence of the Interlayer Coupling on Anneal Temperature in Ni-Fe/Cu Evaporated Multilayer," *J. Appl. Phys.*, in press.
- Brand, P. C., Prask, H. J., Blackburn, J., Fields, R. J., Proctor, T. M., "Possible Standard Specimens for Neutron Diffraction Residual Stress Measurements" in *Neutron Scattering in Materials Science II*, Materials Research Society Symposium Proceedings, edited by D. A. Neumann, T. P. Russell, B. J. Wuensch, Vol. 376, (MRS, Pittsburgh, 1995), p. 429.
- Brand, P. C., Prask, H. J., Hicho, G. E., "Residual Stress in Steel Railroad Track Measured by Means of Neutron Diffraction," *NISTIR* 5912 (1996)p. 27.
- Broholm, C., Aeppli, G., Lee, S.H.-H., Bao, W., DiTusa, J. F., "Strong Magnetic Fluctuations on Transition Metal Oxides," *J. Appl. Phys.* **79**, 5033 (1996).
- Broholm, C., "Proposal for a Doubly Focusing Cold Neutron Spectrometer at NIST," *Nucl. Instr. & Meth.*, in press.

- Butler, P. D., Magid, L. J., Hamilton, W. a., Hayter, J. B., Hammouda, B., Kreke, P. J., "Kinetics of Alignment and Decay in a Highly Entangled Transient Threadlike Micellar Network Studies by SANS," *J. Phys. Chem.* **100**, 442 (1996).
- Cappelletti, R. L., Cobb, M., Drabold, D. A., Kamitakahara, W. A., "A Neutron Scattering and Ab-Initio Molecular Dynamics Study of Vibrations in Glassy GeSe₂," *Phys. Rev. B* **52**, 9133 (1995).
- Cappelletti, R. L., Guerrero, H. M., Yildirim, T., Neumann, D. A., "Lattice Dynamics and Diffraction of K₁C₆₀ in the Orthorhombic Phase: A Neutron Scattering Study," *Phys. Rev. B*, in press.
- Cappelletti, R. L., Kamitakahara, W. A., Didarul, I., "Neutron Scattering Study of Vibrational Modes in Glassy Ge_{1-x}Sn_xSe₂," in *Neutron Scattering in Materials Science II*, Materials Research Society Symposium Proceedings, edited by D. A. Neumann, T. P. Russell, B. J. Wuensch, Vol. 376, (MRS, Pittsburgh, 1995), p. 667.
- Choi, C. S., Staker, M., "Neutron Diffraction Texture Study of Deformed Uranium Plates," **31**, 3397 (1996).
- Choi, C. S., Sharpe, W., Barker, J., "Neutron Diffraction Study of Austempered Ductile Iron," *Metallurgical and Mater. Trans. A* **27A**, 923 (1996).
- Clutter, L. K., editor, *NIST Reactor: Summary of Activities, October 1994 through September 1995*, NISTIR 5829 (1996).
- Clutter, L. K., editor, *Reactor Radiation Technical Activities - 1995*, NISTIR 5751 (1996).
- Copley, J. R. D., "Simulations of Neutron Focusing with Curved Mirrors," *Rev. Sci. Instrum.* **67**, 190 (1996).
- Copley, J. R. D., Neumann, D. A., Kamitakahara, W. A., "Energy Distributions of Neutrons Scattered from Solid C₆₀ by the Beryllium Detector Method," *Can. J. Phys.* **73**, 763 (1995).
- Dura, J. A., Majkrzak, C. F., "In-Situ Neutron Reflectivity of MBE Grown and Chemically Processed Surfaces and Interfaces," *Intl. Workshop on Semiconductor Characterization: Present Status and Future Needs*, edited by D. G. Seiler, W. M. Bullis, and A. C. Diebold, AIP Press 549 (1995).
- Dura, J. A., Pellagrino, J. G., Richter, C. A., "X-Ray Reflectivity Determination of Interface Roughness Correlated with Transport," *App. Phys. Lett.* **69**, 1134 (1996).
- Drews, A. R., Cline, J. P., Vanderah, T. A., Salazar, K., "High-Temperature X-Ray Diffraction Studies of a Precursor Mixture for Pb-substituted Bi-2223 Superconducting Wires," *J. Mat. Res.*, in review.
- Drews, A. R., Wong-Ng, W., Vanderah, T. A., Roth, R. S., "Preparation and Crystal Structure of Sr₆TiNb₄O₁₈," *J. Matl. Res.*, in press.
- Eastman, J. A., Fitzsimmons, M. R., Robinson, R. A., Lynn, J. W., "The Neel Temperatures of Nanocrystalline Chromium," *Appl. Phys. Lett.* **78**, 1364 (1995).
- El-Korchi, T., Gress, D. L., Livingston, R. A., Neumann, D. A., Rush, J. J., "Quantifying Freezable Water in Portland Cement Paste Using Quasielastic Neutron Scattering" in *Neutron Scattering in Materials Science II*, edited by D. A. Neumann, T. P. Russell, B. J. Wuensch, Materials Research Society Symposium Proceedings Vol. 376, (MRS, Pittsburgh, 1995), p. 493.
- Erwin, R. W., Borchers, J. A., Berry, S. D., Lind, D. M., Lochner, E., Shaw, K. A., "Field-Induced Decoupling of NiO-Magnetite Multilayers," in *Neutron Scattering in Materials*

- Science II*, edited by D. A. Neumann, T. P. Russell, B. J. Wuensch, Materials Research Society Symposium Proceedings No. Vol. 376, (MRS, Pittsburgh, 1995), p. 583.
- Feigin, L., Konovalov, O., Wiesler, D. G., Majkrzak, C. F., Berzina, T., Troitsky, V., "Neutron Reflectivity Study of Structural Changes in Barium Stearate Langmuir-Blodgett Films During Annealing," *Physica B* **221**, 185 (1996).
- Feng, Z., Zhu, Y. Y., Zacharia, T., Brand, P. C., Prask, H. J., Blackburn, J. M. "Modeling and Validation of Residual Stress Distribution in a HSLA-100 Disk," Proceedings of the 4th Intn'l. Conference on Recent Trends in Welding Research (Gatlinburg, TN, June 5-8, 1995, ASM, Int'l.), p. 105.
- Fitzsimmons, M. R., Eastman, J. A., Robinson, R. A., Lynn, J. W., "On the Possibility of a Two-State Magnetic Structure for Nanocrystalline Chromium," *J. Nanostructural Mater.* **7**, 179 (1996).
- Gallagher, P. D., Kellog, G. J., Walton, D. G., Mayes, A. M., Lambooy, P., Russell, T. P., Satija, S. K., "Observed Surface Energy Effects in Confined Diblock Copolymers," *Phys. Rev. Lett.*, in press.
- Gehring, P. M., Brocker, C. W., Neumann, D. A., "Design of a High-Flux Backscattering Spectrometer for Ultra-High Resolution Inelastic Neutron Measurements," in *Neutron Scattering in Materials Science II*, edited by D. A. Neumann, T. P. Russell, B. J. Wuensch, Materials Research Society Symposium Proceedings, Vol. 376, (MRS, Pittsburgh, 1995), p. 113.
- Gehring, P. M., Vigliante, A., McMorro, D. F., Gibbs, D., Majkrzak, C. F., Helgesen, G., Cowley, R. A., Ward, R. C. C., Wells, M. R., "Observation of Two Length Scales above T_N in a Holmium Thin Film," *Physica B*, **221**, 398 (1996).
- Glinka, C. J., Nicol, J. M., Stucky, G. D., Ramli, E., Margolese, D., Huo, Q., Higgins, J. B., Leonowicz, M. E., "Small Angle Neutron Scattering Study of the Structure and Formation of MCM-41 Mesoporous Molecular Sieves," *J. Porous Matls.* **3**, 93 (1996).
- Godart, C., Alleno, E., Tominez, E., Gupta, L. C., Nagarajan, R., Hossain, Z., Lynn, J., Sanchez, J. P., "Some Chemical and Physical Properties of Quaternary Borocarbides," *J. Sol. St. Chem.*, in press.
- Goodwin, T. J., Radousky, H. B., Shelton, R. N., Rosov, N., Lynn, J., "Pr and Cu Magnetism in $(\text{Pr}_{1.5}\text{Ce}_{0.5})\text{Sr}_2\text{Cu}_2\text{MO}_{10-\delta}\text{M}=\text{Nb, Ta}$ — Correlations with a Suppression of Superconductivity," *Phys. Rev. B* **55**, in press.
- Grimm, H., Gehring, P. M., Shapiro, S. M., Kahn, R., Rupprecht, A., "Low-frequency Excitations of Oriented DNA," *Phys. B Condensed Matter* **213 & 214**, 780 (1995).
- Gygax, F. N., Amato, A., Feyerherm, R., Schenck, A., Anderson, I. S., Udovic, T. J., Solt, G., "Dynamics of μ^+ in Sc and ScH_x ," *J. Alloys Compounds* **231**, 248 (1995).
- Gygax, F. N., Amato, A., Pinkpank, M., Schenck, A., Anderson, I. S., Solt, G., Udovic, T. J., "Electric Field Gradients Probed by μ^+ SR in Sc and $\alpha\text{-ScH}_x$ Solid Solutions," *J. Alloys Compounds*, in press.
- Hauer, B., Hempelmann, R., Richter, D., Udovic, T. J., Rush, J. J., Bennington, S. M., and Dianoux, A. J., "Ground State and Excited State Hydrogen Tunnelling in $\text{Nb}_{1-x}\text{Ti}_x\text{H}_y$," *Physica B, Condensed Matter* **226**, 210 (1996).
- Hauer, B., Richter, D., Hempelmann, R., Udovic, T. J., Rush, J. J., Kockelmann, W., Jansen, E., Schäfer, W., "Structure and Microdomain of Ordered Niobium Hydrides and Deuterides by Means of Neutron Scattering," *J. Alloys Compounds*, in press.

- Hayes, C., Lartigue, C., Kollmar, A., Copley, J. R. D., Alefeld, B., Mezei, F., Richter, D., Springer, T., "The Focusing Mirror at the ILL Spin-Echo Spectrometer IN15: Experimental Results," *J. Phys. Soc. Jpn.*, in press.
- Henderson, P., Beyer, D., Jonas, U., Karthaus, O., Ringsdorf, H., Heiney, P. A., Maliszewskyj, N. C., Ghosh, S. S., Mindyuk, O. Y., and Josefowicz, J. Y. "Complex Ordering in Thin Films of Di and Tri-Functionalized Hexaalkoxy-Triphenylene Derivatives," *J. Am. Chem. Soc.*, in press.
- Huang, Q., Lynn, J. W., Santoro, A., Chakoumakos, B. C., Cava, R. J., Krajewski, J. J., Peck Jr., W. F., "Neutron Powder Diffraction Study of the Nuclear and Magnetic Structures of $\text{HoNi}_{1.985}\text{Co}_{0.015}\text{B}_2\text{C}$ and HoNiBC ," *Physica C* **271**, 311 (1996).
- Huang, Q., Santoro, A., Lynn, J. W., Erwin, R. W., Borchers, J. A. Peng, J. L., Greene, R. L., "Structure and Magnetic Order in Undoped Lanthanum Manganite," *Phys. Rev. B*, in press.
- Isaacs, E. D., Zsack, P., Broholm, C., Burnes, C., Aeppli, G., Ramirez, A. P., Oglesby, C. S., Bucher, E., Erwin, R. W., "Suppression of the Antiferromagnetic Moment in the Superconducting Phase of UPt_3 ," *Phys. Rev. Lett.*, in press.
- Kamitakahara, W. A., "Dynamics of Li-Carbon and Carbon Solids," *J. Phys. Chem. Solids* **57**, 671 (1996).
- Kamitakahara, W. A., Gompf, F., Neumann, D. A., "Orientational Dynamics in White Phosphorus (P_4)," in *Neutron Scattering in Materials Science II*, edited by D. A. Neumann, T. P. Russell, B. J. Wuensch, Materials Research Society Symposium Proceedings, Vol. 376, (MRS, Pittsburgh, 1995), p. 775.
- Kamitakahara, W. A., Rush, J. J., Rowe, J. M., Prask, H., "Instrumentation for Neutron Scattering at the National Institute of Standards and Technology," in *Neutron Scattering in Materials Science II*, edited by D. A. Neumann, T. P. Russell, B. J. Wuensch, Materials Research Society Symposium Proceedings, Vol. 376, (MRS, Pittsburgh, 1995), p. 25.
- Karen, P., Kjekshus, A., Huang, Q., Karen, V., Mighell, A. D., Santoro, A., "Neutron Powder Diffraction Study of the Crystal Structure of the Oxycarbonate $\text{YBa}_2\text{Cu}_{2.85}[\text{CO}_3]_{0.15}\text{O}_{6.73}$," *Phys. C*, in press.
- Karen, V. L. and Mighell, A. D., "Crystallographic Databases," Editor of a Special Issue of the *NIST J. of Res.*, Vol. 101, May-June (1996).
- Karim, A., Douglas, J. F., Horkay, F., Fetters, L. J., Satija, S. K. "Comparative Swelling of Gels and Polymer Brush Layers," *Phys. B. Condens. Matt.* **221**, 331 (1996).
- Karim, A., Douglas, J. F., Satija, S. K., Wong, A. P. Y., Han, C. C., "Phase Separation in Chemically Reactive Polymer Blend Films," *Macromolecules*, in press.
- Karim, A., Satija, S. K., Gallagher, P., Douglas, J. F., Fetters, L. J., "Neutron Reflection Studies of Swelling of Chemically End-Grafted Polymer Chains," in *Neutron Scattering in Materials Science II*, edited by D. A. Neumann, T. P. Russell, B. J. Wuensch, Materials Research Society Symposium Proceedings, Vol. 376, (MRS, Pittsburgh, 1995), p. 229.
- Kellogg, G. J., Mayes, A. M., Stockton, W. M., Ferreira, M., Rubner, M. F., Satija, S. K., "Neutron Reflectivity Investigations of Self-Assembled Conjugated Polyion Multilayers," *Langmuir*, in press.
- Kellogg, G. J., Walton, D. G., Mayes, A. M., Lambooy, P., Russell, T. P., Gallagher, P. D., Satija, S. K., "Observed Surface Energy Effects in Confined Diblock Copolymers," *Phys. Rev. Lett.*, in press.

- Klosowski, P., Tischler, J., Könnecke, M., "HADES-HDF-Based Data Exchange Standard A Proposal for the Neutron Scattering Community," *Neutron News*, in press.
- Koenig, B. W., Krueger, S., Orts, W. J., Majkrzak, C. F., Berk, N. F., Silverton, J. V., Gawrisch, K., "Neutron Reflectivity and Atomic Force Microscopy Studies of a Lipid Bilayer in Water Adsorbed to the Surface of a Si Single Crystal," *Langmuir* **12**, 1343 (1996).
- Krueger, S., Allen, A. J., Skandan, G., Long, G. G., Hahn, H., Kerch, H. M., "Small-Angle Scattering Methods for Studying the Sintering of Nanophase Ceramic Compacts," in *Neutron Scattering in Materials Science II*, edited by D. A. Neumann, T. P. Russell, B. J. Wuensch, Materials Research Society Symposium Proceedings, Vol. 376, (MRS, Pittsburgh, 1995), p. 359.
- Krueger, S., Ankner, J. F., Satija, S. K., Majkrzak, C. F., Gurley, D. and Colombini, M., "Extending the Range of Neutron Reflectivity Measurements from Planar Lipid Bilayers: Applications to a Model Biological Membrane," *Langmuir* **11**, 3218 (1996).
- Krueger, S., Koenig, B. W., Orts, W. J., Berk, N. F., Majkrzak, C. F., Gawrisch, K. "Neutron Reflectivity Studies of Single Lipid Bilayers Supported on Planar Substrates," in *Neutron in Biology*, edited by B. Schoenborn & R. Knott (Plenum Publishing Corp., New York, 1995), in press.
- Krueger, J., Olah, G. A., Zhi, G., Stull, J., Trehella, J., "Structural Insights into Enzyme Activation by Calmodulin," *Nature Structural Biology*, in press.
- Lartigue, C., Copley, J. R. D., Mezei, F., Springer, T., "Focusing of Neutron Beams Using Curved Mirrors for Small Angle Scattering," *J. Neut. Res.*, in press.
- Lee, S. H., Broholm, C., Aeppli, G., Perring, T. G., Hessen, B., Taylor, A., "Isolated Spin Pairs and Two Dimensional Magnetism in $\text{SrCr}_{9p}\text{Ga}_{12-9p}\text{O}_{19}$," *Phys. Rev. Lett.* **76**, 4424 (1996).
- Lee, S. H., Broholm, C., Aeppli, G., Ramirez, A., Perring, T. G., Carlile, C. J., Adams, M., Jones, T. J. L., Hessen, B. "Spin-glass and Non-spin-glass Features of a Geometrically Frustrated Magnet," *Europhysics Letts.* **35**, 127 (1996).
- Li, W.-H., Lin, Y. F., Wu, S. Y., Hsieh, W. T., Lee, K. C., Lynn, J. W., Lai, C. C., Ku, H. C., "Cu Spin Reorientation in $\text{Tl}(\text{BaSr})\text{PrCu}_2\text{O}_7$," *J. Appl. Phys.* **79**, 6568 (1996).
- Lin, C. C., Jeon, H. S., Balsara, N. P., Hammouda, B., "Spindal Decomposition in Multi-component Polymer Blends," *J. Chem. Phys.* **103**, 1957 (1995).
- Lin, H., Steyerl, A., Satija, S. K., Karim, A., Russell, T. P., "Solvent Penetration into Ordered Thin Films of Diblock Copolymers," in press.
- Lin, Y.-C., Chuang, W. Y., Li, W.-H., Lee, K. C., Lynn, J. W., Yang, C. L., Ku, H. C., "Crystal Structure and Magnetic Ordering of Pr in $(\text{Pb}_{0.5}\text{Cu}_{0.5})_2(\text{Ba}_{0.5})_2\text{PrCu}_2\text{O}_8$," *J. Appl. Phys.*, in press.
- Liu, Y. H., Li, W.-H., Lee, K. C., Lynn, J. W., Ku, H. C., *J. Appl. Phys.*, in press.
- Livingston, R. A., Neumann, D. A., Allen, A., Rush, J. J., "Application of Neutron Scattering Methods to Cementitious Materials," in *Neutron Scattering in Materials Science II*, edited by D. A. Neumann, T. P. Russell, B. J. Wuensch, Materials Research Society Symposium Proceedings, Vol. 376, (MRS, Pittsburgh, 1995), p. 459.

- Livingston, R. A., Neumann, D. A., FitzGerald, S., Rush, J. J., "Quasi-elastic Neutron Scattering Study of the Hydration of Tricalcium Silicate," Conference Proceedings of the 5th International Conference on Neutrons in Research and Industry, in press.
- Long, G. G., Allen, A. J., Krueger, S., Thomas, J., Johnson, D. L., Hwang, C. J., "Small-Angle Scattering Studies of the Microstructure of Silicon Nitride During Processing," in *High Performance Materials in Engine Technology*, edited by P. Vincenzini, Proceedings 8th CIMTEC World Ceramics Congress and Forum on New Materials, Vol. I (CIMTEC, Faenza, Italy, 1995).
- Long, G. G., Kerch, H. M., Krueger, S., Allen, A. J., Burdette, H., "Small-Angle Neutron Scattering in a High-Temperature Furnace," in *Neutron Scattering in Materials Science II*, edited by D. A. Neumann, T. P. Russell, B. J. Wuensch, Materials Research Society Symposium Proceedings, Vol. 376, (MRS, Pittsburgh, 1995), p. 89.
- Lynn, J. W., "Rare Earth Magnetic Ordering in Exchange-Coupled Superconductors," *J. Alloys Compounds*, in press.
- Lynn, J. W., Dogan, F., "Spin Dynamics of Er^{3+} in $\text{ErBa}_2\text{Cu}_3\text{O}_7$," Skanthakumar, S., Lynn, J. W., Dogan, F., *J. Appl. Phys.*, in press.
- Lynn, J. W., Erwin, R., Borchers, J., Huang, Q., Santoro, A., Peng, J.-L., Li, Z. Y., "Unconventional Ferromagnetic Transition in $\text{La}_{1-x}\text{Ca}_x\text{MnO}_3$," *Phys. Rev. Lett.* **76**, 4046 (1996).
- Lynn, J. W., Erwin, R. W., Borchers, J. A., Huang, Q., Santoro, A., Peng, J.-L., Greene, R. L., "Magnetic, Structural and Spin Dynamical Properties of $\text{La}_{1-x}\text{Ca}_x\text{MnO}_3$," *J. Appl. Phys.*, in press.
- Lynn, J. W., Huang, Q., Santoro, A., Cava, R. J., Krajewski, J. J., Peck, Jr., W. F., "Nature of the Magnetic Order in Superconducting and Non-superconducting $\text{HoNi}_{2-x}\text{Co}_x\text{B}_2\text{C}$," *Phys. Rev. B* **53**, 802 (1996).
- Lynn, J. W., Huang, Q., Sinha, S. K., Hossain, Z., Gupta, L. C., Nagarajan, R., Godart, C., "Neutron Scattering Study of Antiferromagnetic Order in the Magnetic Superconductors $\text{RNi}_2\text{B}_2\text{C}$," *Physica B* **224**, 66 (1996).
- Lynn, J. W., Huang, Q., Sinha, S. K., Hossain, Z., Gupta, L. C., Nagaraja, R., Godart, C., "Neutron Scattering Studies of the Magnetic Order in $\text{RNi}_2\text{B}_2\text{C}$," *J. Appl. Phys.* **79**, 5857 (1996).
- Majkrzak, C. F., "Advances in Polarized Neutron Reflectometry," *Physica B* **213 & 214**, 904 (1995).
- Majkrzak, C. F., "Applications of Specular Neutron Reflectometry in Materials Science," Workshop Proceedings, Gordon & Breach Publications, in press.
- Majkrzak, C. F., "Chapter XIII: Polarized Neutrons," in *Handbook of Neutron Scattering*, edited by W. Glaser (Springer-Verlag), in press.
- Majkrzak, C. F., "Fundamentals of Specular Neutron Reflectometry," in *Neutron Scattering in Materials Science II*, edited by D. A. Neumann, T. P. Russell, B. J. Wuensch, Materials Research Society Symposium Proceedings, Vol. 376, (MRS, Pittsburgh, 1995), p. 143.
- Majkrzak, C. F., "Neutron Scattering Studies of Magnetic Thin Films and Multilayers," *Physica B* **221**, 342 (1996).
- Majkrzak, C. F., Berk, N. F., "Exact Determination of the Neutron Reflection Amplitude or Phase," *Physica B* **221**, 520 (1996).
- Maliszewskyj, N. C., Udovic, T. J., Nicol, J. M., "Neutron Vibrational Spectroscopy of

- the H_5O_2^+ Ion and Its Deuterated Analog in Phosphotungstic Acid Hexahydrate," Proc. of the Material Research Society Symposium, Microporous and Macroporous Materials edited by R. F. Lobo et al. Mat. Res. Soc. Sym. Proc., Vol. 431, 203 (1996).
- McMichael, R. D., Watanabe, T., Dura, J., Borchers, J., Chen, P. J., Brown, H. J., Egelhoff, W. F., "Origins of Coercivity Increase in Annealed Symmetric Spin Valves," IEEE Transactions on Magnetics **32**, 4636 (1996).
- Michel, K. H., Copley, J. R. D., "Orientational Fluctuations, Diffuse Scattering, and Orientational Order in Solid C_{60} ," Proceedings of International Winterschool on Electronic Processes, Austria, March 1996, in press.
- Mighell, A. D., Karen, V. L., "NIST Crystallographic Databases for Research and Analysis," NIST J. of Res. **101**, 273, May-June (1996).
- Moudden, A. H., Gehring, P. M., Shirane, G., Matsuda, M., Vasiliu-Doloc, L., Henion, B., Endoh, Y., Tanaka, I., Kojima, H., "High-energy Phonon Dispersion in $\text{La}_{1.85}\text{Sr}_{0.15}\text{CuO}_4$," Phys. B Condensed Matter **213 & 214**, 72 (1995).
- Neumann, D. A., "Quasielastic and Inelastic Neutron Scattering Studies of Layered Silicates," in *Access in Nanoporous Materials*, edited by T. J. Pinnavaia and M. Thorpe (Plenum, New York, 1995), p. 381.
- Nunez, V., Giebultowicz, T. M., Faschinger, W., Bauer, G., Sitter, H., Furdyna, J. K., "Helical Spin Ordering and Interlayer Correlations in Strained-Layer MnTe/CdTe Superlattices," Proceedings of International Congress on Physics of Semiconductors (Vancouver, 1994), in press.
- Nunez, V., Giebultowicz, T. M., Faschinger, W., Bauer, G., Sitter, H., Furdyna, J. K., "Investigation of Magnetic Structure of MnTe/CdTe Multilayers by Neutron Diffraction," in *Neutron Scattering in Materials Science II*, edited by D. A. Neumann, T. P. Russell, B. J. Wuen-sch, Materials Research Society Symposium Proceedings, Vol. 376, (MRS, Pittsburgh, 1995), p. 589.
- Orts, W. J., Revol, J.-F., Godbout, L., Marchessault, R. H., "SANS Study of Chirality and Order in Liquid Crystalline Cellulose Suspensions," in *Neutron Scattering Materials Science II*, edited by D. A. Neumann, T. P. Russell, B. J. Wuen-sch, Materials Research Society Symposium Proceedings, Vol. 376, (MRS, Pittsburgh, 1995), p. 317.
- Orts, W. J., VanderHart, D. L., Bluhm, T. L., Marchessault, R. H., "Cocrystallization in Random Copolymers of Poly[β -Hydroxybutyrate-Co- β -Hydroxyvalerate] and Its Effect on Crystalline Morphology," Can. J. Chem., in press.
- Petit, P., Robert, J., Yildirim, T. and Fischer, J. E., "ESR Evidence for Phonon-mediated Resistivity in Alkali Fullerenes," Phys. Rev. B., **54**, R3764 (1996).
- Ping Zhou, Papanek, P., Lee, R., Fischer, J. E., Kamitakahara, W. A., "Local Structure and Vibrational Spectroscopy of Disordered Carbons for Li Batteries: Neutron Scattering Studies," J. Electrochemical Society, in press.
- Prask, H. J., "Materials Characterization with Cold Neutrons," in *Nondestructive Characterization of Materials VII*, edited by A. L. Bartos, R. E. Green, Jr. and C. O. Ruud, Matls. Sci. Forum **210**, 711 (1996).
- Prask, H. J., Brand, P. C., "Neutron Diffraction Residual Stress Measurement at NIST," in *Proceedings of Nondestructive Characterization of Materials VII*, edited by A. L. Bartos, R. E. Green, Jr. and C. O. Ruud, Matls. Sci. Forum **210**, 155 (1996).

- Prask, H. J., Brand, P. C., "Residual Stress Determination by Means of Neutron Diffraction," Proceedings of the 5th International Conference on Applications of Nuclear Techniques, in press.
- Prince, E., "Structure and Proton Conduction in Pyrochlore-Type Antimonic Acid: A Neutron Diffraction Study," Faraday Society [special issue on Solid State Chem.], in press.
- Prince, E., Wilkinson, C., McIntyre, G. J. "Comparison of the $\sigma[I]/I$ and Least Squares Methods for Integration of Bragg Reflections," J. Appl. Crystallogr., in press.
- Robertson, J. L., Reinhard, L., Neumann, D. A., Moss, S. C., "Static and Dynamic Displacement in α -Phase FeCr," in *Neutron Scattering in Materials Science II*, edited by D. A. Neumann, T. P. Russell, B. J. Wuensch, Materials Research Society Symposium Proceedings, Vol. 376, (MRS, Pittsburgh, 1995), p. 689.
- Rosov, N., Lynn, J. W., Fish, G. W., "Neutron Scattering Study of the Magnetism in a Nanocrystalline/Amorphous Material," in *Neutron Scattering in Materials Science II*, edited by D. A. Neumann, T. P. Russell, B. J. Wuensch, Materials Research Society Symposium Proceedings, Vol. 376, (MRS, Pittsburgh, 1995), p. 595.
- Rowe, J. M., Williams, R. E., Prask, H. J., "Utilization of the NIST Research Reactor," Proceedings of Asian Symposium on Research Reactors, in press.
- Rush, J. J., Udovic, T. J., Berk, N. F., Richter, D., Magerl, A., "Excited-State Vibrational Tunnel Splitting of Hydrogen Trapped by Nitrogen in Niobium," Phys. Rev. B., Rapid Comm., in press.
- Sanders, P. G., Weertman, J. R., Barker, J. G., Eldrup, M., Siegel, R. W., "Structure of Nanocrystalline Pd and Cu Made by Inert Gas Condensation and Compaction," J. Matls. Sci. **11**, 3110 (1996).
- Santodonato, L. J., Neumann, D. A., Erwin, R. W., "Template Mediated Growth of Rare Earth Carbides," J. Am. Chem. Soc., in press.
- Satija, S. K., "Neutron Reflectivity Investigations of Self-Assembled Conjugated Polyion Multilayers," Langmuir, in press.
- Satija, S. K., Zhang, H., Gallagher, P. D., Lindstrom, R. M., Paul, R. L., Russell, T. P., Lambooy, P., Kramer, E. J., "Resonance Enhanced Neutron Standing Waves in Thin Films," in *Neutron Scattering in Materials Science II*, edited by D. A. Neumann, T. P. Russell, B. J. Wuensch, Materials Research Society Symposium Proceedings, Vol. 376, (MRS, Pittsburgh, 1995), p. 259.
- Schreyer, A., Ankner, J. F., Zeidler, Th., Schafer, M., Zabel, H., Majkrzak, C. F., "Direct Observation of Non-Collinear Spin Structures in Fe/Cr[100] Superlattices," Europhys. Letts. **32**, 595 (1995).
- Schreyer, A., Ankner, J. F., Zeidler, Th., Zabel, H., Schafer, M., Wolf, J. A., Grunberg, P., Majkrzak, C. F., "Noncollinear and Collinear Magnetic Structures in Exchange Coupled Fe/Cr(001) Superlattices," Phys. Rev. B **52**, 16066 (1995).
- Schreyer, A., Metoki, N., Zeidler, Th., Bödeker, P., Abromeit, A., Morawe, Ch., Romahn, U., Sonntag, P., Bröhl, K., Zabel, H., Ankner, J.F., Majkrzak, C.F., "Exchange Coupling in Single Crystalline Co/Cu(III) Superlattices," J. Mag. Magn. Matls., in press.
- Sinha, S. K., Feng, Y. P., Melendres, C. A., Lee, D. D., Russell, T. P., Satija, S. K., Sirota, E. B., Sanyal, M. K., "Off-Specular X-Ray Scattering Studies of the Morphology of Thin Films," Physica B, in press.

- Slade, R. C. T., Hall, G. P., Ramanan, A., Nicol, J. M., "A Neutron Scattering Study of Protonic Species in Ammonium Decamolybdate $(\text{NH}_4)\text{Mo}_5\text{O}_{15}(\text{OH})\cdot 2\text{H}_2\text{O}$," J. Mater. Chem., in press.
- Skanthakumar, S., Lynn, J. W., Dogan, F., "Spin Dynamics of Er^{3+} in $\text{ErBa}_2\text{Cu}_3\text{O}_{7-\delta}$," J. Appl. Phys., in press.
- Skanthakumar, S., Lynn, J. W., Rosov, N., Cao, G., Crow, J. E., "Observation of Pr Magnetic Order in $\text{PrBa}_2\text{Cu}_3\text{O}_7$," Phys. Rev. B., in press.
- Slade, R. C. T., Hall, G. P., Ramanan, A., Prince, E., "Structure and Proton Conduction in Pyrochlore-type Antimonic Acid: A Neutron Diffraction Study," Faraday Society Solid State Chemistry Special, in press.
- Springholz, G., Chen, J. J., Frnk, N., Ueta, Y., Marschner, G., Pichler, C., Dresselhaus, M. S., Dresselhaus, G., Giebultowicz, T. M., Nunez, V., Salamanca-Riba, L., "Monolayer Short Period Superlattices of Narrow Gap PbTe and Antiferro-magnetic Wide Band Gap Eute," Proceedings of the International Conference on Narrow Gap Semiconductor (Santa Fe, 1994), in press.
- Stalick, J. K., Prince, E., Santoro, A., Schroder, I. G., Rush, J. J., "Materials Science Applications of the New National Institute of Standards and Technology Neutron Powder Diffraction," in *Neutron Scattering in Materials Science II*, edited by D. A. Neumann, T. P. Russell, B. J. Wuensch, Materials Research Society Symposium Proceedings, Vol. 376, (MRS, Pittsburgh, 1995), p. 101.
- Stalick, J. K., Santoro, A., "Crystal Chemistry of the Substitution Compounds of $\text{YBa}_2\text{Cu}_3\text{O}_7$," in *Current Status and Future Directions in Condensed Matter Physics*, edited by S.K. Mailk (Plenum, New York), in press.
- Stoffel, N. C., Dai, C-A., Kramer, E. J., Russell, T. P., Deline, V., Volksen, W., Wen-li Wu, Satija, S. K., "High Resolution Profiling of the Polyimide-Polyimide Interface," Macromolecules, in press.
- Subramanian, M. A., Toby, B. H., Ramirez, A. P., Marshall, W. J., Sleight, A. W., Kwei, G. H., "Colossal Magnetoresistance without $\text{Mn}^{3+}/\text{Mn}^{4+}$ Double Exchange in the Stoichiometric Pyrochlore $\text{Tl}_2\text{Mn}_2\text{O}_7$," Science, in press.
- Suzuki, M., Suzuki, I. S., Burr, C. R., Wiesler, D. G., Rosov, N., Koga, K., "Structural and Magnetic Properties of CuCl_2 Graphite Intercalation Compounds," Phys. Rev. B **50**, 9188 (1994).
- Suzuki, M., Suzuki, I. S., Wiesler, D. G., Rosov, N., "In-plane Spin Structures on MuCl_2 Graphite Intercalation Compounds," J. Phys. Chem. Sol. **57**, 729 (1996).
- Tarek, M., Tobias, D. J., Klein, M. L., "Molecular Dynamics Investigation of the Surface/Bulk Equilibrium in an Ethanol-Water Solution," J. Chem. Soc., Faraday Transactions **92**, 559 (1996).
- Tobias, D. J., Mar, W., Blasie, V. K., Klein, M. L., "Molecular Dynamics Simulations of a Protein on Hydrophobic and Hydrophilic Surfaces," Biophys. J. **70**, 2993 (1996).
- Udovic, T. J., Huang, Q., Rush, J. J., "Characterization of the Structure of $\text{LaD}_{2.50}$ by Neutron Powder Diffraction," J. Solid State Chem. **122**, 151 (1996).
- Udovic, T. J., Huang, Q., Rush, J. J., "Characterization of the Structure of YD_3 by Neutron Powder Diffraction," J. Phys. Chem. Solids **57**, 423 (1996).
- Udovic, T. J., Nicol, J. M., Cavanagh, R. R., Rush, J. J., Crawford, M. K., Grey, C. P.,

- Corbin, D. R., "Neutron and Raman Spectroscopies of 134 and 134a Hydrofluorocarbons encaged in Na-X Zeolite," in *Neutron Scattering in Materials Science II*, edited by D. A. Neumann, T. P. Russell, B. J. Wuensch, Materials Research Society Symposium Proceedings, Vol. 376, (MRS, Pittsburgh, 1995), p. 751.
- Udovic, T. J., Rush, J. J., Flanagan, T. B., Noh, H., Andersson, Y., "Vibrational Dynamics of Hydrogen and Deuterium in Crystalline Pd_9Si_2 ," *J. Alloys Compounds*, in press.
- Udovic, T. J., Rush, J. J., Huang, Q., Anderson, I. S., "Neutron Scattering Studies of the Structure and Dynamics of Rare-Earth Hydrides and Deuterides," *J. Alloys and Compounds*, in press.
- Vanderah, T. A., Huang, Q., Wong-Ng, W., Chakoumakos, B. C., Goldfarb, R. B., Geyer, R. G., Baker-Jarvis, J., Roth, R. S., Santoro, A., "Preparation, Crystal Structure, Dielectric Properties, and Magnetic Behavior of $\text{Ba}_2\text{Fe}_2\text{Ti}_4\text{O}_{13}$," *J. Sol. State Chem.* **120**, 121 (1995).
- Vasiliu-Doloc, L., Lynn, J. W., Moud den, A. H., de Leon-Guevara, A. M., Revcolevschi, A., J. "Neutron Scattering Investigation of the Structure and Spin dynamics of $\text{La}_{0.85}\text{Ca}_{0.15}\text{MnO}_3$," *Appl. Phys.*, in press.
- Wiesler, D. G., Majkrzak, C. F., "In-Situ Neutron Reflectivity Study of Titanium Anodization," *Electrochemical Soc.*, in press.
- Wiesler, D. G., Majkrzak, C. F., "Growth and Dissolution of Protective Oxide Films on Titanium: An In-Situ Neutron Reflectivity Study," in press.
- Wiesler, D. G., Suzuki, M., Susuki, S., Rosov, N., "Determination of Anomalous Superexchange in MnCl_2 and its Graphite Intercalation Compound," *Phys. Rev. Lett.* **75**, 942 (1995).
- Williams, R. E., "An MCNP Model of the NBSR Core," *Trans. Am. Nucl. Soc.* **73**, 397 (1995).
- Williams, R. E., Rowe, J. M. and Blau, M., "Benchmark of the Nuclear Heat Deposition in the NIST Liquid Hydrogen Cold Source," *Proceedings of the 9th International Symposium on Reactor Dosimetry*, Prague, Sept, 1996, in press.
- Williams, R. E., Rowe, J. M., Kopetka, P., "Safety Analysis of the Liquid Hydrogen Cold Source at the NIST Research Reactor," *Trans. Am., Nucl Soc.* **74**, 238 (1996).
- Wilson, A. J. C., Karen, V. L., Mighell, A., "The Space-group Distribution of Molecular Organic Structures," *Intl. Tables for Crystallography*, Vol. C., in press.
- Wu, S. Y., Li, W-H., Lee, K. C., Lynn, J. W., Yang, H. D., "Two- and Three-Dimensional Magnetic Correlations of Tb in $\text{Pb}_2\text{Sr}_2\text{TbCu}_3\text{O}_8$," *Phys. Rev. B* **54**, 10019 (1996).
- Wu, W. L., Satija, S. K., "High Resolution Profiling of the Polyimide-Polyimide Interface," *Macromolecules*, in press.
- Yildirim, T., et al., "Fulleride Superconductors: Dependence of T_c on Average Molecular Valence in $\text{Na}_2\text{Cs}_x\text{C}_{60}$," *Synthetic Metals.* **77**, 195 (1996).
- Yildirim, T., "Parameters Controlling Superconductivity in Doped-Fullerenes," in *Recent Advances in the Physics and Chemistry of Fullerenes and Related Materials*, edited by K. M. Kadish and R. S. Ruoff, the Electrochemical Society Inc., (1996), p. 1155.
- Yildirim, T., Barbedette, L., Fischer, J. E., Lin, C. L., Goze, C., Rachdi, F., Robert, J., Petit, P., Palstra, T. T. M., "Synthesis and Properties of Mixed Alkali-Alkaline Earth Fullerides," *Phys. Rev. B.* **54**, 11981 (1996).

- Yildirim, T., Barbedette, L., Fischer, J. E., Lin, C. L., Robert, J., Petit, P., Palstra, T. T. M., "T_c vs Carrier Concentration in Cubic Fulleride Superconductors," *Phys. Rev. Lett.* **77**, 167 (1996).
- Yildirim, T., Harris, A. B., Shender, E. F., "Ground State Selection in FCC Antiferromagnets," *Phys. Rev. B*, in press.
- Yildirim, T., Harris, A. B., Shender, E. F., "Three-dimensional Ordering in BCT Antiferromagnets Due to Quantum Disorder," *Phys. Rev. B* **53**, 6455 (1996).
- Yildirim, T., Sachidanandam, R., Harris, A. B., Aharony, A., and Entin Wohlman, O., "Single Ion Anisotropy, Crystal Field Effects, and Spin Waves in R₂CuO₄," *Phys. Rev. B*, in press.
- Zhang, H., "Diffraction of Neutron Standing Waves in Thin Films," *Physica B* **221**, 455 (1996).
- Zhang, H., Satija, S. K., Gallagher, P. D., Dura, J. A., Ritley, K., Flynn, C. P., Ankner, J. F., "Diffraction of Neutron Standing Waves in Thin Films with Resonance Enhancement," *Physica B* **221**, 450 (1996).
- Zhang, H., Satija, S. K., Gallagher, P. D., Dura, J. A., Ritley, K., Flynn, C. P., Ankner, J. F., "Grazing-incidence Neutron Diffraction by Thin Films with Resonance Enhancement," *Phys. Rev. B* **52**, 17501 (1995).
- Abdurashitov, J. N., Nico, J. S., et al., "Results from SAGE II," *Nucl. Phys. B (Proc. Suppl.)* **38**, 54 (1995).
- Abdurashitov, J. N., Nico, J. S., et al., "The Russian-American Gallium Experiment," in *Recontre de Moriond Conference on Electroweak Interactions and Unified Theory*, Les Arcs, France, 1995.
- Abdurashitov, J. N., Nico, J. S., et al., "The Russian-American Gallium Experiment (SAGE) Cr-neutrino Source Measurement," *Phys. Rev. Lett.*, in press.
- Abdurashitov, J. N., Nico, J. S., et al., "SAGE Chromium Experiment," in *International Conference on Neutrino Telescopes*, Venice, Italy, 1996.
- Abdurashitov, J. N., Nico, J. S., et al., "SAGE II Results," in *International Conference on Neutrino Telescopes*, Venice, Italy, 1996.
- Adams, J. M., Catchen, G. L., Fu, J., and Miller, D. L., "Hyperfine Interactions of ¹¹¹In/¹¹¹Cd Probe Atoms on GaAs(111)B Reconstructed Surfaces Measured Using Perturbed Angular Correlation Spectroscopy," *Surf. Sci.* **337**, 118 (1995).
- Adams, J. M., McGarry, E. D., Hawari, A. I., and Venkataraman, R., "The Materials Dosimetry Reference Facility Round Robin Tests of ²³⁷Np and ²³⁸U Fissionable Dosimeters," *Amer. Soc. for Testing and Matls.*, in press.

Independent Publications

- Abdurashitov, J. N., Nico, J. S., et al., "Preliminary Results from the Russian-American Gallium Experiment Cr-neutrino Source Measurement," *Nucl. Phys. B, (Proc. Suppl.)* **48**, 370 (1996).
- Abdurashitov, J. N., Nico, J. S., et al., "Results from SAGE," *Nucl. Phys. B (Proc. Suppl.)* **48**, 370 (1996).
- Almdal, K., Mortensen, K., Koppi, K. A., Tirrell, M. Bates, F. S., "Isotropic and Anisotropic Composition Fluctuations Close to the Order-to Disorder Transition in an Asymmetric Diblock Copolymer Melt Subjected to Reciprocating Shear Fields," *J. Phys. II* **6**, 617 (1996).
- Almdal, K., Mortensen, K., Ryan, A. J., Bates, F. S., "Order, Disorder and Composition

- Fluctuation Effects in Low Molar Mass Hydrocarbon Poly (dimethylsiloxane) Diblock Copolymers," *Macromol.* **29**, 5940 (1996).
- Anderson, D. L., "Ceramic Glaze Analysis by Simultaneous In-Beam PGAA and XRFs," *J. Radioanal. Nucl. Chem.* **192**, 281 (1995).
- Anderson, D. L., Cunningham, W. C., "In-House Reference Material Characterization Using Nuclear Methods," *Trans. Am. Nucl. Soc.* **71**, 21, (1994).
- Anderson, D. L., Cunningham, W. C., "Maple Syrup Analysis for ^{137}Cs , K and B Using a Low-Background Counting System and PGAA," *J. Radioanal. Nucl. Chem.* **194**, 351 (1995).
- Anderson, D. L., Cunningham, W. C., "Nondestructive Determination of Lead, Cadmium, Tin, Antimony, and Barium in Ceramic Glazes by Radioisotope X-ray Fluorescence Spectrometry," *J. AOAC Int.* **79**, 1141 (1996).
- Anderson, D. L., Cunningham, W. C., Lindstrom, T. R., "Concentrations and Intakes of H, B, S, K, Na, Cl, and NaCl in Foods," *J. Food Comp. and Anal.* **7**, 59 (1994).
- Anderson, D. L., Cunningham, W. C., Lindstrom, T. R., Olmez, I., "Identification of Lead and Other Elements in Ceramic Glazes and Housewares Using ^{109}Cd -Induced X-ray Emission," *J. AOAC Int.* **78**, 407 (1995).
- Anderson, D. L., Downing, R. G., and Iyengar, G. V., "Trace Elements in Food Reference Materials: Compositional and Analytical Perspectives," *Fres. J. Anal. Chem.* **352**, 107 (1995).
- Anderson, K. H., Bossy, J., Cook, J. C., and Randl, O. G., Ragazzoni, J-L., "High Resolution Measurements of Rotons in H^4He ," *Phys. Rev. Lett.* **77**, 4043 (1996).
- Andoine Zaror, O., Soria Juarez, R., Zeiller, E., and Zeisler, R. L., "Separation Method to Overcome the Interference of Calcium on the Uranium Determination by ICP-ES," *Fres. J. Anal. Chem.*, in press.
- Baker, J. E., Poster, D. L., Church, T. M., Schudlark, J. R., Ondov, J. M., Dickhut, R. M., Cutter, G., "Loadings of Atmospheric Trace Elements and Organic Contaminants to the Chesapeake Bay," in *Atmospheric Deposition of Contaminants to the Great Lakes and Coastal Waters*, (SETAC Special Publications Series, edited by J. E. Baker), in press.
- Baker, S. M., Wu, L., Smith, G. S., Hubbard, K. M., Nastasi, M., Downing, R. G., and Lamaze, G. P., "Non-Standard Fickian Self-diffusion of Isotopically Pure Boron Observed by Neutron Reflectometry and Depth Profiling," in press.
- Balsara, N. P., Fetters, L. J. Grassely, W. W. Hadjichristidis, N., Krishnamoorti, R., Lohse, D. J., Schulz, D. N. Sissano, J. A., "Melt Chain Dimensions of Poly(Ethylene-1-Butene) Copolymers via Small Angle Neutron Scattering," *Macromolecules*, in press.
- Bao, W., Broholm, C., Aeppli, G., Dai, P., Honig, J. M., Metcalf, P., "Dramatic Switching of Magnetic Exchange in a Classic Transition Metal Oxide: Evidence for Orbital Ordering," *Phys. Rev. Lett.*, in press.
- Bao, W., Broholm, C., Aeppli, G., Honig, J. M., Metcalf, P., "Spin Dynamics in Metallic and Insulating V_2O_3 ," *Phys. Rev. Lett.*, in press.
- Bao, W., Broholm, C., Honig, J. M., Metcalf, P., Trevino, S. F., "Itinerant Antiferromagnetism in the Mott Compound $\text{V}_{1.973}\text{O}_3$," *Phys. Rev. B Rapid Communications*, in press.
- Bates, F. S., Maurer, W., Lodge, T. P., Schultz, M. F., Matsen, M. W., Almdal, K., Mortensen, K., "Isotropic Lifshitz Behavior in Block Copolymer-Homopolymer Blends," *Phys. Rev. Lett.* **75**, 4429 (1995).

- Bates, F. S., Schulz, M. F., Khandpur, A. K., Förster, S., Rosendale, J. H., Almdal, K., Mortensen, K., "Fluctuations, Conformational Asymmetry and Block Copolymer Phase Behavior," *Faraday Discuss. Chem. Soc.*, in press.
- Becker, D. A., "Short Half-Life Activation Analysis in Biomedical and Scientific Research," *Trans. Am. Nucl. Soc.* **74**, 2 (1996).
- Becker, D. A., and Brinkman, D. W., "Recycled Oil," (1996 Revision), *Kirk-Othmer Encyclopedia of Chemical Technology*, Fourth Edition, John Wiley & Sons, New York, 1996.
- Becker, D. A., Greenberg, R. R., Garrity, K. M., and Mackey, E. A., "Accurate Determination of 14 Elements in the New NIST Estuarine Sediment SRM 1646a by NAA," *Trans. Am. Nucl. Soc.* **73**, 4 (1995).
- Becker, D. A., Lindstrom, R. M., and Hosain, T. Z., "International Intercomparison for Trace Elements in Silicon Semiconductor Wafers by NAA," *Am. Inst. of Phys., Proc. Workshop on Semiconductor Characterization: Present Status and Future Needs* **335**, 341 (1996).
- Becker, D. A., Lindstrom, R. M., Langland, J. K., and Greenberg, R. R., "The New NIST Rapid Pneumatic Tube System," *J. Trace and Microprobe Tech.* **14**, 1 (1996).
- Becker, P. R., Mackey, E. A., Demiralp, R., Koster, B. J., and Wise, S. A., "Establishing Baseline Levels of Elements in Marine Mammals through Analysis of Banked Liver Tissues," *Special Publications of the American Chemical Society*, in press.
- Becker, P. R., Mackey, E. A., Demiralp, R., Schantz, M., Koster, B. J., and Wise, S. A., "Persistent Organochlorine, Pesticide Residues, and Trace Elements in Marine Specimens from the National Biomonitoring Specimen Bank at NIST," *Chemosphere*, in press.
- Behlke, M. K., Saraswati, R., Mackey, E. A., Demiralp, R., Vangel, M. G., Levenson, M. S., Mandic, V., Azemard, S., Horvat, M., Morrow, M., Emmons, H., and Wise, S. A., "Certification of Three Mussel Tissue Standard Reference Materials (SRMs) for Methylmercury and Total Mercury Content," *Fres. J. Anal. Chem.*, in press.
- Bender, J. W., Wagner, N. J., "Optical Measurement of the Contributions of Colloidal Forces to the Rheology of Concentrated Suspension," *J. Coll. and Interface Sci.* **172**, 171 (1995).
- Bender, J., Wagner, N. J., "Reversible Shear Thickening in Monodisperse and Bidisperse Colloidal Dispersions," *J. Rheol.* **40**, 899 (1996).
- Bender, J. W., Wagner, N. J., "Structure and Rheology Relations in Colloidal Suspensions: Shear Thinning and Shear Thickening Properties of Dense Suspensions," *Proc. of the AIChE International Forum on Fine Particle Technology*, Denver, 1994.
- Benmouna, M., Hammouda, B., "The Zero Average Contrast Condition," *Prog. in Polymer Science* (in press, 1996).
- Benenson, R., E., Chen-Mayer, H. H., and Sharov, V. A., "A Portable Time of Flight System for Thermal and Cold Neutron Applications," *Rev. Sci. Instrum.*, in press.
- Bergenholtz, J., Romagnoli, A. A., Wagner, N. J., "Viscosity, Microstructure, and Interparticle Potential of AOT/H₂O/n-Decane Inverse Microemulsions," *Langmuir*, 1559 (1995).
- Briber, R. M., Liu, X., Bauer, B. J., "The Collapse of Free Polymer Chains in a Network," *Science* **268**, 395 (1995).
- Butera, R. J., Wolfe, M. S., Bender, J., Wagner, N. J., "Formation of a Highly Ordered

- Colloidal Microstructure upon Flow Cessation from High Shear Rates." *Phys. Rev. Lett.* **77**, 2117 (1996).
- Butler, B. D., Hanley, H. J. M., Straty, G. C., Muzny, C. D., "Gelation under Shear," *Mat. Res. Soc. Symp. Proc.* **376**, (MRS, Pittsburgh, 1995), in press.
- Butler, B. D., Muzny, C. D., Hanley, H. J. M., "Dynamic Structure Factor Scaling in Dense Gelling Silica Suspensions," *J. Phys.: Condens. Matter* **8**, 9457 (1996).
- Carlson, A. D., "Status of the NEANSC Subgroup Working on Improving the $^{10}\text{B}(n, \alpha)$ Standard Cross Sections," *Proc. of the 9th Intl. Symp. on Reactor Dosimetry*, 1996.
- Briber, R. M., Fodor, J. S., Russell, T. P., Miller, R. D., Carter, D. R., Hedrick, J. L., "Characterization of Thin Polymeric Nanofoam Films by Transmissions Electron Microscopy and Small Angle Neutron Scattering," *Proceedings of the Materials Research Society Fall Meeting 1996*, in press.
- Chen-Mayer, H. H., Lamaze, G. P., Mildner, D. F. R., and Downing, R. G., "Neutron Depth Profiling Using a Focused Neutron Beam," in *Neutrons in Research & Industry*, in press.
- Chen-Mayer, H. H., Sharov, V. A., Mildner, D. F. R., Downing, R. G., Paul, R. L., Lindstrom, R. M., Zeissler, C. J., and Ziao, Q. F., "Capillary Neutron Optics for Prompt Gamma Activation Analysis," *J. Radioanal. Nucl. Chem.*, in press.
- Chen-Mayer, H. H., Mildner, D. F. R., Sharov, V. A., Ullrich, J. B., Ponomarev, I., Yu, and Downing, R. G., "Monolithic Polycapillary Neutron Focusing Lenses: Experimental Characterizations," *J. Phys. Soc. Japan*, in press.
- Chow, M. K., Zukoski, C. F., "Gap Size and Shear History Dependencies in Shear Thickening of a Suspension Ordered at Rest," *J. Rheology* **39**, 15 (1995).
- Chow, M. K., Zukoski, C. F., "Nonequilibrium Behavior of Dense Suspensions of Uniform Particles: Volume Fraction and Size Dependence of Rheology and Microstructure," *J. Rheology* **39**, 33 (1995).
- Coakley, K. J., Downing, R. G., and Lamaze, G. P., "Modeling Detector Response for Neutron Depth Profiling," *Nucl. Instrum. Meth.*, **A366**, 137 (1996).
- Cook, J. C., "IN5 Primary Septrometer Upgrade Design Study," ILL internal report No. ILL963CO10T, ILL-Report 96G010T, 1996.
- Cunningham, W. C., and Becker, D. A., "Analytical Uncertainty and Complexity in Development of an INAA Method," *Trans. Am. Nucl. Soc.* **73**, 10 (1995).
- Dannon, Y., Moore, M. S., Koehler, P. E., Littleton, P. E., Miller, G. G., Ott, M. A., Rowton, L. J., Taylor, W. A., Wihelmy, J. B., Yates, M. A., Carlson, A. D., Hill, N. W., Harper, R., and Hilko, R., "Fission Cross-Section Measurements of the Odd-Odd Isotopes ^{232}Pa , ^{236}Np ," *Nuc. Soc. Eng.*, in press.
- Dender, D., Lefmann, K., Reich, D., Broholm, C., Aeppli, G., "Neutron Scattering Study of the $S = 1/2$ 1D Heisenberg Antiferromagnet Copper Benzoate," *Phys. Rev. B*, in press.
- Downing, R. G., Iyengar, G. V., "Methodological Issues in the Analytical Determination of Boron," *Environ. Health Perspect.*, in press.
- Downing, R. G., and Lamaze, G. P., "Non-destructive Characterization of Semiconductor Materials Using Neutron Depth Profiling," *Proc. Intl. Workshop on Semiconductor Characterization: Present Status and Future*

- Needs, (AIP Press, Woodbury, NY, 1996), p. 346.
- Downing, R. G., and Lamaze, G. P., "Near Surface Profiling of Semiconductor Materials Using Depth Profiling," *Semicond. Sci. Tech.* **10**, 1423 (1995).
- Factor, B. J., Mopsik, F. I., Han, C. C., "Dielectric Behavior of a Polycarbonate/Polyester Mixtures Upon Transesterification," *Macromol.*, in press.
- Feng, Y., Weiss, R. A., Karim, A., Han, C. C., Ankner, J. F., Peiffer, D. G., "Kinetics of Mixing at Polymer-Polymer Interface Capable of Forming Intermolecular Complexes," *ACS Polymer*, in press.
- Fetters, L. J., Balsara, N. P., Huang, J. S., Jeon, H. S., Almadal, K., Lin, M. Y., "Aggregation in Living polymer Solutions by Light and Neutron Scattering," *Macromol.* **28**, 4996 (1995).
- Full, A. P., Kaler, E. W., Arellano, J., Puig, J. E., "Microemulsion Polymerization of Styrene: The Effect of Salt and Structure," *Macromolecules* **29**, 2764 (1996).
- Garcia, A., Adelberger, E. G., Magnus, P. V., Swanson, H. E., Wietfeldt, F., E., Tengblad, O., and the ISOLDE Collaboration, "³⁷Ca Beta Decay and the Isobaric Multiplet Mass Equation," *Phys. Rev.*, **C51**, 3487 (1995).
- Gehlsen, M. D., Weimann, P. A., Bates, F. S., Mays, J. W., Wignall, G. D., "Synthesis and Characterization of Poly(vinylcyclohexane) Derivatives," *J. Polym. Sci., Polym. Phys.* **33**, 1527 (1995).
- Gentile, T. R., Thompson, A. K., and Snow, W. M., "Metastability-Exchange Optical Pumping of ³He for Neutron Polarizers," *Bulletin of the Am. Phys. Soc.* **40**, 1620 (1995).
- Greene, G. L., Thompson, A. K., and Dewey, M. S., "A Method for the Accurate Determination of the Polarization of a Neutron Beam Using a Polarized ³He Spin Filter," *Nucl. Instrum. Methods A356*, **177** (1995).
- Greenberg, R. R., "Unique Quality Assurance Aspects of Neutron Activation Analysis," *Proc. 9th Intl. Sym. on Trace Elements in Man and Animals*, in press.
- Grest, G. S., Fetters, L. J., Huang, J. S., Richter, D., "Star Polymers: Experiment Theory, and Simulation," *Adv. in Chem. Phys. XCIV*, ed. by I. Prigogine and A. R. Stuart (John Wiley and Sons, 1996), p. 67
- Guangyong, Xu, DiTusa, J. F., Ito, T., Takagi, H., Broholm, C., Aeppli, G., "Neutron Scattering Study of the One-Dimensional S=1 Antiferromagnet Y₂BaNiO₅," *Phys. Rev. B*, in press.
- Haight, R. C., Bateman, F. B., Grimes, S. M., Brient, C. E., Massey, T. N., Wasson, O. A., Carlson, A. D., and Zhou, H., "Measurement of the Angular Distribution of Neutron-Photon Scattering at 10 MeV," *Fusion Eng. and Design*, in press.
- Hanley, H. J. M., Muzny, C. D., Butler, B. D., "Surfactant Adsorption on a Clay Mineral: Application of Radiation Scattering," submitted to *Langmuir* (1996).
- He, K., Ludtke, S. J., Huang, H. W., Worcester, D. L., "Antimicrobial Peptide Pores in Membranes Detected by Neutron In-Plane Scattering," *Biochem.* **34**, 15614 (1995).
- He, K., Ludtke, S. J., Huang, H. W., Worcester, D. L., "Neutron Scattering in the Plane of Membranes: Structure of Alamethicin Pores," *Biophysical Journal* **70**, 2659 (1996).
- Held, G.A., Kosbar, L.L., Lowe, A.C., Afzali-Ardakani, A., Schroder, U.P., Chan, K.-P., Russell, T.P., Twieg, R.J., Miller, R.P., *Euro Display '96* **16**, 573 (1996).
- Hillmyer, M. A., Bates, F. S., "Influence of Crystallinity on the Morphology

- of Poly(ethyleneoxide) Containing Diblock Copolymers," *Macromol. Sym.*, in press.
- Hillmyer, M. A., Bates, F. S., Ryan, A., Fairclough, P., Almdal, K., Mortensen, K., "Complex Lyotropic-Like Phase Behavior in Solvent Free Surfactants," *Science* **271**, 976 (1996).
- Hjelm, R., P., Douglas, E., P., Benicewicz, B. C., "Solution Structure of Lipid-Crystal Polymers with Small Liquid-Crystal Thermoset Maleimides and Nadimides," *Inter. J. of Thermophysics* **16**, 309 (1995).
- Hjelm, R. P., Schteingart, C., Hofmann, A. F., Sivia, D. S., "Form and Structure of Self-Assembling Particles in Monoolein-Bile Salt Mixtures," *J. Phys. Chem.*, in press.
- Ikkai, F., Shibayama, M., Nomura, S., Han, C. C., "Complexation of Poly(vinyl alcohol)-Congo Red Aqueous Solutions. 3. Dynamic Light Scattering Study," *J. Polym. Sci.*, in press.
- Jach, T., Steel, E., Chen-Mayer, H. H., Ullrich, J., Downing, R. G. and Thurgate, S., "The Characterization of X-ray Polycapillary Optics with a High-resolution X-ray Optical Bench," in *Neutrons in Research & Industry*, Proc. 5th Intl. Conf. on Application of Nuclear Techniques, in press.
- Jacobson, D. L., Allman, B. E., Zawisky, M., Werner, S. A., and Rauch, H., "Neutron Interferometric Measurement of Neutron Pair Correlations for Multiple Detectors," *J. Phys. Soc. Jap.*, in press.
- Jackson, C. L., Barnes, K. A., Morrison, F. A., Mays, J. W., Nakatani, A. I., Han, C. C., "A Shear-induced Martensitic-like Transformation in a Block Copolymer Melt," *Macromol.*, in press.
- Johnson, J. R., Thompson, A. K., Chupp, T. E., Smith, T. B., Cates, G. D., Driehuys, B., Middleton, H., Newbury, N. R., Hughes, E. W., and Meyer, W., "The SLAC High-Density Gaseous Polarized ^3He Target," *NIM A* **356**, 148 (1995).
- Karayianni, E., Jérôme, R., Cooper, S. L., "Small-Angle Neutron Scattering Studies of Low-Polarity Telechelic Ionomer Solutions in Total Scattering," *Macromol.* **28**, 6494 (1995).
- Khandpur, A. K., Forster, S., Bates, F. S., Hamley, I. W., Ryan, A. J., Bras, W., Almdal, K., Mortensen, K., "The Polysoprene-Polystyrene Diblock Copolymer Phase Diagram Near the Order-Disorder Transition," *Macromol.* **28**, 8796 (1995).
- Kline, S. R., Kaler, E. W., "Aggregation of Colloidal Silica by n-Alkyl Sulfates," *Langmuir* **12**, 2402 (1996).
- Kline, S. R., Kaler, E. W., "Interactions in Binary Mixtures: Partial Structure Factors in Mixtures of Sodium Dodecyl Sulfate Micelles and Colloidal Silica," *J. Chem. Phys.* **105**, 3813 (1996).
- Krishnamoorti, R., Graessley, W. W., Dee, G. T., Walsh, D. J., Fetters, L. J., Lohse, D. J., "Pure Component Properties and Mixing Behavior in Polyolefin Blends," *Macromol.* **29**, 367 (1996).
- Koneripalli, N., Levicky, R., Bates, F. S., Ankner, J., Kaiser, Satija, S. K., "Confined-Induced Morphological Changes in Diblock Copolymer Films," *Langmuir*, in press.
- Kuznetsov, I. A., Serebrov, A. P., Stepanenko, I. V., Alduschenkov, A. V., Lasakov, M. S., Kokin, A. A., Yu, A., Mostovoi, A., Yerozolimsky, B. G., and Dewey, M. S., "Measurements of the Antineutrino Spin Asymmetry in Beta Decay of the Neutron and Restrictions on the Mass a Right-handed Gauge Boson," *Phys. Rev. Lett.* **75**, 794 (1995).

- Lamaze, G. P., "A High Efficiency Device for the Detection of Radioactive Xenon Isotopes," Nucl. Instru. Meth., in press.
- Lamaze, G. P., Chen-Mayer, H. H., Langland, J. K., and Downing, R. G., "Neutron Depth Profiling with the New NIST Cold Neutron Source," Surface & Interface Anal., in press.
- Lamaze, G. P., Downing, R. G., "Boron Analysis in Synthetic Diamond Films Using Cold Neutron Depth Profiling," Proc. of the Intl. Workshop on Semiconductor Characterization: Present and Future Needs, Vol. 351 (1996).
- Lauenstein, G. G., Cantillo, A. Y., Koster, B. J., Schantz, M. M., Stone, S. F., Zeisler, R. L., and Wise, S. A., "National Status and Trends Program Speciment Bank: Sampling Protocols, Analytical Methods, Results, and Archive Samples," NOAA Tech. Memorandum NOS ORCA 98, 158 (1996).
- Lin, C. C., Jonnalagadda, S. V., Balsara, N. P., Han, C. C., Krishnamoorti, R., "Neutron Scattering from Multicomponent Flory-Huggins Blends," Macromol. 29, 661 (1996).
- Lin, M. Y., Sinha, S. K., Hanley, H. J. M., Straty, G. C., Peiffer, D. G., Kim, M. W., "Shear-induced Behavior in a Solution of Cylindrical Micelles," Phys. Rev. E 53, R4302 (1996).
- Lindstrom, R. M., Anderson, D. L., and Paul, R. L., "Analytical Applications of Neutron Capture Gamma Rays," Proc. of 9th Int. Symp. on Neutron-Capture Gamma-Ray Spectroscopy and Related Topics, in press.
- Lindstrom, R. M., Ammerlaan, M. J. J., and Then, S. S., "Loss-Free Counting at IRI and NIST", J. Trace Microprobe Tech, 14, 67 (1996).
- Lindstrom, R. M., Becker, D. A., Langland, J. K., and Greenberg, R. R., "The NIST Rapid Irradiation and Counting System," J. Radioanal. Nucl. Chem. in press.
- Lindstrom, R. M., and Asvavijitkulchai, C., "Ensuring Accuracy in Spreadsheet Calculations," Trans. Am. Nucl. Soc. 74, 19, (1996).
- Lindstrom, R. M., Paul, R. L., Heald, A. E., and Langland, J. K., "Improved Cold-Neutron Prompt Gamma Spectrometer," Trans. Am. Nucl. Soc. 74, 106 (1996).
- Lising, L. J., Freedman, S. J., Wasserman, E. G., Fujikawa, B. K., Wilkerson, J. F., Robertson, R. G. H., Elliott, S. R., Greene, G. L., Dewey, M. S., Nico, J. S., Thompson, A. K., Wietfeldt, F. E., Chupp, T. E., Coulter, K. P., Hwang, S., Garcia, A., and Bowles, T. J., "Progress in the Search for Time-Reversal Invariance Violation in Neutron Decay," Bulletin of the Amer. Phys. Soc. 40, 1025 (1995).
- Liu, X., Bauer, B.J., Briber, R.M., "The Conformation of Free Linear Polymer Chains in a Polymer Network", Macromol., in press.
- Liu, Y. C., Chen, S. H., Huang, J. S., "Relationship between the Microstructure and Rheology of Polymeric Micellar Solutions," Phys. Rev. E 54, 1698 (1996).
- Lodge, T. P., Pan, C., Jin, X., Liu, Z., Zhao, J., Maurer, W. W., Bates, F. S., "Failure of the Dilution Approximation in Block Copolymer Solutions," J. Polym. Sci., Phys. 33, 2289 (1995).
- Lusvardi, K. M., Full, A. P., Kaler, E. W., "Mixed Micelles of Dodecyltrimethylammonium Bromide," Langmuir 11, 487 (1995).
- Mackey, E. A., Anderson, D. L., Chen-Mayer, H. H., Downing, R. G., Lamaze, G. P., Lindstrom, R. M., Mildner, D. F. R., Paul, R. L., Greenberg, R. R., "Use of Neutron Beams for Chemical Analysis at NIST," J. Radioanal. Nucl. Chem., 203, 413 (1996).

- Mackey, E. A., Becker, P. R., Demiralp, R., Koster, B. J., Greenberg, R. R., and Wise, S. A., "Bioaccumulation of V and Other Trace Elements in the Liver Tissues of Alaskan Cetaceans," *Arch. Environ. Contam. Toxicol.* **30**, 503 (1996).
- Mackey, E. A., Demiralp, R., Becker, P. R., Koster, B. J., Greenberg, R. R., Wise, S. A., "Trace Element Concentrations in Cetacean Liver Tissues Archived in the National Bio-monitoring Specimen Bank," *Sci. Tot. Environ.*, in press.
- Mackey, E. A., Demiralp, R., Becker, P. R., Wise, S. A., Greenberg, R. R., Early, G., Koster, B. J., "Accumulation of Vanadium, Selenium, Silver, Cadmium, and Mercury in Marine Mammal Livers," *Ann. Clin. Lab. Sci.*, in press.
- Mang, J., Kumar, S., Hammouda, B., "Lyotropic Liquid Crystals under Simple Couette and Oscillatory Shear," *Proc. of Liquid Crystals Conference*, Kent, OH, June 1996, in press.
- Mason, T.G., Palmer, A., Wirtz, D., "Hyper-swollen Vesicles Containing Nematic Liquid Crystal," submitted to *Phys. Rev. E* (1996).
- Matsushita, Y., Torikai, N., Mogi, Y., Noda, I., Han, C. C., "Chain Conformations of Homopolymers Dissolved in a Microdomain of Diblock Copolymer," *Macromol.*, in press.
- Mayer, R. R., Welsh, J., and Chen-Mayer, H., "Focused Neutron Beam Dose Deposition Profiles in Tissue Equivalent Materials: A Pilot Study for BNCT," *Proc. 5th Intl. Conf. on Applications of Nuclear Techniques*, in press.
- McGarry, E. D., Adams, J. M., et al., USNRC Draft Regulatory Guide: DG-1053, "Calculational and Dosimetry Methods for Determining Pressure Vessel Neutron Fluence," United States Nuclear Regulatory Commission, Office of Nuclear Regulatory Research, 1996.
- Mildner, D. F. R., Chen-Mayer, H. H., and Downing, R. G., "Characteristics and Applications of a Polycapillary Neutron Focusing Lens," *Proc. Intl. Symp. on Advances in Neutron Optics and Related Research Facilities*, J. Phys. Soc. Japan, in press.
- Mildner, D. F. R., Chen-Mayer, H. H., Sharov, V. A., "Neutron Focussing Lens Using Capillary Optic," *Proc. 9th Intl. Symp. on Capture Gamma Spectroscopy and Related Topics*, in press.
- Mildner, D. F. R., Chen, H., Sharov, V. A., "Restricted Neutron Transmission Through a Cylindrical Guide Tube," *J. Appl. Cryst.* **28**, 793 (1995).
- Mildner, D. F. R., Chen, H., Sharov, V. A., Downing, R. G., and Xiao, Q. F., "Gain for Neutron Polycapillary Lens as a Function of Wavelength," *Physica B* **213 & 214**, 966 (1995).
- Mildner, D. F. R., Chen-Mayer, H. H., Sharov, V. A., Fokin, V. S., and Feeder, P. L., "The Number of Reflections for Neutron Transmission Through Cylindrical Channels," *J. Appl. Cryst.*, in press.
- Mildner, D. F. R., Sharov, V. A., and Chen-Mayer, H. H., "Neutron Transmission Through Tapered Channels," *J. Appl. Cryst.*, in press.
- Muzny, C. D., Butler, B. D., Hanley, H. J. M., Tsvetkov, F., Peiffer, D. G., "Clay Platelet Dispersion in a Polymer Matrix," *Materials Letters* **28**, 379-384 (1996).
- Muzny, C. D., Butler, B. D., Hanley, H. J. M., "Evolution of the Structure Factor in Gelling Dense Colloidal Silica," *Mat. Res. Soc. Symp. Proc. Vol. 407*, 87 (1996).

- Muzny, C. D., Hansen, D., Straty, G. C., Evans, D. J., Hanley, H. J. M., "Simulation and SANS Studies of Gelation under Shear," Int. J. Thermophysics, in press.
- Nakatani, A. I., Morrison, F. A., Doublas, J. F., Mays, J. W., Jackson, C. L., Muthukumar, M., Han, C. C., "Shear-Induced Shifts in the Order-Disorder Transition Temperature in a Triblock Copolymer Melt", J. Chem. Phys, in press.
- Nico, J. S., Adams, J. M., Eisenhauer, C., Gilliam, D. M., and Grundl, J. A., "²⁵²Cf Fission Neutron Transport Through an Iron Sphere," 9th Intl. Symp. on Reactor Dosimetry, 1996.
- Nico, J. S., with EMIT Collaboration, "Search for Time-Reversal Non-Invariance in Neutron Beta Decay," to be published in XXIth Moriond Conference on Dark Matter in Cosmology, Clocks, and Tests of Fundamental Symmetries, Switzerland, 1995.
- Ondov, J. M. "Size-Spectra, Growth, and Deposition of Urban Aerosol Particles Bearing Minor and Trace Elements from Generic Sources", NATO ASI Series, in press.
- Ondov, J. M., Quinn, T. L., "Influence of Humidity on Aerosol Size and Dry Deposition Fluxes of Trace Elements," in *Atmospheric Deposition of Contaminants to the Great Lakes and Coastal Waters*, SETAC Special Publications Series, edited by J. E. Baker, in press.
- Ottewill, R. H., Rennie, A. R., "Interaction Behaviour in a Binary Mixture of Polymer Particles," Trends in Colloid and Interface Science 100, 60 (1996).
- Parr, R. M., Stone, S. F., and Zeisler, R. L., "Air Pollution Monitoring and Research Using Nuclear Analytical Techniques," IAEA Bulletin, 1996.
- Parr, R. M., Stone, S. F., and Zeisler, R. L., "Environmental Protection: Nuclear Analytical Techniques I Air Pollution Monitoring and Research," IAEA Bulletin 38, 16 (1996).
- Paul, R. L., "Hydrogen Measurements by Prompt Gamma-ray Activation Analysis at NIST," The Analyst, in press.
- Paul, R. L., and Lindstrom, R. M., "Applications of Cold Neutron Prompt Gamma Activation Analysis to Characterization of Semiconductors," Proc. Intl. Workshop on Semiconductor Characterization Present Status and Future Needs, AIP, 342 (1996).
- Paul, R. L., and Lindstrom, R. M., "Cold Neutron Prompt Gamma-ray Activation Analysis at NIST-Current Status," Proc. 9th Intl. Symp. on Capture Gamma-Ray Spectroscopy and Related Topics, in press.
- Paul, R. L., and Lindstrom, R. M., "Measurements of k_0 -factors for Prompt Gamma-Ray Activation Analysis," Proc. 2nd Int'l. k_0 Users Workshop, in press.
- Paul, R. L., and Lindstrom, R. M., "Cold Neutron Prompt Gamma-ray Activation Analysis at NIST-Recent Developments," J. Radioanal. Nucl. Chem., in press.
- Paul, R. L., Privett, H. M., Lindstrom, R. M., Richards, W. J., Greenberg, R. R., "Analysis of Hydrogen in Titanium Alloys by Cold Neutron Prompt Gamma Activation Analysis," Metall. Trans. A, in press.
- Paul, R. L., and Lindstrom, R. M., "Cold Neutron Prompt Gamma-ray Activation Analysis at NIST-Current Status," Proc. 9th Intl. Symp. on Capture Gamma-Ray Spectroscopy and Related Topics, in press.
- Pitt, M. L., Ackerstaff, K., Carr, R. W., Court, G. R., DeSchepper, D., Dvoredsky, A., Gentile, T. R., Golendoukhin, A., Kelsey, J. F.,

- Korsch, W., Kramer, L. H., Li, Y., McKown, R. D., Milner, R., G., Niczyporuk, M., Pate, S. F., Shin, T., Sowinski, J., Steffens, E., Stewart, J., Stock, F., Wise, T., and Zapf-Duren, J., "TOM: A Target Optical Monitor of Polarization and Luminosity for Polarized Internal Gas Targets," Proc. of the Intl. Workshop on Polarized Beams and Polarized Gas Targets," Proc. of the Intl. Workshop on Polarized Beams and Polarized Gas Targets, edited by H. Paetz Gen. Schieck and L. Sydow, World Scientific, Singapore, 1996.
- Rice, B. M., Mattson, W., Grosh, J., Trevino, S. F., "Molecular Dynamics Study of Detonation: I. A Comparison with Hydrodynamic Predictions." Phys. Rev. B. **53**, 611 (1996).
- Rice, B. M., Mattson, W., Grosh, J., Trevino, S. F., "Molecular Dynamics Study of Detonation: II. The Reaction Mechanism," Phys. Rev. B **53**, 623 (1996).
- Sakurai, K., MacKnight, W. J., Lohse, D. J., Schulz, D. N., Sissano, J. A., Lin, J. S., Agamalyan, M., "Blends of Amorphous-Crystalline Block Copolymers with Amorphous Homopolymers. Morphological Studies by Electron Microscopy and Small Angle Scattering," Polymer **37**, 4443 (1996).
- Schulz, M. F., Khandpur, A. K., Bates, F. S., Almdal, K., Mortensen, K., Haikuk, D. A., Gruner, S., M., "Phase Behavior of PS-PVP Diblock Copolymers," Macromol. **29**, 2857 (1996).
- Singh, N., Kudrie, A., Sikka, M., Bates, F. S., "Surface Topography of Symmetric and Asymmetric Polyolefin Block Copolymer Films," J. Phys II (France) **5**, 377 (1995).
- Skripov, A. V., Cook, J. C., Karmonik, C. and Hempelmann, R., "Localized Motion of 4 Atoms in C15-type TaV₂: A Quasielastic Neutron Scattering Study," J. Phys. Cond. Matt. **8**, L319 (1996).
- Sottmann, T., Strey, R., Chen, H.-S., "A SANS Study of Nonionic Surfactant Molecules at the Water-Oil Interface: Area per Molecule, Microemulsion Domain Size and Rigidity," J. Chem. Phys., in press.
- Stone, D. B., Schneider, D. K., Huang, Z., Mendelson, R. A., "The Radius of Gyration of Native and Reductively Methylated Myosin Subfragment-1 from Neutron Scattering," Biophys. J. **69**, 767 (1995).
- Strey, R., Glatter, O., Schubert, K.-V., Kaler, E. W., "Small-Angle Scattering (SANS) of D₂O - C₁₂E₅ Mixtures and Microemulsions with n-Octane: Direct Analysis by Fourier Transformation," J. Chem. Phys. **105**, 1175 (1996).
- Summhammer, J., Hamacher, K. A., Kaiser, H., Weinfurter, H., Jacobson, D. L., and Werner, S. A., "Multiphoton Exchange Amplitudes Observed by Neutron Interferometry," Phys. Rev. Lett. **75**, 3206 (1995).
- Tandon, L., Garrity, K. A., and Becker, D. A., "Determination of Selected Elements in SRM 1548a, Typical Diet," Trans. Am. Nucl. Soc. **74**, 20 (1996).
- Tepe, T., Schulz, M. F., Zhao, J., Tirrell, M., Bates, F. S., Mortensen, K., Almdal, K., "Variable Shear-Induced Orientation of a Diblock Copolymer Hexagonal Phase," Macromol. **28**, 3008 (1995).
- Thompson, A. K., Gentile, T. R., "Status of the NIST Spin Filter Project," J. Neut. Res., in press.
- Wagh, A. G., Rakhecha, V. C., Summhammer, J., Badurek, G., Weinfurter, H., Allman, B. E., Kaiser, H., Hamacher, K., Jacobson, D. L., and Werner, S. A., "Neutron Interferometric Separation of Geometric and Dynamical Phases," J. Phys. Soc. Jap., in press.

- Walker, L. M., Wagner, N. J., "SANS Analysis of the Molecular Order in Poly(*g*-benzyl L-glutamate)/Deuterated Dimethylformamide (PBLG/*d*-DMF) under Shear and during Relaxation," *Macromolecules* **29**, 2298 (1996). Thompson, A. K., Gentile, T. R., and Dewey, M. S., "Progress on Creation of Cold Neutron Spin Filter at NIST Using Polarized ^3He ," *Bulletin of the Amer. Phys. Soc.* **40**, 1620 (1995).
- Weissmüller, J., McMichael, R. D., Barker, J. G., Brown, H. J., Erb, U., Shull, R. D., "Magnetic Microstructure of a Nanocrystalline Ferromagnet-Miromagnetic Model and Small-Angle Neutron Scattering," *Proceedings of the MRS Fall Meeting, Boston, 1996*, in press.
- Wietfeldt, F. E., and Norman, E. B., "The 17 keV Neutrino," *Physics Reports*, **237**, 150 (1996).
- Wietfeldt, F. E., Norman, E. B., Chan, Y. D., da Cruz, M. T. F., Garcia, A., Haller, E. E., Hansen, W. L., Hindi, M. M., Larimer, R. M., Lesko, K. T., Luke, P. N., Stokstad, R. G., Sur, B., and Zlimen, I., "Further Studies on the Evidence for a 17-keV Neutrino in a ^{14}C -doped Germanium Detector," *Phys. Rev. C* **52**, 1028 (1995).
- Xiao, Q. F., Sharov, V. A., Downing, R. G., Chen-Mayer, H. H., and Mildner, D. F. R., "Neutron Beam Control Using Polycapillary," *Proc. Intl. Symp. on Advances in Neutron Optics and Related Research Facilities*, *J. Phys. Soc. of Japan*, in press.
- Xiao, Q. F., Sharov, V. A., Gibson, D. M., Chen, H., Mildner, D. F. R., and Downing, R. G., "Capillary Neutron Optics for Boron Neutron Capture Therapy," *Proc. 6th Intl. Symp. on Neutron Capture Therapy for Cancer*, in press.
- Xu, G., DiTusa, F., Ito, T., Takagi, H., Broholm, C., Aeppli, G., "Neutron Scattering Study of the One-Dimensional $S = 1$ Antiferromagnet," *Phys. Rev. B*, in press.
- Ye, X., Narayanan, T., Tong, P., Huang, J. S., Lin, M. Y., Carvalho, B. L., Fetters, L. J., "Depletion Interactions in Colloid-Polymer Mixtures," *Phys. Rev. E* **54**, 6500 (1996).
- Young, A. M., Timbo, A. M., Higgins, J. S., Peiffer, D. G., Lin, M. Y., "Thermodynamics of Aggregation in Associating Ionomer Solutions," *Polymer* **37**, 2701 (1996).
- Zhao, J., Majumdar, B., Schulz, M. F., Bates, F. S., Almdal, K., Mortensen, K., Hajduk, D. A., Grunner, S. M., "Phase Behavior of Pure Diblocks and Binary Diblock Blends of PE-PEE," *Macromol.* **29**, 1204 (1996).
- Zeisler, R. L., "Environmental Specimen Banking: Contributions to Quality Management of Environmental Measurements," *Amer. Chem. Soc. Spec. Pub. on Environmental Monitoring and Specimen Banking*, ACS Symp. Series, in press.
- Zeisler, R. L., Haselberger, N., Makarewicz, M., Ogris, R., Parr, R. M., Stone, S. F., Valkovic, O., Valkovic, V., and Wehrstein, E., "Nuclear Techniques Applied to Air Particulate Matter Studies," *J. Radionanal Nucl. Chem.*, in press.
- Zeisler, R. L., Markarewicz, M., Grass, F., and Casta, J., "A New Facility for Rapid Neutron Activation Analysis," *Trans. Am. Nucl. Soc.* **74**, 104 (1996).
- Zeisler, R. L., Valkovic, V., and Rossbach, M., "Development of Natural Matrix Reference Materials for Micro-Analytical Nuclear Techniques," *Trans. Am. Nucl. Soc.* **74**, 20 (1996).
- Zielinski, R. G., Kaler, E. W., Paulaitis, M. E., "Microstructure in $\text{D}_2\text{O}/n$ -Hexaethylene Glycol Monododecyl Ether (C_{12}E_6)/ CO_2 Mixtures Determined by Small-Angle Neutron Scattering," *J. Phys. Chem.* **99**, 10354 (1995).

